

Decay and Snapback in Superconducting Accelerator Magnets

Markus Haverkamp

2003

Ph.D. thesis
University of Twente



Twente University Press

Also available in print:

<http://www.tup.utwente.nl/catalogue/book/index.jsp?isbn=9036519500>

Decay and Snapback in Superconducting Accelerator Magnets

Promotiecommissie

Voorzitter:	Prof. dr. ir. A. Blik	Universiteit Twente TNW
Promotor:	Prof. dr. ir. H.H.J. ten Kate	Universiteit Twente TNW
Assistent-promotor:	Dr. ir. B. ten Haken	Universiteit Twente TNW
Deskundige:	Dr. L. Bottura	CERN, Zwitserland
Leden:	Prof. dr. ing. B. van Eijk	Universiteit Twente TNW / NIKHEF
	Prof. dr. H. Rogalla	Universiteit Twente TNW
	Prof. dr. G. van Middelkoop	Vrije Universiteit / NIKHEF
	Prof. dr. G.C. Damstra	TU Eindhoven

The project described in this thesis was carried out as a collaboration between the LHC-MTA group at the European Organisation for Nuclear Research (CERN) in Geneva, Switzerland, and the Low Temperature Division in the Faculty of Science and Technology at the University of Twente in Enschede, The Netherlands. The research has been partially supported by the Technology Foundation STW, applied science division of NWO and the technology programme of the Dutch Ministry of Economic affairs.



Twente University **Press**

Publisher:
Twente University Press,
P.O. Box 217, 7500 AE Enschede, the Netherlands,
www.tup.utwente.nl

Print: Océ Facility Services, Enschede

© M. Haverkamp, Enschede, 2003
No part of this work may be reproduced by print,
photocopy or any other means without the permission
in writing from the publisher.

ISBN 9036519500

Cover design: Distribution of shielding currents in the cross section of a superconducting filament in the coil windings during decay and snapback.

DECAY AND SNAPBACK IN SUPERCONDUCTING ACCELERATOR MAGNETS

PROEFSCHRIFT

ter verkrijging van
de graad van doctor aan de Universiteit Twente,
op gezag van de rector magnificus,
prof. dr. F. A. van Vught,
volgens besluit van het College voor Promoties
in het openbaar te verdedigen
op donderdag 16 oktober 2003 te 16.45 uur

door

Markus Haverkamp
geboren op 4 maart 1972
te Haltern (Duitsland)

Dit proefschrift is goedgekeurd door:

Prof. dr. ir. H. H. J. ten Kate (promotor)

Dr. ir. B. ten Haken (assistent-promotor)

Contents

Chapter 1	Introduction	9
1.1	The Large Hadron Collider	9
1.2	Field quality	11
1.2.1	Multipole fields	11
1.2.2	Technical realization of superconducting accelerator magnets	12
1.2.3	Definition of the field quality in the LHC dipoles	13
1.2.4	Field errors in the LHC dipoles	14
1.2.5	Decay and snapback	15
1.2.6	Compensation of decay and snapback in the LHC	18
1.3	Scope of the thesis	19
Chapter 2	Superconducting Accelerator Magnets	23
2.1	Superconductivity	23
2.1.1	Flux flow, flux creep and the voltage current relation	25
2.1.2	Magnetic behavior	27
2.2	Main dipoles and operating cycles	30
2.3	Coil geometry and field quality	32
2.4	Rutherford cable	36
2.5	Superconducting NbTi wires	38
2.6	Boundary Induced Coupling Currents (BICCs)	40
2.7	Spatially periodic field pattern	43
2.8	Decay and snapback	45
2.8.1	Self-field induced decay	46
2.8.2	Decay induced by field changes in the coil	46
2.8.3	Snapback	47
2.9	Conclusion	47
Chapter 3	Magnetization Measurements on Wires and Coils	49
3.1	Magnetization measurements on small samples	49
3.2	Magnetization measurements on dipole magnets	50
3.2.1	Magnets tested	50
3.2.2	Test facilities	51
3.2.2.1	1 m model dipoles in the ‘Block-4’ laboratory	51
3.2.2.2	15 m long dipoles in the ‘SM-18’ laboratory	52
3.2.3	Rotating coil measurements	53
3.2.4	Measurements with Hall plates	56
3.2.4.1	Basic sextupole sensor (model 1)	58
3.2.4.1.1	Mechanical arrangement	59
3.2.4.1.2	Hall plates	61
3.2.4.1.3	Cabling and acquisition	62
3.2.4.1.4	Calibration	64
3.2.4.2	New version with sextupole and decapole rings	65

3.3	Conclusion	68
Chapter 4 Dependence of Field Decay on the Excitation History		69
4.1	Systematic distribution of harmonics	69
4.2	Correlation between different harmonics	70
4.3	Excitation history	72
4.3.1	Model for the field decay	72
4.3.2	Measurements on short LHC dipole model magnets	73
4.3.2.1	Decay during injection	74
4.3.2.2	Variation of pre-cycle parameters	75
4.3.2.2.1	Flat-top current	75
4.3.2.2.2	Flat-top duration	77
4.3.2.2.3	Pre-cycle ramp rate	80
4.3.2.2.4	Multiple pre-cycles	81
4.3.2.3	Injection reproducibility	82
4.3.2.4	Pre-injection current and duration	84
4.3.2.4.1	Pre-injection current	84
4.3.2.4.2	Pre-injection duration	85
4.3.2.5	Injection parameters	86
4.3.2.5.1	Ramp rate to injection	86
4.3.2.5.2	Injection current	87
4.3.2.5.3	Ramp rate after injection	89
4.4	Conclusion	90
Chapter 5 Filament Magnetization		93
5.1	Numerical model	95
5.2	Formulas for filament magnetization	97
5.2.1	Filament with constant critical current density	97
5.2.2	Filament with field dependent critical current density	100
5.3	Determination of the $J_c(B)$ dependence	101
5.4	Formula development for applied fields with arbitrary direction	104
5.4.1	Impact of a single field sweep with arbitrary direction on a saturated filament	106
5.4.2	Impact of a field sweep and a subsequent rise of the background field	110
5.4.3	Accuracy	115
5.5	Estimation of the flux creep contribution	115
5.6	Conclusion	116
Chapter 6 Decay and Snapback		117
6.1	Demonstration experiment	117
6.1.1	Decay	118
6.1.2	Snapback	122
6.2	Decay and Snapback in the real Accelerator Magnets	126
6.2.1	Magnet 18	126
6.2.2	Magnet 19	128
6.2.3	Magnet 20	131

6.3	Model for decay and snapback in a magnet	135
6.3.1	Details of the model	137
6.3.1.1	Strand positions	137
6.3.1.2	Calculation of the field induced by the currents in the strands	138
6.3.1.3	Penetration field and coil magnetization	141
6.3.1.4	Magnetization contribution to the field components in the center of the coil	142
6.3.1.5	Field changes induced by current redistributions ΔI_k among the strands	143
6.3.1.6	Magnetization changes induced by field changes $\Delta B_{decay}(\xi)$ in the coil	144
6.3.1.6.1	Self-field effect	145
6.3.1.6.2	Impact of the coil field	147
6.3.1.6.3	Impact of the magnetization changes on the field components	149
6.3.2	Analysis	149
6.3.2.1	Correlations between current distribution, spatially periodic field pattern and magnetization	149
6.3.2.1.1	Decay of the spatially periodic field pattern	150
6.3.2.1.2	Decay induced by the self-field in the strands	151
6.3.2.1.3	Decay induced by local field changes in the coil	152
6.3.2.2	Snapback curve	154
6.4	Conclusion	155
Chapter 7 Conclusions		159
Appendix A		163
References		165
Summary		169
Samenvatting		171
Dankwoord		174

Chapter 1

Introduction

A strict control of the temporal and spacial magnetic field uniformity is essential for maintaining particle beams in accelerators. In practice, magnets for high field superconducting particle accelerators like the Large Hadron Collider exhibit a ‘decay’ of the magnetic field and its components during long periods of constant current. The ‘decay’ is especially important during the injection of particles into the machine. As soon as the particles are accelerated and the current in the magnets is ramped up, the field rapidly recovers from the decay. This phenomenon is generally referred to as ‘snapback’. The two effects ‘decay’ and ‘snapback’ strongly affect the beam in the machine and have to be compensated precisely in order to avoid loss of particles. This thesis reports the results of an in-depth study of both effects. In addition, a novel detector is described. In contrast to other systems, the detector has sufficient time resolution during the snapback and can be used for systematic measurements on accelerator magnets or for the online compensation of ‘decay’ and ‘snapback’ in the machine.

1.1 The Large Hadron Collider

The Large Hadron Collider (LHC) at CERN in Geneva, Switzerland is the next major step in the European and worldwide activities on particle accelerators [26]. It will collide two counter rotating proton beams at a nominal center of mass energy of 14 TeV and a nominal luminosity of $10^{38} \text{ m}^{-2}\text{s}^{-1}$. In addition to protons also heavy ions will be brought into collision. Experiments with Pb nuclei ($Z = 82$) will reach collision energies of up to $2 \cdot Z \cdot 7 \text{ TeV} \approx 1150 \text{ TeV}$ and luminosities of up to $10^{31} \text{ m}^{-2}\text{s}^{-1}$.

The LHC accelerator ring is built into the existing 26.7 km long tunnel of the previous Large Electron Positron Collider (LEP) at CERN. The circumference is functionally divided into octants. A structural drawing is shown in figure 1.1. Particles will collide in four points on the ring, corresponding to the so-called insertion points (IP) 1, 2, 5 and 8 in the picture.

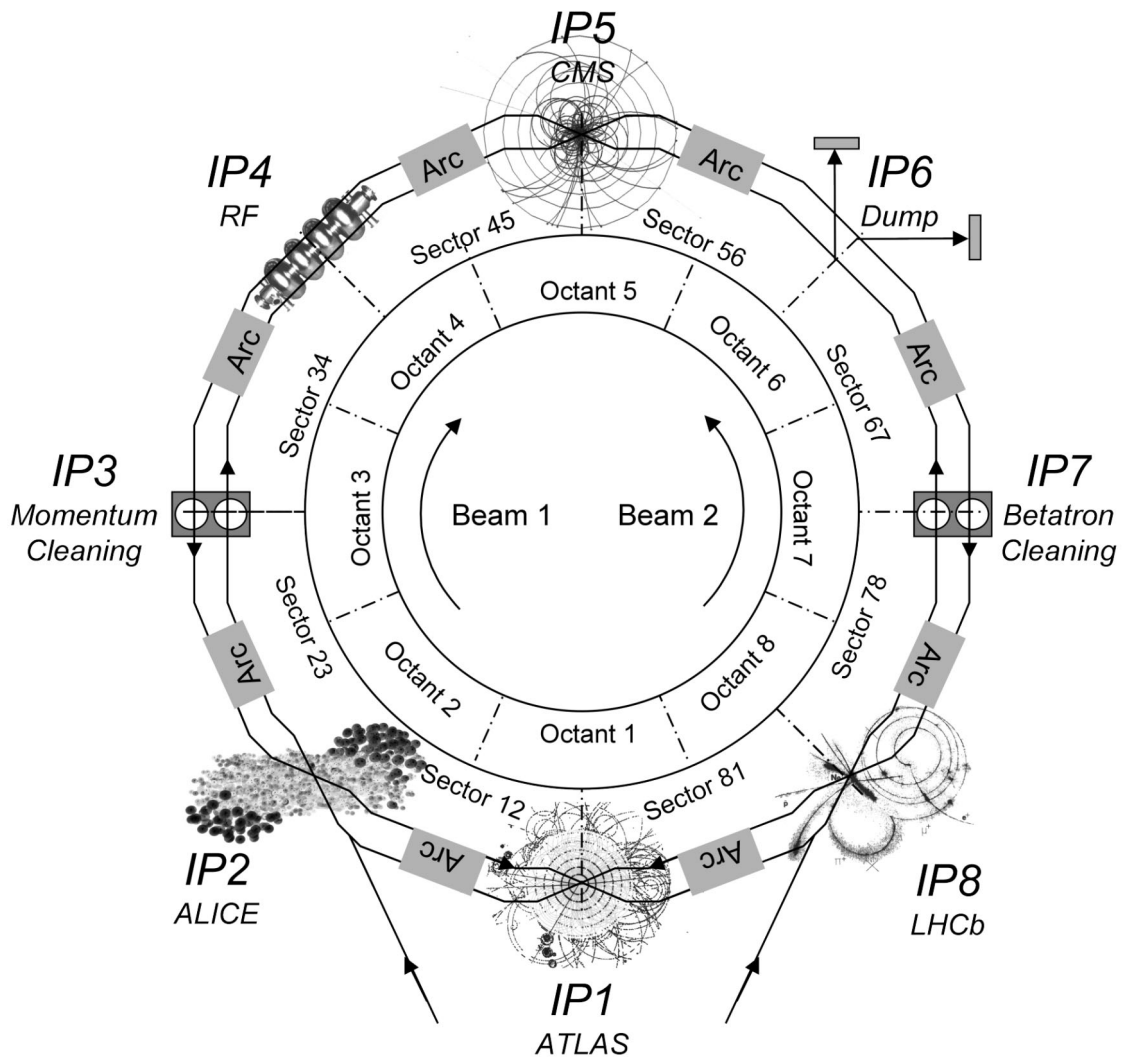


Figure 1.1 Functional drawing of the Large Hadron Collider. Different facilities are installed at the insertions points (IP) of each octant in the machine. The injection systems are located at the insertion points 2 and 8. The two counter rotating beams collide in four different points, where the experimental detectors ATLAS, CMS, ALICE and LHCb are located. The radio frequency cavities (RF) can be found at insertion point 4, and the beam dump is installed at insertion point 6. The insertions 3 and 7 house facilities to clean the beam concerning momentum and orbit. The arcs house optical elements to bend and focus the beam.

ATLAS and CMS are general-purpose experiments for recording proton-proton collisions at high luminosity [23]. Both detectors are based on large superconducting magnet systems and cover a large range of physics: Higgs bosons, supersymmetric particles, the CP-violation and B-physics. ALICE is a heavy-ion detector designed to study the physics of strongly interacting matter and the quark-gluon plasma in nucleus-nucleus collisions

Introduction

[23]. The LHC-B detector will investigate the CP-violation and other phenomena in decays of hadrons with rare flavors, in particular B-mesons [23].

Particle beams are prepared by the existing CERN accelerator chain. The injection systems are located at the insertion points of the octants 2 and 8. Proton beams are injected into the LHC at an energy of 450 GeV. In order to provide beams with the high luminosity that is required for the collision experiments, the particles have to be accumulated during the injection period and subsequently accelerated with ideally no particle loss. The radio frequency cavities are installed at insertion point 4 and accelerate the beams in bunches of about 10^{11} particles, spaced by delays of 25 to 75 ns. Cleaning of the beams concerning orbit and momentum is performed at the insertion points 3 and 7. The beam dump is located at insertion point 6.

Optical elements to bend and focus the beams are installed into the arcs between the insertion points. In the arcs dipole magnets are used to bend the beams of charged particles and lead them along their orbits in the machine. The radius of the existing tunnel of the former electron-positron accelerator LEP at CERN provides a geometric constraint. Under nominal conditions the bending magnets have to achieve a magnetic field of 8.33 T in order to maintain the particles on their orbit around the machine.

Focussing and defocussing quadrupole magnets are placed in alternating order. Apart from dipoles and quadrupoles, the arcs also contain various corrector magnets. Sextupoles affect the chromaticity of the machine. Higher order fields like the decapole affect higher order derivatives of the tune.

Due to the very high current density that has to be obtained in the magnets, the LHC has been designed as a superconducting collider [42]. It will contain 1232 main dipoles, 392 main quadrupoles, several magnets for the insertions like separation dipoles and insertion quadrupoles, and a large number of corrector magnets.

1.2 Field quality

1.2.1 Multipole fields

Multipole fields in particle accelerators are induced by current distributions, which approximate ideal geometries [48]. An ideal ‘normal’ n -pole field is induced by a $\cos(n\theta)$ current distribution, where the current is concentrated on an infinitely thin cylindrical boundary, and where θ is the azimuthal angle. Technically these current distributions are approximated by current shells, where the current is distributed homogeneously inside the shells. Examples of current distributions inducing normal dipole-, quadrupole- and

Introduction

sextupole fields are shown in figure 1.2. If a $\cos(n\theta)$ current distribution is rotated by an angle $\pi/(2n)$, one obtains a $\sin(n\theta)$ distribution inducing a so-called ‘skew’ multipole field. The field amplitude depends on the $(n-1)$ -th power of the radial position.

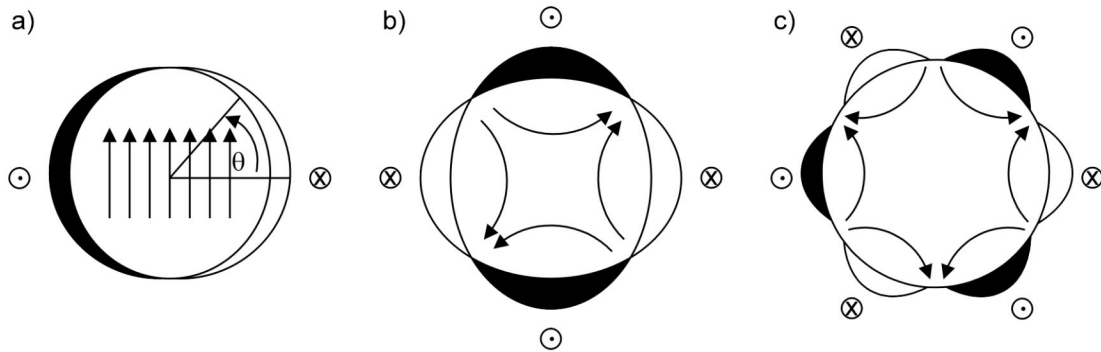


Figure 1.2 Examples of current distributions to generate a) dipole-, b) quadrupole- and c) sextupole fields are shown schematically. The pictures show the current distributions in the cross section of a system which is infinite in the direction perpendicular to the paper plane.

1.2.2 Technical realization of superconducting accelerator magnets

The coils of the superconducting LHC magnets are made from strands containing several thousands of thin superconducting NbTi-filaments embedded in a copper matrix. The strands are manufactured into flat twisted cables, so-called ‘Rutherford-type’ cables. A front view and a side view are shown in figures 1.3a) and b).

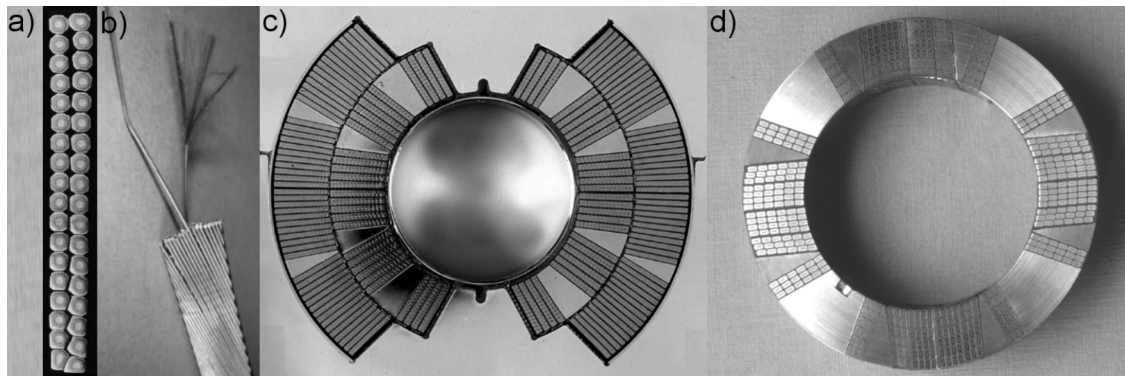


Figure 1.3 a) Front view and b) side view of a flat Rutherford-type cable. c), d) Technical realizations of coils for superconducting accelerator magnets. The cross section c) is a dipole coil with five blocks of cables. d) shows a cross-section of a tuning quadrupole coil.

The $\cos(n\theta)$ shaped current distributions are generated by discretizing the previously introduced homogeneous current shells. A magnet cross section consists of several blocks and layers of flat cable, arranged such that they approximate the $\cos(n\theta)$ shaped current

Introduction

shells. In figure 1.3c) and d) examples are shown for the coils in a main dipole and an insertion quadrupole.

The dipole coil (figure 1.3c) is contained and stabilized by austenitic steel collars, a surrounding iron yoke and a shrinking cylinder. The magnets are cooled with superfluid Helium and operated at a temperature of 1.9 K.

1.2.3 Definition of the field quality in the LHC dipoles

A coordinate system is defined for the description of the field quality in a typical LHC dipole coil. Its origin is placed in the center of the beam tube, with its z -axis parallel to the axis of the magnet. x describes the horizontal and y the vertical coordinate in a magnet cross section. The definition is schematically demonstrated in figure 1.4.

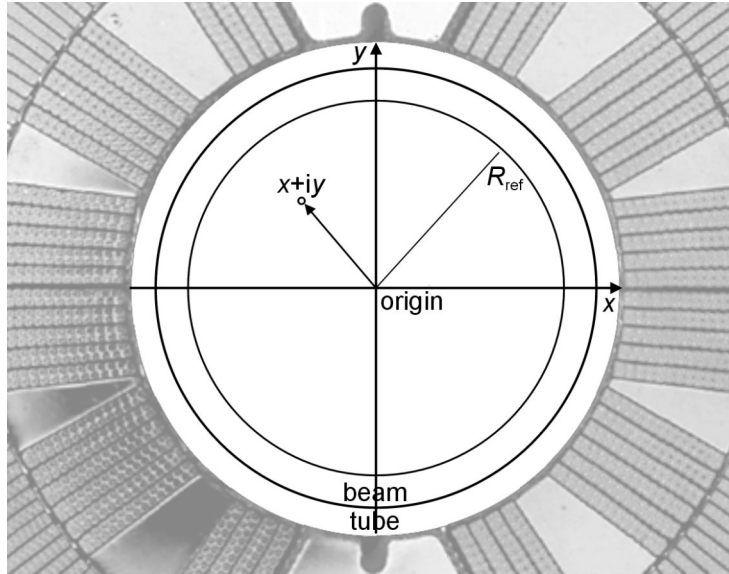


Figure 1.4 The definition of the coordinate system and the reference radius are shown inside the beam tube of a typical LHC dipole.

Throughout the thesis the field in the xy -plane of the beam tube is approximated by the following series [7]:

$$\mathbf{B}(x, y) = B_y + iB_x = \sum_{n=1}^{\infty} (B_n + iA_n) \left(\frac{x + iy}{R_{ref}} \right)^{n-1} = 10^{-4} B_1 \sum_{n=1}^{\infty} (b_n + ia_n) \left(\frac{x + iy}{R_{ref}} \right)^{n-1}. \quad (1.2)$$

B_n and A_n are the normal and skew multipole coefficients, also referred to as field components or field harmonics. b_n and a_n are their normalized values and expressed in so-called standard ‘units’. B_1 is the main field, and the factor 10^{-4} is used for scaling. R_{ref} is the reference radius in the beam-tube. For the LHC R_{ref} is defined as 17 mm.

Introduction

All undesired multipole components other than the main field are referred to as ‘field errors’. For each field component random (R), uncertainty (U) and systematic errors (S) are distinguished. Systematic errors affect all magnets in a similar way. Uncertainty errors systematically affect one arc of the machine. Random errors are different from magnet to magnet.

1.2.4 Field errors in the LHC dipoles

The field errors are significantly influenced by the symmetry of the magnet. In dipole magnets only odd normal multipoles are allowed by the symmetry. With increasing harmonic order the amplitudes strongly decrease in magnitude. In real coils the symmetry is never perfect and therefore even and skew harmonics contribute to the field. In order to achieve the desired field quality, these imperfections have to be minimized and corrected.

Field errors in superconducting dipole magnets have several origins. Geometric field errors result from the deviation of the real current distribution in the coils from the ideal current distribution that is needed to generate the desired magnetic field [10]. At high fields a further deviation is caused by the saturation of the iron yoke. Both contributions are reproducible, can be predicted accurately and correlate with measurements at room temperature.

Additional field imperfections in superconducting magnets are caused by the time dependent and stationary diamagnetic properties of the superconducting material. The contributions of the filament magnetization to the quality of the magnetic field are often referred to as ‘persistent current’ effects, since long lasting shielding currents are responsible for the diamagnetic behavior [56]. Persistent current effects are especially important at the low field level necessary for particle injection. Furthermore, during current ramps coupling currents are induced among the filaments and among the strands of the Rutherford-type cable. These contribute also to the diamagnetic behavior [39]. Persistent and coupling current effects are reproducible, but require the magnet to be measured in the superconducting state in order to precisely determine their magnitude.

In figure 1.5 the behavior of the normal sextupole component b_3 in an LHC prototype dipole is shown as a function of the dipole field, during a so called ‘load-line’ current cycle. During up-ramps the sextupole follows the lower branch of the hysteresis curve. The persistent current effects strongly decrease with increasing field, and the curve approaches the value of the geometric sextupole field error. For fields above 6 T also the yoke saturation is visible. When lowering the dipole field, the sextupole follows the down-ramp branch of the hysteresis curve.

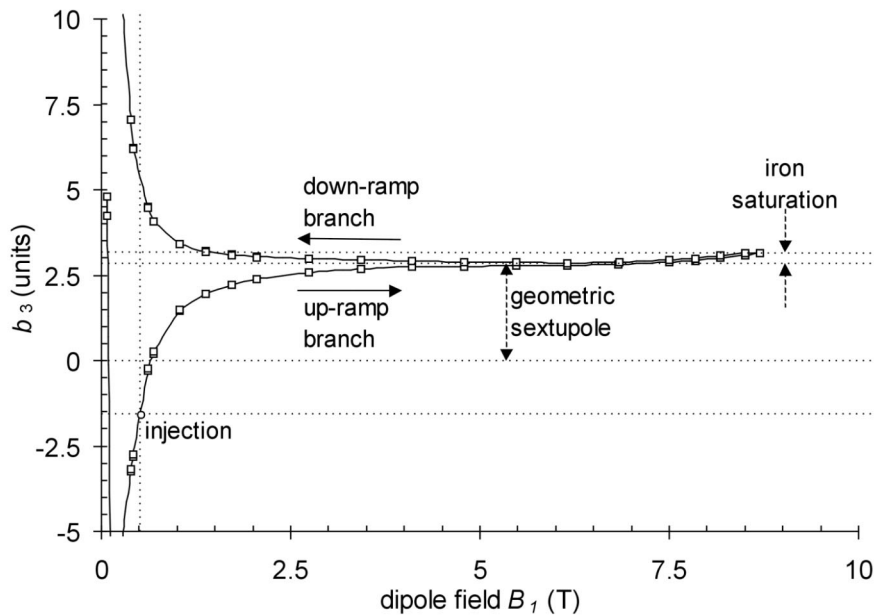


Figure 1.5 The normal sextupole component b_3 shown as a function of the dipole field in the magnet for a so-called ‘load-line’ current cycle.

1.2.5 Decay and snapback

This thesis focusses on another rather new class of effects, which are as well associated with the properties of the superconducting cable. During long periods of constant current all components of the magnetic field show a decay behavior. The decay is especially pronounced at the low level of the magnetic field during injection (about 0.54 T), where the persistent current magnetization is relatively large and has a significant impact on the field. The field components return to the original hysteresis curve as soon as the current ramp restarts, i.e. they ‘snap-back’. An example for b_3 during decay and snapback is shown in figure 1.6 as a function of the time and the dipole field, respectively.

Two different contributions to the field decay were identified during tests on SSC magnets [25]. The first effect is flux creep. It causes a decay with a logarithmic time dependence. The flux creep contribution is not affected by the excitation history and can be stopped by decreasing the magnet temperature. The magnitude of the flux creep decay was found to be in the same range as the relaxation rates measured on short samples of cable [25]. Not very much is known so far about flux creep in LHC strands. Measurements at 2 K have shown that after a decay time of about 1000 s the relaxation of a magnetized sample in a background field of 0.5 T is typically in a range of 1% of the original magnetization [38]. Taking the measured relaxation as an upper limit for flux creep, one can estimate that under typical LHC operation conditions the flux creep contribution should not represent more than 10% of the observed decay amplitude.

Introduction

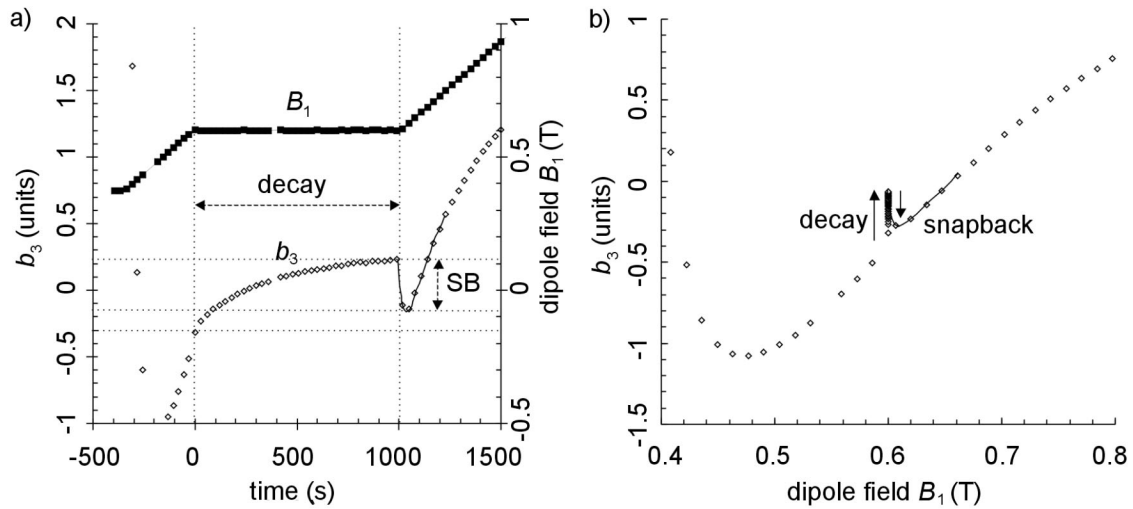


Figure 1.6 a) The dipole field B_1 and the normal sextupole component b_3 are shown as a function of time. The injection field is reached at a time $t = 0$. The sextupole component decays during injection. After about 1000 s the magnet is ramped again. The snapback is clearly visible. b) The same measurement of b_3 is shown as a function of the dipole field, along the up-ramp branch of the hysteresis curve. The decay and snapback are indicated.

The second contribution to the field decay is linked to the structure of Rutherford-type cables. It only appears if the magnet current has been cycled. The decay amplitude strongly depends on the excitation history of the magnet. This contribution to the decay can not be stopped by decreasing the magnet temperature and the measured decay rates are much higher than the flux creep decay rates observed on short conductor samples [25].

The present understanding is that during ramps ‘current imbalances’ are induced in the Rutherford-type cable, where the various strands carry different fractions of the transport current. Trapped currents ΔI , as large as 100 A [51], circulate in various loops formed by strand sections and interstrand contacts, with different time constants of up to several hours and over different distances, only limited by the length of the cable. The average transport current in the cable, however, is not affected. Figure 1.7 shows a sketch of a Rutherford-type cable, where two strands carry the current imbalance.

These currents have been called ‘Boundary Induced Coupling Currents’ (BICCs) or ‘supercurrents’. The arrows in figure 1.7 demonstrate BICCs following the zigzag path along two strands in the cable. In real magnets the BICCs are not limited to two strands only, but are distributed quasi-continuously among the strands in a cable.

Introduction

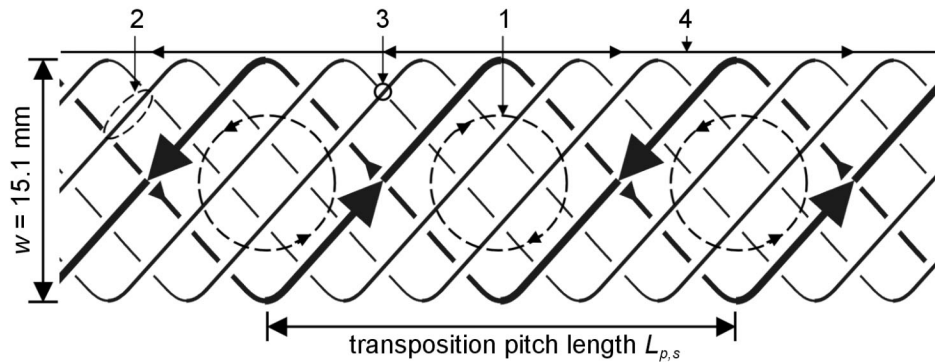


Figure 1.7 Trapped currents follow the zigzag path along the strands in the Rutherford-type cable and circulate in various loops (1) formed by the strand sections (2) and interstrand contacts (3). The loop length (4) can vary from half a twist pitch length up to the entire length of the cable.

The impact of the BICCs can be observed as a spatially periodic pattern in all field harmonics with a wavelength equal to the cable twist pitch. An illustration is shown in figure 1.8. This pattern was first found in the sextupole component of the HERA dipole magnets, when measuring the local field in the magnet bore using a sensor consisting of three Hall probes [18]. The field pattern itself does not significantly affect the beam in the machine, since the resulting oscillations of the particles are small, and since the pattern is averaged out in the field integral along the z -axis.

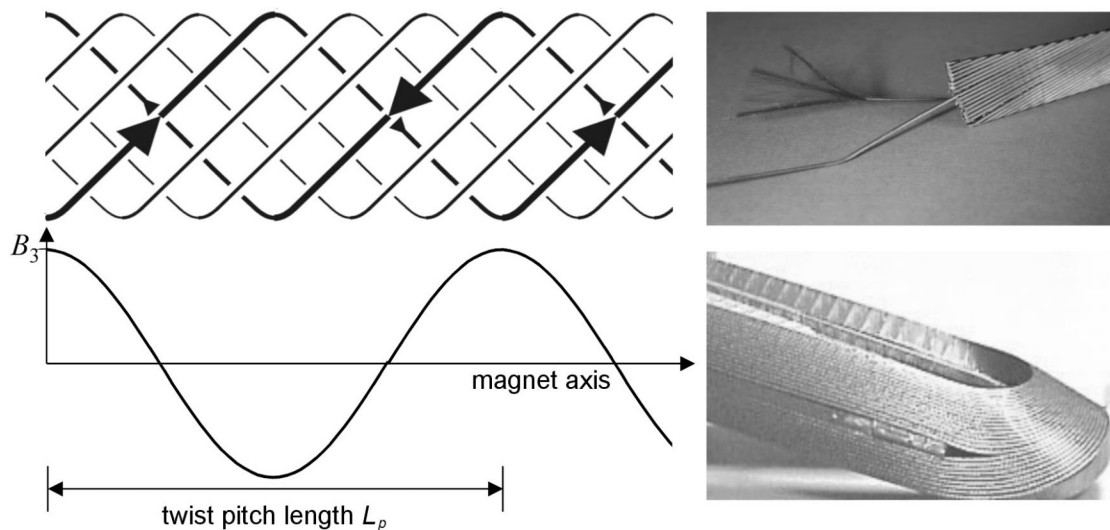


Figure 1.8 The pictures on the right show a Rutherford-type cable and a part of a typical LHC dipole coil. Current imbalances in the Rutherford-type cable cause a spatially periodic pattern, which can be observed in all components of the magnetic field in the coil. The drawings on the left illustrate the current imbalances in the cable and show an example for the periodic field pattern in the center of the coil.

Introduction

In a ‘virgin’-magnet, where the superconducting material is free of persistent currents, and where the excitation current is zero, the periodic field pattern is not present. However, it appears when the current is increased.

During ramps, BICCs are induced especially in regions where the cable is exposed to large variations in field sweep rate and resistances of the interstrand contacts [33], [34], [55]. The field sweeps during ramps are significantly larger than local field changes in the coil induced by BICCs, and for this reason the coil magnetization is only affected by the background field.

However, during periods of constant transport current, as for example during injection, BICCs diffuse along the cable in the magnet and redistribute the transport current among the strands. Various independent measurements [16], [21], [30], [43], [47] have confirmed that as a consequence the spatially periodic field pattern changes with very high time constants.

The diffusion of BICCs during injection changes the local field along the cable and inside the strands. These field changes reduce the coil magnetization, and cause the field decay during injection.

As soon as, after the end of injection, the magnet current and thus the field is ramped up again, the magnetization returns to the up-ramp branch of the original hysteresis curve, which explains the behavior during the snapback. The snapback typically occurs over a range of few tens of mT.

1.2.6 Compensation of decay and snapback in the LHC

The uncorrected effects ‘decay’ and ‘snapback’ cause chromaticity changes in the order of 170 units. Due to the high target luminosity of the LHC, the tolerances will be much stricter than in previous machines [3] and the chromaticity needs to be controlled within one unit. These limitations translate into strict tolerances on the quality of the magnetic field in the bending dipoles and require a very precise control of the field in the magnets [19]. All field components in the dipole magnets are influenced by decay and snapback and several harmonics require an adjustment. In table 1.1 the expected errors and their tolerances are shown for the most important field components.

It is not possible to restart with virgin magnets after every accelerator run, since this would require to bring all magnets in the normal state and to re-cool. In order to minimize the impact of the excitation history on the following run, very well defined current cycles have been elaborated. For the correction of the remaining static and dynamic errors, each arc of the collider is equipped with correction circuits for the most

Introduction

important multipole components. Dynamic errors, such as decay and snapback, require an adjustment of the compensation circuits at all stages of the LHC operation. Each magnet will be measured before it is installed in the tunnel. Tables of measured data will allow to adjust the correction circuits and to compensate the error distribution in the machine to better than 80%.

order	$b_1(S)$	$b_1(R)$	$a_2(R)$	$b_3(S)$	$a_3(U)$	$b_4(U)$	$b_5(S)$
typical error	2.6	0.75	0.8	3.3	0.272	0.084	0.36
tolerance	0.3	0.13	0.8	0.02	0.17	0.07	0.18

Table 1.1 Typical amplitudes of decay and snapback and their tolerances in the LHC (in units). For each field component random (R), uncertainty (U) and systematic errors (S) are distinguished. Systematic errors affect all magnets in a similar way. Uncertainty errors systematically affect one arc of the machine. Random errors are different from magnet to magnet.

The systematic error of the normal sextupole has to be corrected within 0.02 units. This is quite a challenge since the typical sextupole dynamics during injection and during the initial acceleration is in the range of 3.3 units and would imply a very delicate compensation of more than 99%. In addition to tables of experimental data also online measurements from reference magnets and beam parameters can be used for the correction.

The systematic error of the normal decapole $b_5(S)$ has an impact on higher order derivatives of the chromaticity and needs to be corrected within 0.18 units.

1.3 Scope of the thesis

The typical magnitudes of ‘decay’ and ‘snapback’ are many times larger than the tolerances for proper machine performance. This thesis reports the development of methods for the compensation of the two effects in the LHC accelerator and a detailed investigation of the underlying physical mechanisms. Figure 1.9 illustrates the structure of the thesis.

For a long time ‘decay’ and ‘snapback’ were assumed to be caused by flux creep. However, the dependence of the decay amplitude on the excitation history of the magnet and deviations from the expected logarithmic temporal decay can not be explained by flux creep. This shows that another effect is the major contributant. The induction of BICCs during ramps and their diffusion during periods of constant current excitation in the magnets partially explains the decay. However, the snapback is a magnetization phenomenon and calls for a theory explaining also the interaction between current

Introduction

redistribution and coil magnetization. Details on the mechanisms of decay and snapback are explained in chapter 2.

Standard measurements with rotating coils in the bore of magnets do not have enough time resolution for precise snapback measurements and also do not allow accurate local measurements. Measurement techniques with both, a high temporal and spatial resolution are necessary to investigate correlations between the decay, the snapback and the spatially periodic field pattern in the LHC magnets. For this reason an existing prototype of a Hall plate detector for sextupole fields is considerably improved and calibrated. For the first time the device delivers quantitative results. Further on a new prototype with several rings is constructed to allow the simultaneous observation of decay and snapback at several different locations along the spatially periodic pattern. Also the first known technical realization of a decapole sensor with Hall plates is presented in chapter 3.

Chapter 4 presents the continuation of an analysis which had been started by Schneider [49]. On a number of short LHC dipole models the decay amplitude is measured as a function of different parameters in the operation current cycle and the experimental results are compared to a one-time-constant model for the induction of boundary induced coupling currents. The qualitative correspondence between the measurements and the simulation is investigated on the assumption that the diffusion of BICCs is responsible for the field decay. The measured data are also used to establish correlations between the decays in different field components and to statistically analyze the systematic appearance of decay and snapback in different field components.

In chapter 5 the behavior of a single saturated cylindric superconducting filament in a changing magnetic field is analyzed for typical situations appearing in the coil during decay and snapback. Fitting formulas are derived to describe the filament magnetization.

In chapter 6, a small scale well controlled demonstration experiment is described. A cable is twisted from a central strand and six surrounding copper wires, and placed into a stand for magnetization measurements. The strand magnetization is saturated in a background field and a current is applied to the copper wires. The experiment demonstrates that local field changes induced by currents in the copper wires can reduce the strand magnetization, and allows to test the validity of the principle mechanism for the interaction between current redistribution and magnetization, which explains the appearance of decay and snapback in superconducting accelerator magnets.

Finally, the Hall plate detector is used for measurements on real magnets. The experimental data will allow to determine an estimate for the upper limit of a possible

Introduction

Chapter 2
Superconducting
Accelerator Magnets



Chapter 3
Magnetization Measurements
on Wires and Coils



Chapter 4
Dependence of Field Decay
on the Excitation History



Chapter 5
Filament Magnetization



Chapter 6
Decay and Snapback

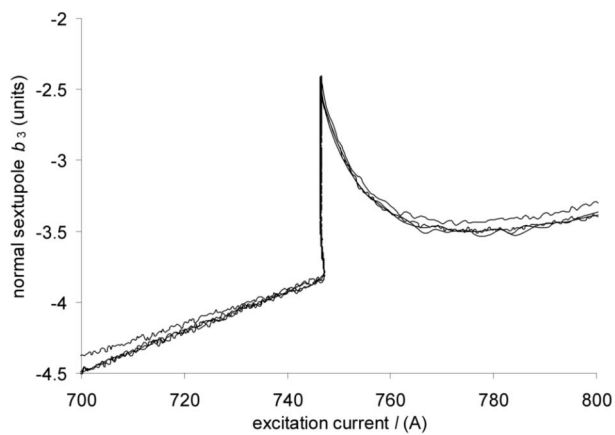
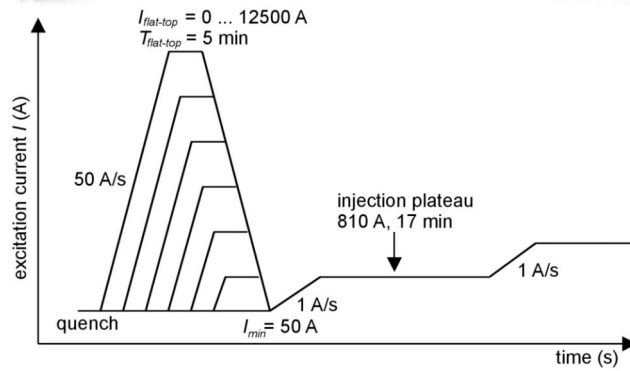
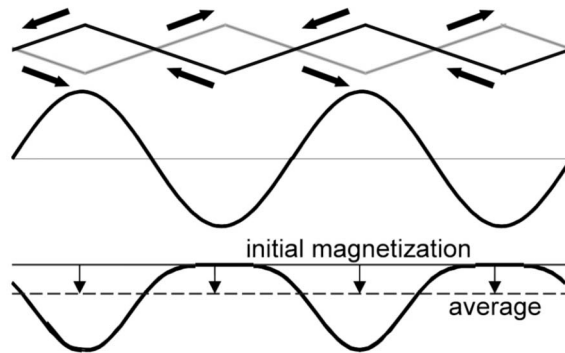


Figure 1.9 Schematical illustration of the thesis structure.

Introduction

flux creep contribution and demonstrate the interaction between current distribution and magnetization as the dominating effect. In addition, correlations between the spatially periodic field pattern, the field decay and the snapback are analyzed.

In order to better understand “Decay and Snapback” in a typical LHC dipole magnet, a numerical model is developed. Realistic values for the redistribution of boundary induced coupling currents in the coil are estimated, and the formulas for the filament magnetization are used to compute the local magnetization change for several cross sectional slices of the magnet. The cross sectional slices are located inside a little more than a cable twist pitch along the axis of the magnet. The numerical model is used to explain the experimental results.

Chapter 2

Superconducting Accelerator Magnets

The magnetic properties of superconducting accelerator magnets are closely linked to the physical properties of the superconductor used in the windings. For this reason, the first part of the chapter summarizes aspects of superconductivity that are important for the research presented in this thesis. Furthermore, the design and functioning of dipole magnets and their cycling procedure is introduced. Also Rutherford-type cables and multi-filamentary NbTi wires are explained. Finally, the sources of non-uniform current distributions among the strands of Rutherford-type cables and the induction and diffusion of boundary induced coupling currents are presented. Also the interaction between current distribution and magnetization is described, and the present understanding of the spatially periodic field pattern, the field component decay and the snapback is summarized.

2.1 Superconductivity

In 1911 Onnes observed a discontinuous resistance drop as soon as mercury is cooled below 4.19 K [20], [52]. This new state of matter with an ‘apparently zero resistance’ is called ‘superconducting’. In 1933 Meissner and Ochsenfeld found that if a superconductor is cooled below its critical temperature T_c in a weak magnetic field, the flux is expelled from the sample. Screening supercurrents flow in a thin surface layer and exactly cancel the magnetic flux inside the superconductor. Perfect conductivity and perfect diamagnetism are preserved up to a thermodynamical critical field B_c . At larger fields $B > B_c$ the flux expulsion no longer takes place and the magnetic field penetrates into the sample. The material transits to the normal state and the magnetic moment is zero. Abrikosov classified superconducting materials into two kinds, type I and type II. Type I superconductors do not admit a magnetic field in the bulk and remain in the superconducting state only as long as the applied field is below B_c .

Superconducting Accelerator Magnets

Alloys like niobium-titanium NbTi or niobium-tin Nb₃Sn and also the high temperature superconductors like Bi₂Sr₂Ca₂Cu₃O_x, Bi₂Sr₂Ca₁Cu₂O_x and Y₁Ba₂Cu₃O_x belong to the large class of type II superconductors. They are characterized by two critical fields, $B_{c,1}$ and $B_{c,2}$. For fields in the range $B_{c,1} < B < B_{c,2}$ the magnetic flux can enter the bulk. The flux-penetrated phase is called the ‘mixed state’ and many materials remain superconducting up to a very high field $B_{c,2}$. Critical parameters of some materials are shown in table 2.1.

Material	Composition	T_c (K)	$B_{c,2}$
NbTi	NbTi	9.3	11 T @ 4.2 K, 14 T @ 1.9 K
Nb ₃ Sn	Nb ₃ Sn	18	23 – 29 T @ 4.2 K
BSCOO-2223	Bi ₂ Sr ₂ Ca ₂ Cu ₃ O _x	110	> 30 T @ 4.2 K
BSCOO-2212	Bi ₂ Sr ₂ Ca ₁ Cu ₂ O _x	87	> 30 T @ 4.2 K
YBCO	Y ₁ Ba ₂ Cu ₃ O _x	92	> 30 T @ 4.2 K

Table 2.1 Typical values for the critical parameters of several materials.

In accelerator magnets a superconducting wire has to be able to carry a large current in the presence of a field in the 10 T range. Type II superconductors have the required properties: they feature large upper critical fields $B_{c,2}$, and high currents are permitted to flow in the bulk material.

For high magnetic fields up to about 23 T Nb₃Sn is used. However, due to its brittleness, the material has to be formed in the final geometry after the coil winding, by a high-temperature heat treatment. Ceramic ‘high- T_c ’ superconductors are very brittle as well, and the development of a reliable and affordable wire manufacturing technique is an extremely challenging task. Due to difficulties to manufacture magnets from Nb₃Sn at a reasonable price, the technical choice for NbTi superconducting technology in the LHC was made with the aim to reach the required 8.33 T reliably and economically.

The three main critical parameters critical temperature T_c , critical field $B_{c,2}$ and critical current density J_c are described by a ‘critical surface’ $J_c(B,T)$. In figure 2.1, the critical surface is plotted for NbTi. Superconductivity prevails everywhere below the surface and normal conductivity above it.

Although the upper critical magnetic field is rather limited, the most outstanding feature of NbTi is its ductility, allowing efficient and relatively simple fabrication methods for wires and cables. At the temperature of liquid helium, NbTi can be used for magnets of moderate strength (up to about 7 T). Cooling with superliquid helium at 1.9 K allows to build magnets with magnetic field levels up to about 9 T.

2.1.1 Flux flow, flux creep and the voltage current relation

Magnetic field penetrates into a type II superconductor in the form of flux lines. Each flux line contains one elementary flux quantum $\Phi_0 = h/2e \approx 2.07 \times 10^{-15} \text{Vs}$. In equilibrium conditions the flux lines form a triangular lattice. A picture of such a lattice in a NbSe₂-film is shown in figure 2.2.

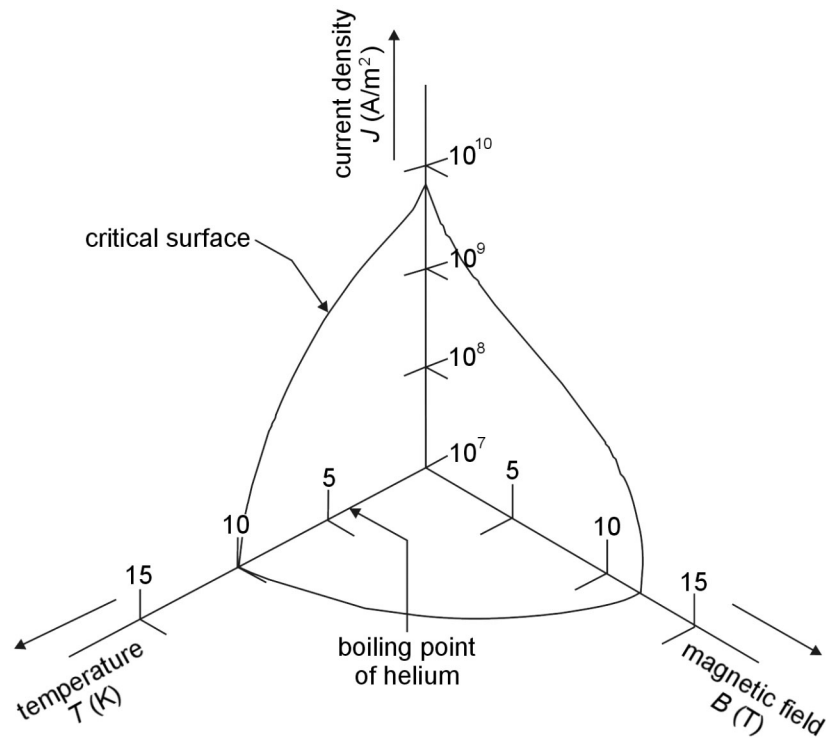


Figure 2.1 The critical current density J_c of NbTi is plotted as a function of temperature T and magnetic field B . The material is superconducting below the surface, and normal conducting above it.

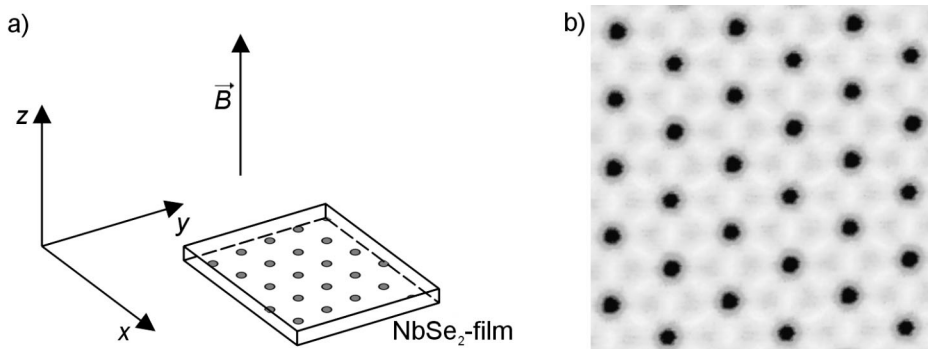


Figure 2.2 a) Layout of the experiment. b) Picture of a triangular flux line lattice in a NbSe₂-film. (STM-measurement of differential conductance [24]).

Superconducting Accelerator Magnets

A superconductor with macroscopic current density \vec{J} inside a magnetic field \vec{B} obeys Maxwell's equation $\vec{\nabla} \times \vec{B} = \mu_0 \vec{J}$. A current density inside the conductor, thus, implies a spatial gradient in the density of the flux lines. The gradient can only be maintained if the flux lines are inhibited from moving freely through the material. In order to be useful for most technical applications, and to enable the superconductor to carry large currents under high magnetic fields, the motion of flux lines has to be prevented by capturing them at so-called pinning centers. The most important pinning centers in niobium-titanium are normal-conducting titanium precipitates in the so-called α -phase. Materials with good pinning are called 'hard superconductors' and these are indeed materials useful for magnets.

A limitation for applications is the so-called 'flux-flow resistivity'. If a current passes through a type II superconductor with weak pinning, exposed to a magnetic field larger than $B_{c,1}$, it exerts a force on the magnetic flux lines, which then begin to move through the material in a direction perpendicular to the current and to the field. The corresponding resistivity is called the 'flux-flow resistivity' ρ_f and given by

$$\rho_f = \frac{B}{B_{c,2}} \rho_n. \quad (2.1)$$

The flux-flow resistivity is a linear function of the magnetic induction, and for $B = B_{c,2}$ it equals the normal-state resistivity of the material ρ_n . In hard superconductors flux flow is prevented by pinning centers. However, also in hard superconductors flux-flow appears if the force on the flux lines is large enough to free them from the pinning centers.

At temperatures $T > 0$ K, flux lines can also be released from their pinning locations due to thermal activation, and leave the superconductor. This phenomenon is known as 'flux creep'. Flux creep manifests itself in the existence of a finite resistivity, even in the subcritical regime $J < J_c$. Experimentally a logarithmic time decay of the magnetization is observed. In the theory of Anderson [1] the pinning centers are represented by potential wells of average depth U_0 and width a , in which bundles of flux lines with an average flux $\langle \Phi \rangle$ are captured. The probability for magnetic flux to leave the potential well due to thermal activation is proportional to the Boltzmann factor

$$P_0 \sim \exp\left(-\frac{U_0}{k_B T}\right). \quad (2.2)$$

If the superconductor carries a current density J , the potential acquires a slope. This slope reduces the effective potential well depth to $U = U_0 - \Delta U$, as demonstrated in figure 2.3. The reduction of the well depth ΔU is proportional to the product of the field and the current density. If a bundle of flux quanta is released from its well, it slides down the slope and leaves the material. Anderson showed that equation (2.2) results in a reduction of the critical current density:

$$J_c(t) = J_c(0) - \frac{k_B T}{\langle \Phi \rangle a l_b} \ln(t). \quad (2.3)$$

l_b is the length of the flux bundle. The result is that for a given temperature and magnetic field, the critical current density is not a constant, but slightly time dependent.

Due to the motion of flux lines, even a hard superconductor is not perfectly free of resistance. In the vicinity of the critical current density, the resistivity is a very steep function of the current density J . The so-called ‘voltage-current characteristic’ of a multi-filamentary superconductor can be described by a power law:

$$\rho(J) = \frac{E_0}{J_c} \left| \frac{J}{J_c} \right|^{N-1}, \quad (2.4)$$

$$E = \rho(J) \cdot J = \text{sign}(J) E_0 \left| \frac{J}{J_c} \right|^N. \quad (2.5)$$

For practical superconductors $E_0 \approx 10^{-4}$ V/m. For $N = 1$ equation (2.5) describes ohmic behavior. Examples for several values of N are shown in figure 2.4a.

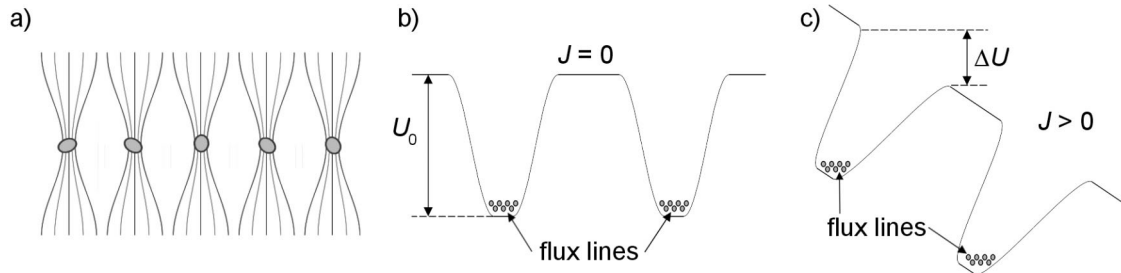


Figure 2.3 Schematic visualization of the flux creep problem. a) Attracting effect of the pinning centers on the flux lines. b) Flux lines and pinning potentials without any external force. c) Reduction of the pinning potentials due to the Lorentz force in the presence of a transport current.

2.1.2 Magnetic behavior

Starting with the observation that the resistivity of a hard superconductor is almost a step function of the current density, C. P. Bean [4], [5] proposed the so-called ‘Critical State Model’, according to which there are only two possible states for the flow of the current in a hard superconductor. The current density is either zero or equals the (positive or negative) critical current density J_c . The dependence of J on the electric field is demonstrated in figure 2.4b. The Bean model corresponds to the case $N \rightarrow \infty$ in equation (2.5), which is also plotted in figure 2.4a.

An initially unmagnetized ‘infinite’ slab of superconductor is exposed to a magnetic field B parallel to its surface. The surfaces of the slab are oriented parallel to the yz -plane, and the magnetic field is applied in y -direction. If the external field is raised from zero to a

small value, a bipolar current density $\pm J_c$ is induced in the slab, flowing in positive and negative z -direction. The induced currents penetrate to such a depth that the shielding field cancels the applied field in the center region. In the region of current flow, the magnetic field exhibits a linear rise in accordance with the Maxwell equation $\vec{\nabla} \times \vec{B} = \mu_0 J_c$. The current and field profile are sketched in figure 2.5a. The magnetization follows the ‘virgin curve’ plotted in figure 2.6.

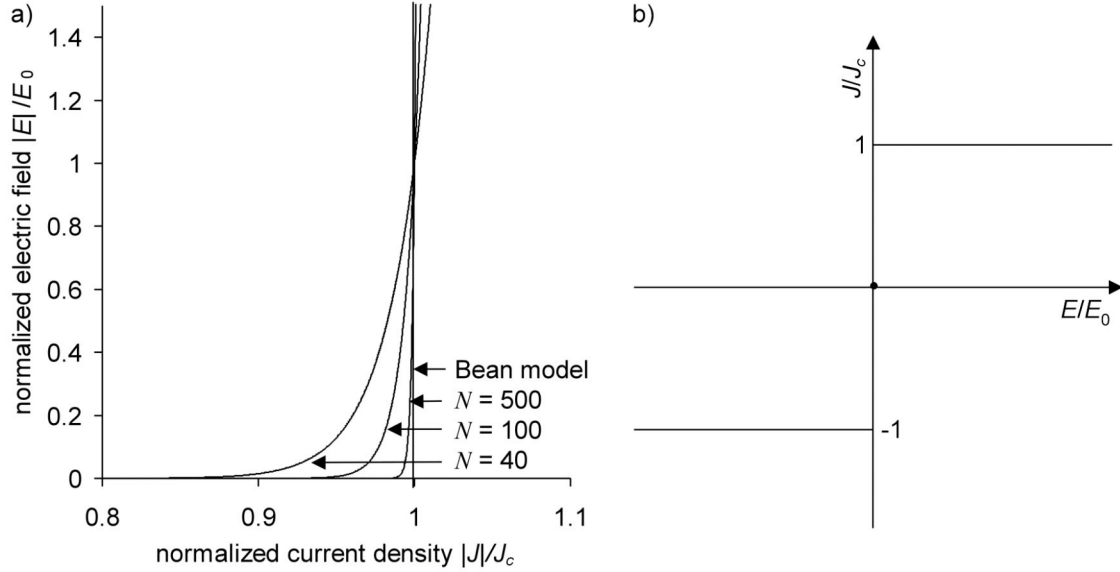


Figure 2.4 a) The normalized electric field is shown as a function of the normalized current density, for power laws with different exponents N in equation (2.5) and for the case of the Bean model ($N = \infty$). b) The normalized current density in a superconductor obeying the Bean model is shown as a function of the electric field. The current density is either zero or equals the positive or negative critical current density.

The current pattern persists as long as the external field is kept constant. If the external field is increased, both, current and magnetic field penetrate deeper into the slab until the center is reached (figure 2.5b). The associated field is called the field of full penetration B_p . Its numerical value depends on the critical current density and on the thickness of the slab. Raising B beyond B_p leads to a non-zero field in the center.

An interesting situation occurs when B is reduced again. A new bipolar current of opposite polarity is induced and the field pattern inside the slab assumes the shape sketched in figure 2.5c. If the external field is cycled, the magnetization of the slab describes a hysteresis curve, which is shown in figure 2.6 (full line).

Figure 2.5d shows the field profile for a case, where the field is decreased before reaching the field of full penetration. The corresponding hysteresis curve for a field cycle with an amplitude smaller than B_p is also shown in figure 2.6 (thin line).

Superconducting Accelerator Magnets

If a type II superconductor is exposed to a time-varying magnetic field, an electric field is induced and its energy is dissipated in the material. The energy loss after a full hysteresis cycle equals the area enclosed by the loop.

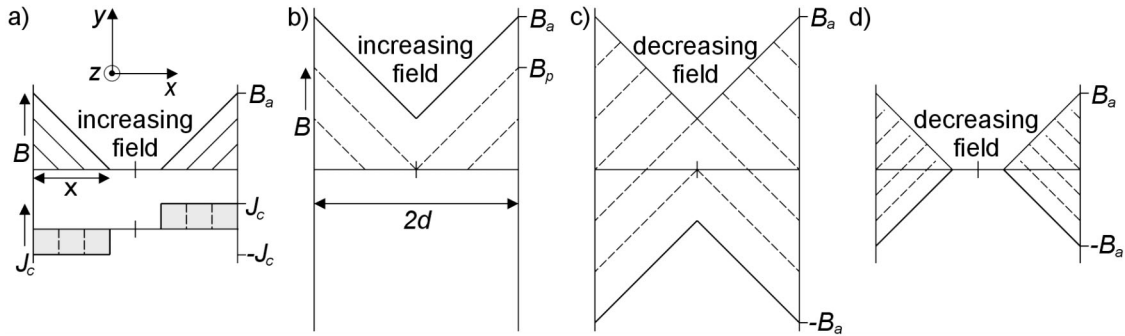


Figure 2.5 A slab of hard superconductor in the 'Critical State' is exposed to an external magnetic field parallel to its surface. a) Initial exposure to a small external field $B < B_p$. b) The external field is raised beyond the penetration field B_p . c) The external field is reduced. d) The field is decreased before reaching the penetration field.

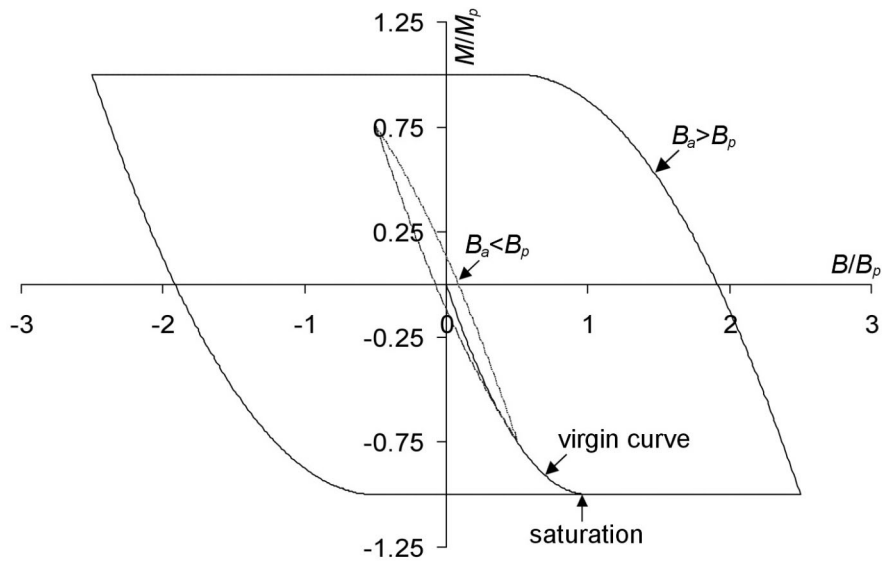


Figure 2.6 Hysteresis curves of a superconducting slab in the 'Critical State'. The magnetization is plotted as a function of the field. The magnetization and field are scaled by the saturation magnetization M_p and the penetration field B_p , respectively. The full line shows a virgin curve and a hysteresis curve with a field amplitude larger than the field of full penetration. The dotted lines describe a hysteresis cycle with a field amplitude smaller than the field of full penetration.

2.2 Main dipoles and operating cycles

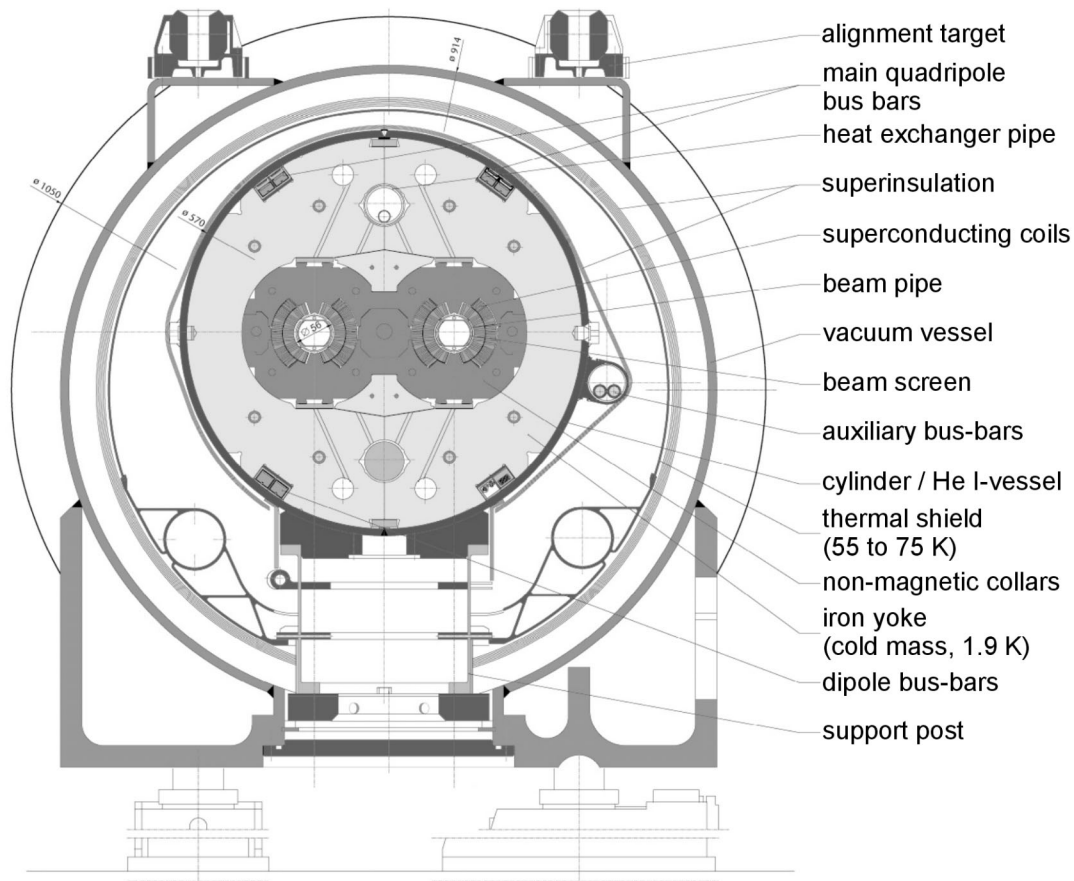


Figure 2.7 Cross section of an LHC twin aperture dipole inside its cryostat.

The cross-section of a twin-aperture LHC dipole magnet is shown in figure 2.7. Its structure is based on a cost-saving ‘two-in-one’ design, where two beam channels with separate coil systems are incorporated within the same magnet structure. The two coils are fixed by a support structure of laminated collars, which define the exact geometry and provide mechanical stability. The collared coils are integrated into an iron yoke, which serves to increase the central field by about 19%, and shields the magnetic field, so that no magnetic field leaves the magnet. Bus bars accommodate the cables to power the magnets of the arcs. They are located in grooves in the iron yoke. The so-called ‘cold mass’ is immersed in a bath of superfluid helium at atmospheric pressure and cooled to 1.9 K by means of a heat exchanger tube, in which two-phase low-pressure helium is circulated and acts as a heat sink. The cold mass is delimited by the inner wall of the beam pipes on the beam side and by a cylinder on the outside. The collars, the iron yoke and the cylinder compress the coil. They maintain the Lorentz forces during excitation, avoid conductor displacements and limit coil deformations. The cylinder improves the

Superconducting Accelerator Magnets

structural rigidity and the longitudinal support. At the same time, it contains the superfluid helium.

A typical scenario for the excitation of a dipole magnet during the operation of the collider is shown in figure 2.8. The excitation current in the magnet is shown as a function of time. At the start of each run, the current is ramped up to an injection level of 739 A. The dipole field at injection is 0.535 T. During the injection of particles (hadrons) into the machine, the current is left constant for a time of typically 1020 s. Subsequently, the particles are accelerated and the magnets are ramped to the nominal current of 11796 A, achieving a nominal dipole field of 8.33 T. In order to minimize errors, an acceleration ramp with four different segments is used. An acceleration parabola slows down the snapback and a subsequent exponential segment minimizes the relative field error contribution due to eddy currents. During the third segment, the current is ramped linearly. The last segment is a deceleration parabola used to reach the nominal current smoothly and to avoid overshoots. After the end of the operation, the magnets are ramped down again.

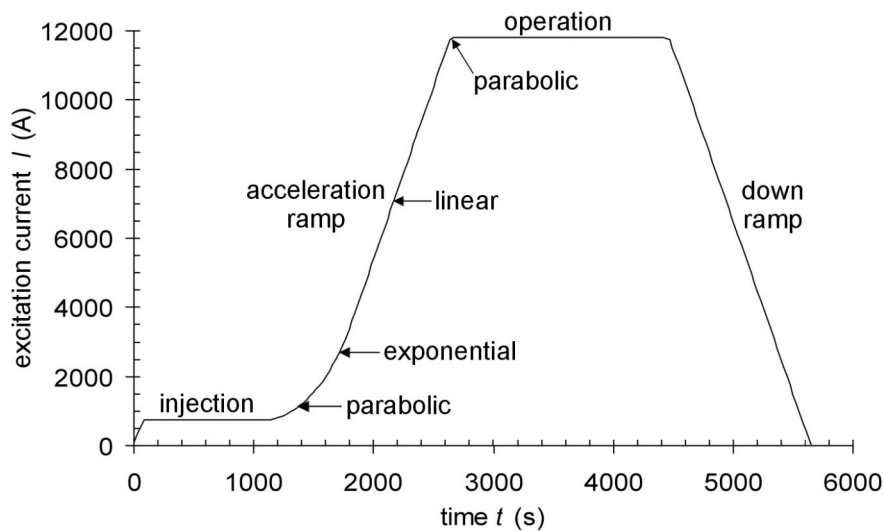


Figure 2.8 Typical scenario for the excitation of a dipole magnet during the operation of the collider. The excitation current in the magnet is shown as a function of time.

Excitation cycles have an important impact, especially on dynamic field errors like decay and snapback. Since before every new run of the LHC collider a transition to the normal state of all magnets is not feasible, the magnets have to undergo an optimized cycling procedure prior to any subsequent operation, in order to establish reproducible conditions.

During systematic magnetic measurements of decay and snapback on LHC dipole magnets a standardized operation cycle is used as a reference. The parameters of the cycle may slightly differ from the final ones during the LHC operation cycle. In figure 2.9 the excitation current during the standard cycle is sketched as a function of time.

An initial quench erases all persistent currents. Afterwards, the operating point is moved away from the virgin curve onto a reproducible hysteresis curve by pre-cycling the magnet to a current of 11850 A for a time of 1800 s. The ramp-rate during the up- and down-ramp of the pre-cycle is 50 A/s. Then the current is ramped up to an injection current of 760 A, following the up-ramp branch of the hysteresis curve, at a constant ramp-rate of 1 A/s. The injection of particles at constant field is simulated for typically 1020 s. Finally, the current is ramped up again with a constant ramp rate of 1 A/s, simulating the acceleration of particles. During experiments single parameters in the current cycle can be varied in order to detect a more or less sensitive decay- and snapback response. In chapter 4 systematic investigations are presented, where the impact of different current cycles is analyzed.

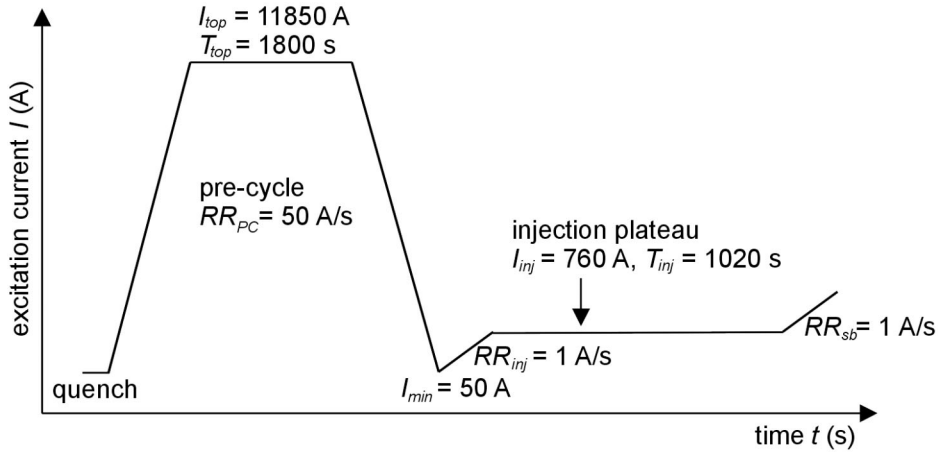


Figure 2.9 Standard current cycle for snapback measurements. The magnet excitation current is sketched as a function of time.

2.3 Coil geometry and field quality

As already mentioned in chapter 1, a $\cos(\theta)$ -shaped current distribution generates an ideal dipole field. Since the coils of superconducting high-field accelerator magnets are made from discrete cables, the $\cos(\theta)$ -shape is approximated by a so-called shell-type configuration.

The coils of the LHC main dipoles consist of two layers of turns. Each layer is divided into blocks, and the blocks are wound from several turns of flat so-called ‘Rutherford-

type cables'. In order to match the $\cos(\theta)$ -shape, blocks are separated by wedges. The cables in both layers have the same width, but different thickness, resulting in the desired gradient of current density for an optimum field quality in the magnet. The number of blocks, the exact positioning, and the number of turns have been the subject of intensive studies for maximizing the field quality. In figure 2.10 a quadrant of the coil cross sections is shown for both, a five- and six-block design. The latest design is based on a six-block geometry with 15 turns in each quadrant of the inner and 26 turns in each quadrant of the outer layer [37].

The blocks are separated by copper wedges in order to orient the cables radially and to create enough degrees of freedom for optimizing the field quality and current density. Perforated glass-epoxy spacers are inserted between the inner and outer layer and provide channels for the circulation of the cooling helium. The electrical insulation to ground consists of superimposed polyimide films and also includes quench protection heaters.

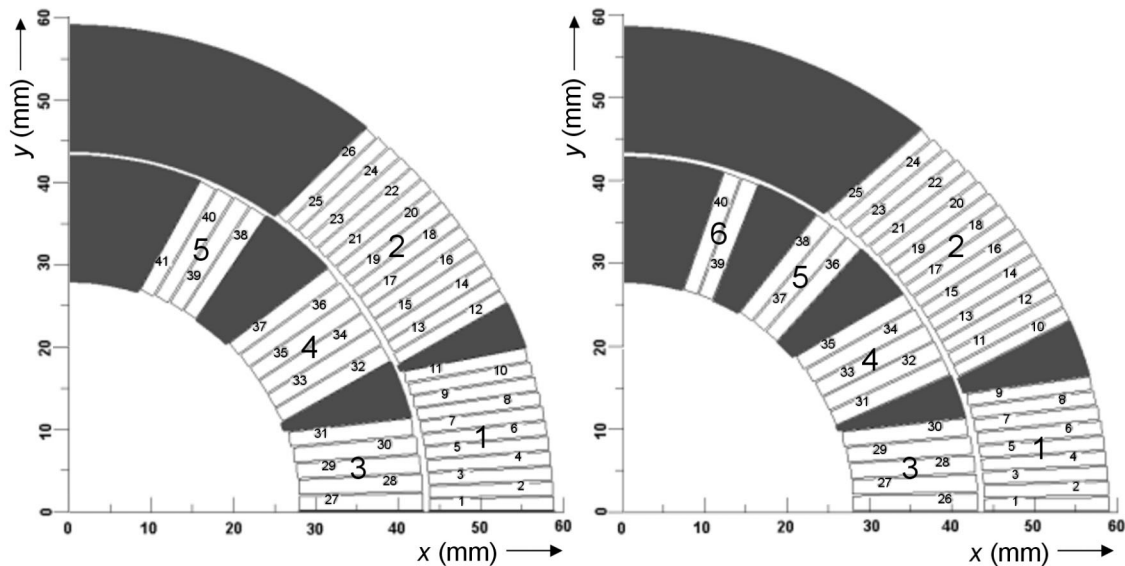


Figure 2.10 Five- (left) and six-block (right) quarter cross section. The coil consists of an inner and an outer layer of winding. The large numbers represent the numbering of the blocks, and the small numbers indicate the turns. The copper wedges are shown in gray.

A map of the magnetic field at injection in a cross section of a typical 6-block magnet is shown in figure 2.11. The arrows indicate the field vectors. For clarification, the intensity of the local field in the coil is also expressed by the grayscale. White represents low field and black represents high field. As already explained in section 1.2.3, the field in the center can be approximated by the multipole series in equation (1.2). The multipole components referred to are the normalized normal harmonics $b_n = B_n 10^4 / B_1$, and the normalized skew harmonics $a_n = A_n 10^4 / B_1$.

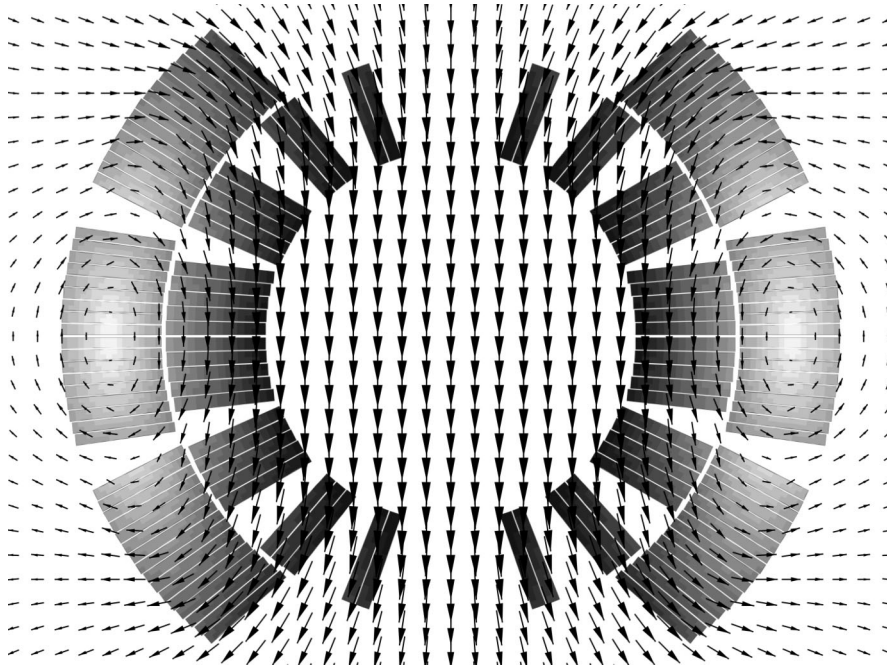


Figure 2.11 The field vectors are shown in a cross section of an LHC main dipole. The absolute local field in the coil is represented by the greyscale. White represents low and dark represents high levels of the local field in the coil [46].

In practical dipole magnets all normal odd harmonics are present since the current distribution always differs from the ideal $\cos(\theta)$ -shape. Due to fabrication tolerances normal-even and skew harmonics can also arise. In twin-aperture magnets with a common mechanical structure additional field errors are introduced due to (non-symmetric) saturation effects in the iron yoke. In figure 2.12 the first fifteen normal and skew field components in the center of a typical LHC main dipole coil are shown. The dipole field is a factor 10^4 larger than the other components. For the compensation of field errors, a small sextupole and a small decapole corrector are attached to the magnet ends.

The coil of the LHC main dipoles has a physical length of 14.6 m. The ends are formed naturally by bending the cable over the beam pipe. This is demonstrated in figure 2.13a. The field distribution in the ends differs considerably from that in the straight part of the magnets. Since the cable is bent over the beam pipe, the field B_{\perp} normal to the large face of the cable reduces to almost zero. Spatial gradients in the field sweep rate $\dot{B}_{\perp} = dB_{\perp}/dt$ induce so-called ‘Boundary Induced Coupling Currents’ (BICCs), which have an important impact on the homogeneity of the magnetic field in the center of the coil [55]. A calculated example for \dot{B}_{\perp} is shown in figure 2.13b, along the length of the inner layer

cable in one pole of the coil in a 1 m long LHC model dipole, for a central field sweep rate of 0.0066 Ts^{-1} . The sharp decreases in \dot{B}_\perp correspond to those parts in the coil where the cable bends around the beam pipe. The position $z = 0$ denotes the connection to the current lead; the other end of the cable is connected to the outer layer of the coil.

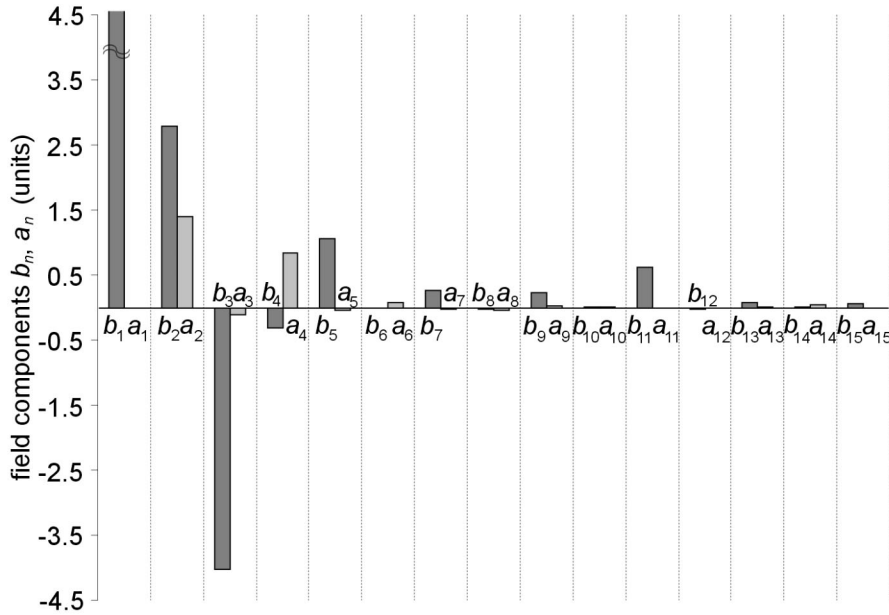


Figure 2.12 The first fifteen normal and skew field components in the center of a typical LHC main dipole coil (MBP2O1) are shown at the beginning of the injection plateau. b_n are the normalized normal and a_n the normalized skew field components.

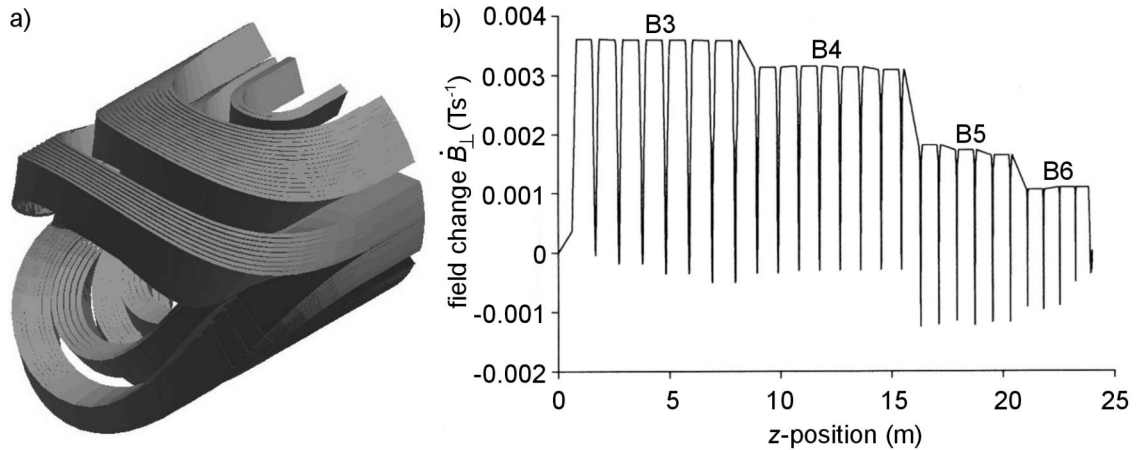


Figure 2.13 a) The coil ends are formed by bending the cable over the beam pipe [46]. b) The field sweep rate \dot{B}_\perp is shown along the length of the cable in the inner layer coil of a 1 m long LHC dipole model magnet. \dot{B}_\perp is the average field change in the cable cross section. The sweep rate of the central field in the coil is 0.0066 Ts^{-1} . The labels indicate the block numbers [55].

Three different types of cable-to-cable connections are present in the coil. The first type is the connection of the cables to the current leads. A second type of connections between different poles is often shunted by a copper bar. These connections are located in the low field region and, due to the matrix material, they have a small resistance in the range of 0.2-0.5 n Ω . Finally, connections between the two layers of the same pole are called splices. They are located in a high-field region. Each splice is made by soldering the two cables over a certain length. The resistance of a splice is typically 0.2-0.5 n Ω at zero field and increases due to the magnetoresistance with a factor of about 2-4 in a central field of 9 T [55]. The magnet end, where the connections are located, is referred to as the ‘connection end’, whereas the opposite end is called the ‘non-connection end’.

2.4 Rutherford cable

In order to limit the inductance and the practical winding cost, accelerator magnets are wound from a flat multi-strand cable. Flat cables were developed for the first time at the Rutherford Laboratory in Oxfordshire, UK. They are generally referred to as ‘Rutherford-type cables’. Photographs are shown in figure 2.14. The cables in the coil are insulated by two half overlapping wraps of Kapton tape and a third wrap of glass-fiber tape with an adhesive, allowing the penetration of superfluid helium. A sketch of a cable with its insulations is shown in figure 2.15. After winding, the adhesive is cured by heating each coil layer in a curing mould.

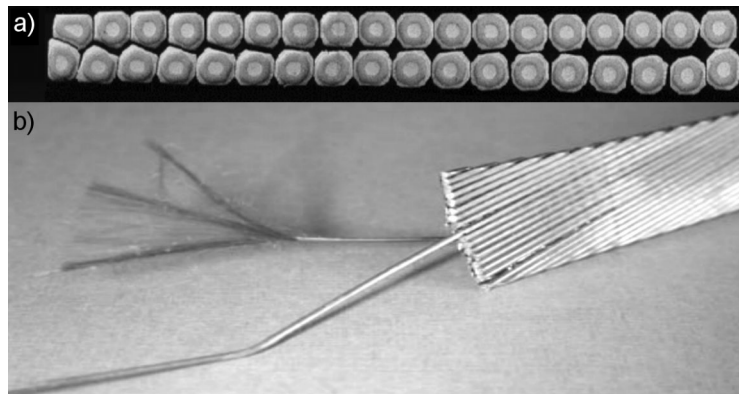


Figure 2.14 a) Cross sectional view and b) side view of a Rutherford-type cable.

A Rutherford-type cable with N_s strands and width w is keystoneed, i.e. manufactured with a slightly trapezoidal cross section to match the azimuthal ‘Roman-arc’ geometry of the blocks in the coil. The keystone angle $\alpha_k = \text{atan}((h_1-h_2)/w)$, see figure 2.16, can be calculated from the thicknesses h_1 and h_2 on both sides. The average thickness of the cable is given by $h = (h_1+h_2)/2$. Rutherford-type cables are twisted along their longitudinal axis. At both edges of the cable, the strands follow a skew path from one

Superconducting Accelerator Magnets

layer to the other. All strands are fully transposed along a ‘transposition pitch length’ $L_{p,s}$, also called ‘twist pitch’.

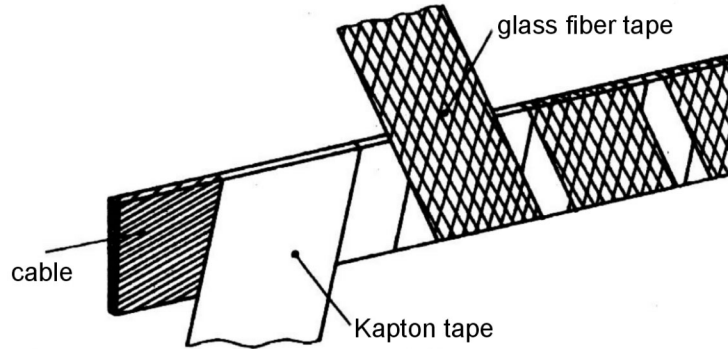


Figure 2.15 Rutherford-type cable enclosed by its insulations, which consists of overlapping layers of Kapton tape with a third layer of glass-fiber tape.

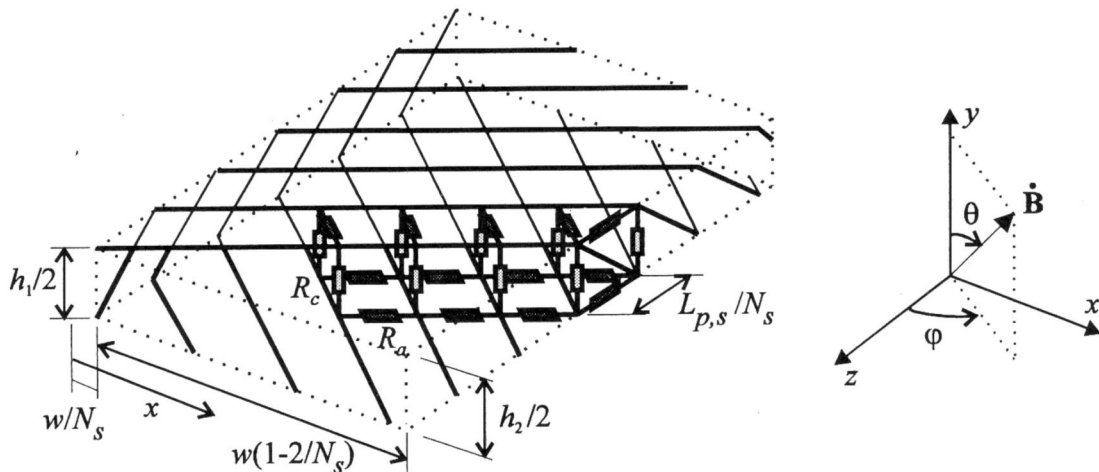


Figure 2.16 Network model of a Rutherford-type cable. The strands are represented by line elements and the average distance between the line currents at both edges and at both layers are $w(1-2/N_s)$ and $h/2$, respectively. The x -coordinate denotes the position across the cable width and is 0 at the physical edge of the cable. The adjacent and contact resistances R_a and R_c are shown in dark and light grey, respectively. The sketch on the right defines the coordinate system and the angles φ and θ .

In the LHC main dipoles, each layer of the coil has a different cable. Specifications for the inner and outer layer cable are summarized in table 2.2.

The electromagnetic properties of the cable can be modelled by a three-dimensional network of nodes interconnected by strand sections and resistances (figure 2.16). The strands are represented by lines with an infinitely thin diameter. Parallel strands following the two faces of the cable are crossing strands from the opposite face. These crossing points are electrically characterized by a cross contact resistance R_c . A second

type of resistance appears between adjacent strands R_a . This network of resistors forms loops in the cable structure.

dipole cable inner layer			dipole cable outer layer		
number of strands	28		number of strands	36	
cable width	15.1	mm	cable width	15.1	mm
cable mid thickness at 50 MPa	1.9	mm	cable mid thickness at 50 MPa	1.48	mm
keystone angle	1.25	°	keystone angle	0.9	°
transposition pitch	115	mm	transposition pitch	105	mm
critical current, 1.9 K, 10 T	> 13750	A	critical current, 1.9 K, 9 T	> 12960	A
cable length	433	m	cable length	751	m

Table 2.2 Characteristic properties of the cables in the inner and outer layers of the coils in the LHC main dipole magnets.

In cables with insulated strands, the current distributes itself among the strands in such a way that the voltages over all strands in the cable are equal. At weak excitation levels the current distribution is dominated by the joint resistance. Only for currents very close to the critical current the strand resistance has to be taken into account, especially for strands with a small N -value. During current ramps, the strand currents change according to their relative self- and mutual inductances. In all these cases, a random distribution has to be expected for the currents in the different strands of the cable.

Also in cables with non-insulated strands joint resistances, strand resistances and self- and mutual inductances contribute to inhomogeneous distributions of the current among the strands. In addition, sweeps of a uniform magnetic field \dot{B} induce so-called ‘Inter-Strand Coupling Currents’ (ISCCs). ISCCs flow in loops through the strands and through the contact resistances of the cable. The ISCCs have a characteristic loop length equal to the cable twist pitch and show time constants of typically 0.01 to 1 s. The magnitude of the ISCCs increases with the cable twist pitch and decreases with the electrical contact resistance between the strands. Another important type of coupling currents is induced due to non-uniformities in the field sweep rate and cross contact resistances. These currents are called ‘Boundary Induced Coupling Currents’ (BICCs) and details are explained in section 2.6.

2.5 Superconducting NbTi wires

The superconducting material for cables in the accelerator magnets is shaped into thin filaments from NbTi, which are surrounded by a very thin niobium-layer and imbedded in a copper matrix. Cross sections of two typical strands are shown in figure 2.17. In order to limit the induction of eddy currents during field sweeps, the filaments in the strands are twisted with a tight pitch. The matrix material at the same time provides mechanical

stability, serves as an electrical bypass of high conductivity and as a heat sink. The strands are annealed and coated in order to increase the contact resistances between strands touching each other in the cable. In LHC main dipoles, the strands are slightly different in the inner and outer layer of the coil. Details are given in table 2.3.

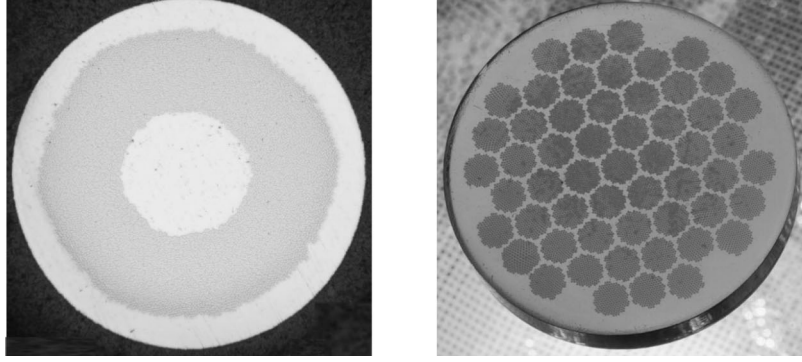


Figure 2.17 Cross sections of LHC dipole inner strands, fabricated using a single stacking (left) and a double stacking method (right).

dipole inner cable strand			dipole outer cable strand		
strand diameter	1.065	mm	strand diameter	0.825	mm
copper to superconductor ratio	> 1.6		copper to superconductor ratio	> 1.9	
filament diameter	7	μm	filament diameter	6	μm
number of filaments in strand	8900		number of filaments in strand	6520	
twist pitch of filament after cabling	15	mm	twist pitch of filament after cabling	18	mm
critical current, 1.9 K, 10 T	> 515	A	critical current, 1.9 K, 9 T	> 380	A

Table 2.3 Parameters for the strands in the inner and outer layers of the LHC main dipole coil.

The strand and cable production for the LHC is spread among different manufacturers. The internal design of the strands is not fixed, but only restricted to the specifications in table 2.3. The most important strand designs are the ‘single stacking’ and the ‘double stacking’ design. Single stacking strands have a central copper core, an outer copper shell and a uniform filament distribution in the rest of the cross section. Double stacking strands have bundles of filaments spaced apart from each other. Both designs are shown in figure 2.17. Between strands from different manufacturers, the $J_c(B,T)$ dependence can vary up to about 10%.

Most magnetic properties of a strand are determined by its filaments. The penetration field B_p and the saturation magnetization M_p of a cylindrical filament with radius R in the ‘Critical State’ exposed to a perpendicular external field are given by

$$B_p = \frac{2\mu_0}{\pi} J_c R, \quad (2.6)$$

and

$$M_p = \frac{4}{3\pi} J_c R. \quad (2.7)$$

The saturated filament magnetization has the value of $+M_p$ in decreasing field, and $-M_p$ in increasing field. In order to go from one branch of the hysteresis loop to the other, the necessary field change is $\Delta B = 2B_p = 3\mu_0 M_p$. (A detailed investigation of the filament behavior in a changing external field is presented in chapter 5). The magnetization of a saturated strand equals $M = \lambda M_p$. $\lambda = (1+r_{Cu,SC})^{-1}$ is the ratio of the superconductor volume to the volume of the strand. The copper to superconductor ratios $r_{Cu,SC}$ for the inner and outer layer strands in the LHC dipoles are given in table 2.3.

During sweeps of the external field so-called ‘Inter-Filament Coupling Currents’ (IFCCs) are induced in a strand. IFCCs flow in loops through the filaments and through the resistive matrix material. Their magnitude increases with the twist pitch of the filaments in a strand and decreases with the resistivity of the matrix material. The IFCCs have characteristic loop lengths equal to the twist pitch of the filaments and decay with time constants of typically 0.01 to 0.1 s.

2.6 Boundary Induced Coupling Currents (BICCs)

The present understanding of the spatially periodic pattern, the field decay and other effects like ramp rate limitations in superconducting accelerator magnets is based on the existence of ‘Boundary Induced Coupling Currents’ (BICCs), also called ‘supercurrents’. BICCs are currents flowing in loops through the strands, through the contact resistances and return through another strand [55]. An illustration is shown in figure 2.18. Their amplitude and loop length can be several orders of magnitude larger than those of the ISCCs. BICCs exhibit large characteristic times, and propagate along the cable. In practical cables, typical time constants of BICCs are in a range between 10 and 10^5 s. BICCs are represented by their amplitude, characteristic length, -time and -propagation velocity. Theoretically, BICCs can also be induced between the filaments of a strand. However, no significant indication was found so far.

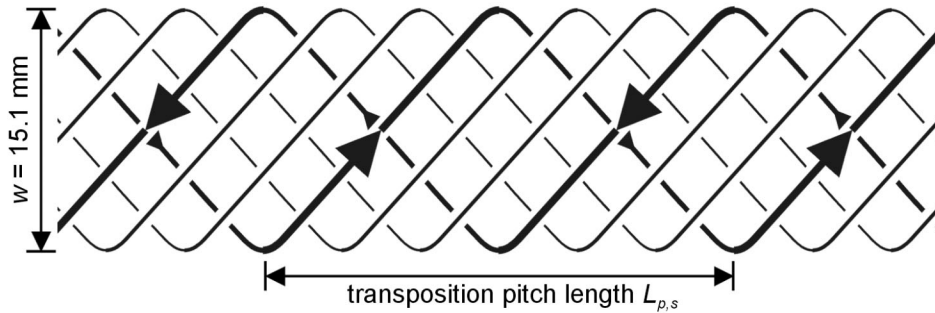


Figure 2.18 Two strands in a Rutherford-type cable carry a current, flowing in a long loop.

During field sweeps, BICCs are induced in parts of the magnet, where spatial gradients in the field sweep rate \dot{B}_\perp (perpendicular to the large face of the cable) or in the contact resistances R_c and R_a exist along the length of the cable. These gradients especially appear in the coil ends, in cable-to-cable connections or connections of the cable to the current leads. A calculated example of \dot{B}_\perp along the length of the inner layer cable of a 1 m long LHC dipole magnet is shown in figure 2.13b. Gradients in the contact resistances mainly appear due to gradients in the transverse pressure, soldered connections or local shorts between the strands or the keystoneing of the cable.

In contrast to the irregular distribution of current imbalances caused by strands with different joint resistances, BICCs have a typical distribution in the cable cross section. Opposite strands in each cable cross section carry BICCs with the same magnitude, but with an opposite sign. Adjacent strands only have slightly different BICCs. A calculated example is shown in figure 2.19, for a 16-strand Rutherford-type cable [55]. Numerical results in chapter 6 will demonstrate that the current imbalances in cables for LHC main dipoles have a maximum typically around 5 A per strand. Due to their regular distribution, the BICCs generate pronounced field errors.

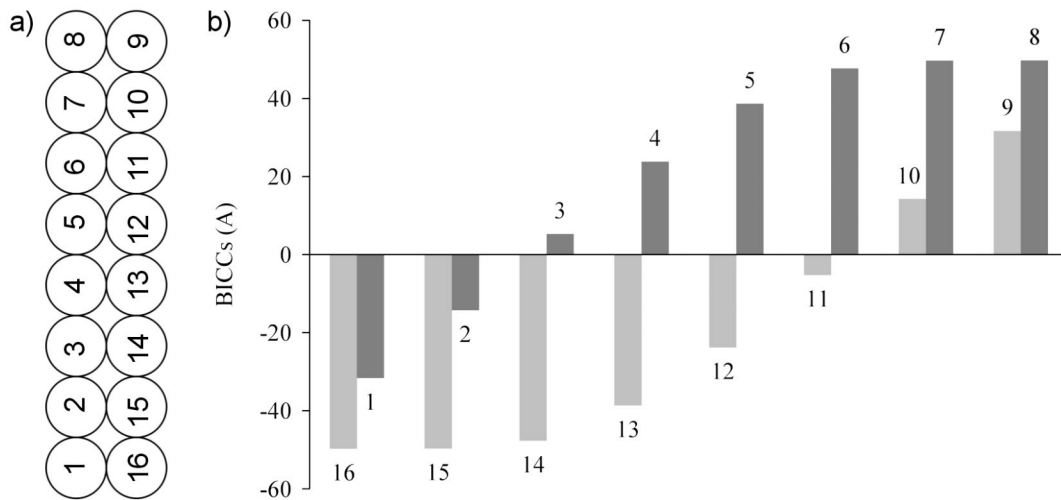


Figure 2.19 a) Numbering of the strand positions in the cross section of a 16-strand Rutherford-type cable. b) Illustration of the BICC magnitude in a 16-strand cable at a certain z -position. The labels indicate the strand positions [55].

Outside the localized gradients of the field sweep rate or the contact resistances, the BICCs decrease along the strands in the cable. This decrease can be quasi-exponential (regime A), quasi-linear (regime B) or described by an intermediate regime. The type of decay is determined by the ratio between R_c and the effective strand resistivity ρ_s . For

Superconducting Accelerator Magnets

small ratios the BICCs decay exponentially with a characteristic length, whereas for large ratios the decay is quasi-linear. At the ends of the cable the BICCs decrease towards 0.

In accelerator dipole coils, a combination of the exponential, the linear and intermediate regime is present. BICCs with relatively small characteristic times in a range between 10^2 and 10^3 s are classified in regime A. Their magnitude is relatively insensitive to contact resistances in the soldered or unsoldered ends of the cable. BICCs with large time constants, typically in a range between 10^4 and 10^5 s, are classified in regime B. They attain large magnitudes if the cable ends are soldered.

Krempasky and Schmidt [33], [34] investigated the induction and diffusion of BICCs in a superconducting two-wire cable, twisted with a pitch L_p and two soldered contacts per pitch with resistance R_c . They exposed the cable to a changing external flux $\dot{\Phi}$, localized in a central loop. A drawing of the test cable is shown in figure 2.20.

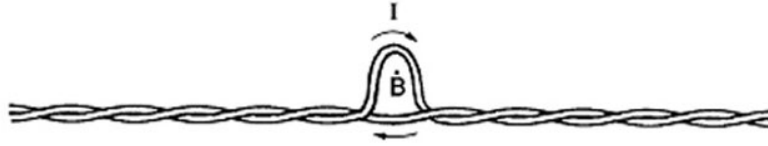


Figure 2.20 Drawing of the cable with a central test loop. Reproduced from [34].

Krempasky and Schmidt show that, in a continuum approximation, the current in each strand can be described by a diffusion equation

$$\frac{\partial^2 I}{\partial z^2} = L' G' \frac{\partial I}{\partial t} \quad (2.8)$$

with a uniform and distributed transverse conductivity G' and inductance L' . The space and time dependent solution for a current in a strand is

$$I(z, t) = \frac{4L\dot{\Phi}}{L_{p,s}R_c\pi^2} \sum_{\substack{k=1 \\ k \text{ odd}}}^{\infty} \frac{(-1)^{(k-1)/2}}{k^2} \sin(\pi kz/L) \cdot (1 - e^{-t/\tau_k}). \quad (2.9)$$

For $k = 1, 3, 5, \dots$ the time constants $\tau_k = \tau/k^2$ increase with the square of the total cable length L :

$$\tau = \pi^{-2} L' G' L^2. \quad (2.10)$$

If the external field sweep is stopped at a time t_1 , the induced currents diffuse, and each term in the sum of equation (2.9) has to be multiplied with a factor $\exp(-(t - t_1)/\tau_k)$.

Bottura, Breschi and Fabbri [12] extended the diffusion equation (2.8) to cables with a generic number of strands. They describe the current diffusion in a multistrand superconducting cable by a system of parabolic partial differential equations, and present

a solution similar to equation (2.9). The induced currents in an N_s strand cable are (N_s-1) times larger, and the diffusion time constants are $N_s/2$ times longer.

2.7 Spatially periodic field pattern

During ramps, boundary induced coupling currents are induced in the Rutherford-type cables of superconducting accelerator magnets. In the center of the coil, these current imbalances can be observed as a spatially periodic pattern along the axis of the magnet, which is sinusoidal within the accuracy of the measurements. This so-called ‘spatially periodic field pattern’ is observed in all field components and results from a superposition of the fields induced by current imbalances in all turns of the coil. It has a period comparable to the transposition pitch of the cable. In LHC model dipoles Schreiner [50] found a wavelength close to the twist pitch length L_p of the cable in the inner layer of the coil. The thick line a) in figure 2.21 illustrates the pattern in a typical LHC dipole at the beginning of injection.

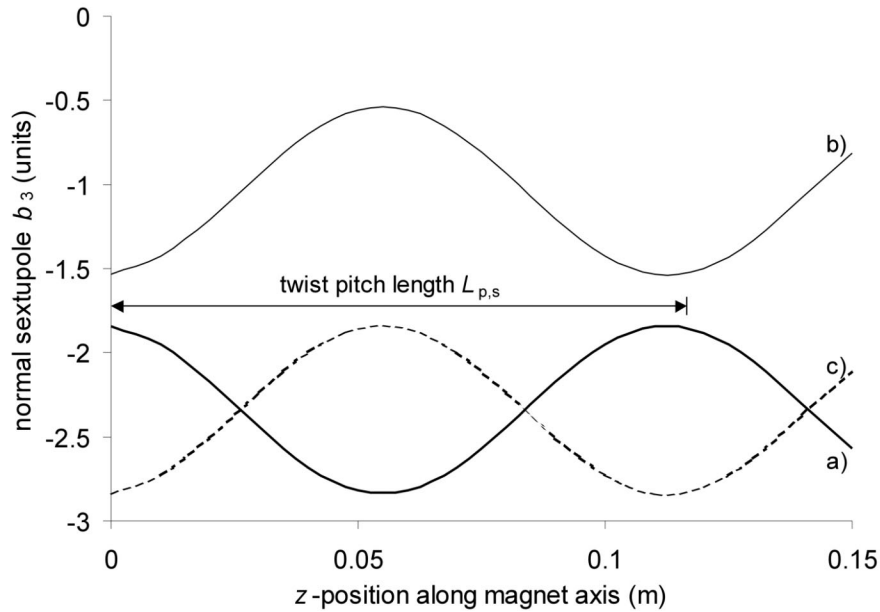


Figure 2.21 a) At the beginning of injection a spatially periodic field pattern in the normal sextupole harmonic b_3 is sketched along the axis of a typical LHC dipole magnet. b) The amplitude changes during injection, and the average value of b_3 decays. c) The amplitude doesn't change during the acceleration ramp. However, due to the snapback, the average value of b_3 moves back to the original hysteresis curve.

The periodic structure persists for several hours, even after de-energizing the magnets. In experiments at CERN, a clear structure is still observed after 81 hours [50]. Due to the properties of the BICCs, the pattern shows a complex time and space dependence, which is strongly influenced by excitation history. The BICCs diffuse during periods of constant

magnet excitation, and the pattern amplitude can increase or decrease, with very long time constants. In several cases a decay after the end of the pre-cycle in a de-energized magnet was described by a linear combination of three decaying exponentials. On a short LHC model dipole time constants of 460 ± 40 s, $(18 \pm 4) \cdot 10^2$ s and $(15 \pm 2) \cdot 10^4$ s were found [50]. The observed exponential decay agrees with the solution of the diffusion equation (2.8).

The diffusion was demonstrated experimentally by Sampson and Ghosh [47]. They exposed a cable winding (without transport current) to a variable external field, and induced a spatially periodic field pattern. A part of the test winding was heated above the critical temperature T_c . The field pattern in this section disappeared. However, boundary induced coupling currents persisted in the superconducting section. After re-cooling to $T < T_c$ the BICCs diffused, and again, the pattern was visible along the entire length of the winding.

Schreiner [50] demonstrated the qualitative correspondence between the pattern behavior and Krempasky's two wire model. He compared the pattern amplitude during the operation of the magnet to a charging capacitor. During up-ramps in a current cycle, the Rutherford-type superconducting cable is charged with a non-uniformly distributed current wave. On the plateau of the pre-cycle this wave diffuses slowly. In other words the current is redistributed among the strands. During the down-ramp, the superconducting cable charges itself with a non-uniformly distributed current wave of opposite sign (antiwave). Again, during the slow up-ramp to injection, a wave with the original sign is induced. As a consequence, the periodic field pattern measured after the current cycle is a composition of diffusing waves which partially cancel [43].

The contact resistances and the number of pitch lengths between the coil heads vary considerably from turn to turn and from magnet to magnet. For this reason, rather different patterns have to be expected for different magnets and for different multipoles in the same magnet. In experiments on 1 m short model dipoles, where nominally identical magnets are exposed to similar excitation histories, the amplitudes of the sinusoidal pattern, measured on different magnets, are spread within one order of magnitude [50]. A linear correlation is found between the amplitudes and the inverse average cross-contact resistances [47], [50]. (The correlation suggests that the BICCs in a magnet are determined by the average cross-contact resistance, and that also the parameters of decay and snapback are directly linked to this value.)

During the pre-cycle, shifts of the periodic pattern are often observed along the axis of the magnet [50]. These longitudinal shifts can be described by a phase shift. After the end of the pre-cycle in a de-energized magnet, the phase remained relatively constant. Since

the BICCs in the magnet are not significantly influenced by the ramp to injection, one can also expect a relatively constant phase during the injection plateau.

The periodic field pattern itself does not significantly affect the accelerator operation. However, during periods of constant magnet excitation, the average strand magnetization is affected by field changes in the coil due to the diffusion of BICCs [29], [57]. During injection, this phenomenon is observed in accelerator magnets as a field decay. Line b) in figure 2.21 shows the periodic pattern at the end of injection. Its amplitude has changed and the average sextupole has increased due to the field decay.

Not very much is known about whether or not the phase changes during the acceleration ramp after the end of injection. The BICCs are assumed to be constant. A possible magnetization contribution to the periodic pattern might change the phase. The new prototype of the Hall detector described in section 3 will help to clarify this point. Line c) in figure 2.21 shows the periodic pattern for the case where the phase doesn't change.

2.8 Decay and snapback

The phenomenon of thermally activated flux creep was originally thought to be the only source of field decay. However, the dependence of the decay on the excitation history of the magnet cannot be explained by flux creep, and shows that flux creep can not be more than a part of the explanation. A rough estimation of a possible flux creep contribution can be derived from equation (2.3). Typical values are $t = 1020$ s, $J_c = 10000$ A/mm², $T = 1.9$ K, $\langle \Phi \rangle = \Phi_0$ (flux quantum), $a = 5$ nm (coherence length) and $l_b = 6$ μ m (filament diameter). With 0.03% the resulting flux creep decay is negligible with respect to the decay measured in real magnets. In section 5 and 6 experimental results are used to confirm the irrelevance of flux creep.

Wolf analyzed several possible alternative mechanisms for the field component decay during injection [57]. All mechanisms explain the reduction of the filament magnetization due to BICCs diffusing along the length of the cables in the coil.

At the start of injection, most filaments in the coil of the magnet are in a saturated state, determined by the previous change of the local field in the coil. During periods of constant background field, the BICCs diffuse along the Rutherford-type cable and cause a redistribution of current among the strands. The current redistributions change the local field in the coil and reduce the average filament magnetization.

The field change induced in the strands can be decomposed into a circular self-field change ΔB_{self} and an external field change ΔB_{ext} . The total field change is then $\Delta B_{total} = \Delta B_{ext} + \Delta B_{self}$. This is demonstrated in figure 2.22a.

2.8.1 Self-field induced decay

As an example of the impact of the change in self-field, in figure 2.22b four filaments are shown in the cross section of a strand. Their magnetization is saturated in y -direction and has a vector which is anti-parallel to the external field B_0 . The local self-field has a different direction with respect to all filaments. The average impact on the x -component perpendicular to the original magnetization vanishes, and only the average parallel or anti-parallel y -component contributes. Locally a y -component anti-parallel to the background field reduces the filament magnetization, whereas a parallel y -component leaves the filament magnetization constant. The average effect over all filaments in the strand is a reduction of the absolute strand magnetization, where the vector doesn't change its direction.

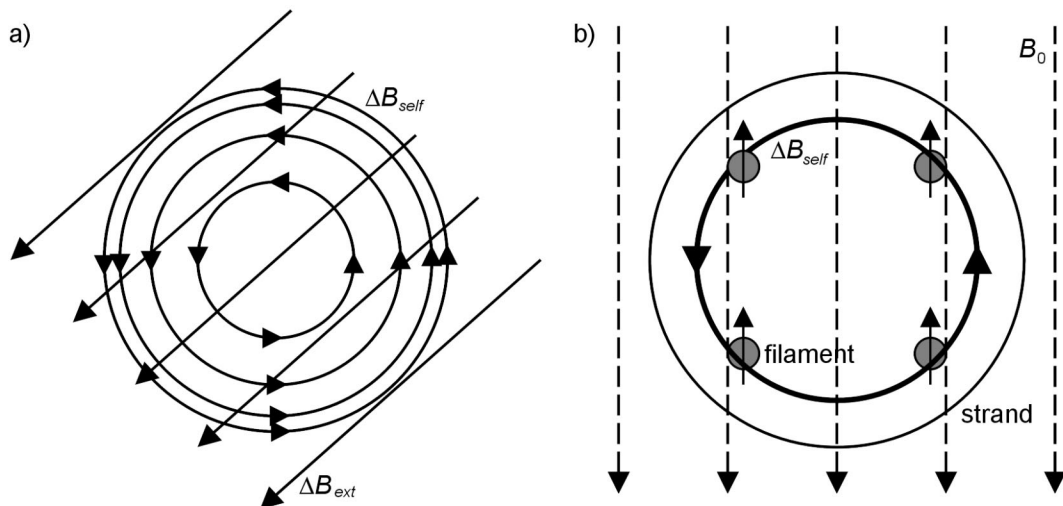


Figure 2.22 a) The field change inside the strands is decomposed in a circular self-field change and an external field change. b) Four magnetized filaments are shown in the cross section of a strand. The magnetization vectors of the filaments are anti-parallel to the background field B_0 (dashed lines). The thick circular arrows represent the self-field change.

2.8.2 Decay induced by field changes in the coil

Figure 2.23 illustrates the mechanism of the magnetization decay induced by field changes in the coil. The diffusion of BICCs (figure 2.23a) during injection changes the external field along the cable (figure 2.23b). The external field change ΔB_{ext} is assumed to be periodic in the cable twist pitch L_p along a path parallel to the cable edge, providing that the current distribution does not change too much over a cable pitch. ΔB_{ext} increases the local field over approximately half a cable twist pitch and decreases it over the next

half. Field changes anti-parallel to the background field reduce the local magnetization. If the field changes are parallel to the background field, the magnetization is saturated and doesn't change. The resulting magnetization is sketched in figure 2.23c. It is considerably lowered over the first half cable twist pitch and changes little over second half. As a net effect, the average cable magnetization decreases and is observed as a 'field decay' in all multipoles.

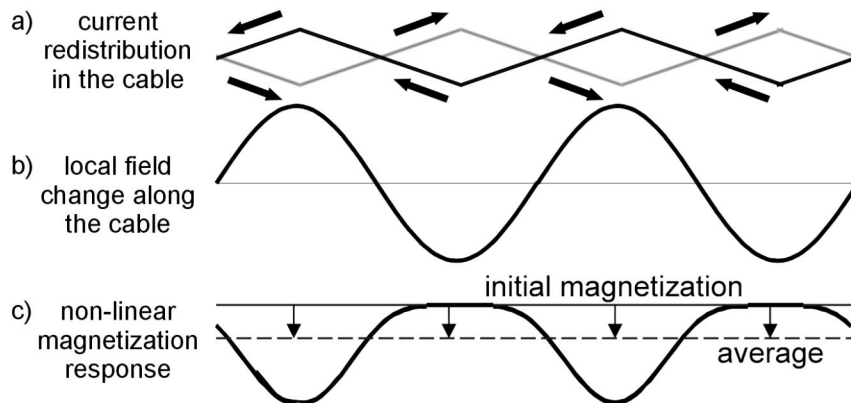


Figure 2.23 a) During injection, BICCs diffuse along the cable in the magnet and cause a redistribution of the currents among the strands. b) The current redistribution causes a change of the local external field along the cable. c) The local field change has a non-linear impact on the magnetization and causes a net decrease of its average value.

2.8.3 Snapback

As soon as the field in the magnet is ramped up again after the end of injection, the coil magnetization rapidly recovers from the decay and follows the course of the original hysteresis curve. The magnetization is re-established within a field increase of typically 20 mT.

2.9 Conclusion

Decay and snapback can significantly affect the performance of the Large Hadron Collider. A good understanding of both effects is essential, and methods have to be developed for their precise compensation in the machine.

Rotating coils are the standard equipment for magnetic measurements in accelerator magnets. However, they do not provide the time-resolution required for precise measurements of the snapback curve. Neither do they allow the simultaneous observation of decay and snapback along a wavelength of the spatially periodic field pattern. In chapter 3 a Hall detector is presented, which can be used for systematic magnetic measurements in accelerator magnets as well as for the envisaged online compensation in

Superconducting Accelerator Magnets

the ring of magnets in the machine. A new version of the detector with several rings allows the simultaneous analysis of decay and snapback at several positions along the periodic pattern.

Decay and snapback vary from magnet to magnet, and strongly depend on the excitation history. The understanding of the response to a given excitation history is essential for their compensation. In chapter 4 measurements after different current cycles and on different magnets are compared to an analytical model with a single time constant.

Finally, the mechanisms of decay and snapback need to be better understood. For this reason, a detailed analytical investigation is performed in chapter 5 and 6.

Chapter 3

Magnetization Measurements on Wires and Coils

This chapter presents specific techniques for analyzing the magnetic performance of wires and coils. At first, a set-up for magnetization measurements on small samples of superconducting material is explained. Subsequently, different 1 m short model dipoles as well as 15 m long prototypes and pre-series magnets are summarized. Standard equipment for magnetic measurements in accelerator magnets are rotating coils, thin pick-up coils that rotate inside the bore of the magnet and produce a signal proportional to the multipole components of the field. An alternative to rotating coils are field component measurements using Hall plates. A system of 2 rings with three Hall plates mounted on each ring allows to compensate the signals for the main dipole field and to measure the sextupole component. The device is used for fast and precise measurements of the decay and snapback. An additional detector with an array of 6 sextupole rings was developed in order to observe decay and snapback over one wavelength of the spatially periodic field pattern. This new detector has two additional rings with 5 Hall plates, allowing measurements of decapole fields. The system can be used for both, magnetic measurements in accelerator magnets and on-line measurements in reference magnets during the operation of the machine.

3.1 Magnetization measurements on small samples

The magnetization of superconducting samples can be measured by means of an integrating coil magnetometer. The set-up shown in figure 3.1a is used by the University of Twente. A sample wire or foil is wound around a cylindrical sample holder and placed between two concentric superconducting pick-up coils. The inner coil is used to improve the mutual induction between the sample and the pick-up set. Two additional empty coils, connected in anti-series with the first set, compensate the signal for the applied field. The magnetic moment m of the sample is proportional to the time integral of the voltage U_{ind} induced across the entire set of coils:

$$m \sim \int U_{ind}(t) dt. \quad (3.1)$$

In order to integrate the induced voltage, the set of pick-up coils is connected in series to a superconducting sensor coil. A sketch of the circuit is shown in figure 3.1b. Since the entire circuit is superconducting, it acts as an integrator. For this reason, the magnetic moment m is proportional to the magnetic field B_s inside the sensor coil and can be read out by a Hall sensor in the sensor coil:

$$U_{Hall} = c \cdot m = c \cdot V_s \cdot M . \quad (3.2)$$

V_s is the volume and M the magnetization of the sample. The constant $c = 0.116 \text{ V/Am}^2$ was determined during the calibration of the set-up.

Both, AC and DC external fields can be applied to the sample independently, by powering the AC and DC magnets. The experiment is performed inside a cylindrical cryostat in a liquid Helium bath at 4.2 K and atmospheric pressure. The reproducibility of the measurements is better than 5%. A detailed description of the set-up is given in [58].

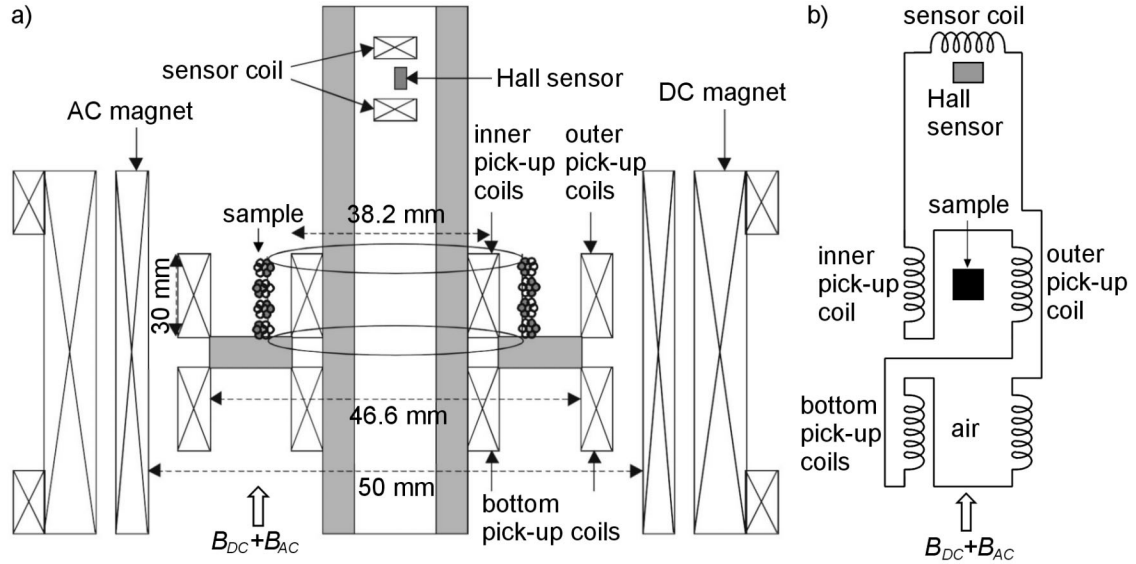


Figure 3.1 a) Longitudinal section of a cylindrical set-up for magnetization measurements on small samples. b) Superconducting circuit showing the sample, the inner and outer top and bottom pick-up coils, the sensor coil and the Hall sensor.

3.2 Magnetization measurements on dipole magnets

3.2.1 Magnets tested

Within the framework of CERN's R&D program for LHC dipoles, three series of 1 m short models, 15 m long prototypes and 15 m long pre-series magnets were manufactured [37], [53]. Several of the magnets were reworked in different 'versions' (V1, V2, V3, V4), by changing the collaring and yoking conditions. At CERN the 1 m and 15 m long

Magnetization Measurements on Wires and Coils

accelerator magnets are tested in two different measurement stations, the ‘Block-4’ laboratory and the ‘SM-18’ facility, respectively. The measurements in ‘Block-4’ are performed with so-called ‘radial’ rotating coils. In ‘SM-18’, both, so-called ‘tangential’ rotating coils and sensors with Hall plates are used.

The magnets discussed within the framework of this thesis are summarized in table 3.1. A simplified numbering is used throughout this book. The 1 m short model magnets 1 to 17 are manufactured with 5 or 6 blocks of cable, as single- or twin aperture magnets. Magnet 18 and 19 are 15 m long 3rd generation prototype dipoles, and magnet 20 is a pre-series magnet, which represents the closest match to the most topical design of the LHC.

<i>number</i>	<i>name</i>	<i>design</i>	<i>apertures</i>	<i>length</i>	<i>laboratory</i>	<i>rot. coils</i>
magnet 1	MBSMS5-V1	5 block	single	1 m	Block-4	radial
magnet 2	MBSMS6-V1	5 block	single	1 m	Block-4	radial
magnet 3	MBSMS12-V1	5 block	single	1 m	Block-4	radial
magnet 4	MBSMS15-V4	6 block	single	1 m	Block-4	radial
magnet 5	MBSMS17-V1	6 block	single	1 m	Block-4	radial
magnet 6	MBSMS17-V3	6 block	single	1 m	Block-4	radial
magnet 7	MBSMS18-V1	6 block	single	1 m	Block-4	radial
magnet 8	MBSMS19-V2	6 block	single	1 m	Block-4	radial
magnet 9	MBSMS22-V1	6 block	single	1 m	Block-4	radial
magnet 10	MBSMS23-V3	6 block	single	1 m	Block-4	radial
magnet 11	MBSMT1-V3	5 block	twin	1 m	Block-4	radial
magnet 12	MBSMT4-V3	6 block	twin	1 m	Block-4	radial
magnet 13	MBSMT5-V3	6 block	twin	1 m	Block-4	radial
magnet 14	MBSMT8-V1	6 block	twin	1 m	Block-4	radial
magnet 15	MBSMT9-V1	6 block	twin	1 m	Block-4	radial
magnet 16	MBSMT9-V2	6 block	twin	1 m	Block-4	radial
magnet 17	MBSMT10-V1	6 block	twin	1 m	Block-4	radial
magnet 18	MBP2O1-V1	6 block	twin	15 m	SM-18	tangential
magnet 19	MBP2O2-V1	6 block	twin	15 m	SM-18	tangential
magnet 20	MBPSO1	6 block	twin	15 m	SM-18	tangential

Table 3.1 Numbering of the magnets referred to in this thesis. (The full name of magnet 20 (MBPSO1) is HCLBB_001-CR001001).

3.2.2 Test facilities

3.2.2.1 1 m model dipoles in the ‘Block-4’ laboratory

Measurements on 1 m model dipoles are performed in a vertical test set-up. A schematical drawing and a picture are shown in figures 3.2a and b, respectively. The magnets are suspended inside a cryostat and cooled with superfluid helium at a temperature of 1.9 K. A λ -plate separates the boiling helium bath above the plate from

Magnetization Measurements on Wires and Coils

the superfluid bath under the plate, both at atmospheric pressure [54]. The superfluid state in the lower portion of the cryostat is achieved by means of a heat exchanger, wherein saturated superfluid helium conditions are obtained via Joule-Thomson expansion of liquid helium from 1 bar to approximately 15 mbar. The λ -plate has a number of leak-tight feed-throughs for superconducting bus-bars, instrumentation wires and a sliding bearing for the rotating shaft used for the magnetic measurements in 'Block-4'. The shaft is rotated by a DC motor mounted on the top end of the shaft, typically with rotation frequencies in the range of 1 Hz. The angular position is read by angular encoders.

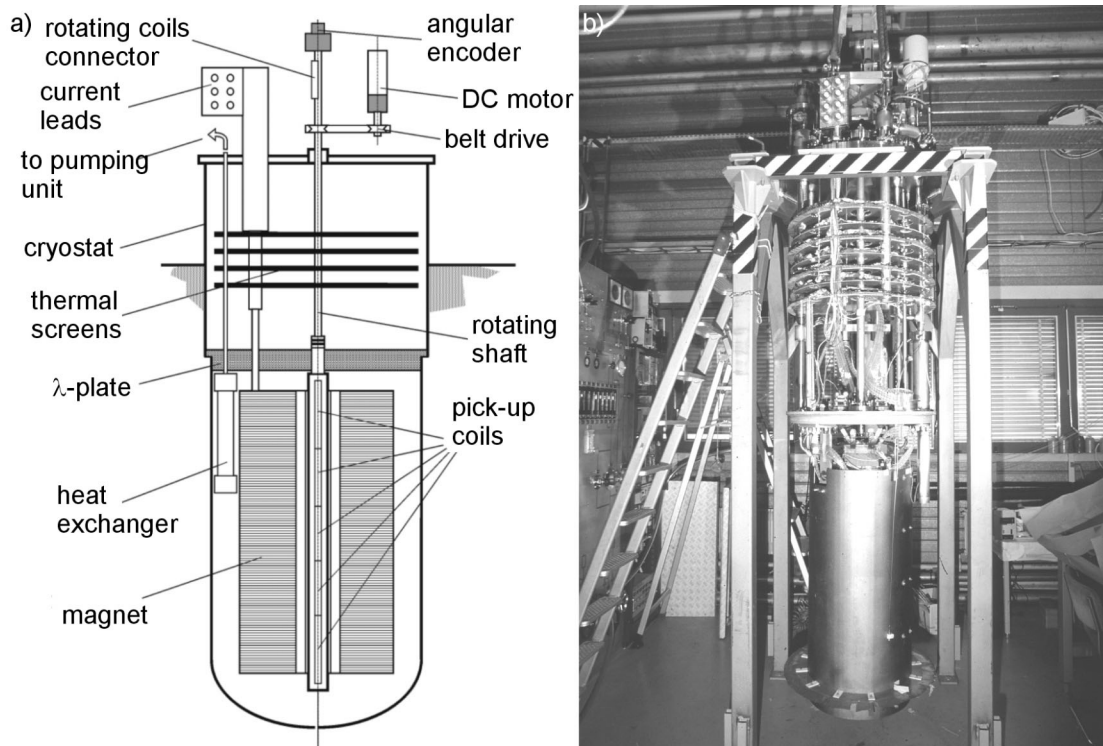


Figure 3.2 a) Vertical section of the set-up for testing 1 m model magnets. b) Photo showing the insert with a magnet attached to it.

3.2.2.2 15 m long dipoles in the 'SM-18' laboratory

The 'SM-18 facility' is being built at CERN to test all superconducting LHC magnets at a temperature of 1.8 K [8]. A picture of a stand for cryogenic tests, quench-performance tests and magnetic field measurements is shown in figure 3.3.

A measurement bench provides the fundament on which 15 m long LHC dipole magnets are aligned with a high mechanical precision. One side of the dipole magnet is connected to a cryogenic 'feed box'. Here, the current leads for the dipole coil are connected to the cables of the power supply. Furthermore, the feed box provides liquid helium for the cold

Magnetization Measurements on Wires and Coils

mass. Both apertures of the LHC dipoles are equipped with anti-cryostats (also called warm bores) with an inner diameter of 40 mm. They allow measurements at room temperature. In ‘SM-18’, both, rotating coils and sensors with Hall plates are used for magnetic measurements. Figure 3.3 shows two long measurements shafts being rotated by a so-called ‘twin rotating unit’.

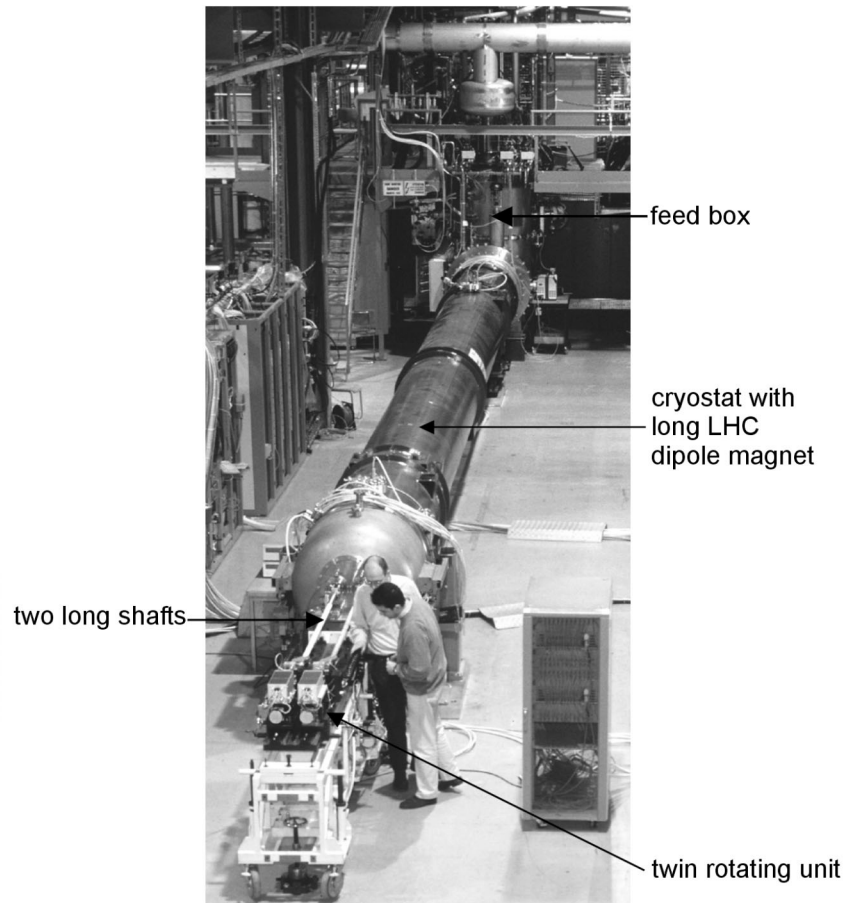


Figure 3.3 Set-up for field measurements on a long dipole magnet in the SM-18 laboratory.

3.2.3 Rotating coil measurements

The standard technique for magnetic measurements in accelerator magnets is the harmonic coil method [31]. This technique is based on a number of flat, longitudinally segmented arrays of pick-up coils, rotating with an angular frequency ω inside the apertures of a magnet. In the presence of a large dipolar main field, a single array of pick-up coils is insufficient to measure multipole field components of higher order (e.g. b_3 , b_5 , b_7 and b_9). The measurements discussed in this thesis are performed with shafts containing three such arrays: A , B and C . A and B are used to compensate the measured signals for the dipole field. The third array C is a spare and is not used for the measurement. The geometry of the pick-up coils in the shaft cross section can be ‘radial’

Magnetization Measurements on Wires and Coils

or ‘tangential’. As an example, figures 3.4a and b schematically show the geometry of the ‘radial’ and ‘tangential’ rotating coils used in ‘Block-4’ and ‘SM-18’, respectively. The number of turns N , the length L and the average complex wire positions z_1, z_2, z_3 and z_4 characterize each shaft.

The shaft used for measurements on 1 m short model dipoles in Block-4 is rotated inside a bath of superfluid helium. Three sequences of 20 cm long pick-up coils measure the field in the central part of the magnet. The pick-up coils in the magnet ends each have a length of 24 cm.

Tangential rotating pick-up coils are used for field measurements on long magnets. A 16 m long shaft is assembled from 13 modules of approximately 1.25 m length. The pick-up coils have a length of 1.15 m, which is exactly ten times the wavelength of the spatially periodic field pattern in the LHC main dipoles. Each pick-up coil delivers a signal proportional to the time derivative of the flux through its windings. The impact of the periodic pattern on the signal is thus averaged out. The shaft covers the 15 m long LHC dipole and the adjacent corrector magnets. All modules are identical and designed to allow an exchange of positions. The coil signals are passed from one part of the assembly to the other by electrical connectors. Ceramic Al_2O_3 was chosen for the support cylinder due to its high rigidity and geometric stability. The ceramic is non-magnetic, non-conducting and, thus, does not affect the magnetic field it is supposed to measure. In order to leave enough space for the installation and operation of the shafts inside the anti-cryostats, its maximum outer diameter is limited to about 36 mm.

Each measurement consists of a little less than three revolutions in forward and backward direction. The shaft is accelerated during a first turn. Afterwards, the signal is read during a full revolution at a constant rotation speed. Finally, during the last turn, the shaft is de-accelerated in order to change the rotation direction. The measurement results are obtained as an average over the forward and backward rotations. The averaging reduces the impact of field changes during the measurement, electronic drifts, systematic offsets and symmetric torsion effects. Due to dead times between the rotations, the best time resolution of the rotation coil system is in the order of 20 s.

The signals induced into the rotating coil array are split in an ‘absolute’ and a ‘compensated’ signal. The dipole field is derived from the absolute signal U_A only. In order to measure higher multipole field components and to compensate the signal for the disturbing contribution of the dipole field, the two pick-up coils (A and B) are electrically connected with opposite polarities. This is shown in figure 3.5a.

Magnetization Measurements on Wires and Coils

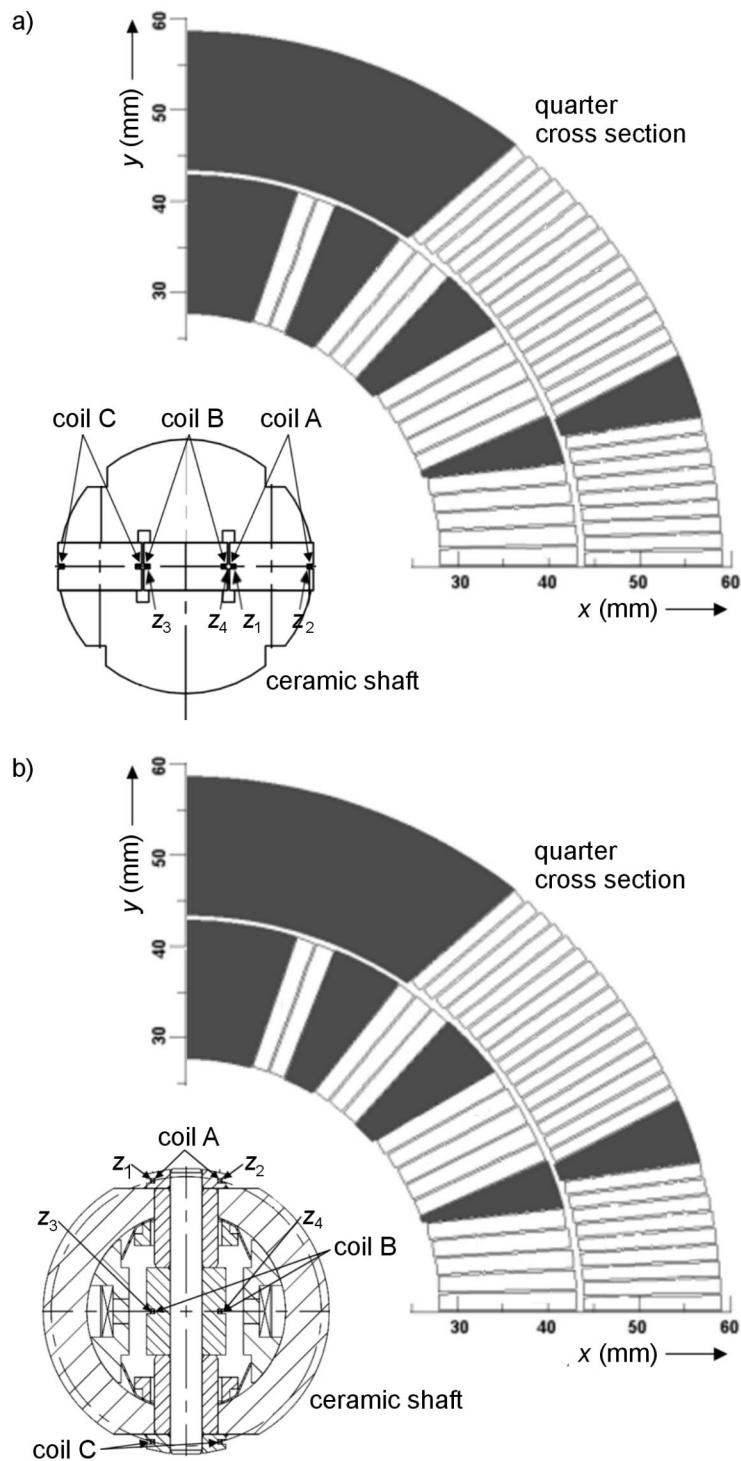


Figure 3.4 The cross section of two different shafts for rotating coil measurements is shown inside a quarter cross section of a dipole coil. a) shows a 'radial' and b) a 'tangential' configuration of the pick-up coils. The radial configuration is used for measurements on 1 m short dipoles in 'Block-4', and the tangential configuration for measurements on 15 m long prototypes and pre-series magnets in 'SM-18'.

Magnetization Measurements on Wires and Coils

In both, radial and tangential arrangements, the pick-up coils A and B are parallel and, thus, always have the same angle with respect to the dipole field. For this reason, the contribution of the dipolar field component B_1 to the compensated signal $U_{comp} = U_A - U_B$ vanishes, and only field components of order $n > 1$ contribute to the signal.

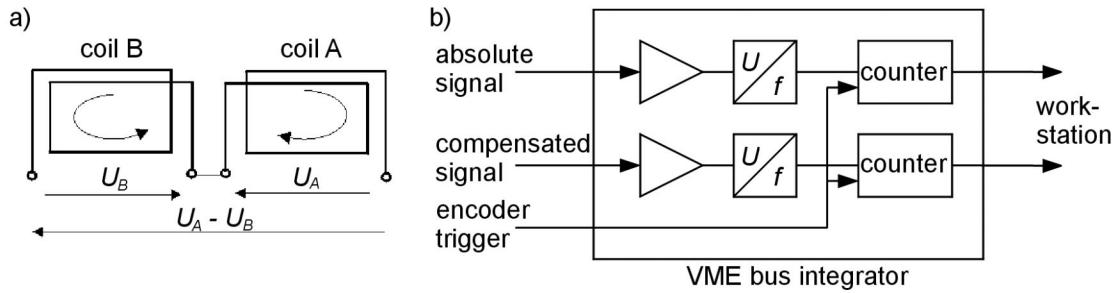


Figure 3.5 a) Connection scheme for absolute U_A and compensated signals $U_A - U_B$. b) The absolute and compensated pick-up coil signals are pre-amplified and converted into frequency. The time integration is represented by the subsequent frequency count. The counters are triggered by an angular encoder. The flux increments $\Delta\Phi_i$ are read out by a software on a workstation.

Voltage signals from the rotating coils are first pre-amplified and then read-out simultaneously by a set of digital integrators. A schematic drawing of the circuit is shown in figure 3.5b. An angular encoder is connected to the shaft. It triggers the integrators in groups of coils. The pre-amplified voltage signals are converted into frequencies. The pulses from the voltage to frequency converter are counted. These counts represent the time integration, which is triggered by pulses from the angular decoder. As a result, the signals are sampled as a function of the rotation angle θ_k in a discrete series of k points for a total of M points uniformly distributed over a full revolution. A software on a workstation controls the integrators, the motor rotating the shaft and the magnet power supply. For every angle θ_k , the magnetic flux Φ_k through the pick-up coils is obtained as a sum over the flux increments $\Delta\Phi_i$.

The rotating coils presented here have an accuracy of 10^{-4} on B_1 and 0.2 mrad on the dipole direction [8]. After twenty consecutive measurements the reproducibility of the harmonics is limited by a random error below 0.01 units. The typical bandwidth of rotating coil measurements is in the range of 0.1 Hz.

3.2.4 Measurements with Hall plates

The observation of the spatially periodic field pattern requires a system with a good spatial resolution. Measurements of the field pattern can be performed with arrays of very short rotating pick-up coils. However, due to long read-out times, the acquisition rate is rather low. The snapback during the acceleration ramp after the end of injection only lasts

a few seconds, and rotating coils do not have the time resolution to accurately measure its time dependence. For this reason a system with an acquisition rate of 1 to 5 Hz is needed.

In order to allow both, a good spatial resolution and higher sampling rates, Hall plates can be used for magnetic measurements [11], [15]. In accelerator dipoles the main field B_1 is a factor 10^4 larger than other multipole components and requires a precise compensation. An arrangement of m Hall plates, equally spaced on the circumference of a ring and oriented radially, allows to suppress all field components with an order lower than m . The measured signal for the field component of order m can be maximized if all Hall plates are placed in the poles of the $2m$ -pole field.

Figures 3.6a and b show an arrangement of 3 Hall plates in a dipolar and a sextupolar field. The sum signal of the three plates is compensated for the dipole field and proportional to the sextupole component.

An expression for the sum signal S of a group of m plates with equal sensitivities in a magnetic field with normal and skew multipole components B_k and A_k , respectively, is given by [15]:

$$S = \sum_{k=1}^{\infty} \left(\frac{R}{R_{ref}} \right)^{(2k-1)m-1} (-1)^{\frac{(2k-1)m-1}{2}} m B_{(2k-1)m} + \sum_{k=1}^{\infty} \left(\frac{R}{R_{ref}} \right)^{2km} (-1)^{km} m A_{2km} . \quad (3.3)$$

R is the radial distance of the active area in the Hall plates from the center of the ring. $R_{ref} = 17$ mm is the reference radius. In an ideal case, where all Hall plates are well aligned and have equal sensitivities, the only multipoles contributing to the total signal S are the normal odd and the skew even multiples of order m .

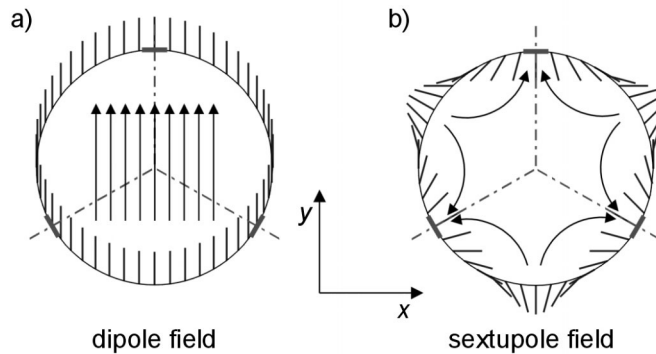


Figure 3.6 The principle of operation is shown for a sextupole arrangement. Three flat Hall sensors are placed on the surface of a cylinder at angles of 0° , 120° , and 240° with respect to the direction of the main field. They measure the projections of the field onto the normal vectors of the three plates. The field lines are indicated for a dipole (on the left) and for a sextupole (on the right).

In an arrangement of three plates the sum signal S is compensated for the dipole, and only normal multipoles of order $3(2k-1)$ (i.e. B_3, B_9, B_{15}, \dots) and skew harmonics of order $6k$ (i.e. $A_6, A_{12}, A_{18}, \dots$) contribute according to:

$$S = \sum_{k=1}^{\infty} 3 \left(\frac{R}{R_{ref}} \right)^{3(2k-1)-1} B_{3(2k-1)} + \sum_{k=1}^{\infty} (-1)^k 3 \left(\frac{R}{R_{ref}} \right)^{6k-1} A_{6k}. \quad (3.4)$$

In the case of a pure sextupole field, this yields

$$S = 3 \left(\frac{R}{R_{ref}} \right)^2 B_3. \quad (3.5)$$

The sum signal of a decapole arrangement with five plates ($m = 5$) is

$$S = \sum_{k=1}^{\infty} 5 \left(\frac{R}{R_{ref}} \right)^{5(2k-1)-1} (-1)^{\frac{(2k-1)5-1}{2}} B_{5(2k-1)} + \sum_{k=1}^{\infty} 5 \left(\frac{R}{R_{ref}} \right)^{10k} (-1)^k A_{10k}. \quad (3.6)$$

In the case of a pure decapole field B_5 , this yields

$$S = 5 \left(\frac{R}{R_{ref}} \right)^4 B_5. \quad (3.7)$$

Examples for sextupole and decapole rings are sketched in figure 3.7.

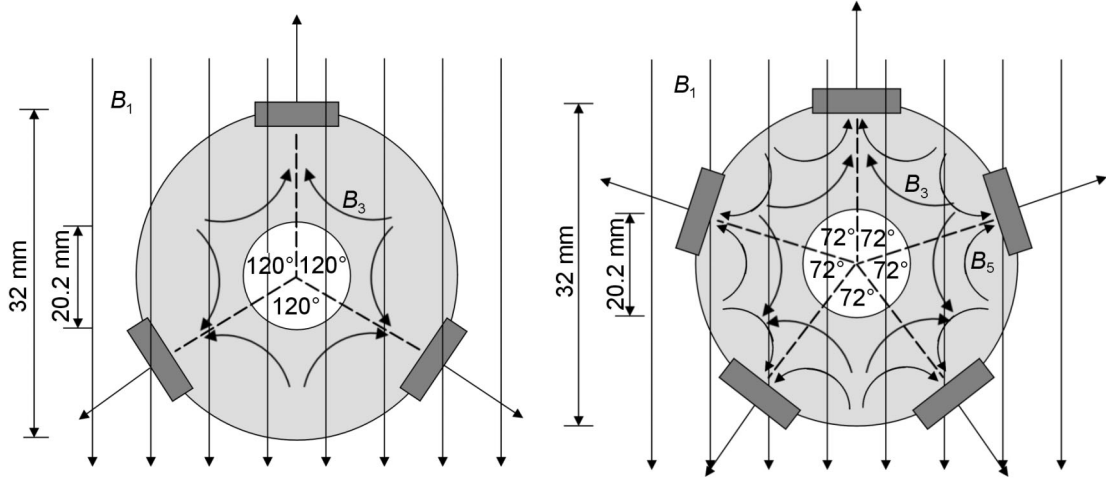


Figure 3.7 Examples are shown for a sextupole ring with 3, and a decapole ring with 5 Hall plates. Also the field lines of the dipole, the sextupole and the decapole field are indicated.

3.2.4.1 Basic sextupole sensor (model 1)

A fast sextupole probe with a data acquisition rate of about 3.3 Hz was developed at CERN [11]. A picture is shown in figure 3.8. The device has two sextupole rings with three Hall plates mounted onto the surface of each ring, with an angular spacing of 120° . If all Hall plates are well aligned and have equal sensitivities, the sum signal of the arrangement is compensated for the main dipole field. In the absence of higher field components, it produces a signal proportional to the sextupole only. An improved calibration procedure invented, for the first time makes it possible to obtain accurate

results. At 0.5 T, the device attains a resolution of 0.015 units, a reproducibility of 0.15 units, an accuracy of 0.3 units and a bandwidth of 3.3 Hz. Sensors with similar properties have also been constructed at HERA [18], [45] and BNL [47].

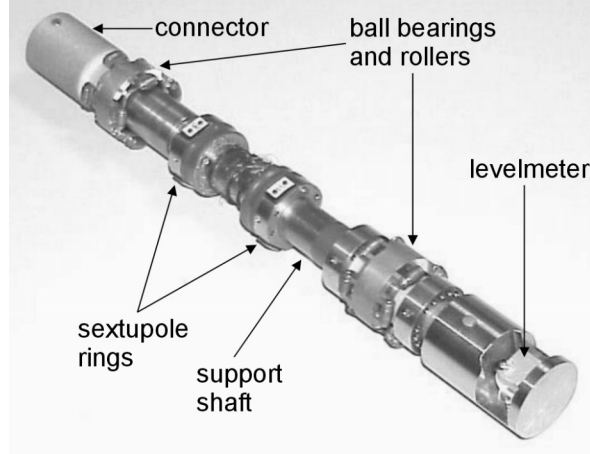


Figure 3.8 First version of a sextupole Hall plate detector.

3.2.4.1.1 Mechanical arrangement

The design of the support rings is shown in figure 3.9. A group of three Hall plates is mounted in special grooves of each ring. The reference surface at the bottom of the grooves has a radius of 14.2 ± 0.02 mm with respect to the rotation axis. Each plate is fixed with a layer of rubber and two screws.

The choice of material for the rings is delicate. The material has to be non-magnetic and with a high electrical resistivity in order to avoid perturbations of the magnetic field, both, in the steady state and during ramps. At the same time a good thermal conductivity is desirable, in order to stabilize the temperature of the three Hall plates on each ring. A titanium alloy ($\text{Ti}_6\text{Al}_4\text{V}$, Grade 5) was chosen due to its high electrical resistivity ($\rho \approx 1.7 \mu\Omega\text{m}$) and adequate thermal conductivity ($k \approx 7 \text{ Wm/K}$). The alloy also has a very small paramagnetic behavior ($\mu_r \approx 1.0002$). Paramagnetic distortions of the main dipole field B_1 possibly contribute to other field components. Since those contributions are proportional to B_1 , they can be taken into account during the calibration.

The two rings are assembled on a support shaft and their distance can be adjusted. A drawing is shown in figure 3.10.

The average signal

$$U_{average} = \frac{1}{2} \left(\sum_{Ring1} U_i + \sum_{Ring2} U_i \right) \quad (3.8)$$

Magnetization Measurements on Wires and Coils

$$U_{\text{difference}} = \frac{1}{2} \left(\sum_{\text{Ring 1}} U_i - \sum_{\text{Ring 2}} U_i \right) \quad (3.9)$$

between the sum signals of the rings is proportional to the local amplitude of the field pattern.

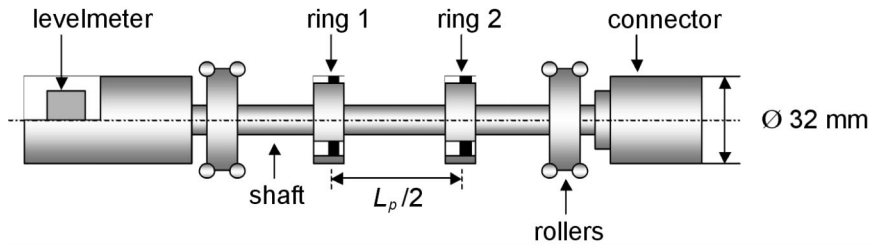


Figure 3.10 Schematic assembly of the sextupole rings on the support shaft, showing the rollers that support the probe in the warm bore of the magnet, as well as the levelmeter and the signal cable connector.

The absolute pattern amplitude can be determined by moving the detector over a length of half a cable twist pitch. The shaft is equipped with rollers and ball bearings in order to move and rotate the device inside the warm bore of a magnet. An on-board measurement of the inclination with respect to gravity is added in order to provide an absolute reference for the angular position. Steel bars are used to insert and rotate the Hall detector in the magnet. Finally, the mechanical assembly is wrapped by a Kapton foil, in order to provide a good thermal insulation against the wall of the warm bore. The Ti-alloy used in the rings has a thermal conductivity much larger than Kapton. In spite of temperature fluctuations in the warm bore, the temperature gradient in the support rings is negligible. It is, thus, possible to avoid a temperature regulation of the sensor.

3.2.4.1.2 Hall plates

The Hall plates are provided by AREPOC, a company in Bratislava, Slovakia. A few of them are shown in figure 3.11. The devices are labelled HHP-NU and made of InSb with unpackaged electrical systems. At an excitation current of 50 mA the plates have sensitivities typically around 222 mV/T.

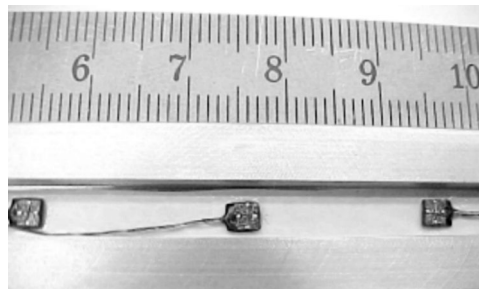


Figure 3.11 Hall Plates from AREPOC, type HHP-NU, with unpackaged electrical systems.

Magnetization Measurements on Wires and Coils

The probes are sorted in groups of three, in order to match the sensitivities on each ring within 0.5%. The small temperature coefficient of about 10^{-4} K^{-1} guarantees a good insusceptibility against gradients or variations of the temperature. Non-linearities smaller than 0.2% in a field range between 0 and 1 T grant a linear behavior of the compensated signal in a limited range around the field level during injection.

3.2.4.1.3 Cabling and acquisition

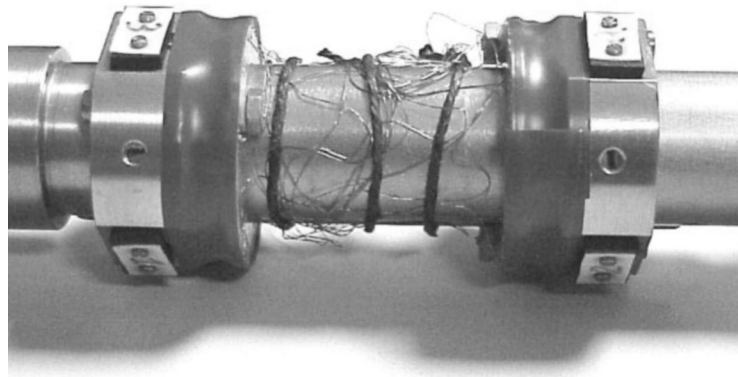


Figure 3.12 The picture shows two rings with 3 Hall plates each, mounted on the shaft of the detector. Printed circuit boards are fixed between the rings. The space between the printed circuit boards and the rings is covered with a protection from plastic. Tiny wires for the Hall plate signals are soldered to the printed circuit boards and lead through a hole in the shaft and through its hollow interior to a connector at one end of the device.

The Hall plate connections are soldered to printed circuit boards, which protect the fragile wires from being ripped off. A picture is shown in figure 3.12. All plates are connected in series with the current source, and conduct the same current of about 50 mA. Thus, current fluctuations affect all Hall plates in a similar way. The input resistance of the Hall plates is small (around 5Ω). For this reason the total voltage (in a range of 1.5 V) is negligible.

A 15 m long twisted cable connects the detector to a distribution box and a data acquisition system. Shielding the cables and distribution box considerably reduces the electronic noise. The voltage signals of the Hall plates are measured by digital nanovoltmeters (DVMs) with a resolution of 100 nV. The current in the magnet is measured by a direct current current transformer (DCCT) and read by a DVM. The DVMs are read out by a data acquisition system. The DVMs are configured as integrating voltmeters with an integration time of 300 ms and synchronized by a trigger. The resulting data acquisition rate is about 3.3 Hz. The 50 Hz background from the power

Magnetization Measurements on Wires and Coils

network, the 300 Hz noise generated by the magnet power supply and the electronic noise are strongly filtered thanks to the integration. The residual noise is typically in the μV range. The Hall plate sensitivities of about 222 mV/T and the DVM resolution of 100 nV lead to a resolution of $0.7 \mu\text{T}$ in the B_3 component. Typical signals are shown in figure 3.13. Details on the development of the present detector are discussed in [6], [11], [30] and [35].

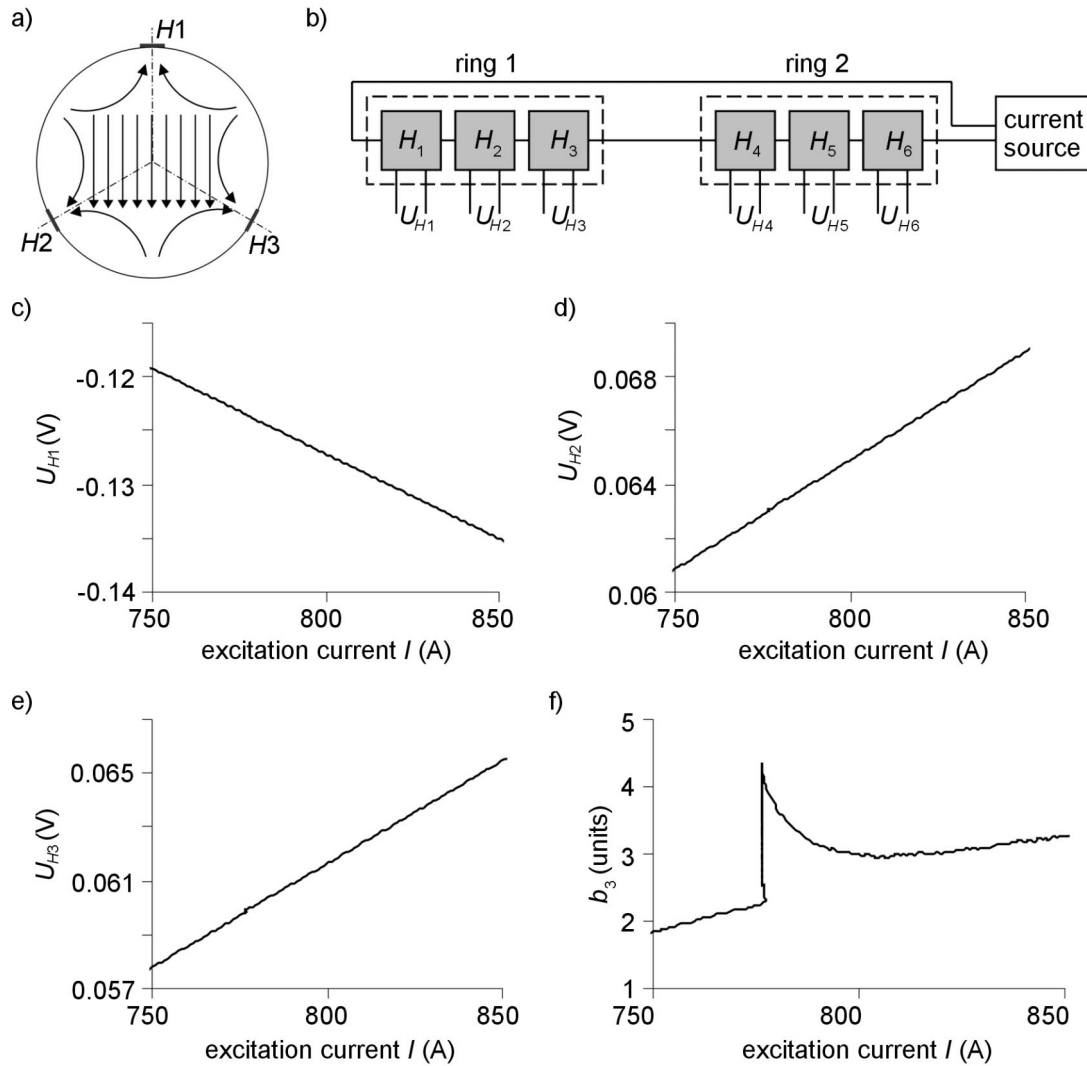


Figure 3.13 a) Three Hall plates on a ring are exposed to a combination of dipolar and sextupolar field components. b) The current in all Hall plates of the detector is connected in series and typically equals 50 mA. c), d) and e) show the measured signals from the Hall plates 1, 2 and 3 on the first ring, as a function of the excitation current in the magnet. The effects decay and snapback are not visible in the uncompensated signals. f) shows the sum of the signals on a ring in units of the normal sextupole.

Magnetization Measurements on Wires and Coils

3.2.4.1.4 Calibration

In order to measure decay and snapback in the normal sextupole component with an accuracy of a few percent, the dipolar component has to be compensated with an accuracy of about 10^{-5} . In practice, different Hall plates have different sensitivities to the field, in addition to a small offset signal. Both, sensitivity and offset are functions of the temperature. It is difficult to find a reference magnet for the calibration, which is homogeneous and accurate in the μT range. Apart from that, also imperfections in the positioning of the plates and the detector disturb a perfect compensation. However, already a rough calibration allows to qualitatively reconstruct hysteresis curves. In order to optimize the calibration, rotating coil measurements are used as a standard. An example for a calibration on the magnet 18 is shown in figure 3.14.

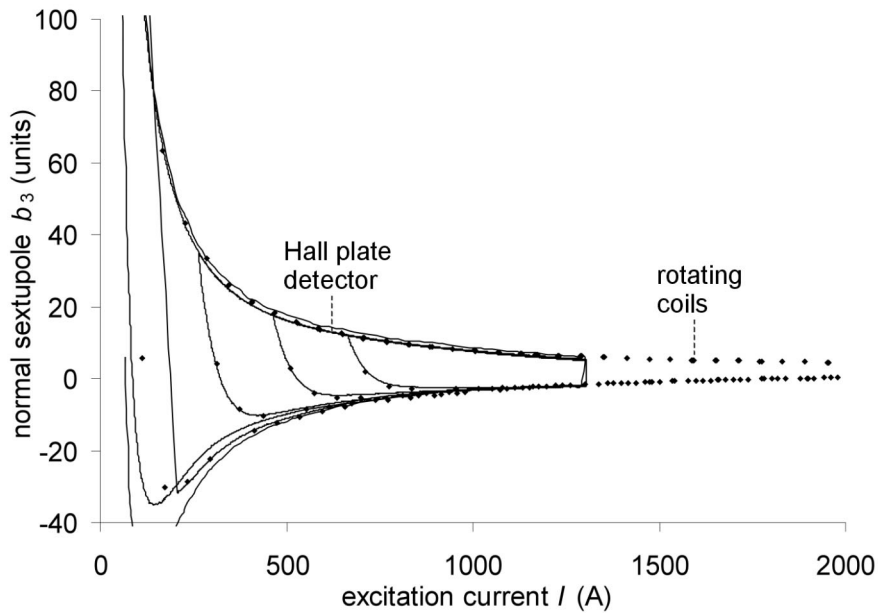


Figure 3.14 Example for a calibration of the Hall detector, performed on magnet 18. The normal sextupole component b_3 is plotted as a function of the excitation current in the magnet. Hysteresis cycles measured with rotating coils (points) and Hall detector (lines) are shown in comparison.

The points indicate rotating coil measurements and the solid lines show the average signal of the two rings in the Hall plate detector. In the easiest case three parameters (A , B , C) for the Hall detector measurements can be fitted to the b_3 measured by the rotating coils: The amplitude of the hysteresis curve, a linear term and an offset:

$$b_3 = A \cdot (U_{H1} + U_{H2} + U_{H3}) / I + B \cdot I + C. \quad (3.10)$$

U_{H1} , U_{H2} and U_{H3} are the signals of the plates on a ring and I is the current in the magnet, which is proportional to the main dipole field B_1 . Non-linearities or differences in the sensitivities of the Hall plates (up to 0.2% below 1 T) can lead to deviations in the curves.

Magnetization Measurements on Wires and Coils

In order to compensate for this effect, the Hall plate signals U_{Hi} in (3.10) can be replaced by low order polynomials:

$$U_{Hi} \rightarrow a_i U_{Hi}^3 + b_i U_{Hi}^2 + c_i U_{Hi} + d_i. \quad (3.11)$$

The adaptation to rotating coil measurements becomes less reproducible as the number of unknown parameters increases. Computer simulations show that better Hall plate linearities can still considerably improve the detector performance.

In most magnets a substantial value of b_9 disturbs the sextupole signal. For example at injection, a b_9 of typically 0.23 units causes an error of about 8%. Higher field components partially compensate each other. For $b_9 = 0.23$ units, $b_{15} = 0.06$ units, $a_6 = 0.08$ units and $a_{12} = -0.0007$ units, the total error is reduced to 2.6%. This contribution varies with the background field and has a maximum of 7% in the interval [0.4 T...0.8 T]. The noise in the measurement usually has an amplitude in the range of 0.05 units. Over a limited range around the injection plateau [0.4 T...0.8 T], the snapback can be measured with a reproducibility of about 0.15 units and an accuracy of about 0.3 units. This represents about 10% of typical snapback amplitudes in the LHC.

Many aspects of the detector can still be improved. Especially important are the mechanics, the electronics and the calibration, since an accuracy of 0.03 units is necessary for the compensation of decay and snapback in the machine. Apart from that, the two rings in the detector do not provide enough information to entirely understand the behavior of the spatially periodic field pattern during decay and snapback. Finally, the detector only measures the sextupole, and doesn't give information about other field components.

3.2.4.2 New version with sextupole and decapole rings

A new version of the Hall detector was constructed recently. A picture is shown in figure 3.15. The new detector has a considerably improved mechanics and electronics, and six sextupole rings allow the simultaneous observation of decay and snapback at different positions along one wavelength of the spatially periodic field pattern. During injection and during the subsequent acceleration ramp, they can be used to investigate the behavior of the amplitude and phase of the (sinus-shaped) field pattern, and to analyze correlations between the spatially periodic field pattern, the field decay during injection and the subsequent snapback.

Apart from the measurement of sextupole fields, two additional sensors with five Hall plates each are implemented, spaced at half a pattern wavelength. These two rings are the first known realization of a decapole sensor with Hall plates and will show whether or not Hall plates are suitable for decapole measurements in the LHC.

Magnetization Measurements on Wires and Coils

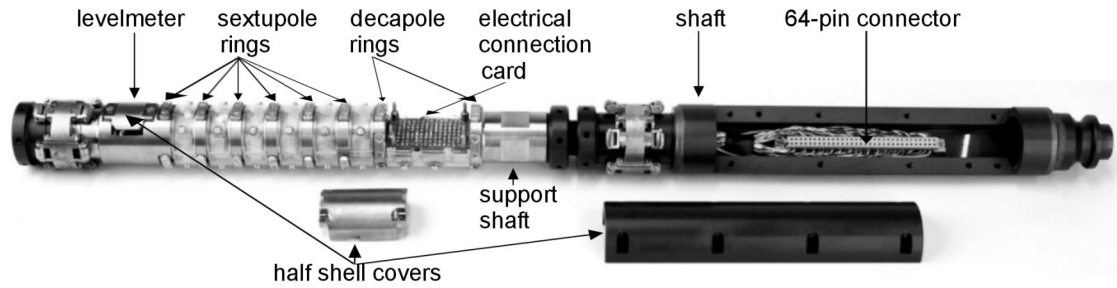


Figure 3.15 The new version of the Hall plate detector.

The detector is developed for magnetic measurements as well as for online-measurements in the reference magnets of the LHC accelerator.

The support shaft, the housing of the levelmeter and the rings of the detector are manufactured in one piece from Ti_6Al_4V , thus avoiding mechanical misalignments of the rings. The piece is 300 mm long, has a diameter of 33 mm, includes the eight rings and contains two flat surfaces, one for the housing of the levelmeter and a second one for an electrical connection card. Both flat surfaces can be covered with half-shell shaped filling pieces. A hole of 15 mm diameter is carved inside the support shaft in order to minimise the quantity of Ti_6Al_4V . The sextupole sensors are placed at 19.2 mm from each other, and the decapole rings have a distance of 57.5 mm. The Hall plates are mounted into grooves on the rings at angular spacings of 120° and 72° , respectively, with an angular tolerance of $\pm 0.05^\circ$. For the fixation of the plates, the same principle is used as in the previous version of the detector.

The front end is equipped with a ball bearing and rollers. A small end from aluminium allows to mount and dismount the ball bearing. At the other end a 300 mm aluminium piece is fixed to the support shaft from Ti_6Al_4V . The piece contains a 64-pin connector and also has a ball bearing with rollers.

An improved extension shaft allows a more precise positioning of the detector and longitudinal scans along the magnet's axis. The detector can be connected to an 'extension shaft' consisting of four tubes, easy to mount and dismount. The detector and the extension shaft are carried by ball bearings and rollers. They allow translations of up to 150 mm and rotations up to a few degrees inside the anti-cryostat. A rotation gear box controls the rotation of the detector.

In the new detector the same kind of Hall plates is used as in the previous version. Eighteen plates measure the sextupole and ten the decapole. The signal wires of the plates are lead through rails on the surface of the support shaft and through machined grooves in

Magnetization Measurements on Wires and Coils

the rings. They are soldered to an electronic connection card located between the decapole sensors. The current wires of the plates are connected in series.

The wires from the connection board are joined by three wires from the levelmeter. They are soldered to the flat connector located in the 300 mm long aluminium piece. The shielded cable from the detector is passed through the hollow interior of the extension shaft and connected to a distribution box.

A new data acquisition system reads out all 28 Hall plates and the current in the magnet. A sketch is shown in figure 3.16.

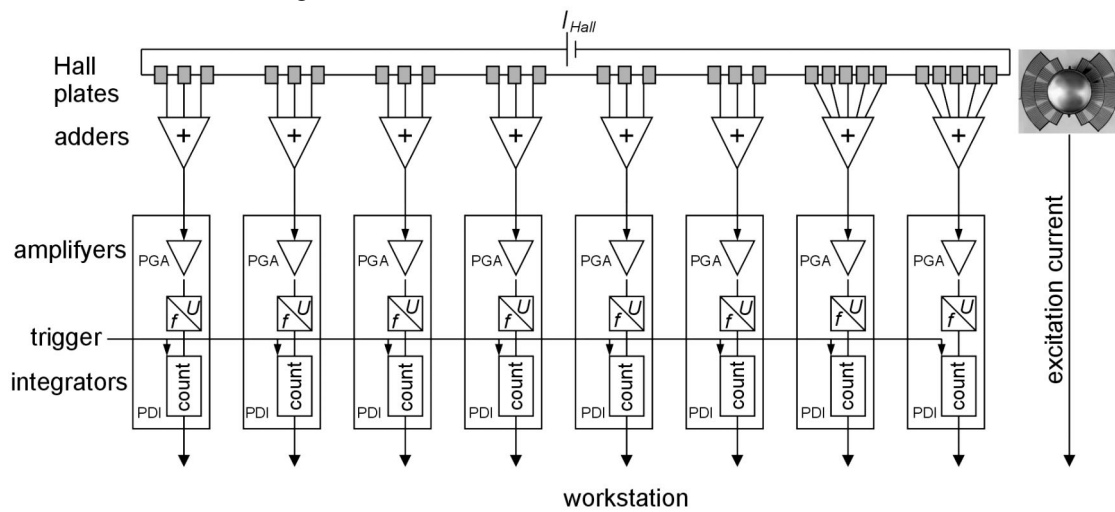


Figure 3.16 Acquisition system for the new prototype of the Hall detector.

The system combines a medium acquisition speed (better than 3.3 Hz) and a precise measurement of the signals. The distribution box contains compensation cards for the sextupole and decapole rings. These compensation cards perform an electronic summation of the Hall plate signals from each ring. The advantage of the electronic compensation is that only 9 instead of 29 signals have to be read out.

The compensated ring signals are amplified by so-called ‘programmable gain amplifiers’ (PGA). The amplified signals are read simultaneously by a set of precision digital integrators (PDI) in continuous mode. The VME-PDIs are triggered externally, by a function generator. The integration of the signal over small time intervals allows to considerably reduce the noise level. The PDIs are configured and read-out by a software on a workstation.

An accuracy of 0.056 units is expected for the sextupole and 0.062 units for decapole measurements. These values represent about 1.7% and 16.7% of the typical snapback amplitudes, respectively. Details on the detector are described in [6].

3.3 Conclusion

Due to long read-out times, rotating coil measurements do not have enough time resolution to accurately measure the snapback curve. As an alternative, a group of Hall plates on a ring can be used to measure different field components. At CERN, an existing Hall plate detector with two sextupole rings was considerably improved and calibrated. For the first time, the device delivers quantitatively correct results. The average over the signals of the two rings contains information about the coil magnetization, and the difference between the signals of the two rings is proportional to the amplitude of the spatially periodic field pattern. The detector can measure the sextupole component with an accuracy of 0.3 units and can be used for online-measurements to compensate the typical snapback in the LHC by 90%.

However, in order to reach the necessary compensation of 99%, the accuracy still has to be improved significantly. Apart from that, the detector can measure the sextupole only, and its two rings do not allow to entirely understand the behavior of the spatially periodic field pattern during decay and snapback.

For this reason a new version of the Hall plate detector was built. A more sophisticated mechanics improves the stability and assures a better alignment of the plates. Together with an improved electronics, the new detector aims to reach a resolution of 0.056 units in the sextupole component. The device contains six sextupole rings and allows to observe decay and snapback simultaneously at different positions along the spatially periodic field pattern. Two additional decapole rings represent the first known realization of a decapole detector with Hall plates. They will show, in how far Hall plates can be used for decapole measurements.

Chapter 4

Dependence of Field Decay on the Excitation History

A statistical analysis of snapback amplitudes measured on different magnets confirms that the decay in allowed field components is distributed systematically, alternating in sign from one allowed component to the next. The decays in non-allowed field components, however, are distributed randomly. In addition, correlations between the decay rates in different field components are analyzed. ‘Decay’ and ‘snapback’ in superconducting accelerator magnets strongly depend on the excitation history. As already mentioned in section 2.8, flux creep cannot explain this behavior. Calculation results obtained with a simple model for boundary induced coupling currents give a rather good qualitative agreement with systematic measurements on several short dipole model magnets, where different parameters in the operation cycle and excitation history are varied. The correspondence between calculated and experimental data demonstrates that boundary induced coupling currents are the principal source of field decay during injection.

4.1 Systematic distribution of harmonics

For the compensation of decay and snapback in the LHC it is important to identify field components that show a systematic appearance of the effects, and field components where decay and snapback statistically average out over all the magnets in the machine. In order to investigate the systematic appearance of decay and snapback, a statistical analysis of measured snapback amplitudes is performed on the set of 1 m model magnets discussed in this thesis (table 3.1). The research presented here is focussed on the more topical mechanical design, and only the results for 6 block twin aperture magnets are taken into account. The snapback amplitudes are measured on each magnet after a standard cycle with an injection duration of 1020 s, and after a modified standard cycle with an injection duration of 10000 s. Figure 4.1 shows average values of the snapback amplitudes in several field components for measurements during 1020 s and 10000 s on

Dependence of Field Decay on the Excitation History

the injection porch. Both, the statistics for 1020 s and 10000 s behave similar, only with higher snapback amplitudes in the case of 10000 s. The snapback amplitudes in non-allowed field components are distributed randomly with positive or negative sign. Their average values are embedded within error bars around zero. Only in the case of allowed field components, a systematic behavior is observed. The snapback amplitudes are distributed either with positive or negative sign, alternating in sign from one allowed field component to the next. The sign always corresponds to a net decrease of the persistent current contribution to the field. Comparable results were obtained in a previous study performed on single aperture magnets, mainly of the 5 block design [49]. Since the decay in non-allowed field components is statistically averaged out over all magnets in the LHC, observations are restricted to allowed harmonics only.

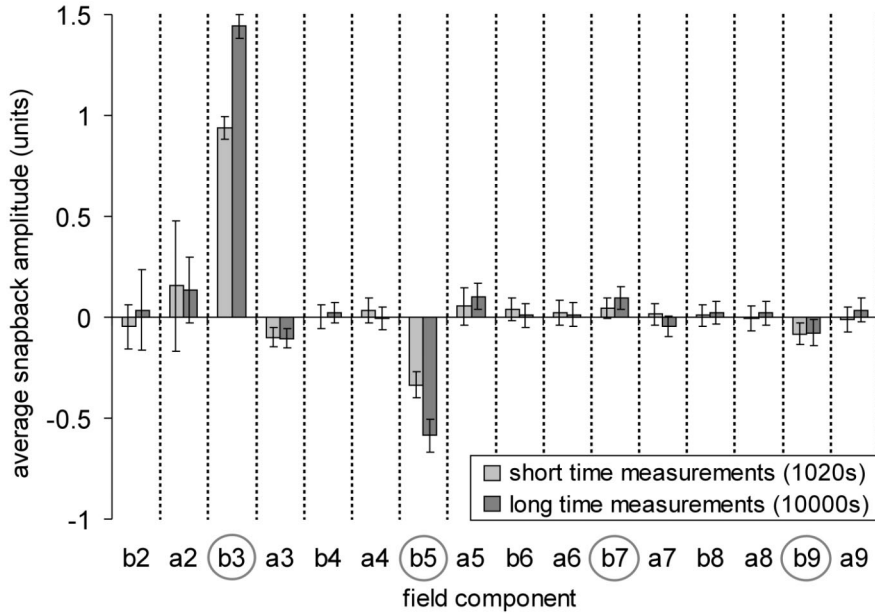


Figure 4.1 The average snapback amplitudes in long and short time measurements are shown for several field components in the magnets.

4.2 Correlation between different harmonics

In previous studies on superconducting magnets at HERA [17] and at CERN [49] correlations were found between the decays in several field components. For a more detailed analysis of these correlations, measurements are performed on several short LHC model dipoles. The decay during injection is measured on each magnet after different current cycles. For every magnet correlations are found between the decays in all field components. Examples of measurements performed on magnets 2 and 17 (see table 3.1) are shown in figure 4.2.

Dependence of Field Decay on the Excitation History

Three different cycles are applied to each magnet. For every measurement the b_5 -decay is plotted as a function of the corresponding b_3 -decay.

A cycle measured on magnet 2, with an injection duration of 10000 s, is shown together with a 1020 s decay measurement after a standard pre-cycle and a pre-injection porch of 30 min. A third measurement is shown for a pre-cycle flat-top current of 4000 A and a flat-top duration of 5 min. All three measurements follow the same correlation between b_3 and b_5 .

The 10000 s decay is also displayed for magnet 17. In addition, measurements with injection durations of 1020 s at 350 A and 1500 A are shown. The initial slopes of all three measurements on magnet 17 are almost equal and represent a characteristic property of the magnet. However, after a certain time the decay at 350 A shows deviations. Most likely the $J_c(B)$ dependence of the superconducting material is responsible for this behavior. Apart from that, the error bars are much larger at 350 A than at 810 A. Non-linearities in the correlations are caused by different decay behavior and time constants in the upper and lower poles, in the two different layers, and in the different blocks of the magnets.

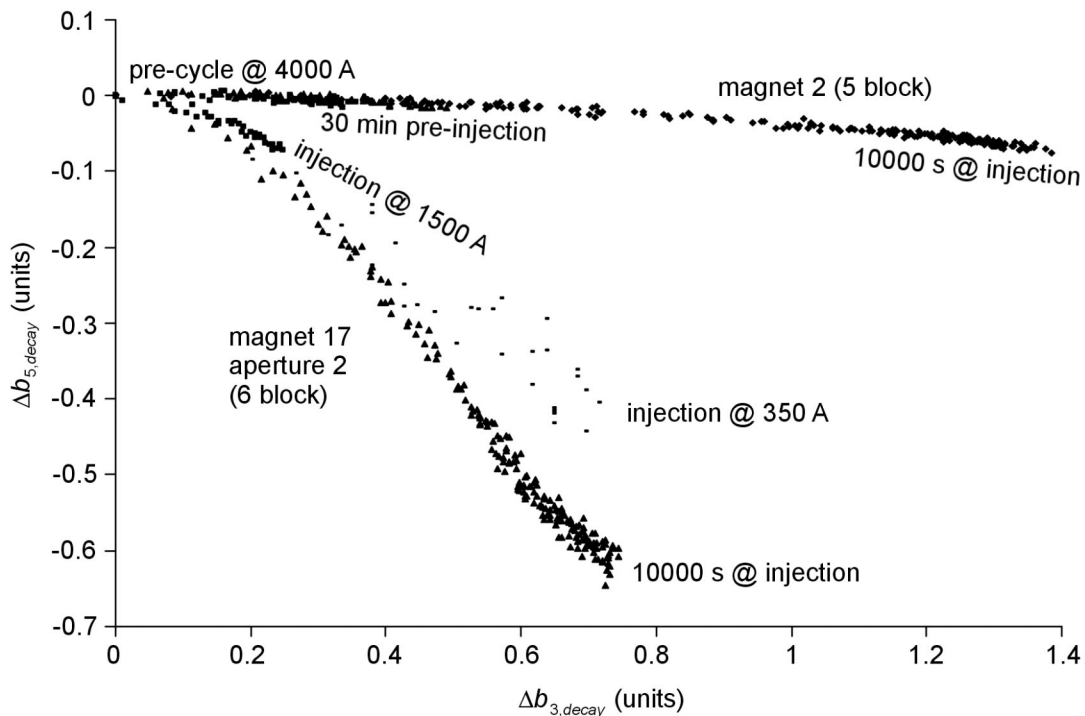


Figure 4.2 The b_5 decay during the injection plateau is plotted as a function of the b_3 decay for magnets 2 and 17 and 3 different cycles per magnet.

4.3 Excitation history

4.3.1 Model for the field decay

According to the present understanding BICCs are induced during ramps and diffuse during periods of constant magnet excitation. As a consequence, the distribution of BICCs varies with the excitation history. The diffusion of BICCs during injection is the driving source of the field decay, and different decay amplitudes have to be expected after different excitation cycles. In order to test the diffusion of BICCs as a valid mechanism for the field decay and to understand the dependence of decay and snapback on the excitation history, a simple model for the induction and diffusion of BICCs is implemented, and predictions from the model are compared to systematic measurements on short model dipoles [49].

The contribution of BICCs to the magnetic field in the center of a coil is a superposition of the fields induced by N_i loops with current I_i and different time constants τ_i . Everywhere in the coil, the magnetic field changes proportional to the transport current I_M in the cable. According to section 2.6, the currents I_i diffuse and decay exponentially during intervals $[t_1 \dots t_2]$ of constant I_M :

$$I_i(t_2) = I_i(t_1) \cdot e^{-\frac{(t_2-t_1)}{\tau_i}}. \quad (4.1)$$

If, however, in a similar time interval I_M is changed at a constant ramp rate \dot{I}_M , then also new currents are induced:

$$I_i(t_2) = I_i(t_1) \cdot e^{-\frac{(t_2-t_1)}{\tau_i}} + \dot{I}_M k_i \left(1 - e^{-\frac{(t_2-t_1)}{\tau_i}} \right). \quad (4.2)$$

k_i is a constant, which depends on the geometry and on the time constant τ_i . If the currents in the strands are far from the critical conditions, subsequent ramps induce current distribution effects which add linearly. Although this approximation is not necessarily fulfilled at high currents, equations (4.1) and (4.2) can be used to qualitatively estimate the BICCs during an arbitrary operation cycle.

The associated pattern amplitudes $b_{n,pp}$ and $a_{n,pp}$ in the n -th normal and skew harmonics respectively, are assumed proportional to a sum of the BICCs with different time constants τ_i :

$$b, a_{n,pp}(t) = \sum_i (c, d_{n,i} \cdot I_i(t)). \quad (4.3)$$

t is the time, and the factors $c_{n,i}$ and $d_{n,i}$ describe the contributions of boundary induced coupling currents with time constants τ_i to the amplitude of the spatially periodic field pattern in the harmonic of order n . In real magnets, BICCs with certain time constants are

Dependence of Field Decay on the Excitation History

often distributed inhomogeneously among different parts of the coil and contribute more or less to different field components.

During injection, the BICCs with time constant τ_i are assumed to change by ΔI_i . The changing BICCs induce local field changes in the coil windings, and have an impact on the coil magnetization which is approximately proportional to $|\Delta I_i|$. A linear approximation for the average decay amplitude is

$$\Delta b_{3,decay} = \sum_i a_i |\Delta I_i| + b. \quad (4.4)$$

The a_i are scaling factors, taking into account the magnetization change per ampere and the correlation between b_3 and the magnetization. The constant b takes into account other possible contributions to the decay, such as higher time constants, of which the time dependence is neglected for simplicity.

4.3.2 Measurements on short LHC dipole model magnets

The model is compared to systematic measurements performed on various 1 m short LHC dipole model magnets [49]. The standard operation cycle is used as a reference. Variations of single parameters in the cycle allow to investigate the response of the field decay to different excitation histories, and multiple pre-cycles are tested as a tool to establish reproducible operation conditions. Due to a restriction in measurement time, it is not possible to perform a detailed analysis on all magnets. However, since a stable statistics is observed for the allowed harmonics (see section 4.1), a representative behavior for all magnets can be deduced from the set of measurements discussed here. In rotating coil measurements where the length of the pick up coils equals a multiple of the cable twist pitch, the snapback amplitude is the best accessible approximation for the amplitude of the field decay.

The experimental results are compared to model calculations, assuming a current loop with one time constant ($N_i = 1$). Although the restriction to a single time constant does not allow precise quantitative predictions of the field decay, the model generally explains the qualitative response to variations in the excitation cycle. Most current cycles are applied to magnet 2 (see table 3.1). For this reason, the parameters in equations (4.1), (4.2) and (4.4) are adapted to fit the behavior of this magnet. $\tau \approx 10$ min, $ka \approx 0.27$ s-units/A and $b \approx -0.62$ units are reasonable values. In figures 4.4, 4.6, 4.10, 4.16, 4.18, 4.20, 4.22, 4.24, 4.28 and table 4.1 calculated values are shown in relation to experimental data.

Dependence of Field Decay on the Excitation History

4.3.2.1 Decay during injection

In order to investigate the time dependence of the decay, the normal sextupole is measured on three different magnets (2, 14 and 17) during an injection duration of 10000 s. Figure 4.3 shows the excitation current as a function of time.

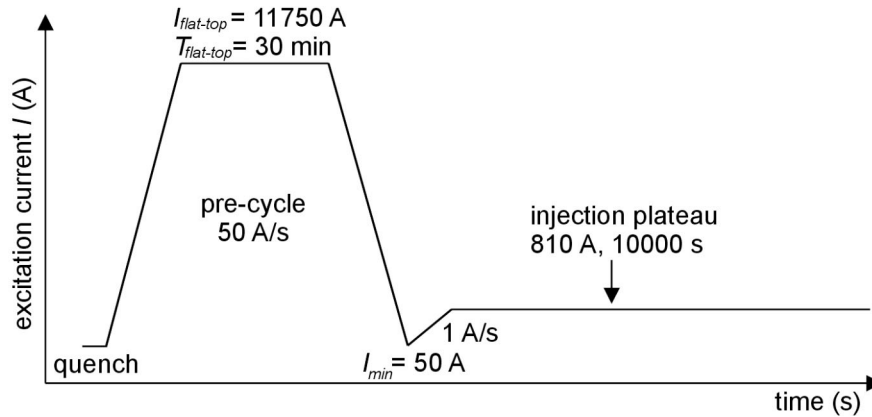


Figure 4.3 The excitation current in the magnet is sketched as a function of time.

Figure 4.4 presents the measured decay of the normal sextupole as a function of time from the beginning of the injection plateau. A comparison between the data for magnet 2 and the simulation result shows that a one time constant model can only serve as a very rough approximation. In order to give a more precise and quantitative explanation, also other time constants have to be taken into account.

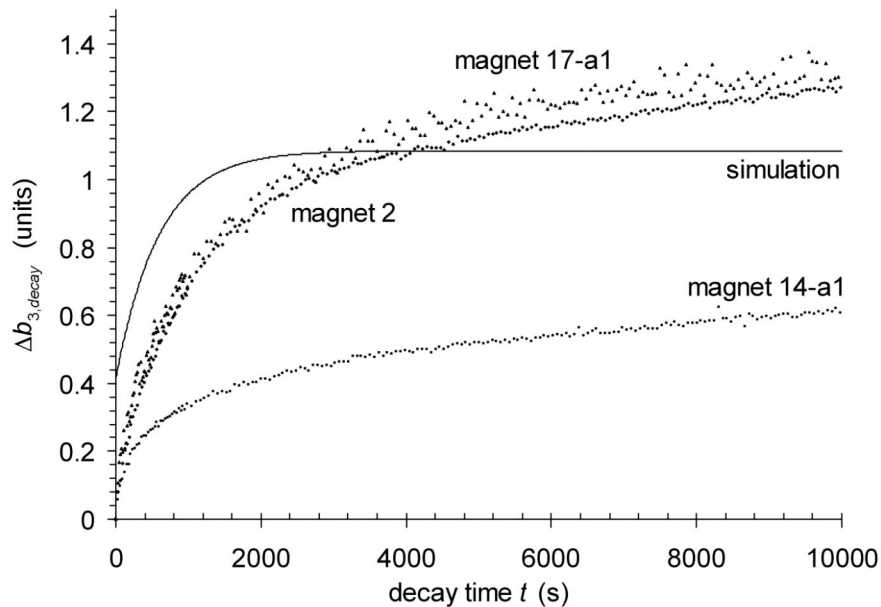


Figure 4.4 The measured and calculated decay amplitudes are shown as a function of time during injection. The abbreviation a1 marks aperture 1 in the twin dipoles.

Dependence of Field Decay on the Excitation History

4.3.2.2 Variation of pre-cycle parameters

4.3.2.2.1 Flat-top current

In order to analyze the response of the field decay to the amplitude of the pre-cycle, and to compare the behaviors of 5 and 6 block magnets, measurements with different pre-cycle flat-top currents are performed on magnets 1-12 (see table 3.1). In order to reduce the overall measurement time, the pre-cycle flat-top duration is shortened to 5 minutes. Figure 4.5 shows the excitation current in the magnets as a function of time.

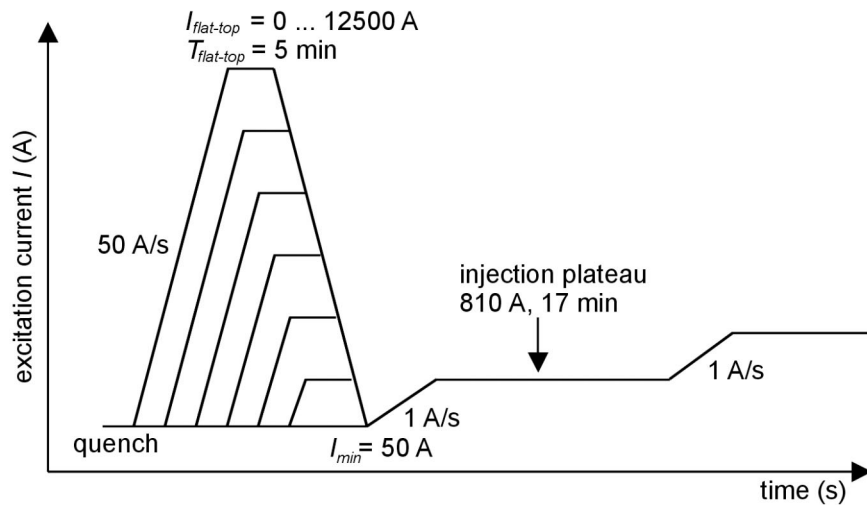


Figure 4.5 For cycles with different pre-cycle flat-top currents, the excitation current in the magnet is sketched as a function of time.

The experimental results are presented in figures 4.6, 4.7 and 4.8, separated into single and twin aperture magnets of the 5 and 6 block designs. In each case, the snapback amplitude in the normal sextupole is shown as a function of the flat-top current. To determine the snapback amplitude, the data measured after the snapback on the up-ramp branch are fitted and the hysteresis curve is extrapolated towards the injection field. The error bars are calculated as a standard deviation of the extrapolated fit and strongly depend on the number of measured data points. Typically the error bars are around 0.05 units.

On magnet 3 (see table 3.1) measurements are performed down to very small pre-cycle currents (figure 4.6). Below 4000 A a deviation from linearity is found. An almost linear increase of the snapback amplitude is observed for higher flat-top currents.

Measurements with small flat-top currents are also performed on magnet 11-aperture 1 (figure 4.8). A non-linear behavior is observed below about 6000 A. Observations of the

Dependence of Field Decay on the Excitation History

periodic pattern decay in the same magnet are published in [15]. They show a change in sign of the pattern decay at a pre-cycle current of about 8000 A.

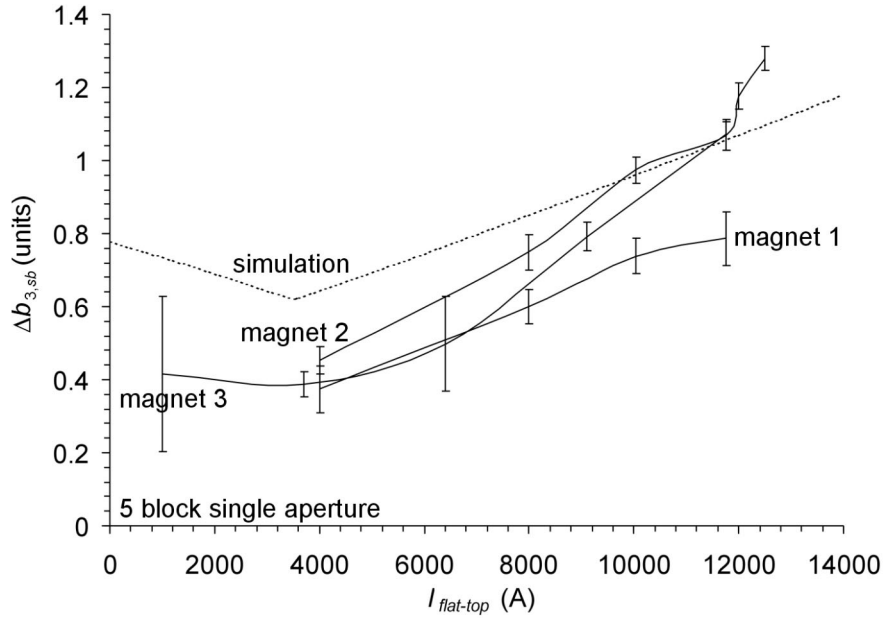


Figure 4.6 Snapback amplitudes measured on 5 block single aperture magnets are plotted as a function of the flat-top current in the pre-cycle. The results for magnet 2 are compared to a simulation based on a single time constant.

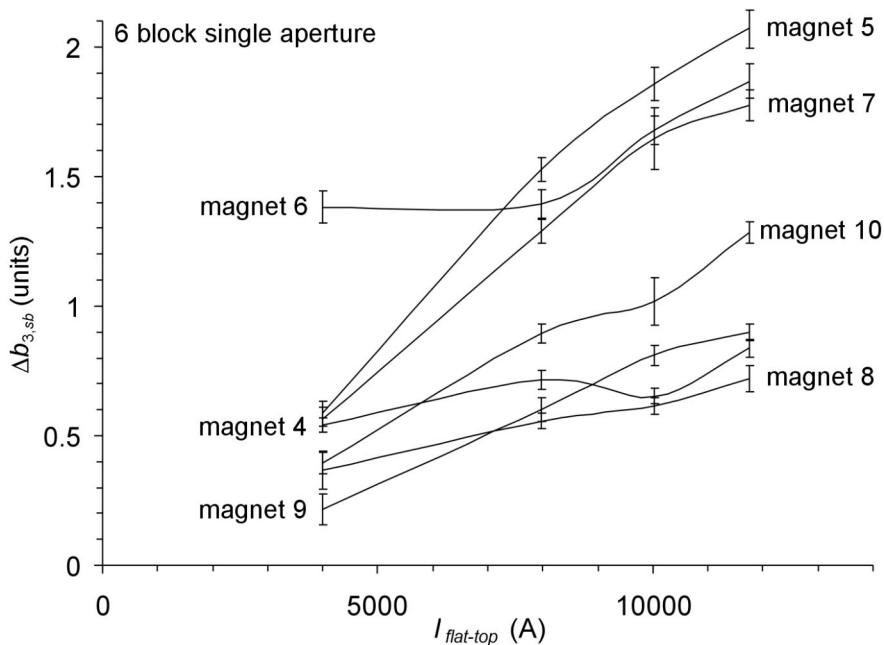


Figure 4.7 Snapback amplitudes measured on 6 block single aperture magnets are plotted as a function of the flat-top current in the pre-cycle.

Dependence of Field Decay on the Excitation History

The observations also correspond to results of experiments performed on SSC magnets [25] and long LHC dipoles [see chapter 6]. On long LHC dipoles, a minimum snapback amplitude and a change in sign of the periodic pattern decay during injection are found for the same pre-cycle current. A correlation similar to equation (4.4) can be expected between the snapback amplitude and the change in the BICCs ΔI during injection.

While varying the flat-top current, the calculated ΔI due to BICCs change sign at a pre-cycle current of about 3500 A. This causes a minimum snapback amplitude and qualitatively agrees with the measured data (figure 4.6).

In most cases, the 6 block magnets (4-10 and 12-17, figure 4.7 and 4.8) tend to show a higher snapback amplitude and a stronger dependence on the flat-top current than the 5 block ones (1-3 and 11, figure 4.6 and 4.8). Possible reasons for this behavior are different distributions of the contact resistances or different geometries of the field changes in the coil induced during injection. The snapback amplitudes in both apertures of the twin aperture magnet 12 have a similar behavior (figure 4.8).

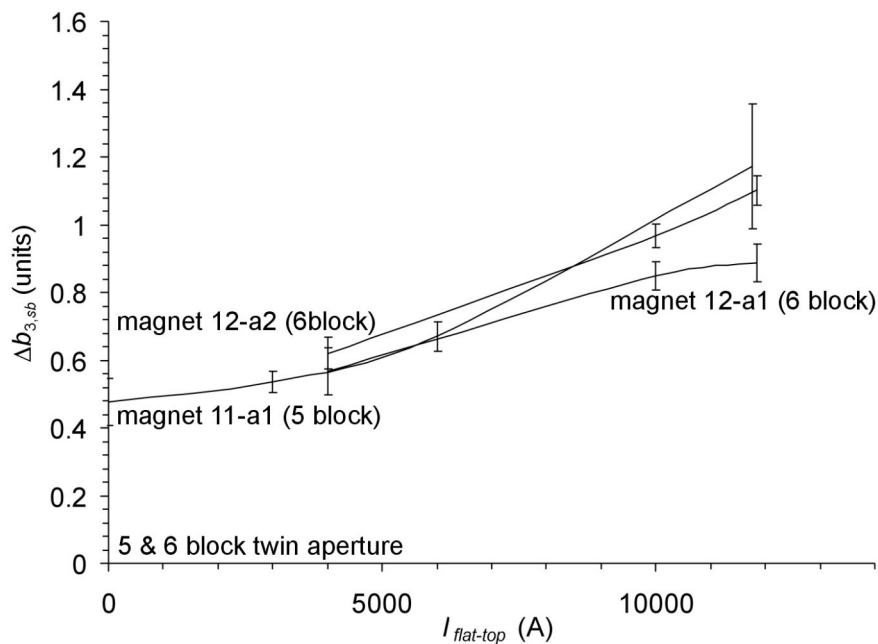


Figure 4.8 Snapback amplitudes measured on twin aperture magnets of both designs are plotted as a function of the flat-top current in the pre-cycle. The abbreviations a1 and a2 mark the different apertures in the twin dipoles.

4.3.2.2.2 Flat-top duration

In order to analyze the impact of the pre-cycle duration on the field decay, and to compare the behaviors of 5 and 6 block magnets, measurements with different pre-cycle

Dependence of Field Decay on the Excitation History

flat-top durations are performed on various magnets. Figure 4.9 shows a sketch of the current in the magnet as a function of time.

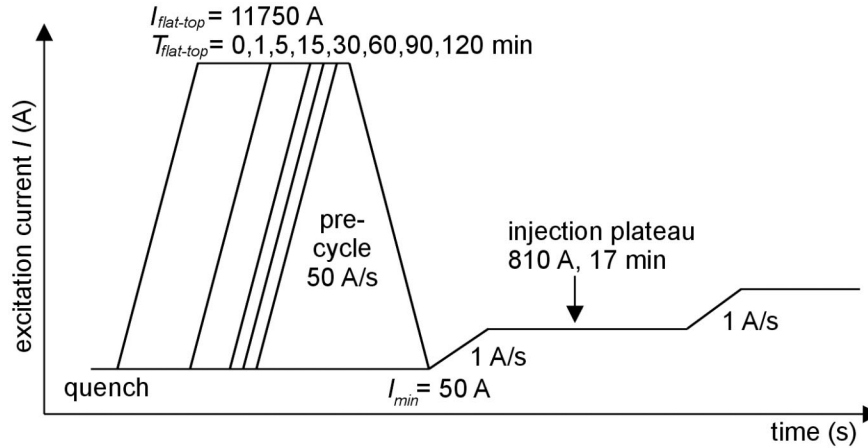


Figure 4.9 A sketch of the excitation current in the magnet is shown as a function of time. The variation of the flat-top duration is indicated.

The experimental results are shown in figures 4.10, 4.11 and 4.12, separated into single and twin aperture magnets of the 5 and 6 block designs. In each case the snapback amplitude in the normal sextupole is displayed as a function of the flat-top duration.

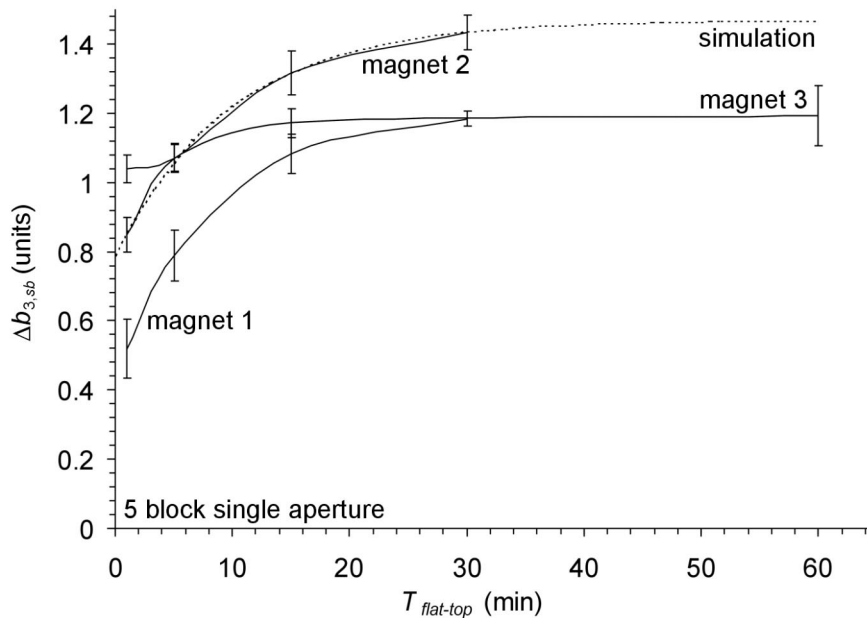


Figure 4.10 Snapback amplitudes measured on 5 block single aperture magnets are shown as a function of the flat-top duration in the pre-cycle. The results for magnet 2 are compared to a simulation based on a single time constant.

Dependence of Field Decay on the Excitation History

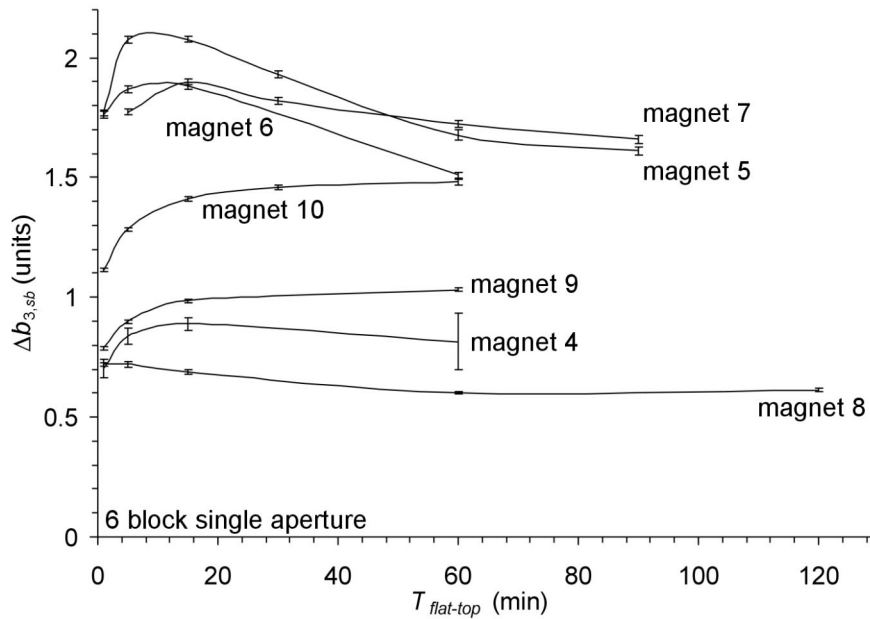


Figure 4.11 Snapback amplitudes measured on 6 block single aperture magnets are shown as a function of the flat-top duration in the pre-cycle.

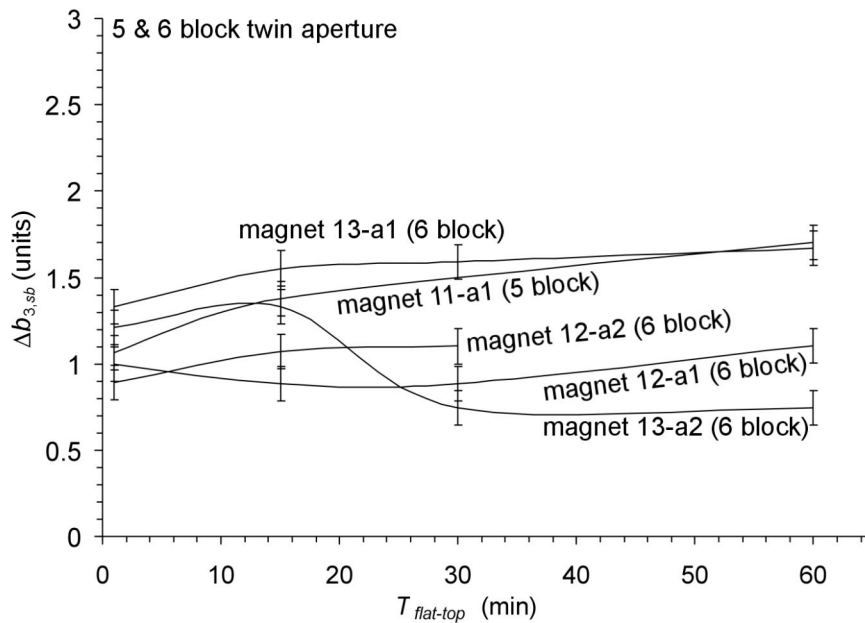


Figure 4.12 Snapback amplitudes measured on twin aperture magnets of both designs are shown as a function of the flat-top duration in the pre-cycle. The abbreviations a1 and a2 mark the two apertures in the twin dipoles.

The 5 block magnets (figure 4.10) show an ‘exponential’ increase and a saturation for increasing flat-top durations. The exponential behavior qualitatively corresponds to the

Dependence of Field Decay on the Excitation History

measured decay of the periodic pattern amplitude during injection [16]. The simulations agree with measurements on magnet 2. A very quick saturation is observed for magnet 3.

The snapback amplitudes of most 6 block magnets (figure 4.11) increase to a maximum at a flat-top duration of about 10 to 20 minutes, decrease significantly above this threshold, and possibly saturate for higher flat-top durations. This behavior shows that at least two time constants are necessary to describe the qualitative behavior of the 6 block magnets.

Also the snapback amplitudes measured on twin aperture magnets (see figure 4.12) of the 5 block and the 6 block design show this behavior. However, the snapback amplitudes measured on the two apertures of a magnet are not correlated.

4.3.2.2.3 Pre-cycle ramp rate

In order to understand the impact of ramp rate during the up- and down-ramp in the pre-cycle, three different experiments are performed on magnet 2. The snapback amplitudes are determined after a standard pre-cycle, after a pre-cycle with a fast up-ramp and a slow down-ramp, and finally after a pre-cycle with a slow up-ramp and a fast down-ramp. The total pre-cycle duration is kept constant. Figures 4.13 and 4.14 show the current in the magnet during a ‘fast-slow’ and a ‘slow-fast’ cycle as a function of time.

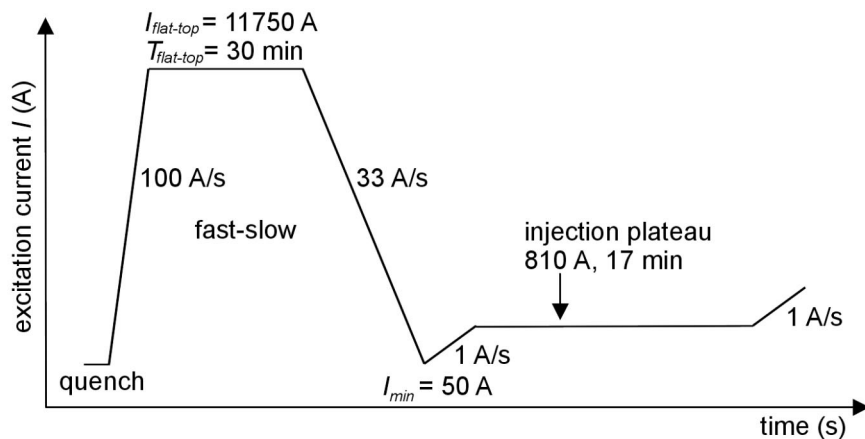


Figure 4.13 The excitation current in the magnet is sketched as a function of time for a cycle with a fast up-ramp and a slow down-ramp in the pre-cycle.

The ramp speeds, the measured and the calculated snapback amplitudes are documented in table 4.1. The relative difference in amplitude with respect to the standard pre-cycle is around $\pm 10\%$. The higher value is observed during the ‘slow-fast’ cycle. The simulation qualitatively shows the same behavior.

Dependence of Field Decay on the Excitation History

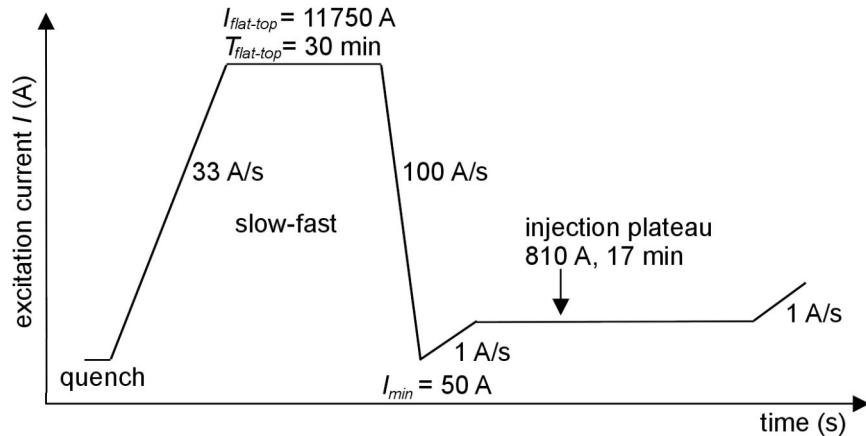


Figure 4.14 The excitation current in the magnet is sketched as a function of time for a cycle with a slow up-ramp and a fast down-ramp in the pre-cycle.

cycle type	ramp rate A/s (up-ramp)	ramp rate A/s (down-ramp)	b_3 -snapback (units)	relative difference to standard cycle	simulated relative difference
fast-slow	100	33	1.3	-11%	-6%
slow-fast	33	100	1.6	10%	7%
standard	50	50	1.4		

Table 4.1 The measured snapback amplitudes are given for pre-cycles with different ramp rates. For each cycle also the relative difference to the standard cycle is shown. The last column shows the relative difference of the simulated values.

4.3.2.2.4 Multiple pre-cycles

The magnets in the LHC will not be thermally cycled before every run. For this reason, the reproducibility of decay and snapback is of high importance for the operation of the accelerator. Multiple pre-cycles are tested as a possible tool to establish reproducible conditions. Figure 4.15 shows the excitation current as a function of time.

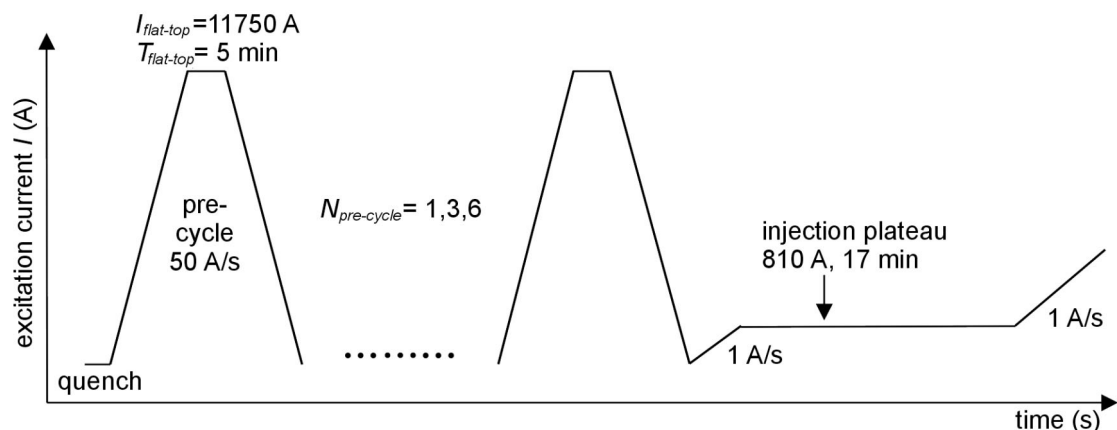


Figure 4.15 The excitation current is drawn as a function of time, for current cycles with different numbers of pre-cycles.

Dependence of Field Decay on the Excitation History

After an initial quench, a sequence of 1, 3 and 6 pre-cycles with flat-top durations of 5 minutes is applied to two magnets, followed by an injection porch.

Figure 4.16 presents the measured snapback amplitudes in the normal sextupole as a function of the pre-cycle number. For all magnets, a fast saturation is observed after several pre-cycles. The results for magnet 2 qualitatively agree with the simulation, and show that multiple pre-cycles can be used to improve the reproducibility of decay and snapback in the accelerator.

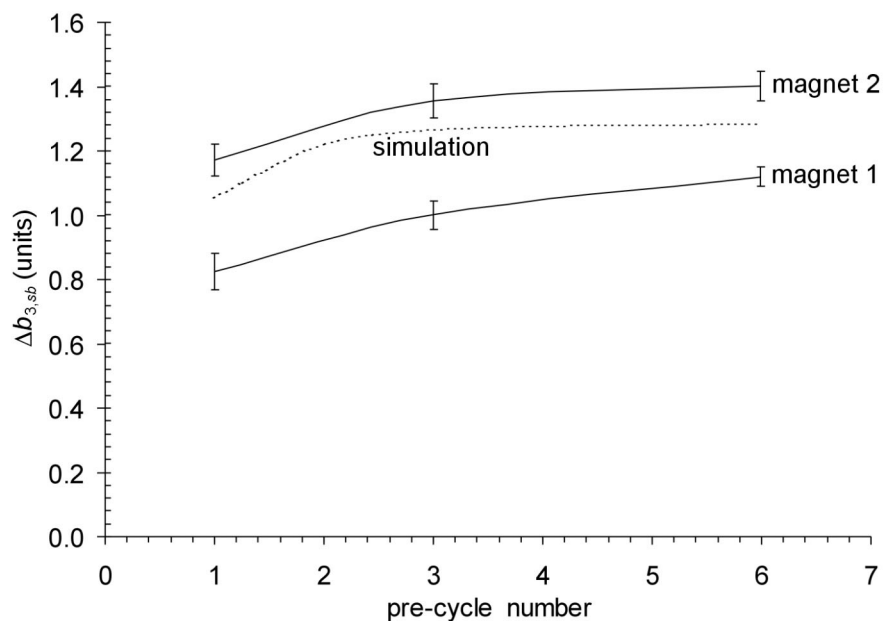


Figure 4.16 Measured and calculated snapback amplitudes are plotted as a function of the pre-cycle number.

4.3.2.3 Injection reproducibility

The superconducting LHC magnets will not be quenched or thermally cycled before every run of the collider. For this reason it is important to know in how far the snapback amplitude is reproducible during the operation after having performed a number of successive runs. In order to investigate the reproducibility, a test is performed on two different magnets. After an initial quench, a typical operation cycle with a 5 minute flat-top duration is applied to the magnets. The cycle is followed by three additional operation cycles without quenching in between. Every cycle lasts about 45 min. In figure 4.17 the excitation current in the magnets is sketched as a function of time.

Dependence of Field Decay on the Excitation History

The amplitude of the measured and calculated sextupole snapback is determined during the initial phase of each acceleration ramp. Figure 4.18 shows the amplitude of the sextupole snapback as a function of the total cycle number.

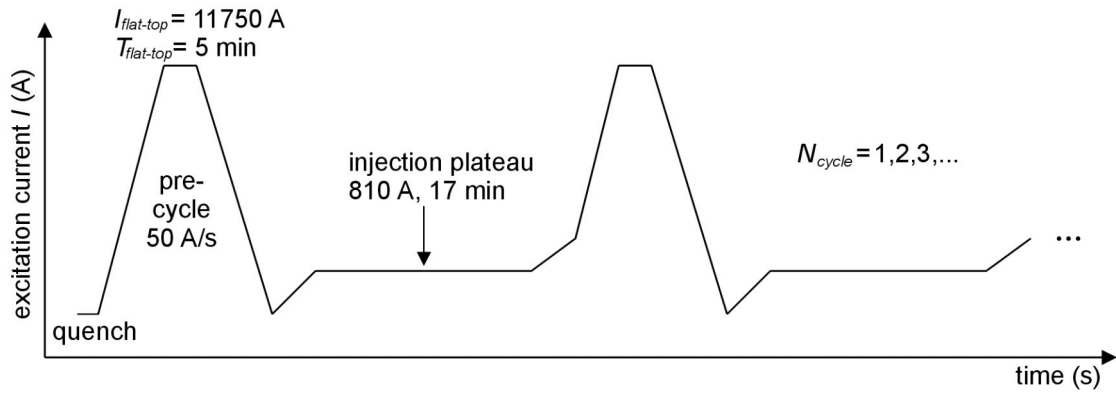


Figure 4.17 For a series of cycles with no quench in between, the excitation current is sketched as a function of time.

The results demonstrate that in ‘periodic’ operation, after performing a sequence of similar collision experiments, the snapback amplitudes are expected to converge towards a constant value. The simulation qualitatively agrees with the snapback amplitudes measured on magnet 2.

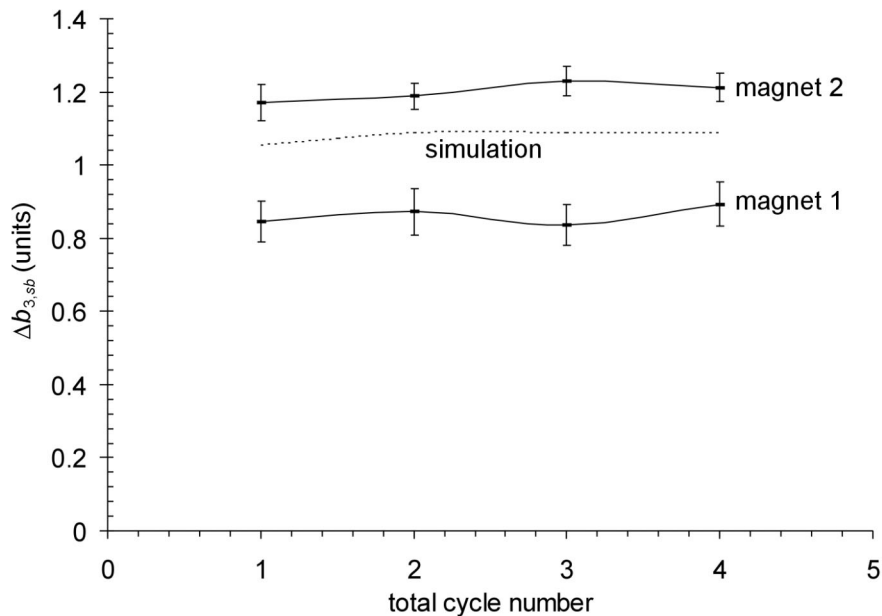


Figure 4.18 The measured and simulated snapback amplitudes are shown as a function of the number of subsequent operation cycles.

Dependence of Field Decay on the Excitation History

4.3.2.4 Pre-injection current and duration

A pre-injection porch at a current 25 to 75 A lower than the injection plateau is known to reduce the snapback amplitude significantly [9]. For the compensation of decay and snapback in the LHC it is necessary to find the optimum current and duration in the pre-injection porch, and to estimate the approximate reduction of the snapback amplitude. For this reason several experiments are performed on different magnets.

4.3.2.4.1 Pre-injection current

Cycles with pre-injection currents of 735 A, 760 A and 785 A are used during a first series of measurements. In each case, the pre-injection duration is 300 seconds. The time between the end of the pre-cycle and the injection porch is held constant. The sketch in figure 4.19 shows the current in the magnet as a function of time.

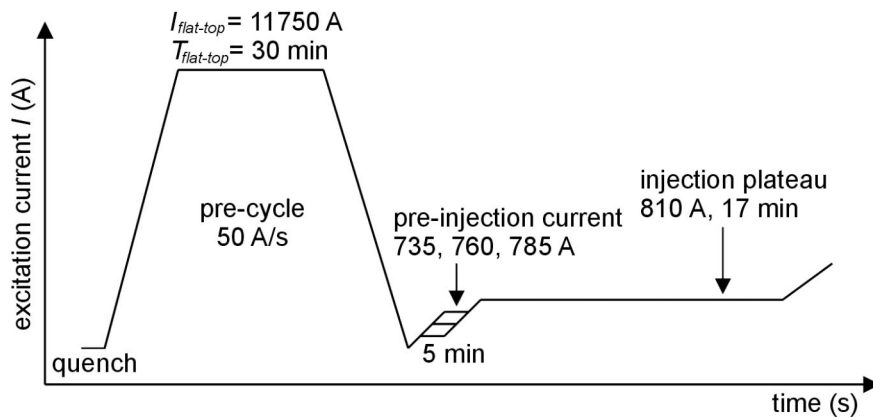


Figure 4.19 For cycles with different pre-injection currents, the excitation current is sketched as a function of time.

In figure 4.20 the snapback amplitudes measured on 3 different magnets are pictured as a function of the pre-injection current. In all cases the sextupole snapback behavior is not significantly affected by the pre-injection current. The strongest reduction is obtained for a pre-injection porch current of 785 A. The snapback amplitude in magnet 2 is reduced by about 25% with respect to the standard cycle, the ones in magnet 8 and 9 are reduced by about 20%. The simulation qualitatively agrees with measurements on magnet 2.

Dependence of Field Decay on the Excitation History

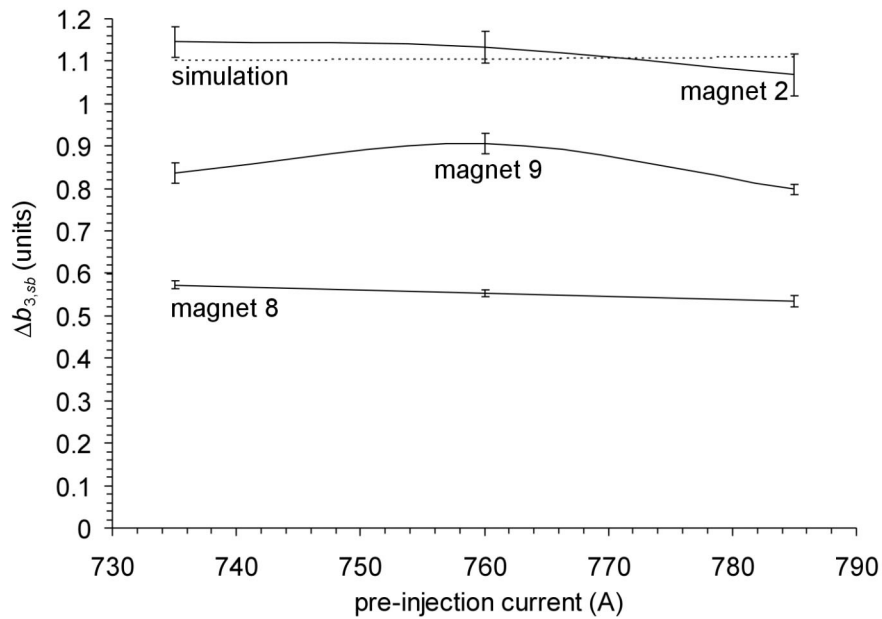


Figure 4.20 The snapback amplitudes measured on magnet 2, 8 and 9 and the calculated snapback amplitudes are shown as a function of the pre-injection current.

4.3.2.4.2 Pre-injection duration

In order to investigate the impact of the pre-injection porch duration on the snapback amplitude, a second series of measurements is performed with pre-injection durations of 1, 5, 15 and 30 min. Figure 4.21 shows the current during all cycles as a function of the time.

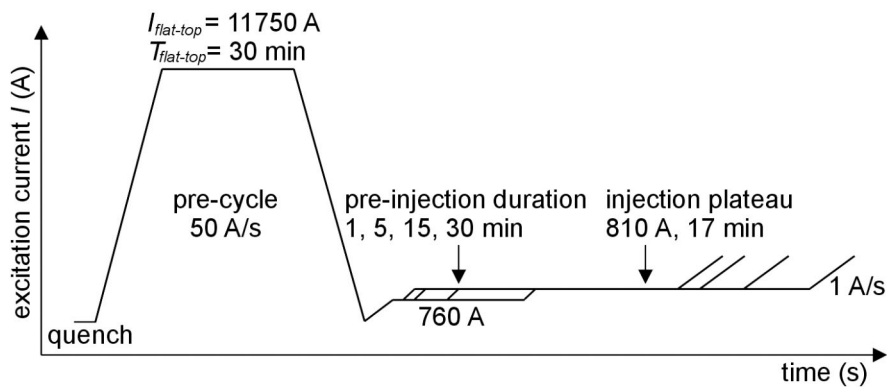


Figure 4.21 For cycles with different pre-injection durations, the excitation current is sketched as a function of time.

The measured snapback amplitudes are presented in figure 4.22 as a function of the pre-injection duration. After 30 minutes of pre-injection duration, the snapback amplitude of the 5 block magnet 2 is reduced by about 55%. The two 6 block magnets 8 and 9 saturate faster, and reduce the snapback amplitude by about 22% and 42%, respectively.

Dependence of Field Decay on the Excitation History

Magnet 8 only shows a very weak dependence on parameter variations in the operation cycle. This was also observed during other measurements on magnet 8.

The simulation qualitatively agrees with the results for magnet 2.

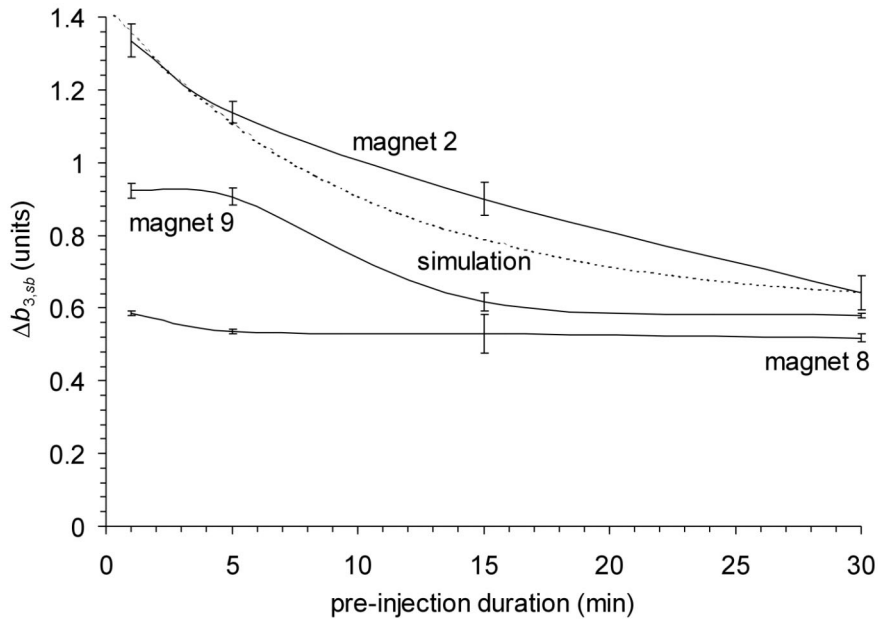


Figure 4.22 The measured and calculated snapback amplitudes are shown as a function of the pre-injection duration.

4.3.2.5 Injection parameters

4.3.2.5.1 Ramp rate to injection

In a subsequent series of tests, the impact of the ramp to injection on the snapback amplitude is analyzed for ramp rates of 0.5, 1, 2 and 4 A/s. The time between the end of the pre-cycle and the injection porch is left constant in all runs. The slowest ramp (0.5 A/s) starts directly after reaching the minimum current and the fastest one starts after a waiting time of 1330 s. Figure 4.23 shows the excitation current as a function of time.

In figure 4.24 the measured and calculated snapback amplitudes are plotted as a function of the ramp rate to injection. The amplitude of the sextupole snapback measured on magnets 1 and 2 clearly increases with higher ramp rates. However, the simulation has a different tendency. The impact of other time constants can explain this behavior.

Dependence of Field Decay on the Excitation History

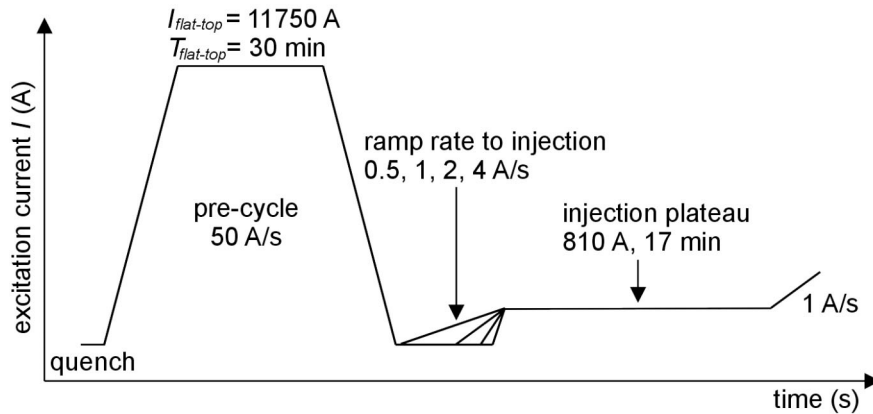


Figure 4.23 The current in the magnet is sketched as a function of time. The ramp rate to injection is varied.

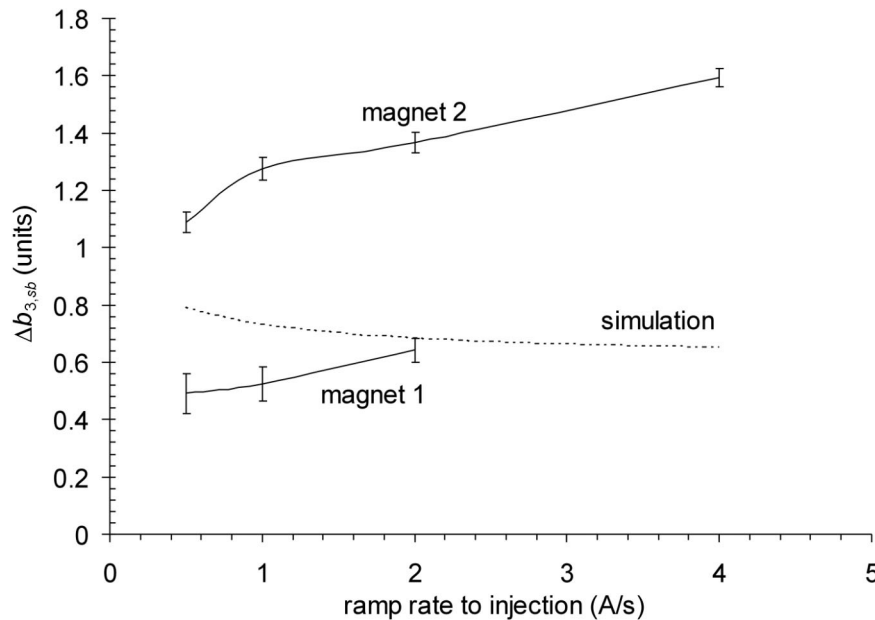


Figure 4.24 The measured and calculated snapback amplitudes are shown as a function of the ramp rate to injection.

4.3.2.5.2 Injection current

It is important for the operation of the LHC to understand the impact of different injection currents on the snapback amplitude. The field in the coil during injection is relatively low, and the penetration fields of the filaments in the coil are much larger than typical field changes in the coil. For this reason, the $J_c(B)$ dependence is expected to only slightly affect the magnetization decay. The BICCs in the coil are basically determined by the pre-cycle, and the ramp to injection is expected to only add a small linear contribution to the magnetization decay.

Dependence of Field Decay on the Excitation History

In order to analyze the influence of different injection currents on the snapback amplitude, a series of measurements is performed on the 6 block twin aperture magnets 15, 16 and 17. The cycles are slightly different from magnet to magnet. The current in magnet 15 is ramped to injection at a constant rate, directly after the end of the pre-cycle. For magnet 17 the time between pre-cycle and injection plateau is kept constant, and a waiting time is introduced between the end of the pre-cycle and the ramp to injection. Again the ramp rate is kept constant. Also in the third experiment on magnet 16 the time between pre-cycle and injection is kept constant. However, in this case the ramp rate is changed and no waiting time is used. In figure 4.25, this last series of current cycles is sketched as a function of time.

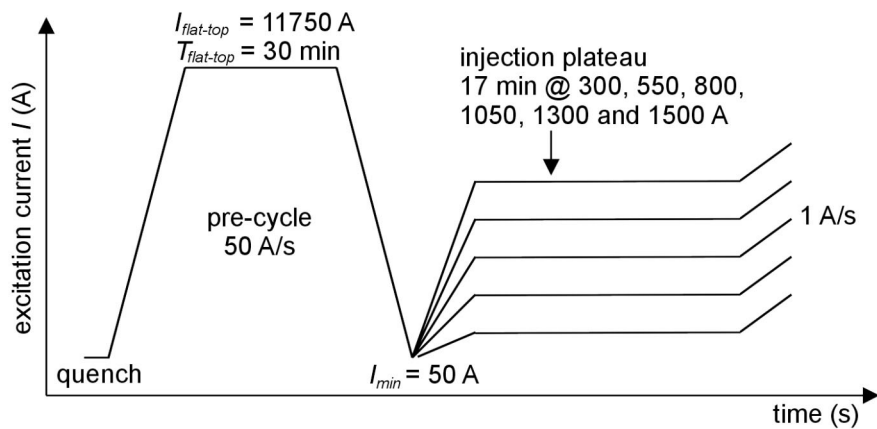


Figure 4.25 For cycles with different injection currents, the excitation current in magnet 16 is sketched as a function of time.

Figure 4.26 shows the measured non-normalized sextupole component $B_3 = b_3 B_1 10^4$ as a function of the injection current. The measurements on magnet 16 and 17 are linear within the error bars. Only the behavior of magnet 15 shows non-linearities, which are possibly due to the different times between the end of the pre-cycle and the beginning of the injection plateau.

Dependence of Field Decay on the Excitation History

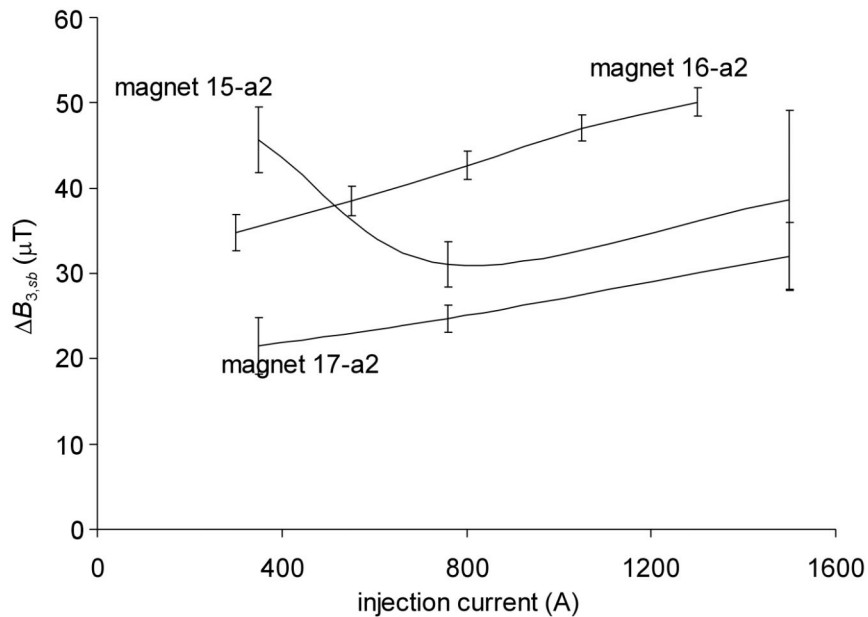


Figure 4.26 The measured non-normalized snapback amplitudes are shown as a function of the injection current. The abbreviations a1 and a2 mark the apertures 1 and 2 in the twin dipoles.

4.3.2.5.3 Ramp rate after injection

In order to investigate the dependence of the snapback amplitude on the ramp rate during the snapback, excitation cycles are performed on magnet 2 with ramp rates of 0.05, 0.1, 0.5 and 1 A/s. In figure 4.27 the excitation current during these cycles is sketched as a function of the time.

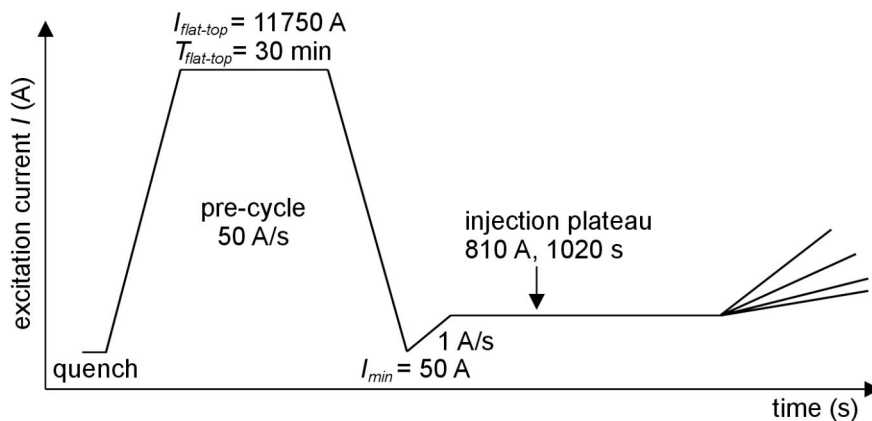


Figure 4.27 For different ramp rates after injection, the excitation current is sketched as a function of the time.

The snapback is due to a remagnetization of the superconducting filaments in the coil and typically happens during a field sweep in the range of only a few mT. Since the

Dependence of Field Decay on the Excitation History

superconductor magnetization does not depend on the ramp rate, and since the BICCs are not significantly changed during a field sweep of only a few mT, a constant snapback amplitude is expected.

Figure 4.28 shows the measured and calculated snapback amplitudes as a function of the ramp rate after injection. Their values are almost constant within the error bars, and the ramp rate does not have a significant impact on the amplitude of the sextupole snapback. The experimental results qualitatively agree with the expected behavior.

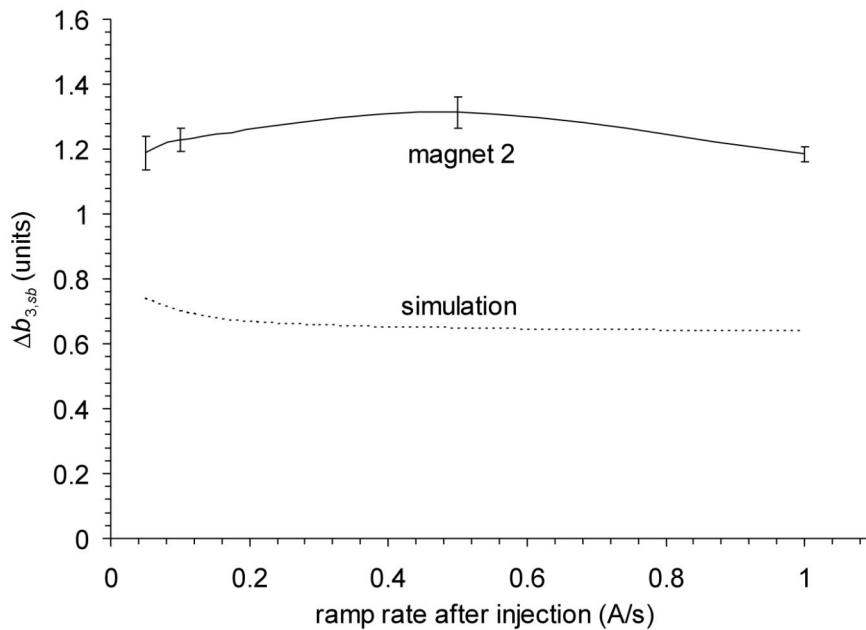


Figure 4.28 The measured and simulated snapback amplitudes are plotted as a function of the ramp rate after injection.

4.4 Conclusion

A statistical analysis of the data measured on various magnets shows that the decay in allowed field components is distributed systematically, alternating in sign from one allowed component to the next. The sign of the decay always represents a net decrease of the average coil magnetization. The decays in non-allowed field components, however, are distributed randomly. Since the non-allowed components are statistically averaged out over all dipole magnets in the machine, the investigations can be restricted to allowed field components only.

Finally, the correlation between the decay rates in different field components are analyzed. In the LHC this correlation can be used as a scaling law. It is sufficient to know

Dependence of Field Decay on the Excitation History

the decay behavior in only one field component, like for example the normal sextupole. The behavior of all other components can consequently be derived from the correlations.

A numerical model with a single time-constant is implemented, in order to qualitatively describe the induction and diffusion of boundary induced coupling currents in a coil. A systematic comparison between measured and calculated data has demonstrated that the interaction between current and magnetization in the coil can explain the qualitative dependence of decay and snapback on the excitation history of a magnet.

The measurements show that three parameters in the excitation cycle are particularly important: The pre-cycle flat-top current, the pre-cycle flat-top duration and the pre-injection duration. The pre-injection current does not affect the snapback amplitude significantly. Multiple pre-cycles can be used to establish reproducible operation conditions at the beginning of each run in the collider. Also in 'periodic' operation, after having performed a sequence of similar collision experiments, the snapback amplitudes can be expected to converge towards a constant value.

In the future it might become possible to accurately describe the snapback amplitudes in each magnet with the model, using a finite number of time constants. The time constants can possibly be obtained by optimizing the model with respect to measurements performed on real magnets. In order to be able to find the time constants in such an optimization, the measurement cycle should comprise a number of different features, as for example pre-cycles with different flat-top currents and flat-top durations, and different pre-injection durations which are representative for the entire range of measurements described in this chapter.

It is demonstrated as well that most 6 block magnets show higher snapback amplitudes and a stronger dependence on the flat-top current than magnets with a 5 block design. Most 5 block magnets show an exponential increase of the snapback amplitude with the pre-cycle flat-top duration. The snapback amplitude in the 6 block magnets generally increases to a maximum with the pre-cycle flat-top duration and decreases again. For this reason more than one time constant is necessary to describe the behavior of the 6 block magnets.

Chapter 5

Filament Magnetization

A detailed understanding of the filament magnetization behavior in changing magnetic fields is obligatory for the investigation of the decay and snapback in superconducting accelerator magnets. For this reason the impact of external field changes on the current distribution and magnetization in a saturated cylindrical type II superconducting filament is analyzed for characteristic cases appearing in the coil. Model calculations are used to investigate filaments exposed to field changes at arbitrary angles in a plane perpendicular to the filament axis, and after a subsequent field increase in the direction of the original background field. Fitting formulas are developed to describe the filament magnetization, and their parameters are adapted to the calculated data. In addition also the $J_c(B)$ dependence of a typical filament is derived from hysteresis curves measured on LHC dipole strands. Finally, it is shown how far the decay of the filament magnetization during injection is affected by flux creep.

Local field changes in superconducting accelerator magnets have an important impact on the coil magnetization. Especially during the injection of particles into the storage ring at about 0.54 T, the initially (mostly) saturated type II superconducting filaments in the strands are exposed to local field changes due to current redistributions in the coil. After the end of injection, the background field is increased again, and the filament magnetization ‘snaps back’ to the original hysteresis curve.

A detailed understanding of the filament behavior in changing magnetic fields is necessary to investigate decay and snapback. In order to reduce the analysis to the basic effect, the filaments are assumed to be solid and perfectly cylindrical with radius R and cross section S . A coordinate system is defined with its z -axis parallel to the filament's axis. The center of the filament cross section is placed in the origin. A sketch of the coordinate system is shown in figure 5.1.

Deviations of real filaments from the cylindrical shape are assumed not to contribute to average values, due to the very high number of filaments in the strands. In addition, the background magnetic field perpendicular to the filament axis is supposed to be

Filament Magnetization

homogeneous. In accelerator magnets, non-perpendicular fields (at angles up to about 10°) are present due to the twisting of filaments inside each strand, the zig-zag path of strands in the Rutherford-type cable and (at even larger angles) in the coil ends of the magnets. These deviations are disregarded. Finally also the Meissner phase for $B < B_{c,1}$ is neglected.

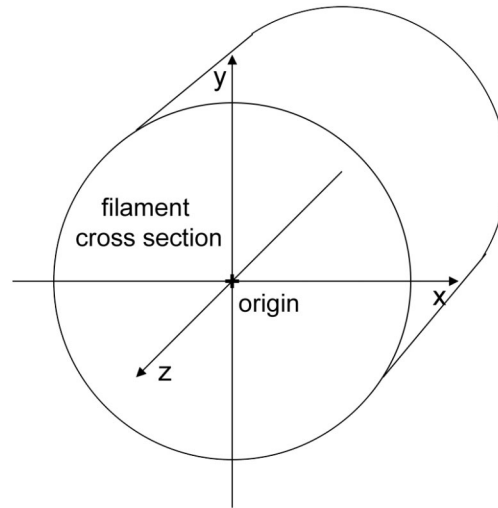


Figure 5.1 Definition of the coordinate system with its z-axis parallel to the filament's axis and its origin placed in the center of the round filament cross section.

Two aspects of the filament behavior are especially important. The first one is the dependence of the critical current density on the magnetic flux density: $J_c(B)$. The second aspect concerns the impact of external field changes with arbitrary direction on the current distribution and magnetization in a saturated filament with constant critical current density J_c . In situations where the magnetic flux density is large enough, both aspects can be treated separately.

The two aspects mentioned above can not generally be treated analytically, and formulas for the distribution of shielding currents and filament magnetization are only known for very specific cases [28], [40], [41], [57].

Four different situations are investigated in this section. Analytical approximations and formulas derived from numerical data are known for the magnetization of filaments with constant critical current density, zero transport current, and field changes parallel to the background field [28]. A rough analytical approximation is also known for the case where the filament carries a transport current. If the $J_c(B)$ dependence is known, the magnetization of a filament with field dependent critical current density and without transport current can be approximated analytically or calculated numerically. Finally, a saturated filament without transport current and constant critical current density is

discussed, exposed to a field change at an arbitrary angle with respect to the original background field, and a subsequent increase of the background field. Typical situations are analyzed numerically and fitting formulas are derived from the calculated data.

A numerical model is used to describe the penetration of magnetic flux in a superconducting filament. The model is used to iteratively derive the $J_c(B)$ dependence from experimental data, by comparing measurements and calculations, and to analyze the impact of changing magnetic fields on the current distribution and magnetization of a saturated cylindrical superconducting filament.

5.1 Numerical model

Several algorithms exist to model the penetration of magnetic flux into a superconductor e.g. [14], [28], [36], [40], [44]. The algorithm of Brandt [14] calculates the distribution of shielding current density J due to a penetrating perpendicular field and is based on the iteration of the integral equation:

$$J(\vec{r}, t) = \frac{-1}{\mu_0} \int_s Q^{-1}(\vec{r}, \vec{r}') [A(\vec{r}', t) + x' B_y - y' B_x] dS' , \quad (5.1)$$

where $\vec{r} = (x, y)$ and $\vec{r}' = (x', y')$ are vectors in the xy -plane and $B = (B_x, B_y)$ is the flux density. The integral is discretized and the inversion of the integrator Kernel

$$Q(\vec{r}, \vec{r}') = \frac{1}{2\pi} \ln |\vec{r} - \vec{r}'| \quad (5.2)$$

is performed by matrix-inversion. Each step of the iteration can be calculated as a simple matrix multiplication. No boundary conditions need to be implemented and no approximation for the current boundaries in the filament is necessary.

The vector potential \vec{A} only has a component in z -direction and is calculated as a time integral of the electric field:

$$A = - \int_0^t E(t) dt . \quad (5.3)$$

The electric field can be expressed as a function of J and B :

$$E(J, B) = \rho(J, B) J , \quad (5.4)$$

where ρ is the resistivity. Equation (2.4) is modified to describe a power law for $J \ll J_c(B)$ and a linear normal state resistivity for $J \gg J_c(B)$:

$$\rho(J, B) = r_0 B \frac{(J / J_c(B))^{(N-1)}}{1 + (J / J_c(B))^{(N-1)}} , \quad (5.5)$$

Filament Magnetization

where r_0 is a constant. Equations (5.4) and (5.5) describe ohmic behavior for $N = 1$ and the Bean model for $N = \infty$. In figure 5.2a the electrical field is shown as a function of the normalized current density for several values of N , and for the case of the Bean model.

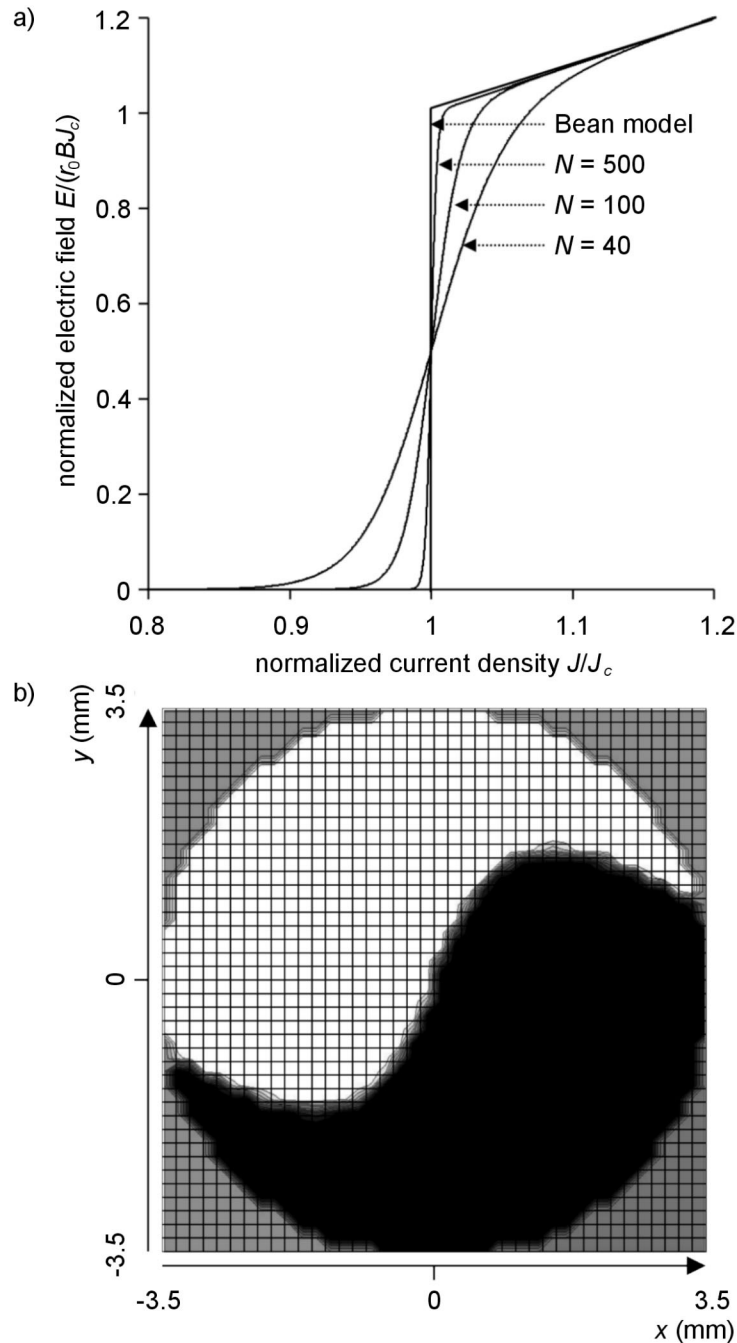


Figure 5.2 a) The normalized electric field is plotted as a function of the normalized current density for $N = 40, 100, 500$ and in the case of the Bean model ($N = \infty$). b) The filament cross section is discretized in a grid of 40×40 points. The white and black regions show currents flowing parallel and anti-parallel to the z -axis, respectively. Regions outside the filament cross section are shown in grey.

Filament Magnetization

For LHC strands N is typically in the range of 30 to 100, depending on the background field and temperature.

The magnetization can be calculated by integrating the current density across the filament section:

$$\bar{M} = \frac{1}{\pi R^2} \iint_s J(x, y) \begin{pmatrix} y \\ -x \end{pmatrix} dx dy. \quad (5.6)$$

The numerical results are valid for a filament with arbitrary radius and critical current density. The following normalization makes it easier to apply the results of the calculations to arbitrary filaments:

$$x_n = \frac{x}{R}, \quad y_n = \frac{y}{R}, \quad j = \frac{J}{J_c}, \quad m = \frac{M}{J_c R}, \quad b = \frac{B}{\mu_0 J_c R}. \quad (5.7)$$

The normalized cylindrical filament cross section is sampled on a rectangular grid with $2n$ (n integer) points inside an interval $[-1\dots 1]$ on each axis. An example of the discretization of the current distribution in a filament cross section is shown in figure 5.2b. The accuracy of the algorithm is mainly limited by the discretization of the grid, since an increasing grid size requires a large amount of memory, which considerably slows down the calculation. Details on the accuracy are given in section 5.3 and 5.4. See [14] for more details on the model.

5.2 Formulas for filament magnetization

The hysteresis behavior of a filament exposed to a changing external field parallel and anti-parallel to the y -axis is analyzed here. In first approximation, the critical current density J_c is taken constant, and approximate formulas are presented to describe the filament magnetization during a full hysteresis cycle. Also the impact of a transport current is estimated. As a second step the impact of the $J_c(B)$ dependence on the hysteresis curve is dealt with. For external fields in the range of the penetration field, the local field profile in the filament cross section has an important impact on the critical current density and causes distortions of the hysteresis curve. However, for $B \gg B_p(0)$ the $J_c(B)$ dependence and the hysteresis can be treated independently.

5.2.1 Filament with constant critical current density

A hard superconductor compensates any external field by inducing a shell of shielding currents. The shielding field and the induced magnetization are always oriented anti-parallel to the vector of the field change. The ideal current shell to shield a perfect dipolar field has a $\cos(\theta)$ -distribution on the circular boundary of the filament cross section.

Filament Magnetization

However, in real filaments the current shells are not located on the boundary, but penetrate into the superconducting material. Starting from the ‘virgin state’, the magnetization follows the so-called ‘virgin curve’. The current boundaries in the filament cross section can be approximated by ellipses [2]. This is shown schematically in figure 5.3a. However, with increasing field, the shape of the shells deviates more and more from an ellipse.

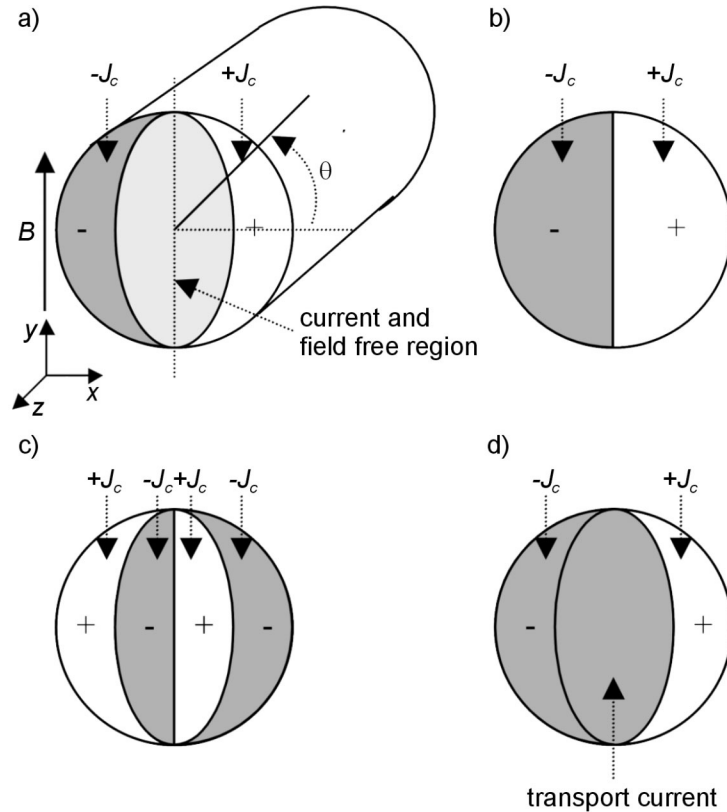


Figure 5.3 Sketch of the shielding currents induced in a cylindrical superconducting filament by a varying external field B . The surfaces in white and dark grey represent currents flowing with the critical current density in positive or negative z -direction, respectively. Light grey represents zones free of current. a) The current boundaries are approximated by ellipses. The saturated state is shown in b). c) If the field is decreased, a new shell of shielding currents is induced. d) If a filament with transport current is exposed to an external field sweep $\Delta B > B_p$, the transport current is assumed to flow in a central elliptical region.

The highest field that can be shielded is the so-called penetration field B_p , where the entire cross section is filled with current. Figure 5.3b shows the current density in the fully penetrated filament. For a superconductor in the Critical State [4] with constant critical current density, the penetration field B_p and the saturation magnetization M_p are given by equation (2.6) and (2.7).

Filament Magnetization

With $b = B/B_p$ and $m = M/M_p$, the following third order approximation of the virgin curve is valid within 6% [28]:

$$m_{\text{third-order}}(b) = \begin{cases} ((1-b)^3 - 1), & 0 \leq b \leq 1 \\ -1, & b > 1. \end{cases} \quad (5.8)$$

The applied field may be raised to values much larger than B_p . In this case the shielding currents are distributed in the same way as in figure 5.3b. However, the field is not entirely shielded in the interior. A full hysteresis curve is shown schematically in figure 5.4, where the normalized magnetization is sketched as a function of the field. For $B \gg B_p(0)$, the normalized magnetization on the up-ramp branch is

$$m_{\text{up-ramp branch}}(b) = -1. \quad (5.9)$$

Consider now the case that the ramp direction is reversed at a maximum field B_{\max} . The decreasing field inverts the polarity of the current distribution in a region close to the surface. A new shell of shielding currents penetrates the filament cross section from the outside. The new current pattern is shown schematically in figure 5.3c.

In order to go from one branch of the hysteresis curve to the other and to invert the polarity of the magnetization, the background field has to change by two times the penetration field. This is illustrated in figure 5.4.

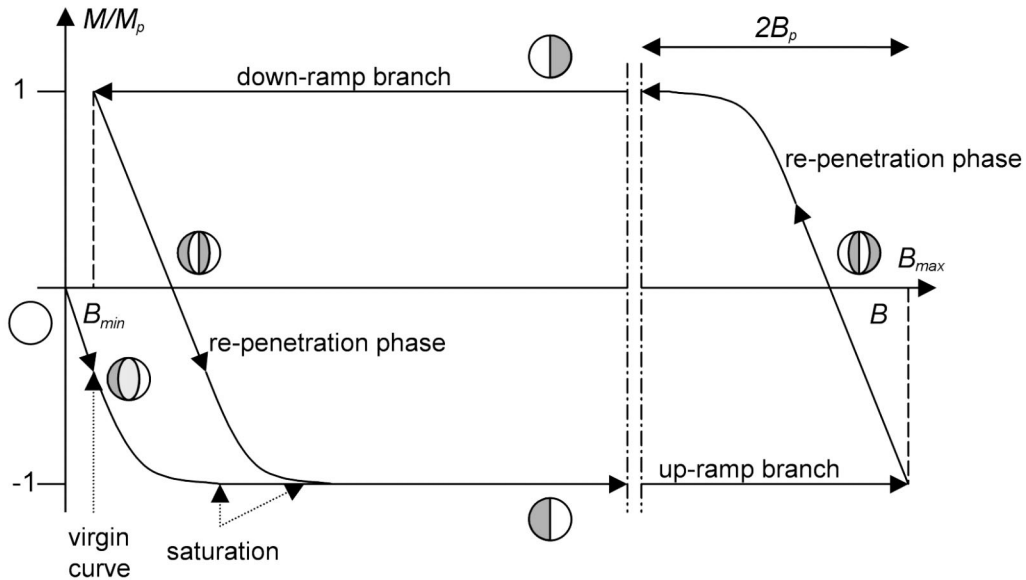


Figure 5.4 The normalized magnetization of a filament in the Critical State (constant critical current density) is shown schematically as a function of the background field B . The hysteresis is a consequence of the 'memory' of the shielding currents. The circles in the picture indicate the state of the shielding currents in the filament cross section.

Filament Magnetization

For saturated filaments it is, thus, convenient to normalize the induction B as $b = B/(2B_p)$. A useful approximation for the down-ramp re-penetration between $B_{max} - 2B_p < B < B_{max}$ is

$$m_{down-ramp\ penetration}(b) = 1 + 2(b_{max} - b - 1)^3. \quad (5.10)$$

For $B < B_{max} - 2B_p$ the down-ramp branch is reached

$$m_{down-ramp\ branch}(b) = 1. \quad (5.11)$$

At a certain minimum B_{min} the field is increased again. The up-ramp re-penetration between $B_{min} < B < B_{min} + 2B_p$ can be expressed by:

$$m_{up-ramp\ penetration}(b) = -\left(1 + 2(b - b_{min} - 1)^3\right). \quad (5.12)$$

If a filament with transport current I_t is exposed to a field sweep $\Delta B > B_p$, the transport current is confined to a small elliptical region in the center (figure 5.3d) and flows with the critical current density J_c [28]. Thus, the transport current reduces the magnetization of an otherwise saturated filament by a factor of $\left(1 - (I_t/I_c)^2\right)$, where I_c is the critical current. In the LHC, this correction is negligible near the injection field of 0.54 T, where $I_t \ll I_c$.

5.2.2 Filament with field dependent critical current density

In a real filament, the penetration field B_p and the saturation magnetization M_p are not constant, but depend on the field dependent critical current density $J_c(B)$. Shielding currents affect the field profile in the filament cross section and cause an inhomogeneous distribution of the critical current density. For low magnetic fields in the range of $B_p(0\text{ T})$, this so-called self-field effect results in a considerable distortion of the hysteresis curve.

If, however, $B \gg B_p(0\text{ T})$, the self-field effect can be neglected and B_p and M_p are proportional to $J_c(B)$:

$$B_p(B) \approx \frac{2\mu_0 R}{\pi} J_c(B) \text{ and } M_p(B) \approx \frac{4R}{3\pi} J_c(B). \quad (5.13)$$

The normalized field and magnetization in saturated filaments with field dependent critical current density are defined by

$$b = \frac{B}{2B_p(B)} \text{ and } m = \frac{M}{M_p(B)}. \quad (5.14)$$

The denominator $2B_p(B)$ takes into account that the polarity of the shielding currents has to be inverted in order to go from one hysteresis branch to the other. For $B \gg B_p(0\text{ T})$ a

Filament Magnetization

field dependent hysteresis curve can be approximated using the equations (5.9)-(5.12), together with the field dependent normalizations in equation (5.14).

In figure 5.5 a calculated hysteresis curve is shown for a typical LHC inner strand at 4.2 K. The first critical field $B_{c,1}$ and other effects like filament bridging or non-cylindrical filaments are neglected. The figure also shows an envelope proportional to $J_c(B)$. For fields $B \gg B_p(0 T)$, the envelope agrees very well with the hysteresis branches. However, the self-field effect causes significant deviations at fields near zero.

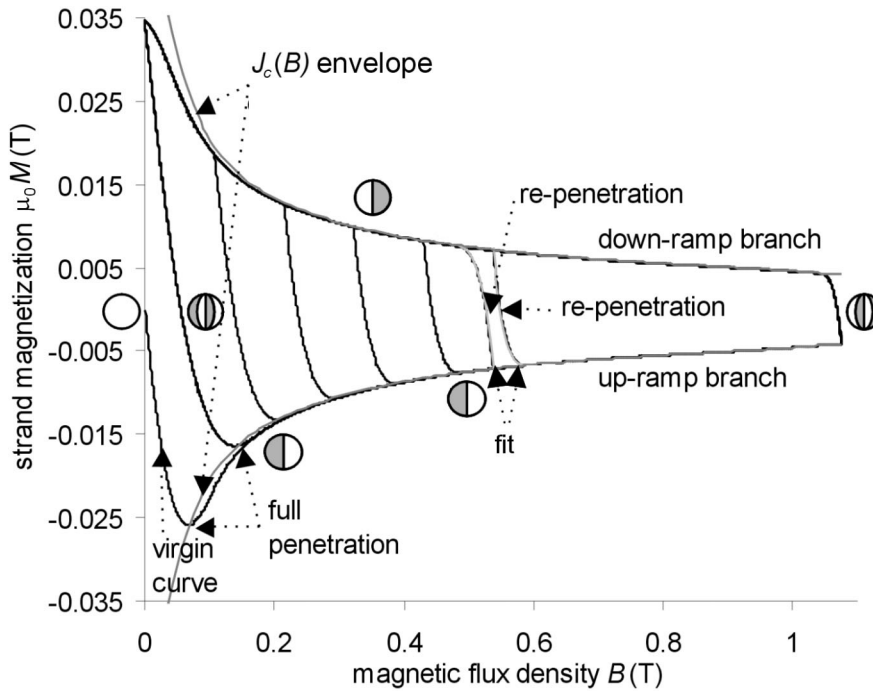


Figure 5.5 Calculated magnetization of a typical LHC inner strand at 4.2 K is shown as a function of magnetic field. The calculations are performed using the Brandt algorithm and an implemented $J_c(B)$ dependence. For $B \gg B_p(0 T)$, the hysteresis curve approaches an envelope proportional to $J_c(B)$. Also shown are fits for the re-penetration phases, when reversing the ramp direction at a background field of 0.54 T.

For both, the up-ramp and the down-ramp branch, the ramp direction is reversed at a background field of 0.54 T. The third order fitting formulas (5.10) and (5.12) are also shown in the figure. They coincide very well with the calculated data.

5.3 Determination of the $J_c(B)$ dependence

Measurements of the $J_c(B, T)$ dependence are usually performed as transport current measurements on superconducting strands exposed to a precisely defined applied field at

Filament Magnetization

constant temperature. However, especially at low field, the self-field induced by the transport current in the multifilamentary wire gives a relatively large contribution to the local field and thus to the current profile in its cross section and adds a significant error to the measurement. An alternative approach is to derive the $J_c(B)$ dependence at constant temperature from hysteresis curves measured on a strand without transport current. For fields B much higher than the filament penetration field $B_p(0 \text{ T})$, the hysteresis amplitude is directly proportional to $J_c(B)$. However, for fields in the order of $B_p(0 \text{ T})$ and lower, one can expect an influence of the local field profile in the filaments on the critical current density. Eventually also filament bridging, the critical field $B_{c,1}$ of the Meissner phase and non-cylindrical filaments affect the magnetization. In NbTi $B_{c,1}$ is typically about 20 mT at 1.9 K and 15 mT at 4.2 K. At very low fields, these effects make it especially difficult to derive the $J_c(B)$ dependence of the superconductor from hysteresis measurements.

The algorithm previously introduced in this chapter can take into account the dependence of the critical current density $J_c(B(x,y))$ on the local field in the cross section of a filament. A first approximation is to take $J_c(B)$ proportional to the amplitude along the down-ramp branch of the hysteresis curve. Especially at low field, an iterative comparison between measured and calculated data allows to improve the $J_c(B)$ approximation step by step. After each calculation the new approximation for $J_c(B)$ is calculated by multiplying $J_c(B)$ with the ratio between the measured and calculated magnetization on the down-ramp branch.

The dotted curves in figure 5.6 show measured hysteresis curves of a typical LHC strand at 4.2 K. The full lines show numerical data calculated for a round filament cross section discretized on a grid of 20×20 points, using a constant N -value of 40 in equation (5.5). The calculated hysteresis curves describe very well the experimental data. Below 0.2 T small deviations are still visible, primarily due to the inaccuracy in $J_c(B)$ at very low fields. Hysteresis curves are measured and calculated also for hysteresis cycles with different minimum fields.

An optimized approximation for $J_c(B)$ at 4.2 K is displayed in figure 5.7. For fields between 0 and 1 T, $J_c(B)$ can be described by a fitting formula (without physical relevance):

$$J_c(B) = \frac{1}{c_1 + c_2(B/c_3)^{c_4}} + c_5 + c_6 B + c_7 B^2 + c_8 B^3. \quad (5.15)$$

The constants are $c_1 = 2.180 \cdot 10^{-11} \text{ m}^2/\text{A}$, $c_2 = 1.424 \cdot 10^{-11} \text{ m}^2/\text{A}$, $c_3 = 3.999 \cdot 10^{-2} \text{ T}$, $c_4 = 1.877$, $c_5 = 2.358 \cdot 10^{10} \text{ A/m}^2$, $c_6 = -4.829 \cdot 10^{10} \text{ A/(Tm}^2\text{)}$, $c_7 = 5.373 \cdot 10^{10} \text{ A/(T}^2\text{m}^2\text{)}$ and $c_8 = -2.302 \cdot 10^{10} \text{ A/(T}^3\text{m}^2\text{)}$.

Filament Magnetization

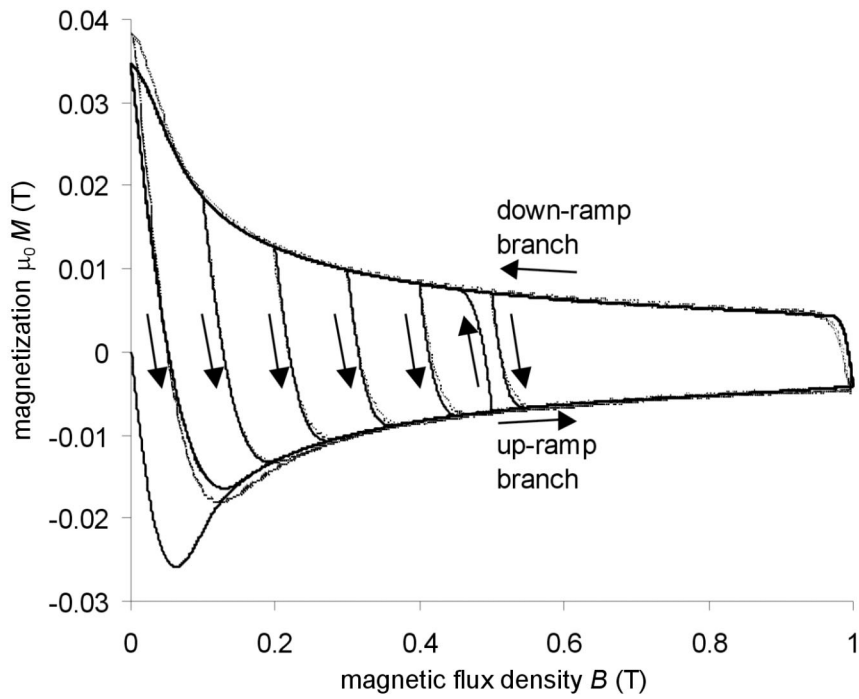


Figure 5.6 The measured (dotted line) and calculated (full line) magnetization of a typical LHC strand at 4.2 K are shown as functions of the magnetic flux density B .

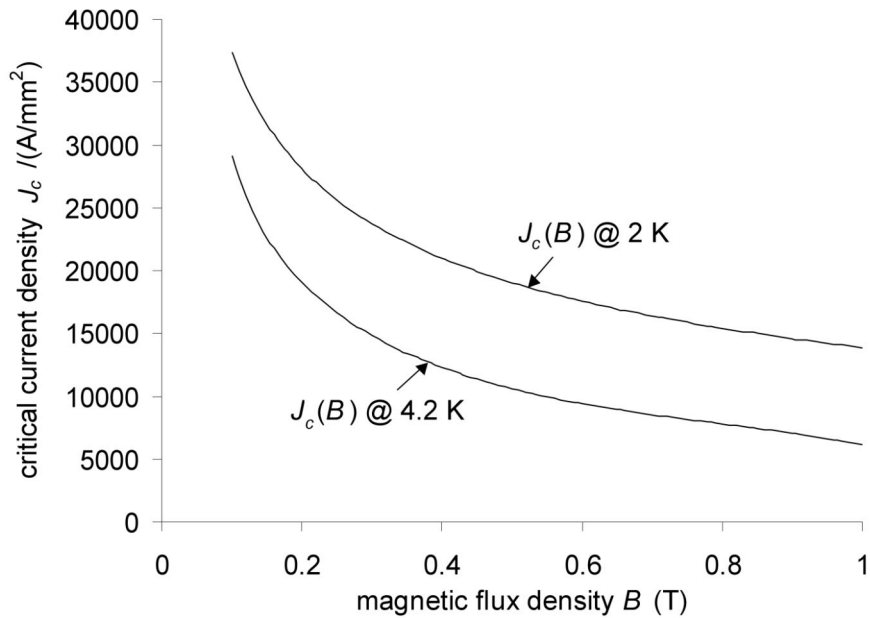


Figure 5.7 Optimized approximations for the critical current density J_c in a typical filament of an LHC inner strand are shown as functions of B , for ambient temperatures of 2 K and 4.2 K.

Filament Magnetization

Kassoul assumed the Critical State approximation and used an algorithm based on finite elements to model the current distribution in cylindrical filaments. He derived the $J_c(B)$ dependence at 2 K from data measured on typical LHC inner strands [32]. A typical $J_c(B)$ dependence at 2 K is plotted in figure 5.7, which is implemented into a numerical model for the coil, described in section 6. The curve can be described by the following formula:

$$J_c(B) = c_1 \left(\frac{B}{c_2} \right)^{c_3} \left(1 - \frac{B}{c_2} \right) / B. \quad (5.16)$$

The parameters are $c_1 = 7.147 \cdot 10^{10}$ TA/m², $c_2 = 13.51$ T and $c_3 = 0.6$.

In figure 5.8 the relative difference $(J_c(2 \text{ K}) - J_c(4.2 \text{ K})) / J_c(2 \text{ K})$ between the $J_c(B)$ dependences at both temperatures is displayed as a function of the field B . It converges towards 1 for $B \geq B_{c,2}(4.2 \text{ K})$ and towards a finite positive value at $B = 0$.

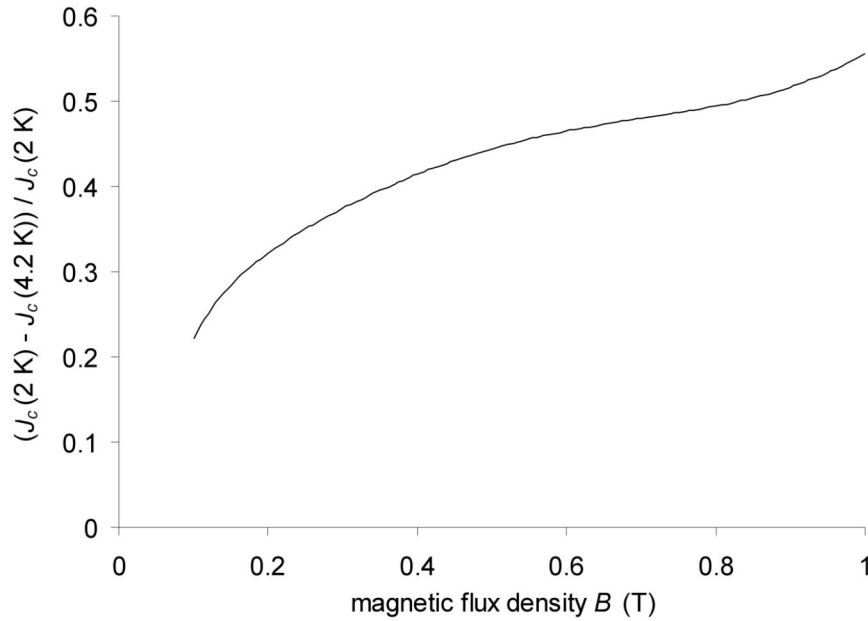


Figure 5.8 The relative difference between the $J_c(B)$ dependences at 2 and at 4.2 K is shown as a function of the field B .

The errors of the derived $J_c(B)$ dependences are within 10% of the absolute values.

5.4 Formula development for applied fields with arbitrary direction

This section considers the magnetization of a filament subject to a field change in any direction, still perpendicular to the filament axis. For simplicity, the critical current density J_c is taken constant and independent of the magnetic field.

Filament Magnetization

A background field $\vec{B}_0 = -B_0 \vec{e}_y$ with B_0 equal or greater than B_p is applied to the filament, and the saturated magnetization in y -direction equals $\vec{M} = M_p \vec{e}_y$. A local field change in the coil is represented by $\Delta\vec{B}_d = -(\Delta B_{d,x}, \Delta B_{d,y})$, and applied perpendicular to the filament and at an angle φ with respect to \vec{B}_0 . As a result the shielding currents in the cross section of the superconductor redistribute, hence resulting in a change of the magnetization vector in amplitude and direction. Finally, the snapback is represented by an increase in amplitude of the background field ΔB_{sb} . Consequently, current distribution and magnetization tend towards their original configuration. Some of the configurations are sketched in figure 5.9. In the following analysis the impact of external field changes on the current distribution and magnetization of the filament is investigated in detail.

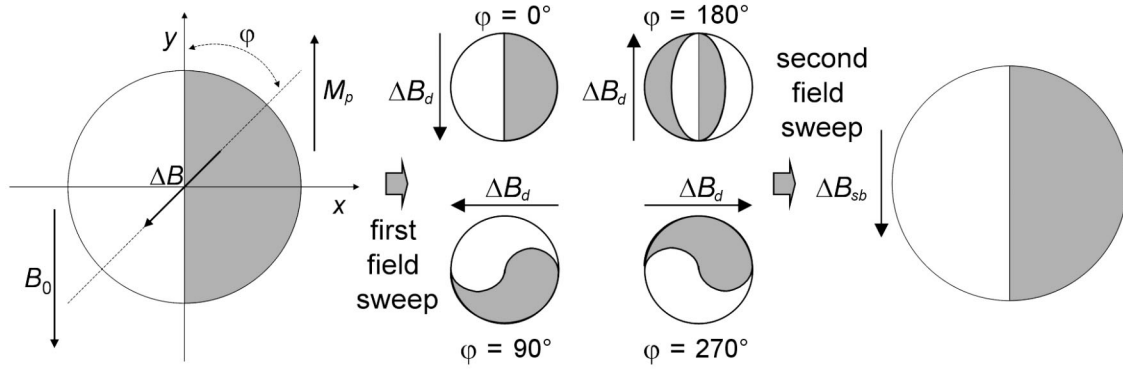


Figure 5.9 The impact of an external field change ΔB_d on the distribution of shielding currents in a saturated filament is sketched at different angles with respect to the original background field B_0 . A second field sweep ΔB_{sb} parallel to the background field brings the magnetization back to the original state.

The numerical algorithm of Brandt is used to develop formulas for the magnetization, that hold in all situations typically appearing during decay and snapback.

A useful normalization for the field changes ΔB_d and ΔB_{sb} is

$$\Delta b_d = -\frac{\Delta B_d}{2B_p} \quad \text{and} \quad \Delta b_{sb} = -\frac{\Delta B_{sb}}{2B_p}. \quad (5.17)$$

For filaments without transport current in homogeneous background fields, the shielding currents are anti-symmetric with respect to the origin: $J(x, y) = -J(-x, -y)$. As a consequence, also the magnetization components after field sweeps at angles φ and $2\pi - \varphi$ have symmetries. The x -components are anti-symmetric and the y -components are symmetric:

$$M_x(\varphi) = -M_x(2\pi - \varphi), \quad (5.18)$$

$$M_y(\varphi) = M_y(2\pi - \varphi). \quad (5.19)$$

Thus, the problem can be restricted to $0^\circ \leq \varphi \leq 180^\circ$. Equation (5.1) only needs to be integrated over half a cross section and the integrator Kernels are divided by a factor 2.

The Critical State model [4] and the case of no flux flow are approximated, using a high N -value of 500 in equation (5.5) (compare figure 5.2a). A typical LHC filament with $R = 3.5 \mu\text{m}$ and $J_c = 1.06 \cdot 10^{10} \text{ A/m}^2$ is assumed. However, the results do not depend on R and J_c , and the validity of the algorithm for arbitrary radius and critical current density is guaranteed by the normalizations in equation (5.7). The round filament cross section is meshed with a rectangular grid of 40×40 points as shown in figure 5.2b.

The analysis is split in two parts. The first part describes conditions characteristic for the decay. The saturated filament is exposed to field changes at different angles and of different amplitudes, and fitting formulas are adapted to the calculated magnetization data. The formulas are quite accurate and allow the precise prediction of the magnetization as a function of the angle φ and the field sweep ΔB_d .

The development of formulas for the snapback is much more complicated, since the snapback depends on the decay. For this reason, the second part of the analysis describes characteristic conditions during both, decay and snapback. The saturated filament is exposed to field changes at different angles, with different amplitudes and different subsequent increases of the background field. Also in this case fitting formulas are developed. Due to the huge amount of data, however, these formulas are considerably less accurate, and will only be used to calculate the snapback. The formulas follow an approach, which is very different from the one used for the decay only.

5.4.1 Impact of a single field sweep with arbitrary direction on a saturated filament

Field changes are applied to the saturated filament in angular intervals of 5° , between 0° and 180° with respect to the initial background field of 0.5 T. In each case ΔB_d is increased from 0 to 0.3 T. If a field change is applied at an angle $\varphi = 0^\circ$, the magnetization does not change, and one finds $M_x = 0$ and $M_y = M_p$. The case of $\varphi = 180^\circ$ corresponds to the re-penetration branches of the hysteresis curve, where the ramp direction is reversed (equation (5.10) and (5.12)). The shielding currents initially present in the filament have to change sign and only saturate after a field sweep of $2B_p$. Also here M_x equals 0. In analogy to the third order approximation in equation (5.12), an analytical approximation of M_y for $|\Delta B_d| \leq 2B_p$ is given by

Filament Magnetization

$$M_y = M_p \left(-1 + 2(1 - \Delta b_d)^3 \right). \quad (5.20)$$

The magnetization saturates for field sweeps $\Delta b_d \gg 1$ at an arbitrary angle φ :

$$\vec{M}_{sat}(\varphi) = M_p \begin{pmatrix} \sin(\varphi) \\ \cos(\varphi) \end{pmatrix}. \quad (5.21)$$

A useful normalization for the magnetization components is

$$m_x(\varphi, \Delta b_d) = \frac{M_x(\varphi, \Delta B_d)}{M_p \sin \varphi}, \quad (5.22)$$

$$m_y(\varphi, \Delta b_d) = \left(1 - \frac{M_y(\varphi, \Delta B_d)}{M_p} \right) / (1 - \cos \varphi). \quad (5.23)$$

A third order approximation is used as a reference and subtracted from the normalized magnetization components in equation (5.22) and (5.23). The 'error functions' f_x and f_y describe the deviation of m_x and m_y from equation (5.20):

$$f_x(\varphi, \Delta b_d) = m_x(\varphi, \Delta b_d) - 1 + (1 - \Delta b_d)^3, \quad (5.24)$$

$$f_y(\varphi, \Delta b_d) = m_y(\varphi, \Delta b_d) - 1 + (1 - \Delta b_d)^3. \quad (5.25)$$

In order to fit f_x and f_y , the following expression is used:

$$f_{x,y}(\varphi, \Delta b_d) = A(\Delta b_d/b_s)^\alpha (1 - (\Delta b_d/b_s))^\beta ((\Delta b_0 - \Delta b_d)/b_s)^\gamma. \quad (5.26)$$

The exponents α , β , γ , the amplitude A , the saturation field $b_s = B_s/(2B_p)$ and the zero position Δb_0 are functions of φ and can be adapted to calculated data.

In figure 5.10 the impact on the shielding currents in the superconductor is demonstrated for field sweeps ΔB_d of 5, 10, 20 and 40 mT, at angles φ of 0° , 90° and 180° . A field sweep parallel to the background field does not affect the current distribution. Field variations at an angle $\varphi = 90^\circ$ with respect to the background field first redistribute the currents flowing very near to the surface, resulting in a current distribution resembling the chinese 'Yin-Yang' sign. Only after a field sweep $\Delta B_d \gg 2B_p$ the current distribution saturates with an orientation that is rotated by 90° with respect to the original configuration. A field sweep at $\varphi = 180^\circ$ induces a current shell of opposite polarity and saturates in a current distribution, which is rotated by 180° with respect to the original configuration.

Filament Magnetization

M_x , M_y , m_x , m_y , f_x and f_y are plotted in figure 5.11 as functions of φ and ΔB_d . For $\Delta b_d = 0$ and all angles φ , M_x equals zero, and M_y equals M_p . For $0 < \Delta B_d < 2B_p$ the maximum of M_x slightly deviates from the angle $\varphi = 90^\circ$, and M_y has its minimum at $\varphi = 180^\circ$. The values saturate for $\Delta B_d \gg 2B_p$, and attain the saturation values described by equation (5.21). The normalized components m_x and m_y describe the magnetization with respect to the saturation values. m_x and m_y are zero for $\Delta b_d = 0$. For some angles φ they reach a maximum at certain values of Δb_d , and saturate for $\Delta B_d \gg 2B_p$ with a value of 1. f_x and f_y describe the deviation of m_x and m_y from the third power term in equation (5.24) and (5.25). Both, f_x and f_y equal zero at $\Delta b_d = 0$, reach different maxima and minima, and saturate at values of zero for $\Delta B_d \gg 2B_p$.

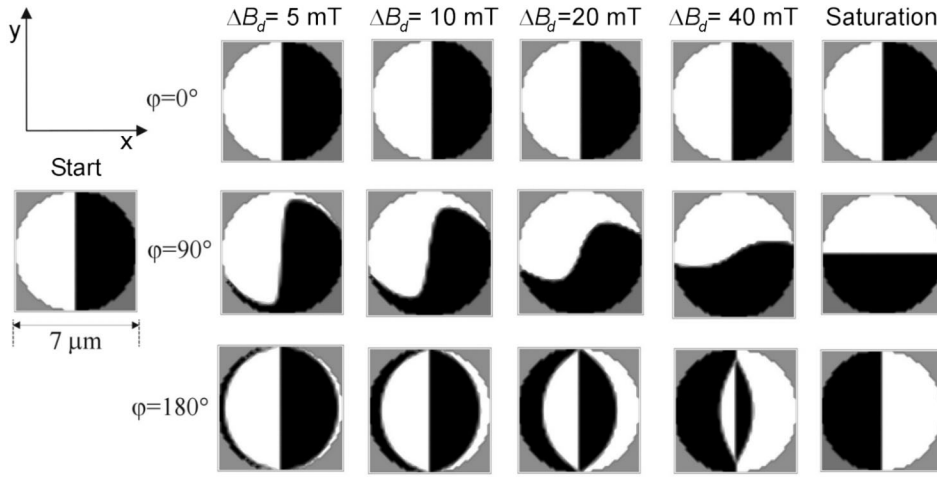


Figure 5.10 The distribution of shielding currents in the filament cross section is shown for different field changes at angles φ of 0° , 90° and 180° . The white and black regions show currents flowing parallel and anti-parallel to the z -axis, respectively. Regions outside the filament cross section are shown in grey.

The wiggles in the curves are caused by the effect of the discretization on the current distribution. They are visible in particular in plots of the normalized and reference subtracted data.

f_x and f_y can be described by equation (5.26) with constant exponents $\alpha = \gamma = 1$ and $\beta = 11.24$. A , b_s and Δb_0 are expanded as third order polynomials

$$p(\varphi_r) = \sum_{n=0}^3 p_n \varphi_r^n \quad (5.27)$$

in $\varphi_r = \varphi/360^\circ$. The coefficients for A , b_s and Δb_0 are shown in table 5.1.

Filament Magnetization

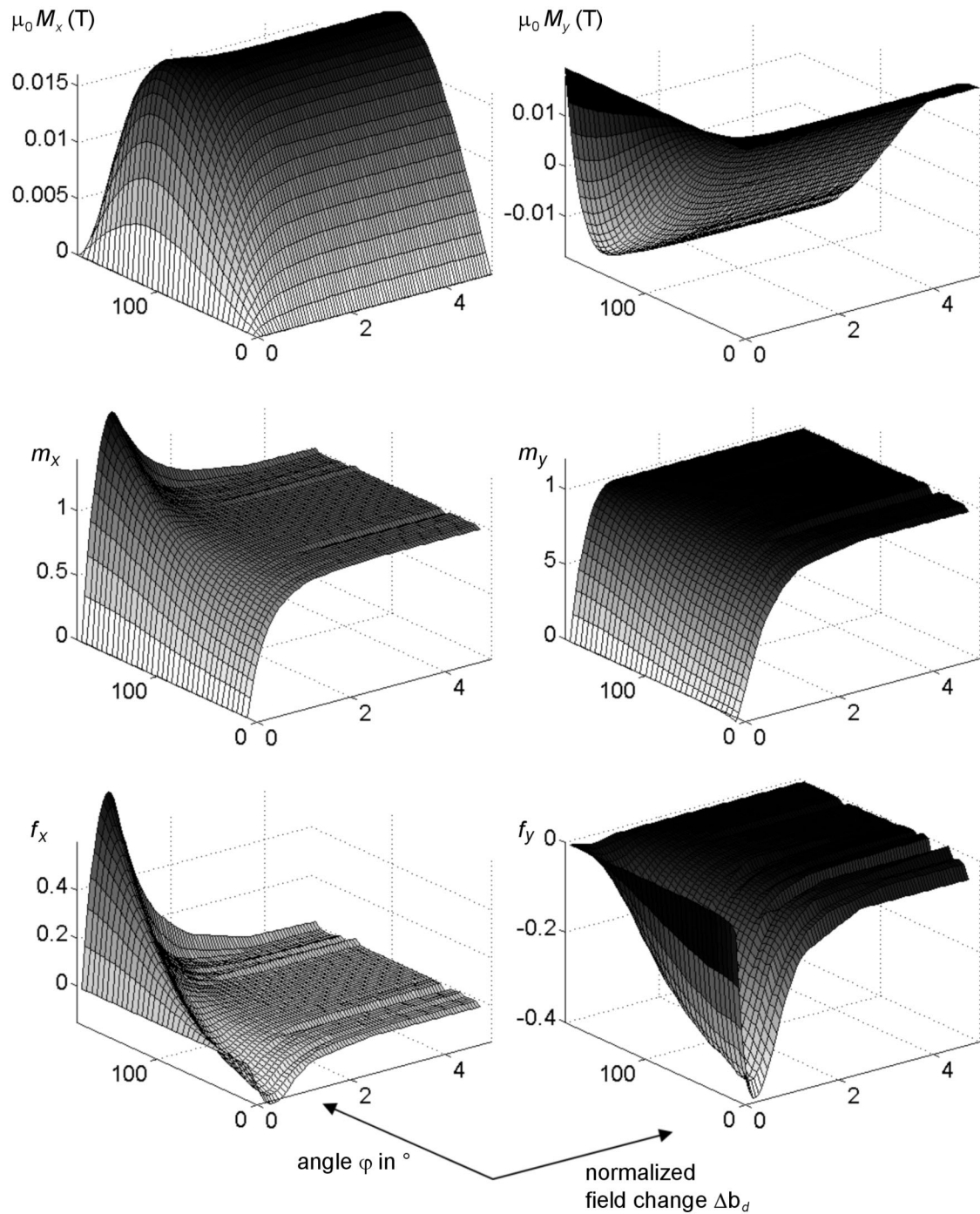


Figure 5.11 The magnetization components M_x and M_y , the normalized components m_x and m_y , and the 'error functions' f_x and f_y are shown as functions of the angle φ and the normalized field change Δb_d .

Filament Magnetization

f_x	p_0	p_1	p_2	p_3	f_y	p_0	p_1	p_2	p_3
A	61.3	-177	131	106	A	19.5	90.7	-156	-203
b_s	4.20	-8.15	23.9	1.22	b_s	5.03	-13.6	54.6	-68.4
Δb_0	-0.159	5.53	-43.6	143	Δb_0	-1.88	6.94	-13.5	16.9

Table 5.1 Fitting parameters.

5.4.2 Impact of a field sweep and a subsequent rise of the background field

Field changes of different amplitudes ΔB_d are applied to the filament, in angular intervals of 10° , between 0° and 180° with respect to the original background field of 0.5 T. In each case the amplitude ΔB_d is increased in steps of 7.5 mT, from 0 T to 0.3 T. Finally, a second field sweep ΔB_{sb} is applied in the direction of the original background field. ΔB_{sb} is increased from 0 T to 0.3 T. The geometry is sketched in figure 5.9.

Figure 5.12 shows examples of the behavior of shielding currents after a first field sweep $\Delta B_d = 22.5$ mT at an angle of $\varphi = 90^\circ$ with respect to the original background field, for various amplitudes of the second field sweep ΔB_{sb} . In the first row the picture on the left shows the current distribution for $\Delta B_{sb} = 0$. It resembles a chinese ‘Yin-Yang’ sign similar to the ones in figure 5.10. Current distributions are shown for amplitudes of the second field sweep ΔB_{sb} , which are increased in steps of 9.3 mT, from zero to a saturation value $\gg 2B_p$. The current distribution after the saturation agrees with the ‘start’ situation before the decay in figure 5.10.

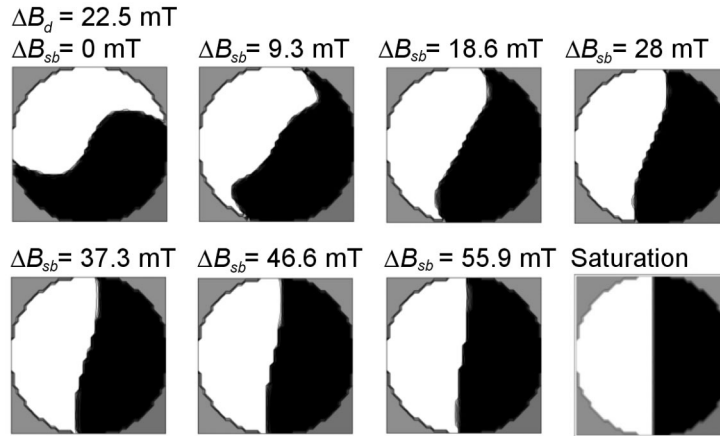


Figure 5.12 Examples for the distribution of shielding currents are shown after two consecutive field sweeps. The first one, ΔB_d , has an amplitude of 22.5 mT and penetrates at an angle of $\varphi = 90^\circ$. The current distributions are shown for different amplitudes of the second field sweep ΔB_{sb} in the direction of the original background field. The white and black regions show currents flowing parallel and anti-parallel to the z -axis, respectively. Regions outside the filament cross section are shown in grey.

Filament Magnetization

For every angle φ , every field change Δb_d and every amplitude for the subsequent rise of the background field Δb_{sb} , the behavior of the magnetization components M_x and M_y can be fitted as a linear combination

$$M_x(\varphi, \Delta b_d, \Delta b_{sb}) = M_p(B) \left\{ \begin{array}{l} a_{\text{exp},x}(\varphi, \Delta b_d) f_{\text{exp},x}(\varphi, \Delta b_d, \Delta b_{sb}) + \dots \\ a_{\text{poly},x}(\varphi, \Delta b_d) f_{\text{poly},x}(\varphi, \Delta b_d, \Delta b_{sb}) \end{array} \right\} \quad (5.28)$$

$$M_y(\varphi, \Delta b_d, \Delta b_{sb}) = M_p(B) \left\{ \begin{array}{l} -a_{\text{exp},y}(\varphi, \Delta b_d) f_{\text{exp},y}(\varphi, \Delta b_d, \Delta b_{sb}) - \dots \\ 2a_{\text{poly},y}(\varphi, \Delta b_d) f_{\text{poly},y}(\varphi, \Delta b_d, \Delta b_{sb}) + 1 \end{array} \right\}. \quad (5.29)$$

of an exponential function

$$f_{\text{exp},x,y}(\varphi, \Delta b_d, \Delta b_{sb}) = \exp(-\Delta b_{sb}/b_{\text{exp},x,y}(\varphi, \Delta b_d)) \quad (5.30)$$

and a third order polynomial

$$f_{\text{poly},x}(\varphi, \Delta b_d, \Delta b_{sb}) = \left\{ \begin{array}{l} (b_{\text{poly},x}(\varphi, \Delta b_d) - \Delta b_{sb})^3 \\ 0 \end{array} \right. \text{ for } \left. \begin{array}{l} \Delta b_{sb} < b_{\text{poly},x} \\ \Delta b_{sb} \geq b_{\text{poly},x} \end{array} \right\} \quad (5.31)$$

$$f_{\text{poly},y}(\varphi, \Delta b_d, \Delta b_{sb}) = \left\{ \begin{array}{l} (1 - \Delta b_{sb})^3 \\ g(\Delta b_d) \end{array} \right. \text{ for } \left. \begin{array}{l} \Delta b_{sb} < 1 \ \& \ \Delta b_{sb} < \Delta b_d \\ \text{else} \end{array} \right\} - g(\Delta b_d) \quad (5.32)$$

with

$$g(\Delta b_d) = \left\{ \begin{array}{l} (1 - \Delta b_d)^3 \\ 0 \end{array} \right. \text{ for } \left. \begin{array}{l} \Delta b_d < 1 \\ \Delta b_d \geq 1 \end{array} \right\}. \quad (5.33)$$

The saturation magnetization of the y-component is taken into account by the constant 1 in equation (5.29). A factor 2 in the polynomial part represents the maximum magnetization change of $2M_p(B)$ in the case of $\varphi = 180^\circ$, where the polarity of the magnetization is inverted. For fields $B \gg B_p$, the field dependent factor $M_p(B)$ takes into account the impact of the $J_c(B)$ dependence.

In figures 5.13 and 5.14 the parameters $a_{\text{poly},x}$, $b_{\text{poly},x}$, $a_{\text{exp},x}$, $b_{\text{exp},x}$, $a_{\text{poly},y}$, $a_{\text{exp},y}$ and $b_{\text{exp},y}$ are displayed as functions of φ and Δb_d . The parameters for the x-component are plotted in figure 5.13, the ones for the y-component in figure 5.14.

The parameter $a_{\text{poly},x}$, describing the contribution of the third order polynomial to M_x , has a maximum at small angles ($0^\circ < \varphi < 90^\circ$), and a minimum at large angles ($90^\circ < \varphi < 180^\circ$). For arbitrary values of Δb_d , $a_{\text{poly},x}$ can be fitted by the following expression:

Filament Magnetization

$$a_{poly,x}(\varphi, \Delta b_d) = c_{poly,x,0}(\Delta b_d) \left| \left(\frac{\varphi}{180^\circ} \right)^{c_{poly,x,1}(\Delta b_d)} \cdot \left| 1 - \left(\frac{\varphi}{180^\circ} \right)^{c_{poly,x,2}(\Delta b_d)} \right| (\varphi - c_{poly,x,3}(\Delta b_d)) \right|. \quad (5.34)$$

The extrema reach their largest values for small values of Δb_d .

The zero-position of the third order polynomial $b_{poly,x}$ increases exponentially with the angle φ :

$$b_{poly,x}(\varphi, \Delta b_d) = d_{poly,x,0}(\Delta b_d) + d_{poly,x,1}(\Delta b_d) \exp\left(-\frac{180^\circ - \varphi}{30^\circ}\right). \quad (5.35)$$

$b_{poly,x}$ attains negative values for small values of Δb_d .

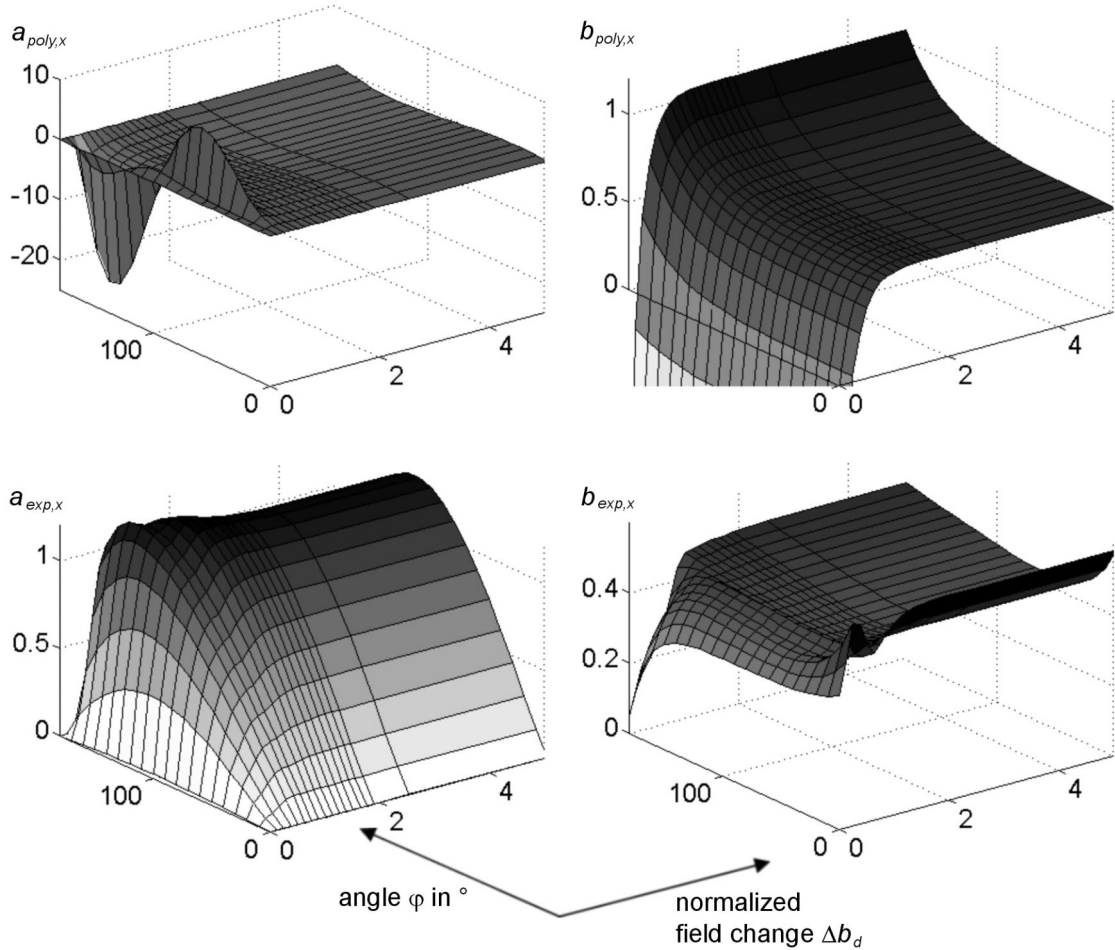


Figure 5.13 The parameters $a_{poly,x}$, $b_{poly,x}$, $a_{exp,x}$ and $b_{exp,x}$ for the magnetization component M_x are shown as functions of φ and Δb_d .

$a_{exp,x}$ is the amplitude of the exponential contribution to M_x . It has a maximum for $0^\circ < \varphi < 180^\circ$ and decreases to zero at angles φ of 0° and 180° :

Filament Magnetization

$$a_{\text{exp},x}(\varphi, \Delta b_d) = c_{\text{exp},x,0}(\Delta b_d) \left| \left(\frac{\varphi}{180^\circ} \right) \right|^{c_{\text{exp},x,1}(\Delta b_d)} \cdot \left| 1 - \left(\frac{\varphi}{180^\circ} \right) \right|^{c_{\text{exp},x,2}(\Delta b_d)}. \quad (5.36)$$

$a_{\text{exp},x}$ also decreases to zero for small values of Δb_d .

$b_{\text{exp},x}$ is the penetration length of the exponential function and can be fitted as a sum of a constant, a linear term and two exponentials:

$$b_{\text{exp},x}(\varphi, \Delta b_d) = d_{\text{exp},x,0}(\Delta b_d) + d_{\text{exp},x,1}(\Delta b_d) \left(\frac{\varphi}{180^\circ} \right) + \dots \\ d_{\text{exp},x,2}(\Delta b_d) \exp\left(-\frac{\varphi}{d_{\text{exp},x,3}(\Delta b_d)} \right) + d_{\text{exp},x,4}(\Delta b_d) \exp\left(-\frac{180^\circ - \varphi}{d_{\text{exp},x,5}(\Delta b_d)} \right). \quad (5.37)$$

For small values of Δb_d , $b_{\text{exp},x}$ decreases to values > 0 .

The contribution $a_{\text{poly},y}$ of the third order polynomial to M_y increases from 0 at $\varphi = 0$ to values around 1 at $\varphi = 180$. A fitting formula is:

$$a_{\text{poly},y}(\varphi, \Delta b_d) = \sum_{i=1}^4 c_{\text{poly},y,i}(\Delta b_d) \left(\frac{\varphi}{180^\circ} \right)^i. \quad (5.38)$$

$a_{\text{poly},y}$ goes through a minimum and increases slightly for small values of Δb_d .

The amplitude $a_{\text{exp},y}$ of the exponential contribution to M_y has a maximum and decreases to zero at angles φ of 0° and 180° . It can be fitted by:

$$a_{\text{exp},y}(\varphi, \Delta b_d) = c_{\text{exp},y,0}(\Delta b_d) \left| \left(\frac{\varphi}{180^\circ} \right) \right|^{c_{\text{exp},y,1}(\Delta b_d)} \cdot \left| 1 - \left(\frac{\varphi}{180^\circ} \right) \right|^{c_{\text{exp},y,2}(\Delta b_d)}. \quad (5.39)$$

For small values of Δb_d , $b_{\text{exp},x}$ has a maximum and decreases to 0.

The penetration length $b_{\text{exp},y}$ of the exponential contribution can be described as a sum of a constant, a linear term and two exponentials:

$$b_{\text{exp},y}(\varphi, \Delta b_d) = d_{\text{exp},y,0}(\Delta b_d) + d_{\text{exp},y,1}(\Delta b_d) \left(\frac{\varphi}{180^\circ} \right) + \dots \\ d_{\text{exp},y,2}(\Delta b_d) \exp\left(-\frac{\varphi}{d_{\text{exp},y,3}(\Delta b_d)} \right) + d_{\text{exp},y,4}(\Delta b_d) \exp\left(-\frac{180^\circ - \varphi}{d_{\text{exp},y,5}(\Delta b_d)} \right). \quad (5.40)$$

$b_{\text{exp},y}$ converges to values > 0 for small values of Δb_d .

Filament Magnetization

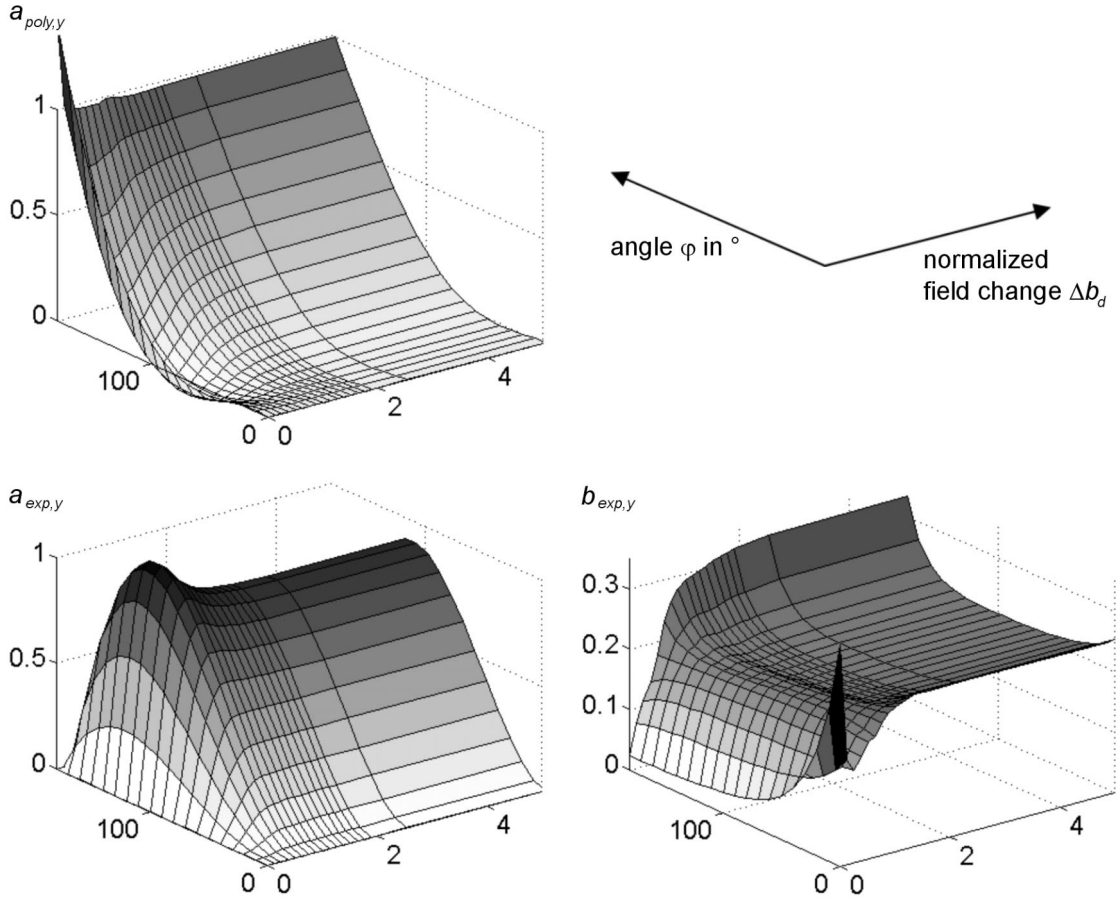


Figure 5.14 The parameters $a_{poly,y}$, $a_{exp,y}$ and $b_{exp,y}$ for the magnetization component M_y are shown as functions of φ and Δb_d .

The remaining parameters $c, d_{poly,exp,x,y,i}$ are functions of Δb_d . They are approximated by a sum of a constant, an exponential term and two different power laws:

$$c, d_{exp,poly,x,y,j}(\Delta b_d) = e + f \cdot \exp(-\Delta b_d/g) + \dots$$

$$h \cdot \begin{cases} |\Delta b_d - k|^l & \text{for } \Delta b_d < k \\ 0 & \text{for } \Delta b_d \geq k \end{cases} + m \cdot \begin{cases} |\Delta b_d - n|^o & \text{for } \Delta b_d < n \\ 0 & \text{for } \Delta b_d \geq n \end{cases}, \quad (5.41)$$

$$d_{exp,x,0,1}(\Delta b_d) = e + f \cdot \begin{cases} 1 - \exp(-(\Delta b_d - k)/g) & \text{for } \Delta b_d > k \\ 0 & \text{for } \Delta b_d \leq k \end{cases} + \dots$$

$$h \cdot \begin{cases} |\Delta b_d - k|^l & \text{for } \Delta b_d < k \\ 0 & \text{for } \Delta b_d \geq k \end{cases} + m \cdot \begin{cases} |\Delta b_d - n|^o & \text{for } \Delta b_d < n \\ 0 & \text{for } \Delta b_d \geq n \end{cases}. \quad (5.42)$$

The optimized fitting parameters $e, f, g, h, k, l, m, n, o$ are summarized in table A.1 in Appendix A.

5.4.3 Accuracy

Inaccuracies appear due to a limited N -value in equation (5.5) and a limited mesh discretization. The N -value of 500 contributes with less than 0.5%. The grid of 40×40 points affects the calculations in particular at angles φ of 45° and 135° , where the field change is diagonal to the grid. For angles φ with small values of $\sin(\varphi)$ or $(1 - \cos(\varphi))$ the normalized data in equations (5.22) and (5.23) are less accurate. The inaccuracies in M_x and M_y are less than 2% of M_p . The fitting formulas in equation (5.22) to (5.27), together with the parameters in table 5.1, are inaccurate within 3% of M_p . However, due to limitations in memory and computing time, the formulas (5.28) to (5.42), together with table A.1, describing the filament magnetization after two consecutive field sweeps, were adapted to a relatively coarse meshed set of data. Apart from that, the optimization of the significantly increased amount of parameters is an extremely delicate task. The inaccuracy of the formulas for M_x and M_y is limited to about 10% of M_p .

5.5 Estimation of the flux creep contribution

During initial investigations of decay and snapback at different accelerators, flux creep was thought to be the main contribution for the field decay [17], [25], [27]. However, after a careful study of the mechanism, nowadays the conclusion is that the effects are determined by an interaction between diffusing boundary induced coupling currents and the coil magnetization. In order to clarify, whether or not flux creep still significantly contributes to the decay, a rough estimation for the upper limit of flux creep is made.

Not very much is known so far about flux creep in LHC strands. However, measurements at 2 K have shown that after a decay time of about 1000 s the relaxation of a magnetized sample in a background field of 0.5 T is limited to about 1% of the original magnetization [38]. This measured relaxation can be taken as an upper limit for the flux creep contribution.

At injection, measured hysteresis curves of the normal sextupole component have amplitudes around 10 units. Assuming that the magnetization of all filaments in the coil decays by about 1% due to flux creep, the measured sextupole field component may decrease by about 0.1 unit maximum. In real magnets the flux creep contribution depends on the local background field. For this reason an extra factor 2 is used to take into account all uncertainties. Typical snapback amplitudes in LHC dipole magnets are around 2 units. Under characteristic LHC operation conditions, a possible flux creep contribution can not be larger than 10 % of the observed decay amplitude.

5.6 Conclusion

The magnetization behavior of a saturated cylindrical type II superconducting filament in the coil of a superconducting accelerator magnet is analyzed for situations typically appearing during the injection of particles into the machine, and their subsequent acceleration.

As a first step, a method is presented to iteratively derive the field dependence of the critical current density at low field from comparisons between measured and calculated data. The method takes into account the field profile in a filament cross section. The $J_c(B)$ dependence derived for a NbTi strand can be used to calculate the magnetization of a strand at 1.9 and 4.2 K.

As a second step, the current distribution and magnetization in a saturated cylindrical type II superconducting filament with constant critical current density is analyzed for changing external fields perpendicular to the filament's axis, and fitting formulas are adapted to the calculated magnetization data. For fields well above the penetration field, the field dependent critical current density and the fitting formulas allow to describe the behavior of a typical filament in the coil during decay and snapback. The formulas can also be used for similar situations, appearing in many other applications of superconductivity. In the case of a field dependent critical current density $J_c(B)$ and $B \gg B_p(0 T)$ a field dependent value of the penetration field $B_p(B)$ has to be implemented into equation (5.17).

Finally, a rough estimation shows that the contribution of flux creep will not exceed 10% of the typical field decay.

Chapter 6

Decay and Snapback

In order to better understand decay and snapback, an experiment is performed, demonstrating the two principle effects in a single superconducting wire. A round cable is twisted with the superconducting wire in the center and six surrounding copper wires generating the applied field. The model cable is wound around a sample holder and placed in a stand for magnetization measurements. A current applied to the twisted copper wires induces a magnetic field with a spatially periodic pattern along the strand. The influence of different currents is analyzed. The experimental data closely corresponds to the results of model calculations for a superconducting strand in a changing magnetic field. The Hall detector described in section 3 is used to investigate decay and snapback in real accelerator magnets. Measurements are performed on several 15 m long LHC dipoles. Correlations are found between the decay, the snapback and the spatially periodic field pattern in each magnet. After having analyzed the behavior of a single wire and after having performed Hall detector measurements on real magnets, the model is extended to simulate the decay and snapback in a coil. Assumptions are made for realistic current redistributions in the coil, and the response of the filament magnetization is calculated, using the formulas derived in chapter 5. The mechanisms described in section 2 are tested, and the numerical results are compared to the experimental data.

6.1 Demonstration experiment

A demonstration experiment was developed in order to study the interaction between the current redistribution and magnetization during decay and snapback, and to give an example for the mechanisms described in chapter 2. A cable, twisted from an LHC inner strand and six surrounding insulated copper wires, is wound around a sample holder. A cross section of the model cable is shown in figure 6.1a, and the sample in figure 6.1b. The sample is placed in a stand for magnetization measurements at 4.2 K. A description of the magnetization stand is given in section 3. The magnetic moment of the strand is saturated in a background field.

Decay and Snapback

The twisted copper wires are used as a current shell, in order to experimentally simulate the local field changes in the coil of a superconducting accelerator magnet, induced by current redistributions during injection. Three wires on one side are connected with a current of positive, and the other three wires with a current of negative polarity. The currents induce a dipolar field with a spatially periodic pattern in the central strand of the cable.

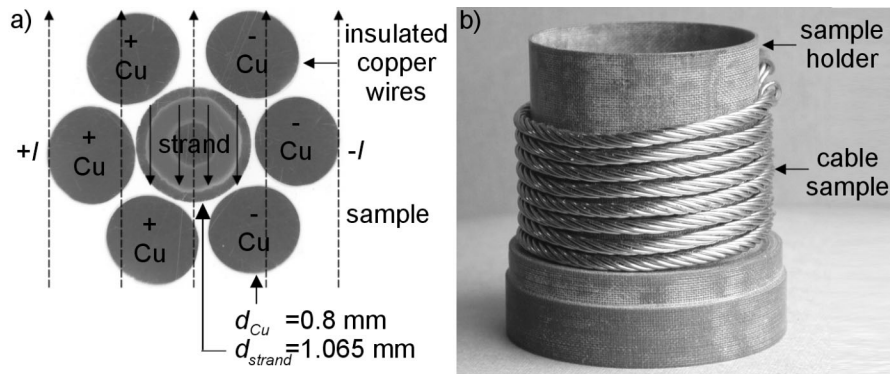


Figure 6.1 a) Cross section of the test cable, wound from an LHC inner strand and 6 surrounding copper wires. The arrows with dotted lines show the background field, and the arrows with full lines show the induced dipolar field in the central strand. b) The twisted cable sample is wound around a sample holder.

Along the length of the strand, the field in a plane parallel to the cross section of the cable periodically changes its angle with respect to the original strand magnetization. The period is equal to the twist pitch length. The induced field changes the magnetization in the central strand. Figures 6.2a, b and c show schematical drawings of the twisted model cable, the induced local field and the reduction of the magnetization in the strand. The magnetization is particularly reduced in regions where its vector is not parallel to the background field. In analogy to the ‘decay’ during injection, the net effect is a decrease of the average magnetization. As soon as the external field is increased, the magnetization is reestablished and the ‘snapback’ is visible.

6.1.1 Decay

Before starting the experiment, the magnetic moment of the strand is saturated in a constant external background field of 0.5 T. In order to analyze the response of the strand magnetization to a current in the copper wires, the current is then increased from 0 to 90 A, and finally cycled back and forth several times, between 90 A and –90 A.

As soon as a current in the copper wires produces an additional applied field in the strand, the average sample magnetization is reduced. Figure 6.3 shows the measured sample magnetization (dotted line) as a function of the current in the copper wires (i.e.

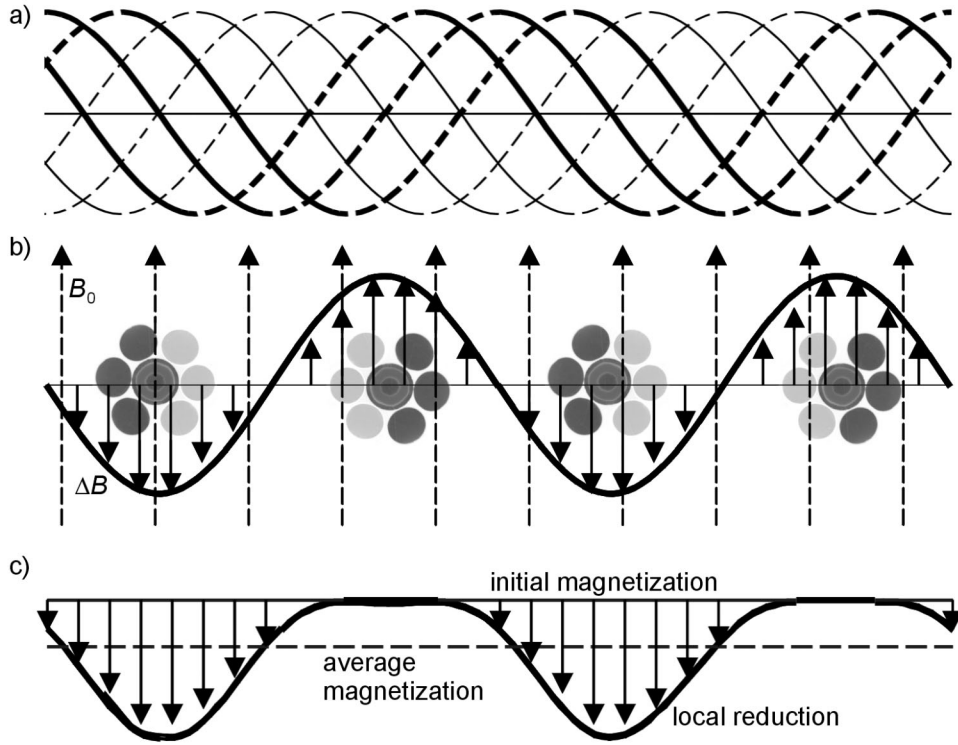


Figure 6.2 a) Schematic drawing of the twisted model cable. The thin and thick lines represent wires carrying currents with positive and negative polarity, respectively. b) The arrows with dotted lines indicate the background field and the arrows with full lines show the projection of the local field change induced by the current in the copper wires. c) The local strand magnetization is especially reduced in regions where the local field change is not parallel to the background field. The net effect is a reduction of the average magnetization (dotted line).

the applied field on the strand). The magnetization is changed in parts of the strand, where the induced field ΔB_d is not parallel to the background field. In parts of the strand, where the current loops of the cable generate a field ΔB_d parallel to the background field, the magnetization follows the up-ramp branch. Within the accuracy of the measurements, the net effect on the central strand is a demagnetization with an exponential dependence on the current I_{copper} in the copper wires and on the induced field ΔB_d :

$$M_{strand}(I_{copper}) = -\gamma\lambda M_p \exp\left(-\frac{I_{copper}}{I_{decay}}\right) = -\gamma\lambda M_p \exp\left(-\frac{\Delta B_d}{B_{decay}}\right). \quad (6.1)$$

M_p is the saturation magnetization of a filament in Bean's Critical State model. λ is the fraction of superconducting material in the cross section of the strand and γ a factor taking into account other effects, such as coupling between the filaments or deviations from the Critical State model due to a finite N -value in equation (5.5). I_{decay} and B_{decay} are constant parameters. $I_{decay} \approx 90$ A corresponds to $B_{decay} \approx 22$ mT. The field induced by the current in the copper wires reduces the magnetization by

Decay and Snapback

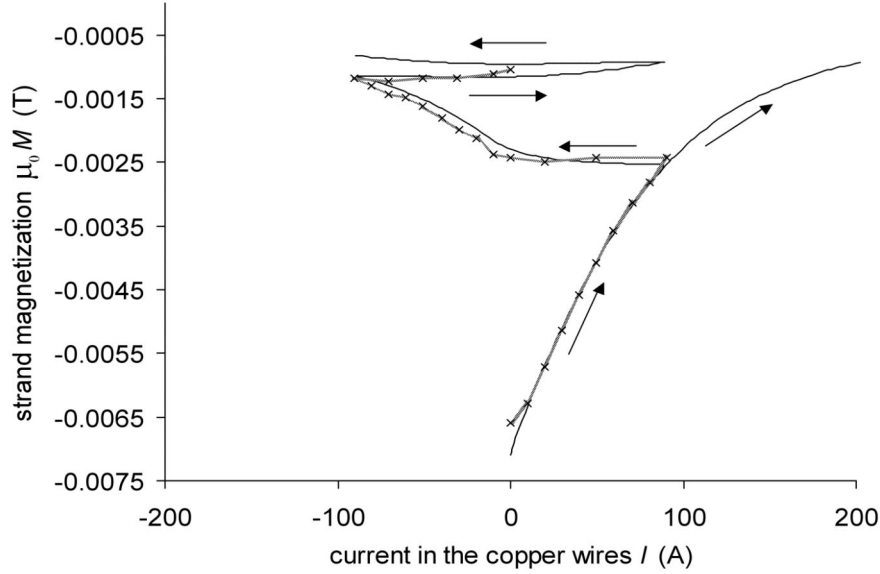


Figure 6.3 The sample magnetization is shown as a function of the current in the copper wires. The dotted curve shows measured data and the full ones are calculated with the algorithm by Brandt [14].

$$\Delta M_{decay}(\Delta B_d) = -\gamma \lambda M_p \left(\exp\left(-\frac{\Delta B_d}{B_{decay}}\right) - 1 \right). \quad (6.2)$$

For small currents, every additional ampere decreases the magnetization by about 0.05 mT. For higher currents (above 50 A) a saturation behavior is clearly visible. For fields much larger than B_p , a critical current dependence can be implemented into equation (6.2), taking $M_p(B, T)$ and $B_p(B, T)$ proportional to $J_c(B, T)$:

$$\Delta M_{decay}(\Delta B_d) = -\gamma \lambda M_{p,0} \frac{J_c(B, 4.2K)}{J_{c,0}} \left(\exp\left(-\frac{\Delta B_d}{B_{decay}} \frac{J_{c,0}}{J_c(B, 4.2K)}\right) - 1 \right), \quad (6.3)$$

where $M_{p,0} = M_p(0.54T, 4.2K)$, $B_{p,0} = B_p(0.54T, 4.2K)$ and $J_{c,0} = J_c(0.54T, 4.2K)$ are constant parameters.

After having reached a maximum of 90 A, the current is reduced again. As a consequence, the saturated half twist pitches of the cable are demagnetized and the previously demagnetized ones are magnetized and saturated again. The average magnetization remains constant, until 0 A is reached. A current of opposite polarity further reduces the magnetization in the currently demagnetized half twist pitches and leaves the magnetization in the saturated ones constant. The average sample magnetization is thus further reduced, but with a considerably smaller slope.

Decay and Snapback

After reaching -90 A, the current is increased another time and, once again, the magnetization remains constant. Repeated measurements show that, with every new increase of the current, the slope is getting smaller and smaller. A demagnetization behavior quite similar to what is measured here has been observed in correction coils of the HERA accelerator [41].

In order to give a precise and quantitative explanation for the behavior observed, the magnetic field along the strand induced by the twisted copper wires has to be taken into account in detail. It changes its direction along the strand, with respect to the direction of the stationary background field. This is illustrated in figure 6.4.

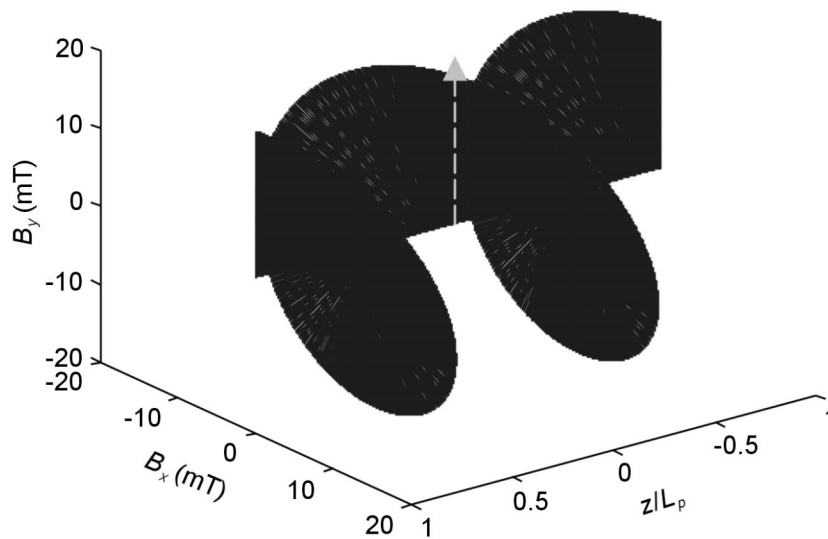


Figure 6.4 Field in the central strand, induced by currents in the copper wires, along a length of two twist pitches. The dashed arrow indicates the direction of the background field.

The behavior is simulated, using the algorithm by Brandt [14] with an implemented $J_c(B)$ dependence at 4.2 K, a grid of 20×20 points, an N -value of 40 in equation (5.5), and taking field changes of equal magnitudes and at 24 different angles with respect to the original magnetization (figure 6.5). The full line in figure 6.3 shows the average magnetization found for the 24 different calculations as a function of the amplitude of the field change. In order to make a comparison with the experimental data, every ampere of current in the copper wires is assumed to induce an average field of 0.245 mT (average field in strand cross section), which is close to the expected value. A demagnetization and a saturation behavior is observed for increasing current and the simulation describes very well the experimental results. In a second calculation, the increase of the demagnetizing field is stopped at 22 mT, which corresponds to a current of 90 A in the copper wires. Afterwards, the demagnetizing field is cycled several times between +22 mT and -22 mT. The simulation shows a behavior similar to the experimental data.

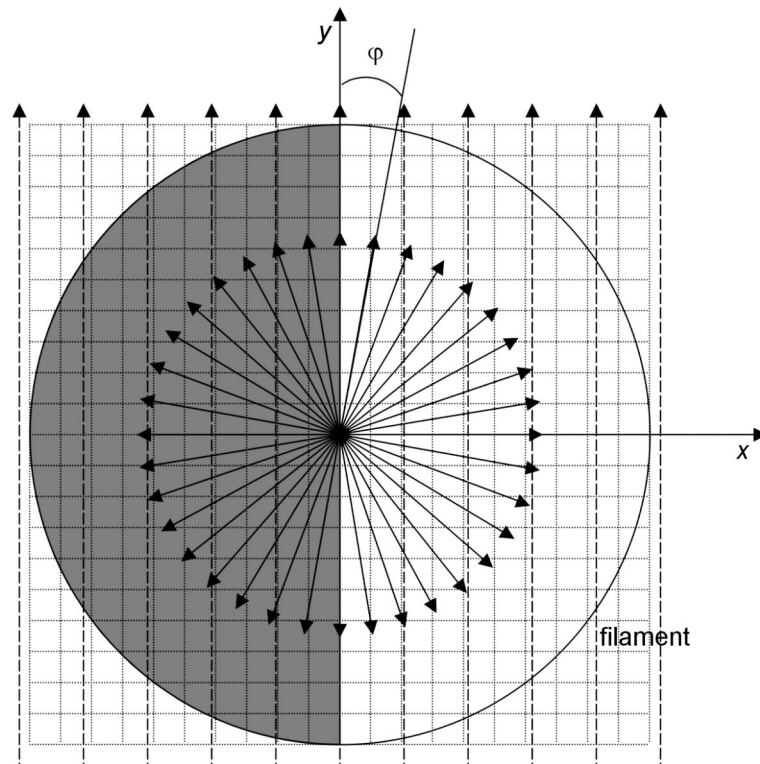


Figure 6.5 Cross section of a filament in a grid of 20×20 points, exposed to a background field in y -direction (dashed arrows) and a field sweep at 24 different angles (full arrows). The dark and white colors represent currents flowing in opposite directions.

6.1.2 Snapback

Figure 6.6 shows a measured hysteresis curve, where the sample magnetization (dotted line) is plotted as a function of the background field. On the up-ramp branch, the ramp is stopped at 0.5 T (see also the magnification in the insert). During a period of constant background field, the current in the copper wires is increased from 0 to 80 A. A demagnetization can be seen very clearly. When ramping up the external field again, the demagnetization is cancelled and the magnetization ‘snaps back’ to the hysteresis curve. With respect to the original hysteresis curve, the one after the snapback is displaced upward by a constant shift of around 0.6 mT. This shift is due to the magnetic moment of a residual uncompensated current loop of the copper wires. Decays and snapbacks are also performed on the down-ramp branch of the hysteresis curve, using demagnetization currents with different polarities. The shifts after the snapbacks are proportional to the currents applied.

Also a simulated snapback (full curve) is shown in figure 6.6, for a field range between 0.4 and 0.6 T, and plotted together with the measured data (dotted curve). A

Decay and Snapback

magnification is displayed in the insert. The demagnetization and subsequent remagnetization during the ramp of the background field are calculated for 24 equidistant angles. The calculated demagnetization amplitudes and snapback phases very well agree with the experimental data.

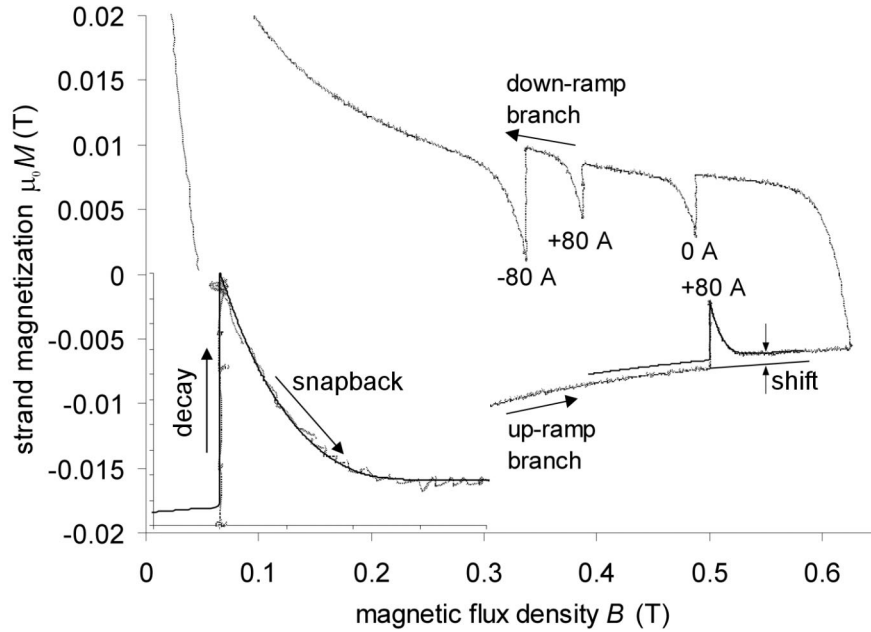


Figure 6.6 The sample magnetization is plotted as a function of the external field. The dotted line shows a measured hysteresis curve with several decays and snapbacks. The full line between 0.4 and 0.6 T displays calculated data, where the ramp was stopped at 0.5 T. The insert shows a magnification.

The snapback curves can be approximated, within the error bars of the measurements, by a sum of the original hysteresis curve $M_0(B)$ and an exponential decay with two free parameters, an amplitude ΔM_{sb} and a snapback penetration field B_{sb} :

$$M(B) = M_0(B) + \Delta M_{sb} \cdot e^{-\frac{B-B_0}{B_{sb}}}, \quad (6.4)$$

where B_0 represents the background field during the demagnetization. If all residual current loops are compensated correctly, the parameter ΔM_{sb} is equal to the decay amplitude ΔM_{decay} , which is given by equation (6.3).

Another experiment is performed on a different cable sample (with a different twist pitch length). In order to analyze correlations between ΔM_{sb} and B_{sb} , snapback measurements are performed at the same background field, but with different demagnetization currents. In figure 6.7 the strand magnetization measured during the snapback is plotted as a function of the background field increase.

Decay and Snapback

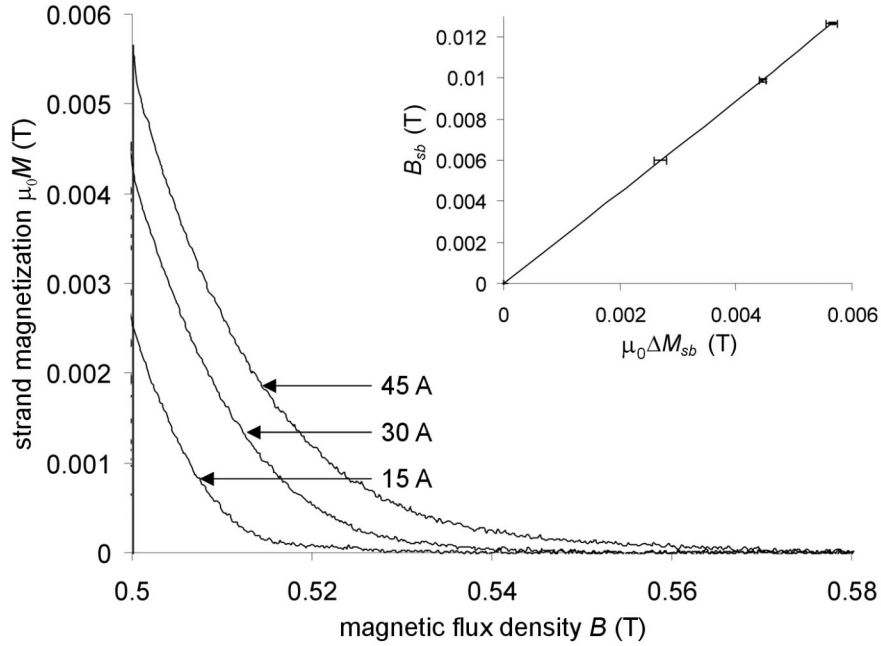


Figure 6.7 For different demagnetization currents in the copper wires, the sample magnetization during decay and snapback is shown as a function of the background field. In each case the demagnetization was performed at $B_0 = 0.5$ T. The insert shows the snapback penetration field B_{sb} as a function of the snapback amplitude ΔM_{sb} . The two parameters are proportional.

The shifts due to uncompensated current loops and the original hysteresis curve $M_0(B)$ are subtracted from the data. The parameters ΔM_{sb} and B_{sb} are determined from exponential fits. The insert shows B_{sb} as a function of the snapback amplitude ΔM_{sb} . A linear correlation with slope $A = 2.2 \pm 0.2$ is observed following

$$B_{sb} = A \cdot \mu_0 \Delta M_{sb}. \quad (6.5)$$

Since the filaments in the strand are saturated at the beginning of each experiment, A is significantly larger than the ratio between the penetration field B_p and the saturation magnetization M_p of a ‘virgin’-filament: $A > B_p/(\mu_0 M_p) = 1.5$. On the other hand, due to the spiral nature of the field induced by the twisted copper wires, A is notably smaller than the ratio between the field change $2B_p$ (to go from the up-ramp branch of the hysteresis curve to the down ramp branch) and the saturation magnetization M_p : $A < 2B_p/(\mu_0 M_p) = 3$.

On the sample from the first experiment snapback measurements are also performed at different levels of the background field B_0 . In each case, the sample is first demagnetized at a constant background field, either by increasing or decreasing the currents in the copper wires by the same amount (80 A). The snapback is then observed during the subsequent increase of the background field. Figure 6.8 shows the measured

Decay and Snapback

magnetization as a function of the background field. The shifts are again due to uncompensated current loops.

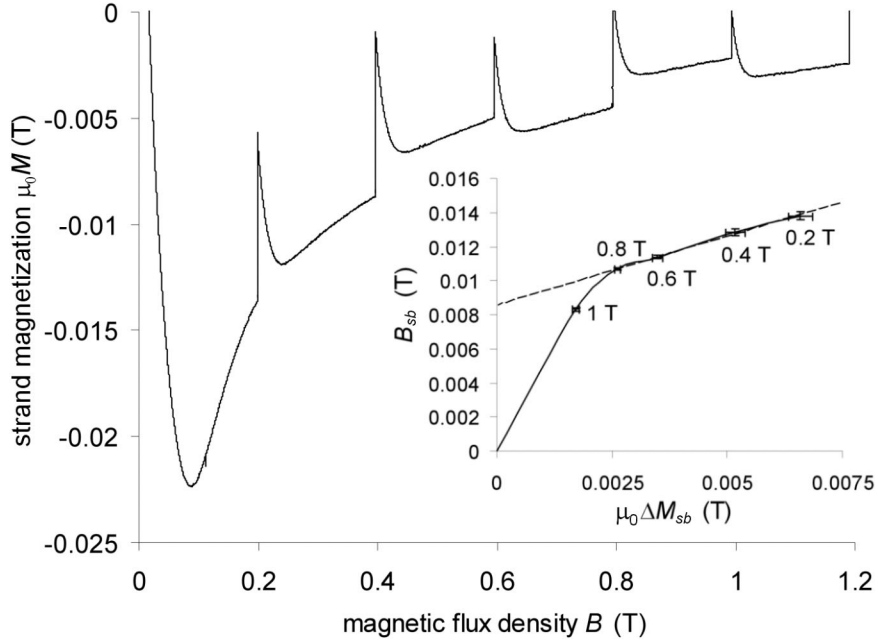


Figure 6.8 The measured sample magnetization is shown as a function of the background field. Snapbacks are performed at different field levels ($B_0 = 0.2, 0.4, 0.6, 0.8$ and 1 T). The insert shows the snapback penetration field B_{sb} as a function of the snapback amplitude $\mu_0\Delta M_{sb}$.

The correlation between the snapback penetration field B_{sb} and the snapback amplitude ΔM_{sb} is shown in the insert. At background fields B_0 between 0.2 and 0.8 T, the parameters are linearly correlated with slope $A = 0.80 \pm 0.05$ and offset $C = (0.0086 \pm 0.0003)$ T following

$$B_{sb} = A \cdot \mu_0\Delta M_{decay} + C. \quad (6.6)$$

$J_c(B)$ decreases with an increasing background field B_0 , and reduces both, the filament penetration field B_p and the saturation magnetization M_p . At the same time, the field change ΔB_d , induced by the current in the copper wires, is equal in all measurements. As long as ΔB_d does not exceed $2B_p$, the snapback penetration field B_{sb} is a linear function of ΔM_{sb} . For background fields B_0 beyond about 0.8 T, the magnetization decay is limited by the exponential saturation in equation (6.3). The snapback penetration field B_{sb} can not exceed $2B_p(B) \sim J_c(B)$. At $B_0 = B_{c,2}$ both parameters converge towards 0.

6.2 Decay and Snapback in real Accelerator Magnets

In order to investigate decay and snapback on real accelerator magnets, a number of measurements is performed on three 15 m long LHC dipoles: magnet 18, magnet 19 and magnet 20 (see section 3.2.1 for details on the magnets). Several parameters in the standard current cycle were varied, and the response of decay and snapback to those variations is measured with the sextupole Hall plate detector described in section 3.

6.2.1 Magnet 18

First a current cycle with a pre-cycle flat-top current of 11500 A is used, and the ramp-rate after injection is varied between 1, 2, 5 and 7 A/s. In figure 6.9, the magnet excitation current is sketched as a function of time.

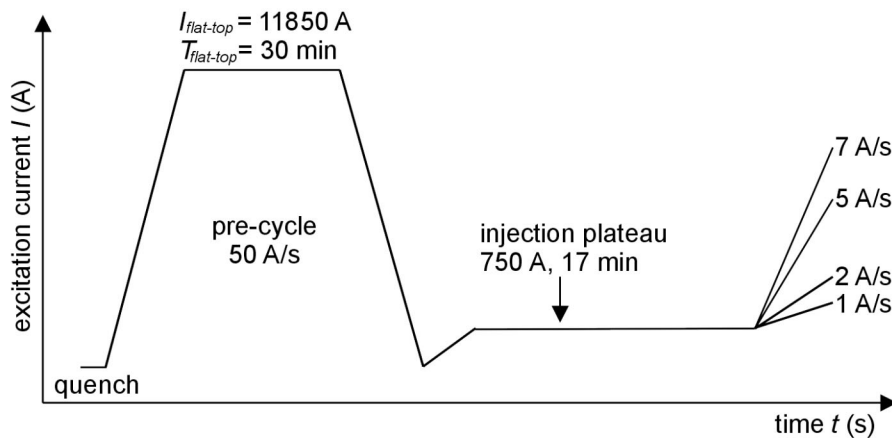


Figure 6.9 Sketch of the excitation current as a function of time. Cycles are performed with ramp-rates after injection of 1, 2, 5 and 7 A/s.

The average measured signal of the two rings during decay and snapback is shown in figure 6.10. Within the accuracy of the measurements, the snapback does not change with the ramp-rate.

The difference between the signals of the two rings is a measure for the local amplitude of the periodic pattern along the axis of the magnet. In figure 6.11, this parameter is traced for a complete operation cycle. The bumps in some parts of the curve are due to the very high ramp-rate of 50 A/s in the pre-cycle.

The pattern amplitude changes during injection. However, after injection, the pattern is not influenced by the snapback. The same behavior is verified also on other magnets and for different injection currents. This indicates that the spatially periodic field pattern is not significantly influenced by the magnetization changes during decay and snapback.

Decay and Snapback

(The assumption is also supported by the observation that snapback amplitudes measured by both rings of the detector are always very similar.)

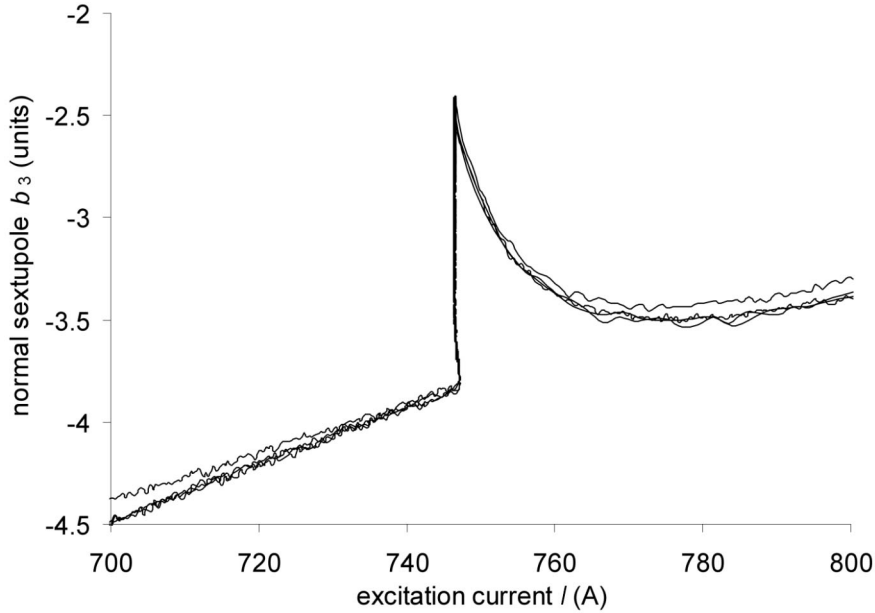


Figure 6.10 The average signal of the two rings in the Hall detector is shown as a function of the excitation current flowing in the magnet. The decay and snapback of the normal sextupole b_3 in magnet 18 are measured for ramp rates after injection of 1, 2, 5 and 7 A/s (injection field ~ 0.54 T).

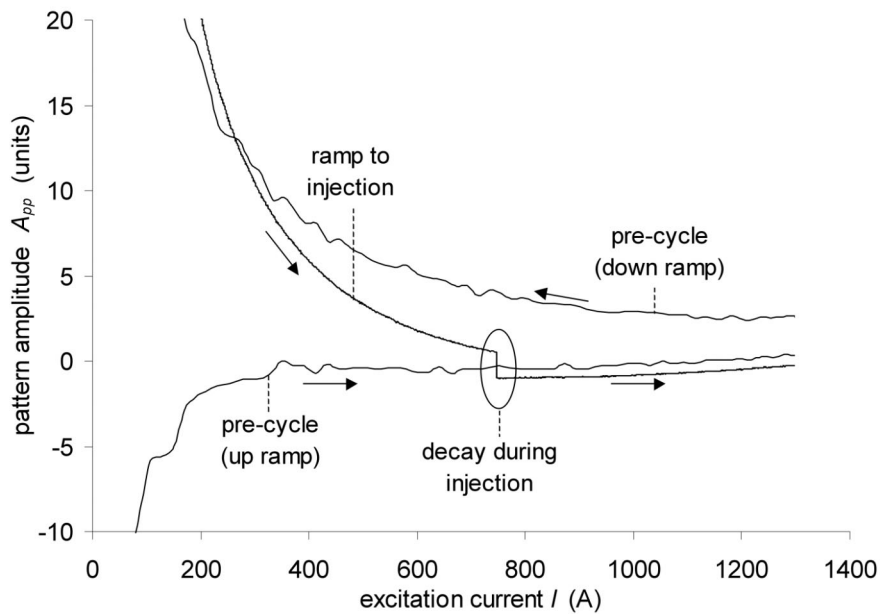


Figure 6.11 The local amplitude A_{pp} of the spatially periodic field pattern in the normal sextupole component is shown as a function of the excitation current during an operation cycle on magnet 18.

6.2.2 Magnet 19

In a second experiment snapback cycles are performed with pre-cycle flat-top currents of 0, 1000, 2000, 4000, 8000 and 11850 A. In each case a flat-top duration of 5 minutes is used. In addition, a measurement is performed with a 5 min pre-cycle at 11850 A and an injection duration of 10000 s. In figure 6.12 the excitation current during all cycles is sketched as a function of the time.

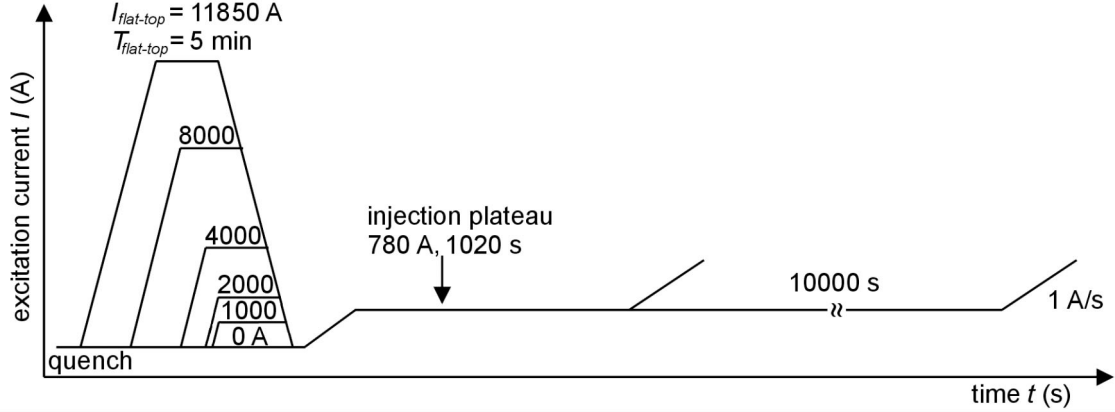


Figure 6.12 Sketch of the excitation current as a function of time. Cycles are performed with different pre-cycle flat-top currents. In an additional measurement a pre-cycle flat-top current of 11850 A, a pre-cycle flat-top duration of 5 min and an injection duration of 10000 s are used.

Figure 6.13 shows the measured normal sextupole b_3 as a function of the excitation current. The snapback curves are affected by current overshoots of the magnet power supply. These overshoots have a similar magnitude and represent a systematic error in the range of about 0.2 units.

The snapback curves can be fitted by the exponential function

$$\Delta b_{3,\Delta M,average}(\Delta B_1) = \Delta b_{3, sb} \exp(-\Delta B_1 / B_{sb}). \quad (6.7)$$

ΔB_1 describes the increase of the dipole field during the snapback. The snapback penetration field B_{sb} and the amplitude $\Delta b_{3, sb}$ in different measurements are correlated. This is demonstrated in the insert. Within the accuracy of the measurements and the fits, the correlation can be described by $B_{sb} = A \Delta b_{3, sb}$. The slope A equals 0.0051 ± 0.0004 T/unit. A multiplication with the ratio between the hysteresis amplitudes of an LHC dipole magnet (with $I_{inj} = 780$ A) and a single strand at 4.2 K and 0.5 T makes the slope comparable to the previously described demonstration experiment (section 6.1.2). One can assume that the average strand in the coil is exposed to a field which is statistically a factor 1.9 smaller than the field B_1 in the center. Dividing by 1.9 yields $A \approx 3$, which is significantly larger than the value of 2.2 obtained in the demonstration experiment.

Decay and Snapback

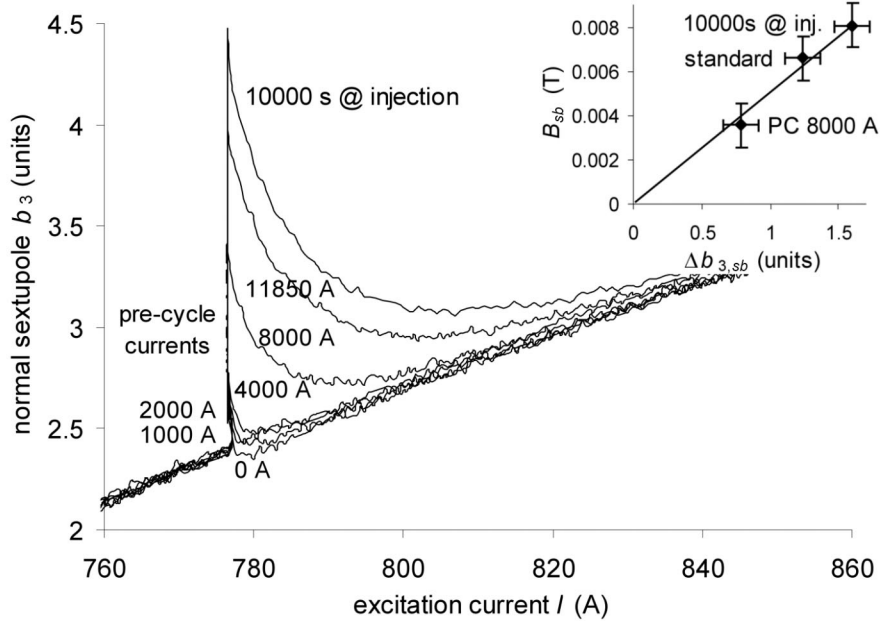


Figure 6.13 The decay and snapback of the normal sextupole component b_3 , measured on magnet 19, is shown as a function of the excitation current, for several cycles with different pre-cycle flat-top currents and one cycle with an injection duration of 10000 s. Three of the snapback measurements are fitted using an exponential. In the insert, the snapback penetration fields B_{sb} are plotted as a function of the snapback amplitude $\Delta b_{3, sb}$.

Figure 6.14 shows the decay of the normal sextupole component b_3 as a function of the time on the injection plateau, for the measurement with a 5 min pre-cycle at 11850 A and an injection duration of 10000 s. The decay can be very well described by a linear combination of three exponentials $\exp(-t/\tau_i)$ with time constants $\tau_1 = 62$ s, $\tau_2 = 358$ s and $\tau_3 = 2123$ s.

In figure 6.15, the magnetization decay Δb_3 during injection is plotted as a function of the measured pattern decay ΔA_{pp} , for all measurements on magnet 19. The spread in the data is mostly due to noise in the power supply.

The final decay amplitudes correspond to the snapback amplitudes in figure 6.13, and for this reason possible errors due to an inaccurate compensation of the spatially periodic field pattern in the Hall detector are neglected. In analogy to the numerical model, and within the accuracy of the measurements, all plots describe the same linear and possibly also symmetric correlation between Δb_3 and ΔA_{pp} :

$$\Delta b_3 = a \left| \Delta A_{pp} \right| + c. \quad (6.8)$$

Decay and Snapback

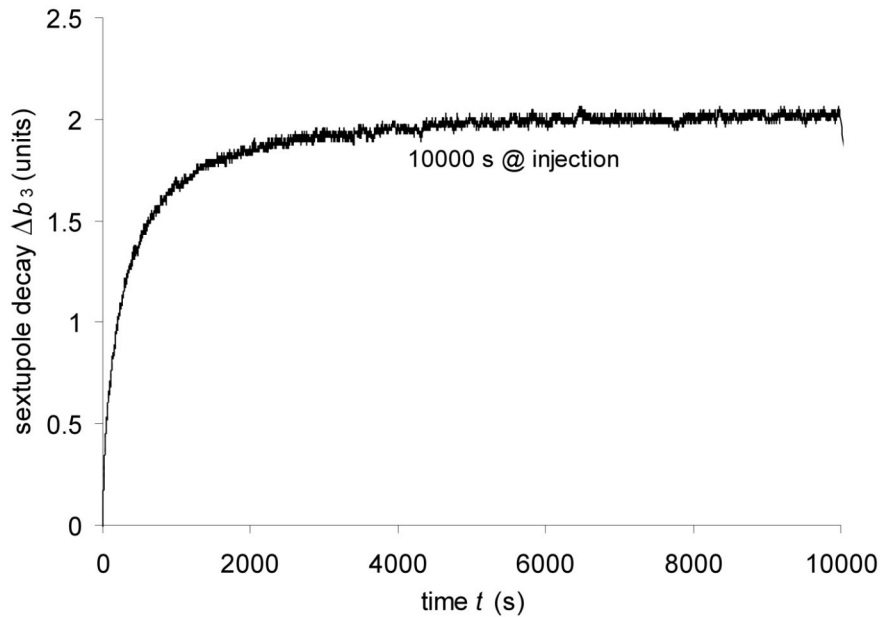


Figure 6.14 The decay of the normal sextupole component b_3 is shown as a function of time on the injection plateau. The measurement was performed on magnet 19 with a 5 min pre-cycle at 11850 A.

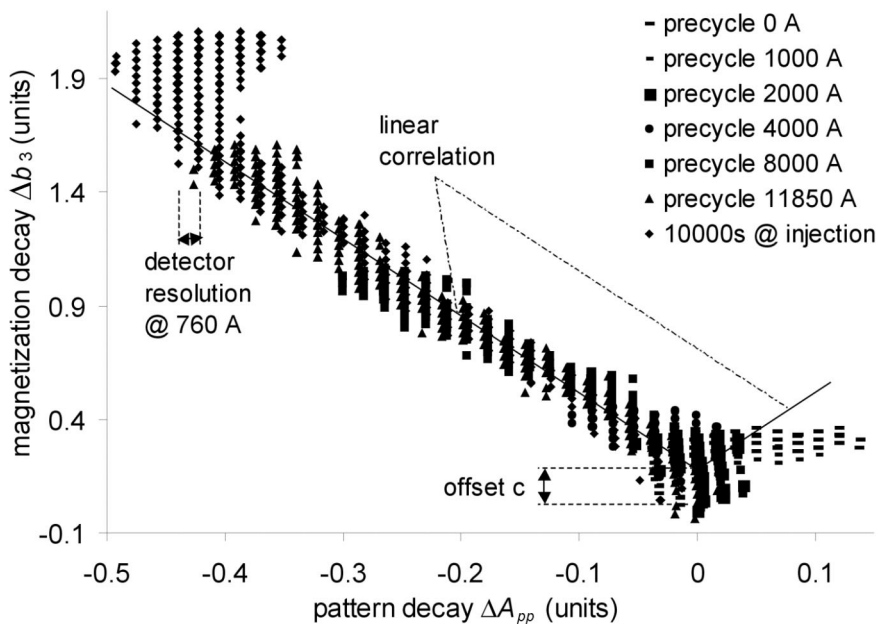


Figure 6.15 For all current cycles performed on magnet 19, the magnetization decay Δb_3 during injection is plotted as a function of the pattern decay ΔA_{pp} .

where a is a proportionality factor. The offset c is in the same range as the current overshoots. After a long time at injection, the 10000 s measurement shows a certain reversal of the pattern decay at a constant magnetization. The reversal indicates the existence of current redistributions with long time constants competing with the original

Decay and Snapback

decay. It is either caused by a demagnetization of the filaments due to successive current redistributions with alternating directions as demonstrated in figure 6.3, or by contributions of different blocks in the coil.

In figure 6.16 the change in pattern amplitude ΔA_{pp} during injection and the snapback amplitude $\Delta b_{3, sb}$ are plotted as functions of the pre-cycle flat-top current. Within the accuracy of the measurements, the change of the periodic pattern amplitude indicates a linear behavior and a change in sign at a flat-top current close to 2000 A. The snapback amplitude indicates a minimum close to 2000 A. For high and for low flat-top currents, linear extrapolations of the snapback data are shown in the figure. Both straight lines cross at a point, which is still inside the error bars and has an offset comparable to c .

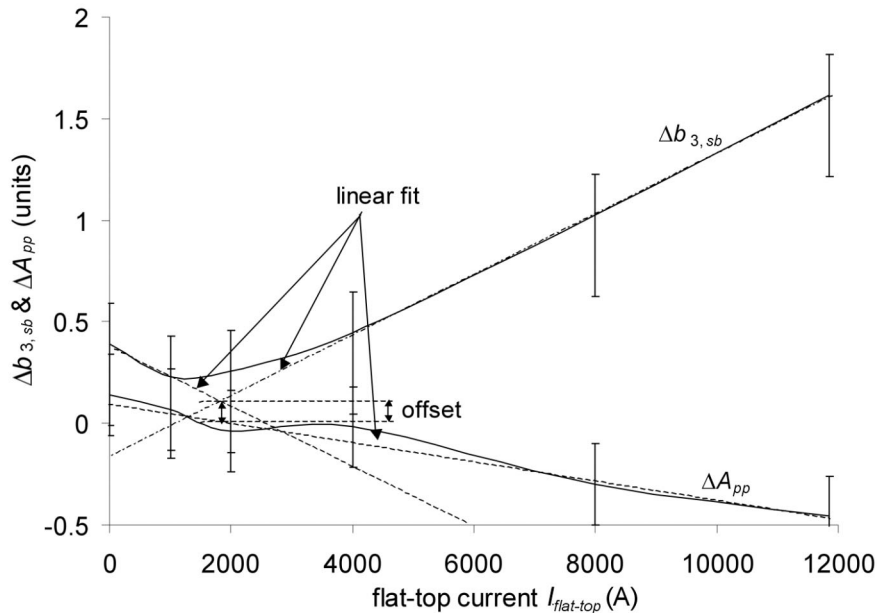


Figure 6.16 The measured snapback amplitude $\Delta b_{3, sb}$ and the measured decay of the periodic pattern amplitude ΔA_{pp} are plotted as functions of the pre-cycle flat-top current, for the cycles performed with different pre-cycle flat-top currents on magnet 19.

6.2.3 Magnet 20

A third run is performed on magnet 20. Cycles with injection currents of 300, 550, 800 and 1050 A are applied. A 30 min flat-top duration is used in the pre-cycle, and the time between the pre-cycle and injection is left constant. In figure 6.17 the excitation current is sketched as a function of the time.

For the cycle with $I_{inj} = 550$ A, the measured sextupole component during decay and snapback is plotted in figure 6.18, as a function of the excitation current. The measurement shows a decay amplitude, which is smaller than the snapback amplitude.

Decay and Snapback

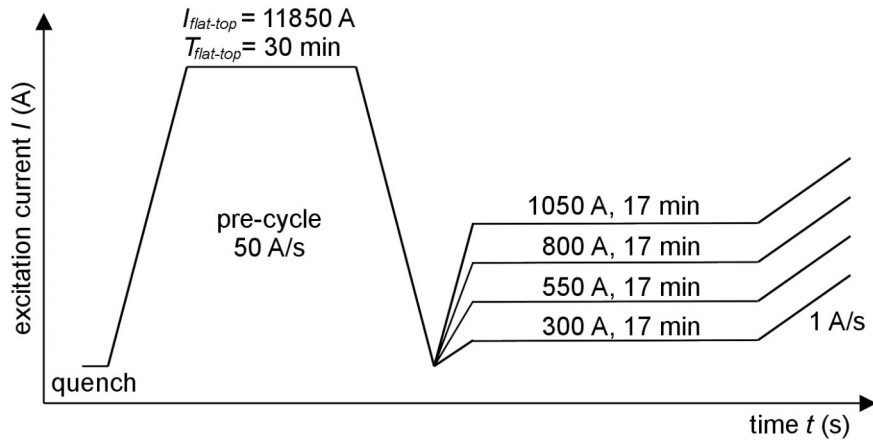


Figure 6.17 Sketch of the excitation current as a function of time. Cycles were performed with different levels of the excitation current during injection.

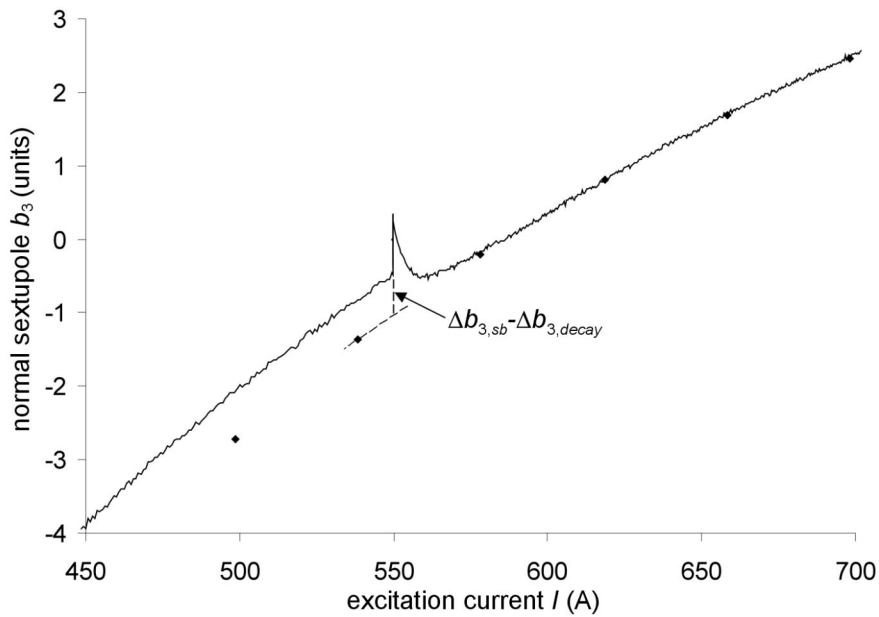


Figure 6.18 The sextupole component measured during the cycle with an injection current of 550 A is plotted as a function of the excitation current. The points mark a measurement with rotation coils, for a cycle without injection plateau.

This peculiarity shows that the change in amplitude of the spatially periodic field pattern is not completely compensated in the sum signal of the two rings in the Hall detector, and still has an impact on the measurement of the normal sextupole. Similar observations were made also during the other measurements on magnet 20. A possible explanation are local gradients of the field pattern along the axis of the magnet.

Decay and Snapback

The non-normalized amplitude of the decay $\Delta B_{3,decay}$ is plotted in figure 6.19, as a function of the injection current. It remains constant within the error bars. At the same time, also the non-normalized change in amplitude of the spatially periodic field pattern was found to be independent of the injection current. For this reason also the snapback amplitudes $\Delta B_{3,sb}$ should be independent of the injection current.

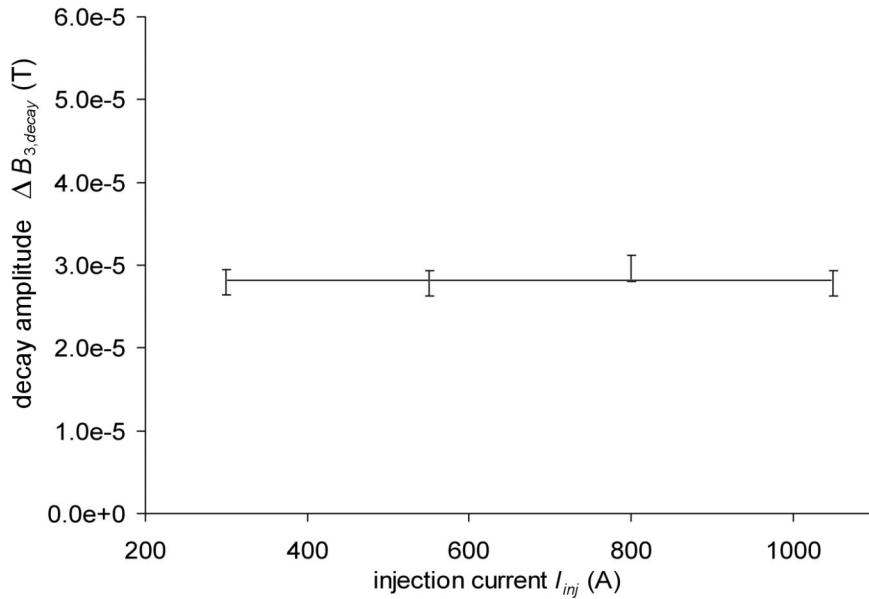


Figure 6.19 On magnet 20 the non-normalized decay amplitude $\Delta B_{3,decay}$ was measured for cycles with several injection currents. The time between the pre-cycle and the injection plateau was held constant.

In figure 6.20 the sextupole decay during injection is plotted as a function of the pattern decay. All measurements follow a linear correlation. The impact of the uncompensated pattern decay on the sextupole decay affects all measurements in the same way, since the non-normalized change in pattern amplitude does not depend on the injection current.

In comparison to the previous experiment, the detector rings have a different position with respect to the phase of the periodic pattern. For this reason the sign and magnitude of ΔA_{pp} differ from figure 6.15. Magnet 20 is powered by a power supply with improved control. No significant overshoots are observed, and the noise remains small. The measurements at different injection currents have slightly different small offsets c (e.g. ~ 0.05 units @ 800 A), which mainly appear during the first 10 s of the decay. Apart from that, within the accuracy of the measurements, no other significant indication towards flux creep is found.

Decay and Snapback

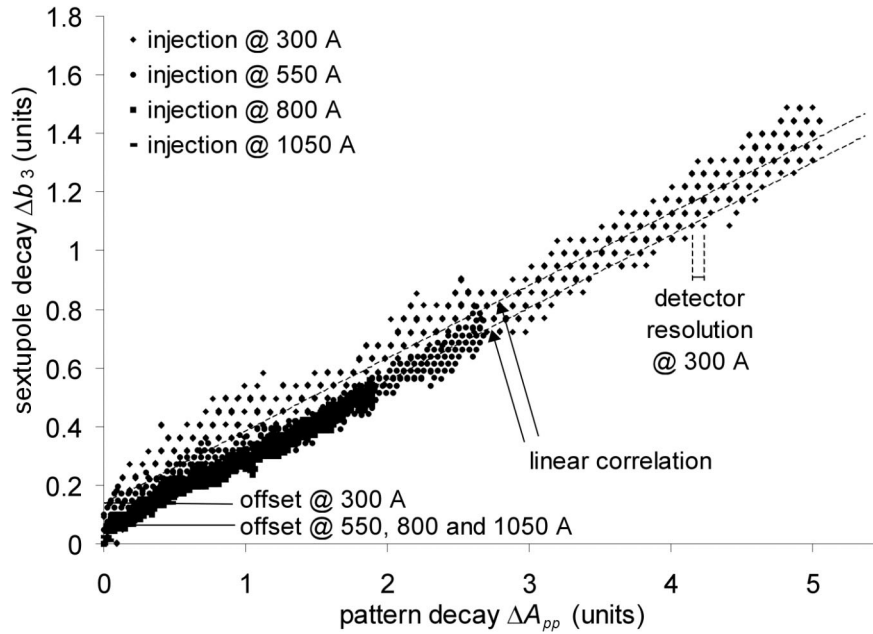


Figure 6.20 The magnetization decay Δb_3 during injection is plotted as a function of the pattern decay ΔA_{pp} , for measurements at different injection currents performed on magnet 20.

Two additional cycles are performed on the same magnet, with and without a 5 min pre-cycle, during 10000 s at an injection current of 760 A. A third measurement has a 5 min pre-cycle with a flat-top current of 8000 A and an injection duration of 1020 s.

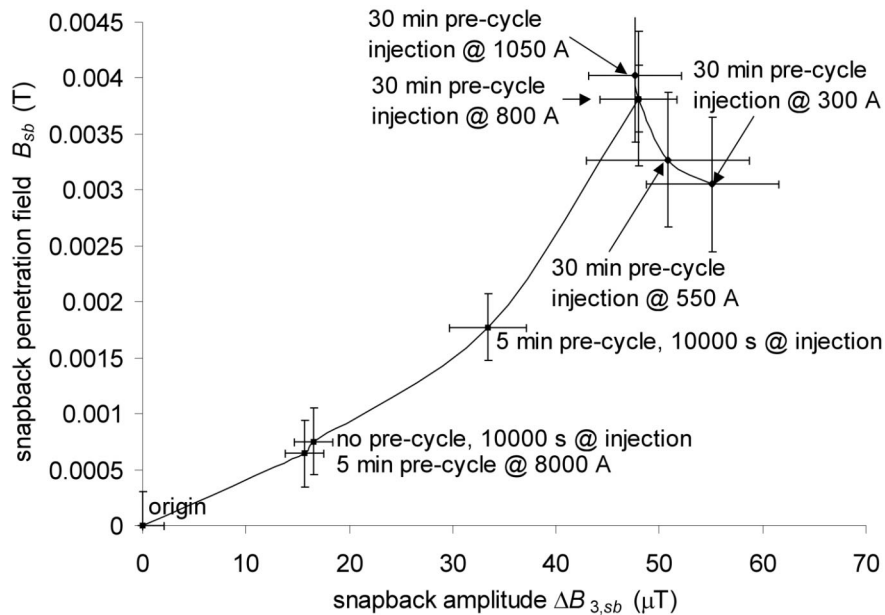


Figure 6.21 The snapback penetration field B_{sb} is plotted as a function of the non-normalized snapback amplitude $\Delta B_{3, sb}$, for all measurements on magnet 20.

Decay and Snapback

In figure 6.21 correlations between the snapback penetration field B_{sb} and the snapback amplitude $\Delta B_{3, sb}$ are shown for all measurements. Two possibly distinct types of behavior are observed. Measurements performed at the same injection current all obey a similar correlation. However, a different correlation is observed, if the injection level changes. From the physical point of view, the first correlation at a constant injection current can be explained by the dependence of BICCs in the coil on the excitation history of the magnet. At different injection currents, however, the non-normalized snapback amplitudes and penetration fields only differ within the error bars. From the constant decay amplitudes in figure 6.19 and the constant pattern decay one would expect constant snapback amplitudes. The snapback penetration fields differ by about 1 mT and are eventually due to the $J_c(B)$ dependence of the superconducting material.

6.3 Model for decay and snapback in a magnet

After having demonstrated the principle mechanism of decay and snapback in a single strand, the analysis is now extended to the behavior of the coil in a dipole magnet. A model for the coil is presented, and numerical results are compared to the Hall detector measurements above. The model takes into account twisted cables as well as the positions of all strands for several different cross sectional slices of the coil. All slices are perpendicular to the axis of the magnet, and placed at equal distances within a little more than one twist pitch length of the cable. The simulations presented in this chapter are performed for 31 slices along an overall length of 0.015 m, which is a little more than one cable twist pitch. A picture is shown in figure 6.22.

The computer program consists of about 450 lines of Matlab code. On a 1 GHz computer a single run needs about one hour of computing time.

The origin of the coordinate system is placed in the center of the first slice cross section. The axis-names x , y and z determine three perpendicular directions: the horizontal, the vertical and the axis of the magnet. In each turn i of the coil, the cable has a different phase Φ_i with respect to the twist pitch. The definition of the coordinate system corresponds to figure 1.4 and the phases Φ_i are demonstrated in figure 6.23. The phases strongly vary from magnet to magnet and are generally unknown. They add a large amount of freedom to the system. In the model, different alternatives are simulated. All phases are either set to zero, shifted by 180° from turn to turn, or random.

An approximation is calculated for the field in the coil during injection, disregarding the magnetization contribution, assuming a homogeneous distribution of the current among the strands, and taking each strand as a straight and infinite current line. All filaments in

Decay and Snapback

the coil are assumed to be saturated, and the magnetization is taken proportional to the $J_c(B)$ dependence of the strands and anti-parallel to the vector of the local field in the coil.

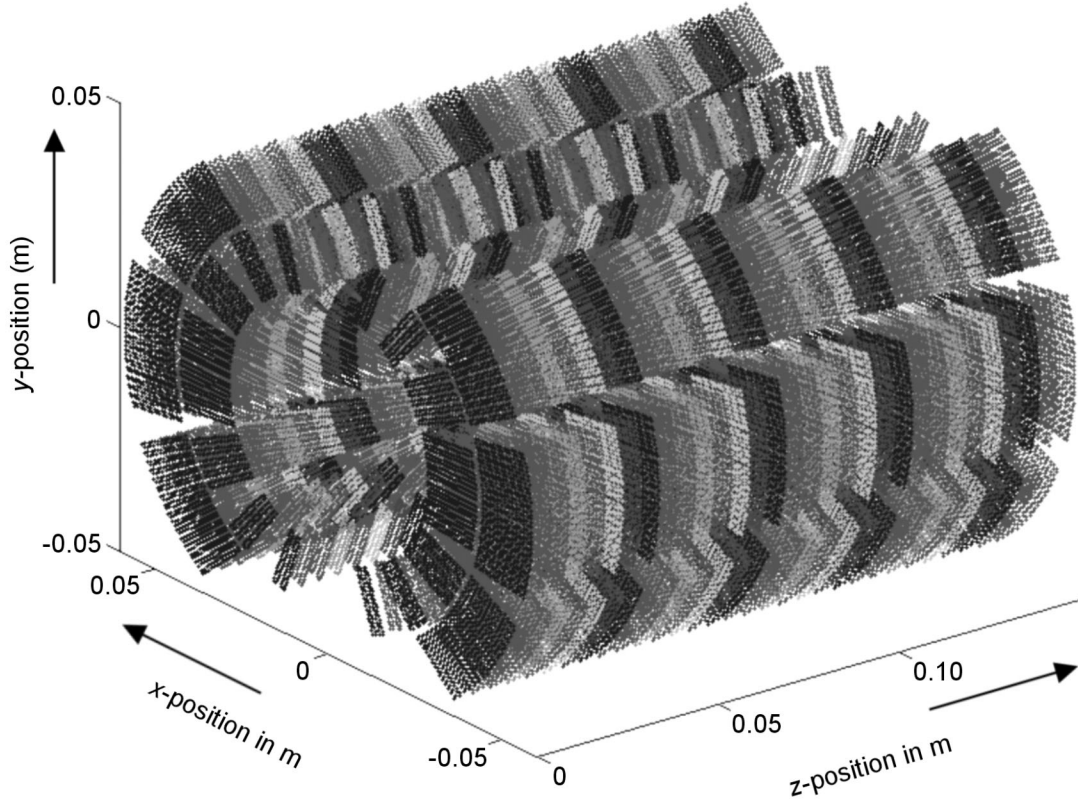


Figure 6.22 The strand positions in 31 cross sectional slices of an LHC-type of dipole magnet are plotted inside a three-dimensional coordinate system. The slices are located between $z = 0$ and $z = 0.150$ m, separated by gaps of 0.005 m.

The currents in the strands redistribute during injection. In the model, assumptions are made for typical values of the current change ΔI_k in every strand. The induced field change $\Delta \mathbf{B}_{\Delta}(x,y)$ and the change of the current contribution to the sextupole field component $\Delta b_{3,\Delta}$ are calculated for every slice. The formulas developed in chapter 5 are used in order to calculate the impact of these field changes on the coil magnetization $\Delta \mathbf{M}_{\Delta}(x,y)$ and the change of the magnetization contribution $\Delta b_{3,\Delta M}$ to the sextupole field component.

After the end of injection, the field $\mathbf{B}(x,y)$ in the coil is increased for particle acceleration. The formulas in chapter 5 are used to calculate the snapback as a function of the absolute dipole field $B_1 = |\mathbf{B}(0,0)|$, for both, the coil magnetization $\Delta \mathbf{M}_{sb}(x,y)$ and the sextupole component $\Delta b_{3,sb}$.

Decay and Snapback

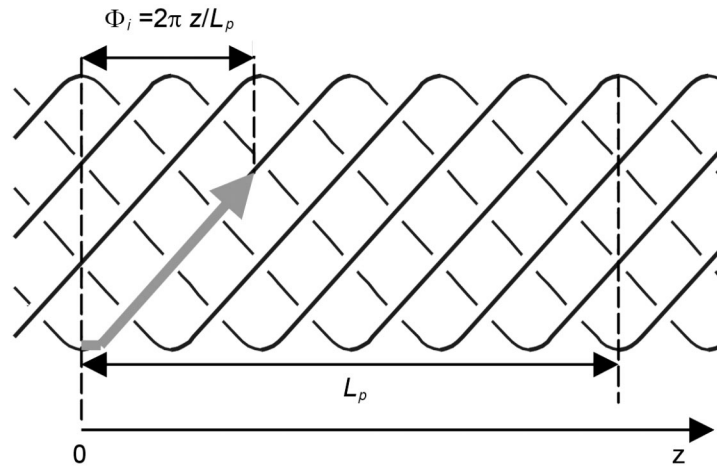


Figure 6.23 Sketch of a Rutherford-type cable along the z -axis. The phases Φ_i define the positions of all strands in a turn at a certain length z along the twist pitch of the cable.

6.3.1 Details of the model

6.3.1.1 Strand positions

The geometric parameters of the LHC dipoles are well known and the positions of the cables in the cross section of a coil can be taken from sources like [22]. The cross section of the cable in each turn ($i=1\dots 160$) can be represented by a keystone quadrangular envelope. Its four corners ($x_{corner}(c,i), y_{corner}(c,i)$), $c=1\dots 4$, are taken from the source

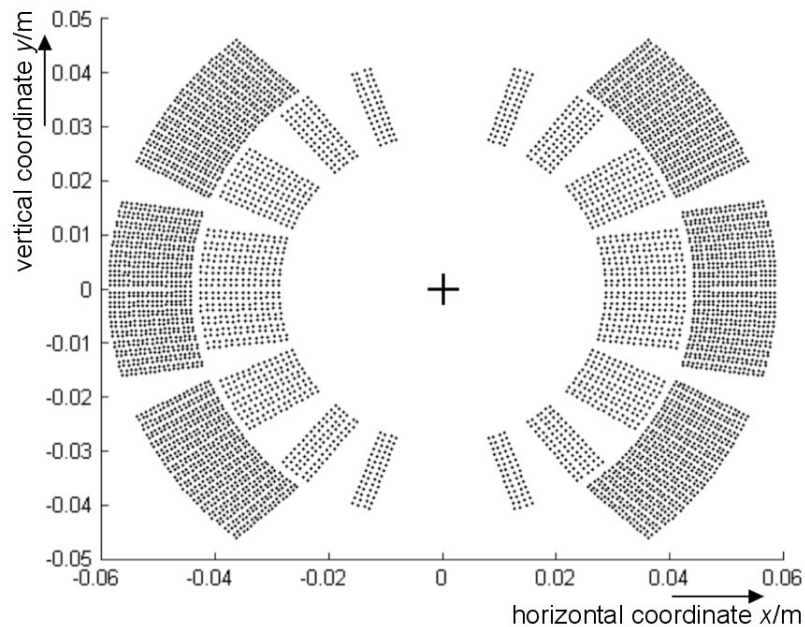


Figure 6.24 Calculated strand positions are shown in the cross section of an LHC dipole coil across the xy -plane.

referenced above. However, the Rutherford-type cables are twisted along the magnet axis, and the phases of twisting generally differ from turn to turn. A particular challenge is to determine the precise position of each strand for a cross sectional cut at an arbitrary length z along the magnet's axis. An approach by Bottura [13] is used, where the twisting of the Rutherford-type cable is taken into account. In figure 6.24 calculated strand positions are shown in the cross section of an LHC dipole in the xy -plane.

6.3.1.2 Calculation of the field induced by the currents in the strands

In this sub-section formulas are presented for the calculation of the magnetic field in the coil. The cable twist pitch ($L_{p,inner} = 115$ mm, $L_{p,outer} = 105$ mm) in the LHC dipoles is comparable to the diameter of the coil cross section. The strand currents I_k follow the zig-zag path along the strands, and induce a magnetic field, which has to be calculated as a three dimensional Biot-Savart integral over the entire coil:

$$\vec{B}(\vec{r}) = \frac{\mu_0}{4\pi} \int d^3r' \frac{j(\vec{r}') \times (\vec{r} - \vec{r}')}{|\vec{r} - \vec{r}'|^3}. \quad (6.9)$$

The current density in the turns of the coil is assumed parallel to the axis of the magnet:

$\vec{j}(\vec{r}) \approx j(\vec{r})\vec{e}_z$. This yields:

$$\vec{B}(\vec{r}) = \frac{\mu_0}{4\pi} \int_{-\infty}^{\infty} \int_{-\infty}^{\infty} dx' dy' \frac{\begin{pmatrix} -(y-y') \\ (x-x') \end{pmatrix}}{\sigma(x, y, x', y')^3} \int_{-\infty}^{\infty} dz' j(x', y', z') f_{\sigma(x, y, x', y')}(z-z'), \quad (6.10)$$

with

$$f_{\sigma}(z) = \left| 1 + \frac{z^2}{\sigma^2} \right|^{-3/2} \quad (6.11)$$

and

$$\sigma(x, y, x', y') = \sqrt{(x-x')^2 + (y-y')^2}. \quad (6.12)$$

The integration of equation (6.10) along the axis of the magnet can thus be expressed as a mathematical convolution of the current density with $f_{\sigma}(z)$. As a result, the effective current density is smoothed along the z -axis with a full width half maximum of 2σ . In figure 6.25 examples of $f_{\sigma}(z)$ are plotted as a function of z , for different values of σ .

The field in the coil induced by currents in adjacent strands is smoothed along the z -axis with a full width half maximum of about $2\sigma = 1$ mm (figure 6.25d). Likewise, the field in the coil induced by currents at 1 cm distance is smoothed with $2\sigma = 1$ cm (figure 6.25c).

Decay and Snapback

In the center of the coil ($x = y = 0$), the field induced by currents in the inner layer is smoothed along the z -axis with a full width half maximum 2σ between 5.5 cm and 8.8 cm (figure 6.25b).

The field in the center, induced by currents in the outer layer is smoothed with a full width half maximum 2σ between 8.8 cm and 12 cm (figure 6.25a), which is similar to the twist pitch length of the cable. For this reason, and due to the large distance of the outer layer from the center, measurements of the spatially periodic pattern in LHC dipoles reveal a pattern wavelength equal to the twist pitch in the inner layer [50].

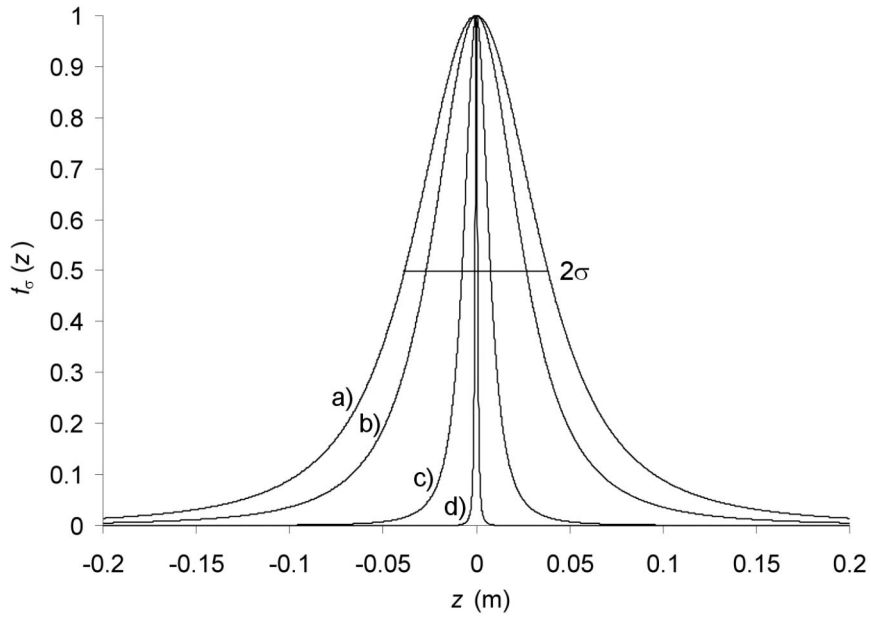


Figure 6.25 For different values of σ , $f_d(z)$ is plotted as a function of z . a) $\sigma = 0.05$ m, b) $\sigma = 0.035$ m, c) $\sigma = 0.01$ m and d) $\sigma = 0.001$ m.

In order to limit the necessary computing times to the time frame of this thesis, the model presented here is based on a two dimensional integration in the xy -plane. The impact of the integration along the z -axis is treated analytically. This approach is legitimated by the fact that only the field integral along the z -axis has a significant impact on the accelerator performance. The response of the strand magnetization is relatively linear for small changes of the local field in the coil. Errors are assumed to average out in the integrated values.

For field calculations, the coordinates of a point in the coil cross section are expressed in complex notation: $\xi = x + iy$. The strand positions in a slice are, thus, described by $\xi_k = x_k + iy_k$, with a strand index k . The strands are assumed to be locally straight, and

Decay and Snapback

parallel to the z -axis. The Biot-Savart integral is reduced to two dimensions in the xy -plane, and the field is expressed as a sum over straight current lines I_k :

$$B_l(\xi) = B_y(\xi) + iB_x(\xi) = \frac{\mu_0}{2\pi} \sum_k I_k \left\{ \frac{1}{\xi - \xi_k} + \frac{\frac{\mu_r - 1}{\mu_r + 1}}{\xi - \frac{R_{yoke}^2}{\xi_k^*}} \right\}. \quad (6.13)$$

If ξ equals a strand position ξ_n , the terms in equation (6.13) are only summed for $k \neq n$. The second term in the bracket takes into account image currents in the iron yoke of the magnet. R_{yoke} is the inner yoke radius and μ_r its magnetic permeability. In practice, R_{yoke} is around 0.0977 m and at low field μ_r is in the order of 2000. In figure 6.26 the calculated field B is shown in a typical LHC dipole coil at injection, with all strand currents set to $I_k = 739 \text{ A} / N_s(i)$. ($N_s(i)$ is the number of strands in turn i).

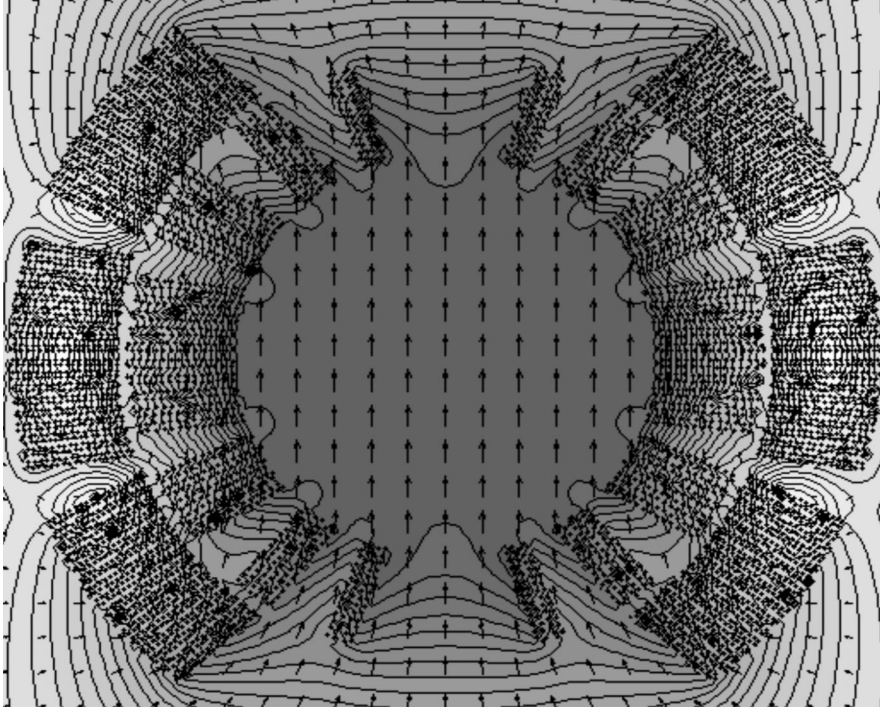


Figure 6.26 The calculated field in an LHC dipole at injection is shown along a coil cross section in the xy -plane. The arrows represent the field vectors and the equipotential lines follow equal levels of the absolute field. Light grey indicates low fields and the dark grey represents a field level of about 0.54 T.

The multipole components b_n and a_n are obtained from a Taylor expansion of equation (6.13). The normal sextupole component is

Decay and Snapback

$$b_{3,l} = -\frac{\mu_0 R_{ref}^2 10^4}{2\pi B_1} \sum_k I_k \operatorname{Re} \left\{ \frac{1}{\xi_k^3} + \frac{\frac{\mu_r - 1}{\mu_r + 1}}{\left(\frac{R_{yoke}^2}{\xi_k^*} \right)^3} \right\}. \quad (6.14)$$

6.3.1.3 Penetration field and coil magnetization

At injection, all superconducting filaments in the coil are assumed to be saturated. The assumption is not generally fulfilled for certain strands in block 1, where the amplitude of the background field is lower than the filament penetration field. At injection, this is the case for an estimated 50 out of 5280 strands in the coil.

Also the self-field in the filaments is neglected. The filament penetration field and the magnetization amplitude of all strands is taken proportional to the field dependent critical current density at 1.9 K.

The field in the coil is essentially proportional to the transport current in the cable. At the low injection field also the magnetization contributes, especially in parts of block 1 and 2. However, in the inner layer, which mainly contributes to the field in the center of the coil, the local field due to the transport current is several times larger than the magnetization contribution. For this reason, during ramps, the direction of the field vectors in the model coil is assumed not to change significantly.

The magnetization vectors of all strands are assumed anti-parallel to the vectors of the local background field:

$$B_{p,k} = \frac{J_c(|B(\xi_k)|)}{J_c(0.54 T, 1.9 K)} B_{p,inner,outer}(0.54 T, 1.9 K), \quad (6.15)$$

$$M_k = -\frac{B(\xi_k)}{|B(\xi_k)|} \frac{J_c(|B(\xi_k)|)}{J_c(0.54 T, 1.9 K)} M_{inner,outer}(0.54 T, 1.9 K). \quad (6.16)$$

The parameters $B_{p,inner}(0.54 T, 1.9 K)$, $B_{p,outer}(0.54 T, 1.9 K)$, $M_{inner}(0.54 T, 1.9 K)$ and $M_{outer}(0.54 T, 1.9 K)$ describe the filament penetration field and strand magnetization in the inner or outer layer of the coil at a temperature of 1.9 K and for an applied field of 0.54 T. The calculated absolute magnetization is shown in figure 6.27, along a cross section in the xy -plane. The accuracy of the values exceeding 30 mT in the peaks of block 1 is very limited, since many strands are not saturated. However, as already mentioned, this is only the case for about 50 out of 5280 strands in the coil.

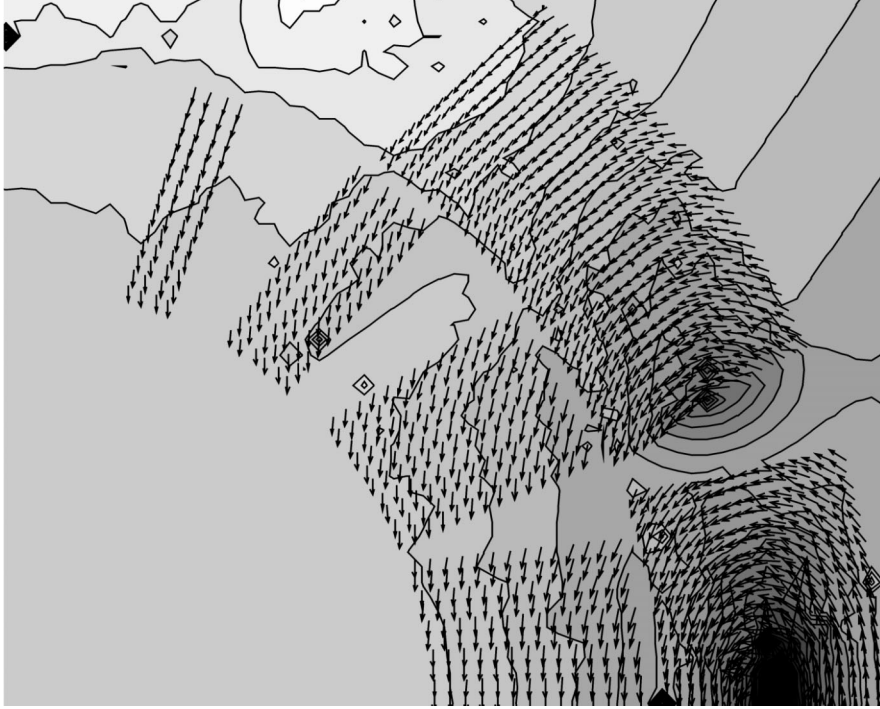


Figure 6.27 The calculated magnetization is shown along a quarter cross section in the xy -plane. The arrows represent magnetization vectors, and the equipotential lines follow equal levels of the (4th route) of the absolute strand magnetization. Light grey indicates a low, and dark grey a high strand magnetization. For simplicity the equipotential lines and the greyscale also show extrapolated values outside the blocks. In a real coil the magnetization outside the blocks is zero.

6.3.1.4 Magnetization contribution to the field components in the center of the coil

The contribution of the strand magnetization to the components of the magnetic field in the center of the coil is given by:

$$b_{n,M} = -\frac{\mu_0 n R_{ref}^{(n-1)} 10^4}{2B_1} \sum_k R_k^2 \operatorname{Re} \left\{ \frac{M_k^*}{\xi_k^{(n+1)}} - \left(\frac{\mu_r - 1}{\mu_r + 1} \right) \frac{\xi_k^{*(n-1)} M_k}{R_{yoke}^{2n}} \right\}, \quad (6.17)$$

$$a_{n,M} = -\frac{\mu_0 n R_{ref}^{(n-1)} 10^4}{2B_1} \sum_k R_k^2 \operatorname{Im} \left\{ \frac{M_k^*}{\xi_k^{(n+1)}} - \left(\frac{\mu_r - 1}{\mu_r + 1} \right) \frac{\xi_k^{*(n-1)} M_k}{R_{yoke}^{2n}} \right\}. \quad (6.18)$$

For the normal sextupole harmonic, this yields:

$$b_{3,M} = -\frac{\mu_0 3 R_{ref}^2 10^4}{2B_1} \sum_k R_k^2 \operatorname{Re} \left\{ \frac{M_k^*}{\xi_k^4} - \left(\frac{\mu_r - 1}{\mu_r + 1} \right) \frac{\xi_k^{*2} M_k}{R_{yoke}^6} \right\}. \quad (6.19)$$

Decay and Snapback

6.3.1.5 Field changes induced by current redistributions ΔI_k among the strands

In all allowed field components, the decay during injection has so far only been observed experimentally as an average reduction of the absolute hysteresis amplitude. For this reason, the magnetization decay in the different blocks of the coil has to be approximately proportional to the absolute local magnetization, since otherwise some field components could also experience negative decays.

In the model presented here, the diffusion of boundary induced coupling currents during injection is taken into account by a current imbalance with amplitude $\Delta I_{turn}(i)$ in each turn ($i = 1, \dots, 160$) of the coil. The current imbalance is assumed to obey a *cos*-distribution among the strands. The current change ΔI_k in each strand k of turn i can thus be expressed as:

$$\Delta I_k = \Delta I_{turn}(i) \cdot \cos\left(2\pi \frac{(k - k_i + 1)}{N_s(i)}\right), \quad (6.20)$$

where k_i represents the strand with the lowest index in turn i . Typical values for $\Delta I_{turn}(i)$ range from 0.5 A to 5 A. An example is shown in figure 6.28. For the simulation, a constant amplitude $\Delta I_{turn}(i) = \Delta I_{turn}$ is assumed in all turns.

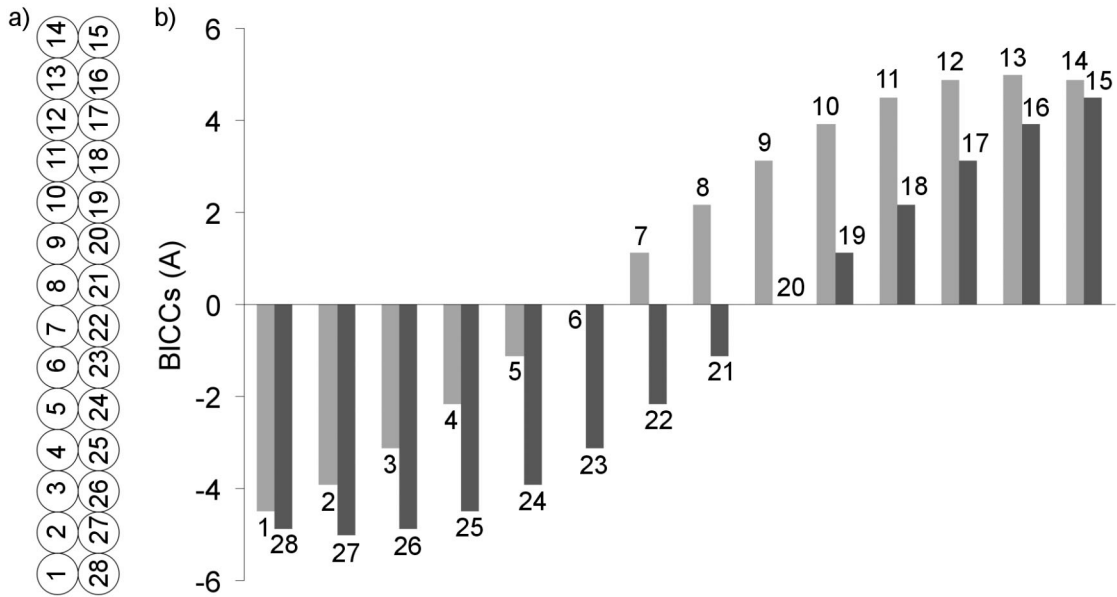


Figure 6.28 a) Numbering of the strands in the cross section of an LHC inner layer dipole cable. b) Example for the distribution of BICCs among the strands ($\Delta I_{turn} = 5$ A).

Due to the contact and adjacent resistances in the Rutherford-type cable, the strands in each turn are in electrical contact. Previous investigations [34], [55] have shown that current imbalances in the cable are especially induced in parts of the coil with strong

Decay and Snapback

inhomogeneities in the contact resistances and the field sweep rate. In the model described here, the current changes ΔI_k remain constant within a few cable twist pitches along the magnet's axis. This is generally the case in the central part of the magnet. The field change in the coil due to the current redistributions ΔI_k is:

$$\Delta B_{\Delta}(\xi) = \frac{\mu_0}{2\pi} \sum_k \Delta I_k \left\{ \frac{1}{\xi - \xi_k} + \frac{\frac{\mu_r - 1}{\mu_r + 1}}{\xi - \frac{R_{yoke}^2}{\xi_k^*}} \right\}. \quad (6.21)$$

As an example, figure 6.29a and b show the direction of the vectors of the local field B_l and the field change ΔB_{Δ} in each strand of block 6 along a cross section in the xy -plane, respectively (all phases Φ_i are assumed to be zero).

Equation (6.14) allows to calculate the contribution of the redistributed currents to the normal sextupole field component in the center of the coil:

$$\Delta b_{3,\Delta} = -\frac{\mu_0 R_{ref}^2 10^4}{2\pi B_1} \sum_k \Delta I_k \operatorname{Re} \left\{ \frac{1}{\xi_k^3} + \frac{\frac{\mu_r - 1}{\mu_r + 1}}{\left(\frac{R_{yoke}^2}{\xi_k^*} \right)^3} \right\}. \quad (6.22)$$

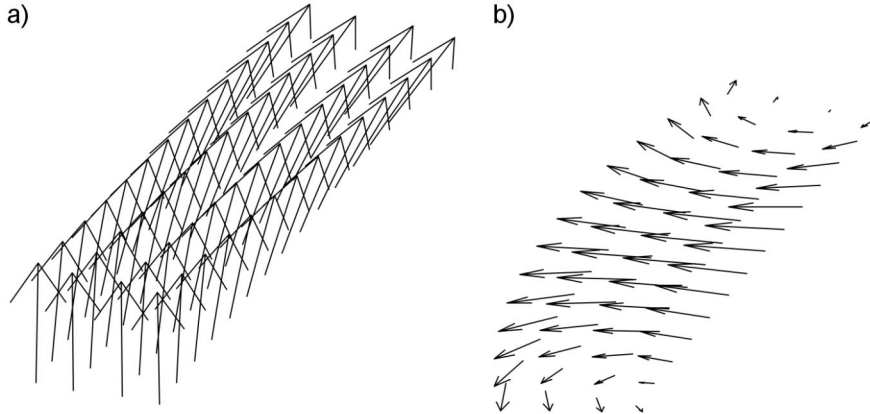


Figure 6.29 The direction of the vectors of a) the local field B_l and b) the field change ΔB_{Δ} in each strand of block 6 is shown along a cross section in the xy -plane. (All phases Φ_i are assumed to be zero.)

6.3.1.6 Magnetization changes induced by field changes $\Delta B_{decay}(\xi)$ in the coil

The current redistributions during injection induce local field changes $\Delta B_{decay}(\xi) = \Delta B_{\Delta}(\xi)$ and reduce the coil magnetization. A possible feedback of the

Decay and Snapback

magnetization on the field is neglected. The field changes in each strand k are due to a circular self-field contribution (demonstrated in figure 6.30a) and an external contribution induced by all other strands in the coil. For small field changes, both effects can be treated separately:

$$\Delta B_{decay}(\xi) = \Delta B_{decay,self}(\xi) + \Delta B_{decay,ext}(\xi). \quad (6.23)$$

6.3.1.6.1 Self-field effect

The self-field inside each strand k has a vector in tangential direction (see figure 6.30a). If the filaments are homogeneously distributed inside the strand cross section, the self-field only depends on the current change ΔI_k and on the radial position r inside the strand:

$$\Delta B_{decay,self}(\xi) = \Delta \vec{B}_\phi(\Delta I_k, r) = \frac{\mu_0 \Delta I_k}{2\pi} \frac{r}{R_k^2} \vec{e}_\phi. \quad (6.24)$$

At the beginning of injection, the magnetization of all filaments in strand k is saturated and anti-parallel to the direction of the background field $\vec{B}(\xi_k)$. The impact of $\Delta \vec{B}_\phi$ on the filament magnetization can be calculated using the equations (5.22)-(5.27). The net effect is a reduction of the average strand magnetization. Its vector, however, does not change its direction. Components of the filament magnetization perpendicular to the original vector of the strand magnetization average out, and do not appear in the sum over all filaments in the strand cross section.

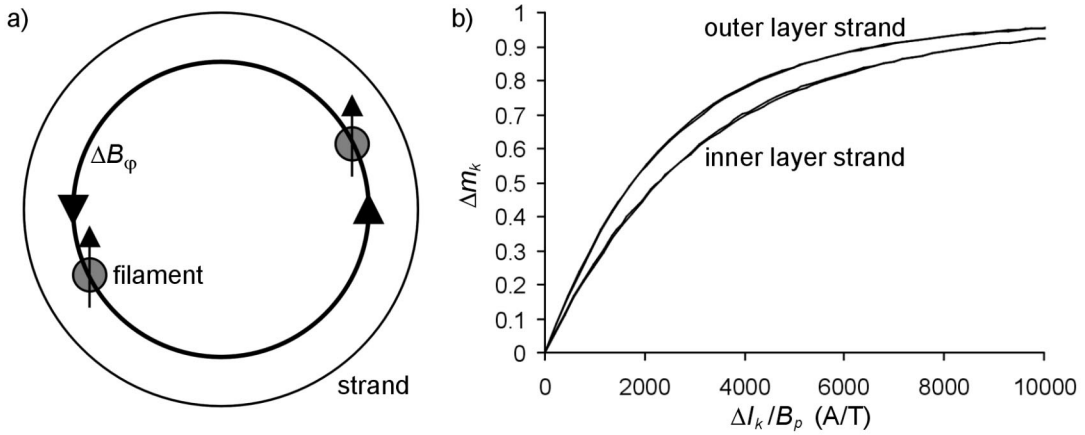


Figure 6.30 a) Impact of a circular self-field on the magnetization of two saturated filaments. The net effect is a reduction of the average strand magnetization. b) For an inner- and outer-layer strand with a homogeneous distribution of filaments inside their cross section, the decrease of the normalized magnetization due to the self-field is plotted as a function of the normalized current change.

Decay and Snapback

The decrease of the normalized magnetization $\Delta m_k = (M_{0,k} - M_k)/M_{0,k}$ is shown in figure 6.30b for an inner and outer layer strand with a homogeneous distribution of filaments inside their cross sections. The calculated data can be fitted by

$$\Delta m_k(\Delta i_k) = 1 - A_d \cdot \exp(-\Delta i_k / i_{p,1}) - (1 - A_d) \cdot \exp(-\Delta i_k / i_{p,2}). \quad (6.25)$$

$\Delta i_k = \Delta I_k / B_p$ is the current change in strand k , normalized by the filament penetration field. The parameters A_d , $i_{p,1}$ and $i_{p,2}$ are summarized in table 6.1. After the end of injection, the field in the superconducting coil of the accelerator magnets is increased, and the magnetization decrease disappears again. The behavior of the strand magnetization during the snapback can be calculated using the equations (5.28)-(5.42). In figures 6.31a and b the normalized magnetization decrease Δm_k is plotted as a function of the normalized current change Δi_k and of the normalized field increase Δb_{sb} during the snapback. The curves can be fitted by

$$\Delta m_k(\Delta i_k, \Delta b_{sb}) = A_{sb,1}(\Delta i_k) \cdot \exp\left(-\frac{\Delta b_{sb}}{b_{sb,1}(\Delta i_k)}\right) + A_{sb,2}(\Delta i_k) \cdot \exp\left(-\frac{\Delta b_{sb}}{b_{sb,2}(\Delta i_k)}\right), \quad (6.26)$$

with

$$A_{sb,1,2}(\Delta i_k) = c_{1,2} + d_{1,2} \cdot \exp\left(-\frac{\Delta i_k}{e_{1,2}}\right), \quad (6.27)$$

and

$$b_{sb,1,2}(\Delta i_k) = f_{1,2} + g_{1,2} \cdot \exp\left(-\frac{\Delta i_k}{h_{1,2}}\right) + o_{1,2} \cdot \exp\left(-\frac{\Delta i_k}{p_{1,2}}\right). \quad (6.28)$$

The parameters are given in table 6.1. The vector of the strand magnetization after the decay (equation (6.25)) and / or snapback (equation (6.26)) is

$$\vec{M}_k = (1 - \Delta m_k) \vec{M}_{0,k}. \quad (6.29)$$

	A_d	$i_{p,1}$	$i_{p,2}$	c_1	c_2	d_1	d_2	e_1	e_2	f_1	f_2	g_1	g_2	h_1	h_2	o_1	o_2	p_1	p_2
inner layer strand	0.136618	10011.34	2868.279	-4.16288	5.110858	-0.31634	-0.63164	2879.844	3295.178	0.153536	0.167249	-0.15092	-0.16419	1742.869	1900	0.005464	0.005022	200	200
outer layer strand	0.094193	10009.13	2294.882	-2.7183	3.696309	-1.76077	0.782759	2879.845	3295.172	0.163337	0.178015	-0.15439	-0.16862	1742.869	1900	0.005464	0.005022	200	200

Table 6.1 The parameters in equations (6.25), (6.27) and (6.28) are shown for typical inner layer and outer layer strands in LHC dipoles.

Decay and Snapback

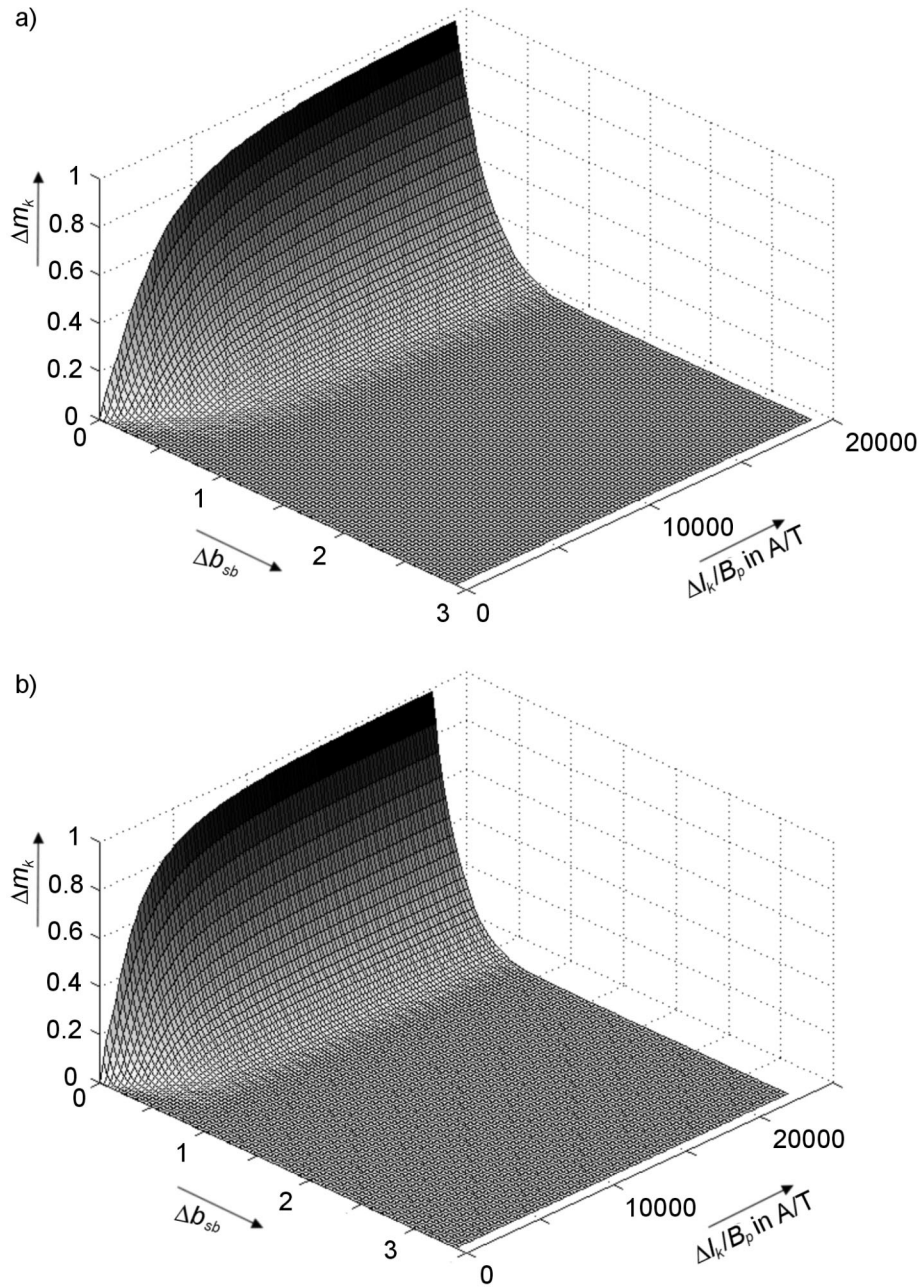


Figure 6.31 a) For an inner layer strand, and b) for an outer layer strand, the normalized magnetization decrease is plotted as a function of the normalized current change and of the normalized field increase during the snapback.

6.3.1.6.2 Impact of the coil field

In order to quantify the impact of the external field changes on the magnetization of strand k , the local field $B(\xi)$ and the local field change $\Delta B_{decay,ext}(\xi)$ in the coil are assumed to be spatially homogeneous on the scale of a strand cross section. All filaments in a strand, thus, behave in the same way, and the response of the strand magnetization to

Decay and Snapback

the field change can be calculated using the formulas (5.22)-(5.27) and (5.28)-(5.42), which were derived for single filaments in chapter 5. The amplitude of the normalized field change $\Delta b_{d,k}$, the amplitude of the background field B_k , and the angle φ_k between $\Delta \vec{B}_{decay,ext}(\xi_k)$ and $\vec{B}(\xi_k)$ (see figures 5.9 and 6.32a) are determined for each strand k :

$$\Delta b_{d,k} = |\Delta B_{decay,ext}(\xi_k)| / (2B_{p,k}), \quad (6.30)$$

$$B_k = |B(\xi_k)|, \quad (6.31)$$

$$\varphi_k = \text{sign}(\Delta \vec{B}_{decay,ext}(\xi_k) \times \vec{B}(\xi_k)) \cdot \arccos \left(\frac{\text{Re}(B^*(\xi_k) \Delta B_{decay,ext}(\xi_k))}{|B(\xi_k)| |\Delta B_{decay,ext}(\xi_k)|} \right). \quad (6.32)$$

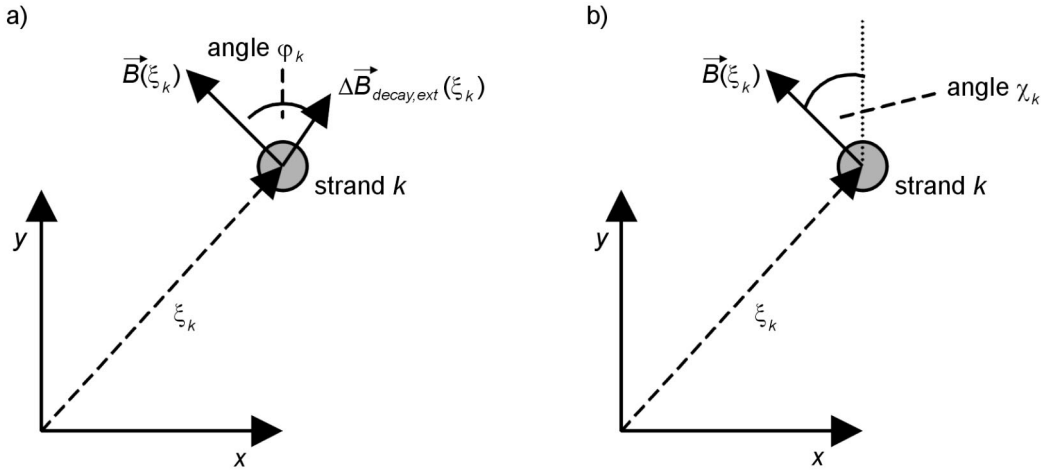


Figure 6.32 The angles φ_k and χ_k are demonstrated. a) φ_k is defined as the angle between the local field change $\Delta \vec{B}_{decay,ext}(\xi_k)$ and the local field $\vec{B}(\xi_k)$ in the coil. b) χ_k is defined as the angle between the magnetic field $\vec{B}(\xi_k)$ and the y-axis.

During the snapback every strand is exposed to a field change $\Delta B_{sb}(\xi_k)$, which is assumed to be proportional to the rise of the dipole field $\Delta B_1(0)$ in the center of the coil

$$\Delta B_{sb}(\xi_k) = B(\xi_k) \frac{\Delta B_1(0)}{B_1(0)}. \quad (6.33)$$

A normalization of the field change during the snapback is given by

$$\Delta b_{sb,k} = |\Delta B_{sb}(\xi_k)| / (2B_{p,k}). \quad (6.34)$$

For every strand k , the angle χ_k between the field $\vec{B}(\xi_k)$ and the y-axis can be calculated from:

Decay and Snapback

$$\chi_k = \text{sign}(B_x(\xi_k)) \cdot \arccos\left(\frac{B_y(\xi_k)}{|B(\xi_k)|}\right). \quad (6.35)$$

The definition of the angle is given in figure 6.32b.

The formulas in chapter 5 allow to calculate the impact of field changes in the coil on the magnetization of each strand. They can be implemented to calculate the decay only, or both, decay and snapback. In the latter case, the accuracy is considerably lower. The formulas deliver the magnetization components M_x and M_y in a coordinate system with its y -axis anti-parallel to $B(\xi_k)$. M_x still has to be corrected for the sign of φ_k . In coordinates of the coil, the magnetization change in strand k can be expressed as:

$$\begin{pmatrix} \Delta M_{x,k} \\ \Delta M_{y,k} \end{pmatrix} = - \begin{pmatrix} \cos \chi_k & \sin \chi_k \\ -\sin \chi_k & \cos \chi_k \end{pmatrix} \cdot \begin{pmatrix} \text{sign}(\varphi_k) \cdot M_x(\varphi_k, \Delta b_{d,k}, \Delta b_{sb,k}) \\ M_y(\varphi_k, \Delta b_{d,k}, \Delta b_{sb,k}) - |M_k| \end{pmatrix}. \quad (6.36)$$

6.3.1.6.3 Impact of the magnetization changes on the field components

The impact of the magnetization changes in the coil on the field components b_n and a_n in the center of the coil can be determined from equation (6.17) and (6.18). In particular, this yields for the sextupole component:

$$\Delta b_{3,M} = -\frac{\mu_0 3R_{ref}^2 10^4}{2B_1} \sum_k R_k^2 \text{Re} \left\{ \frac{\Delta M_k^*}{\xi_k^4} - \left(\frac{\mu_r - 1}{\mu_r + 1} \right) \frac{\xi_k^{*2} \Delta M_k}{R_{yoke}^6} \right\}. \quad (6.37)$$

6.3.2 Analysis

Simulations of the coil magnetization are performed at the injection level, based on 31 cross sectional slices of the coil, which are located between $z = 0$ and $z = 0.150$ m, and separated by gaps of 0.005 m. This model is shown in figure 6.22. The simulations, thus, cover a little more than a cable twist pitch, which equals 0.115 m in the inner and 0.105 m in the outer layer of the LHC dipole coil. Three cases are analyzed for the phases Φ_i . All phases are either set to zero, shifted by 180° from turn to turn, or random.

6.3.2.1 Correlations between current distribution, spatially periodic field pattern and magnetization

Simulations are performed for current imbalances ΔI_{turn} with values between 0 and 5 A, in steps of 0.5 A. For every cross sectional slice of the coil, the changes in the sextupole component $\Delta b_3 = \Delta b_{3,\Delta I} + \Delta b_{3,\Delta M,self} + \Delta b_{3,\Delta M,ext}$ due to the current imbalances $\Delta I_{turn}(i)$, and due to the self-field induced and externally induced magnetization changes ΔM_k in the coil, are calculated separately.

Decay and Snapback

6.3.2.1.1 Decay of the spatially periodic field pattern

Along the axis of the magnet, all numerical results of the two-dimensional Biot-Savart approximation demonstrate a sinusoidal shape of the current contribution $\Delta b_{3,\Delta I}$ to the decay of the spatially periodic field pattern in the normal sextupole. As an example, figure 6.33 shows $\Delta b_{3,\Delta I}$ as a function of the z -coordinate for a random arrangement of the phases Φ_i and for several values of the current imbalance ΔI_{turn} . In order to take into account the different twist pitches of the Rutherford-type cable in the inner and outer layer of the coil, $\Delta b_{3,\Delta I}$ is described by a linear combination of two \sin - terms with different wavelengths and different phases. In most cases, however, the term for the outer layer can be neglected. The amplitude $\Delta b_{3,\Delta I,max}$ varies linearly with ΔI_{turn} . The slope $\Delta b_{3,\Delta I,max}/\Delta I_{turn}$ very much depends on the phases and ranges from 0.03 to 2.2 units/A.

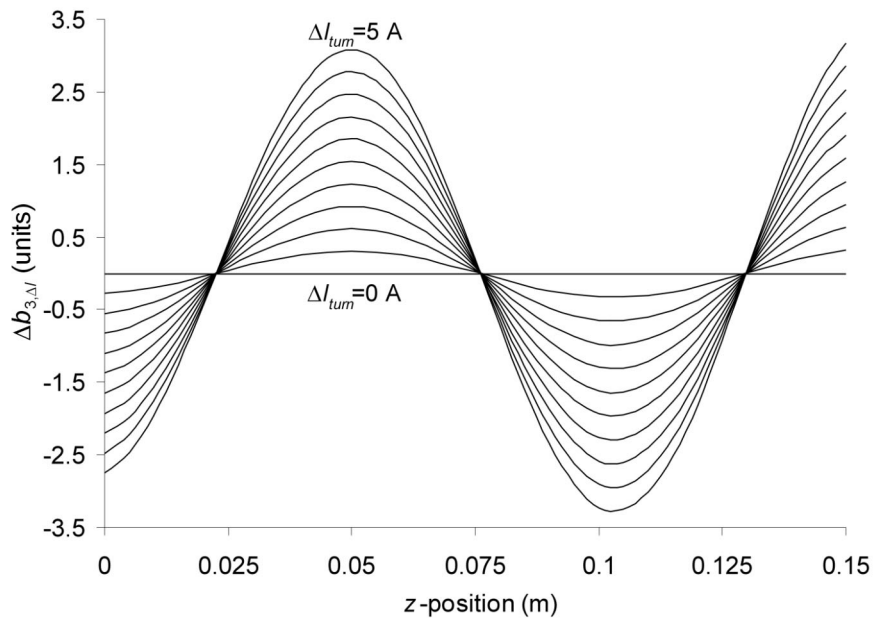


Figure 6.33 $\Delta b_{3,\Delta I}$ is plotted as a function of the z -coordinate along the cable covering a little more than a cable twist pitch. The calculations are performed as a two-dimensional approximation of the Biot-Savart integral, for a magnet with a random arrangement of phases Φ_i and for several values of the current imbalance ΔI_{turn} .

The convolution in equation (6.10) transforms sinusoidal contributions from any part of the coil into a contribution which is again sinusoidal along the z -axis, only with a significantly reduced amplitude. An analytical assessment shows that the convolution reduces the amplitude of the pattern decay induced by current redistributions in the inner layer by a factor of about 0.3, and the amplitude of the pattern decay induced by current redistributions in the outer layer by a factor of about 0.15. The spatially periodic field pattern is predominantly influenced by the inner layer. For this reason an additional factor

Decay and Snapback

of about 0.3 is necessary to compare the calculated curves in figure 6.33 to measured data.

In a magnet where the phases are shifted by 180° from turn to turn, the periodic field pattern has an extremely small amplitude, since the contributions of successive turns compensate each other. Higher pattern amplitudes are achieved if all turns have a zero phase. In certain arrangements with random phases, each block induces a different contribution to the magnetic field component, and for this reason many times even larger decay amplitudes can be observed.

In real LHC prototype and pre-series dipoles, the measured amplitudes of the spatially periodic field pattern only vary within a factor 2. The BICCs induced in different magnets possibly have similar amplitudes and the phases are eventually correlated, due to the geometry or due to the manufacturing process.

6.3.2.1.2 Decay induced by the self-field in the strands

In the following analysis the contributions of the self-field and the external field in the coil to the field decay during injection are treated separately. The self-field in the strands decreases the absolute strand magnetization, however, the direction of the magnetization vector doesn't change. As a result, the decay of $\Delta b_{3,\Delta M,self}$ is approximately constant along a twist pitch length, and does not significantly add to the amplitude and phase of the spatially periodic field pattern.

This agrees very well with the experimental observation that the amplitude of the field pattern doesn't show a snapback, and that the snapback amplitudes measured with both rings of the Hall detector always have the same magnitude. However, the computed amplitude of the self-field induced decay is significantly smaller than the decays observed in real magnets.

The decay $\overline{\Delta b_{3,\Delta M,self}}$ (averaged along one twist pitch length) is proportional to the current imbalance ΔI_{turn} . This is demonstrated in figure 6.34. Calculations performed for magnets with different arrangements of the phases in all cases show decays with similar magnitudes.

Simulations for different excitation currents during injection ($I_{inj} = 300, 550, 739, 800$ and 1050 A) show a constant non-normalized sextupole decay

$$\overline{\Delta B_{3,\Delta M,self}} = B_1 10^{-4} \overline{\Delta b_{3,\Delta M,self}} = constant. \quad (6.38)$$

Decay and Snapback

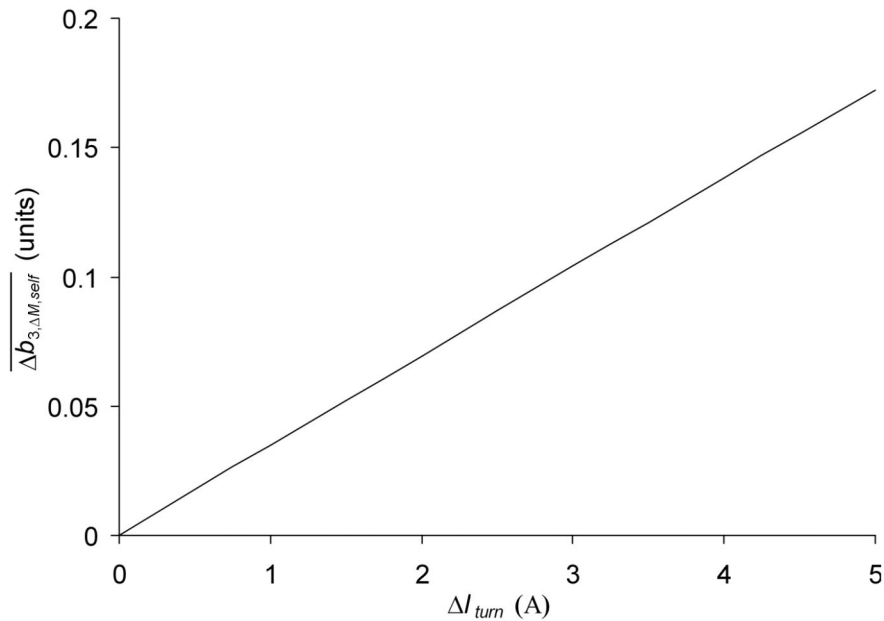


Figure 6.34 Calculations were performed for a magnet with a random arrangement of the phases Φ_i and for several values of the current imbalance ΔI_{turn} . The average decay $\overline{\Delta b_{3,\Delta M, self}}$ induced by a changing self-field is plotted as a function of ΔI_{turn} .

6.3.2.1.3 Decay induced by local field changes in the coil

The current redistributions in the coil induce local field changes with vectors that are not necessarily parallel to the local field (see e.g. figure 6.29). The contribution of the field changes to different field components can vary along the twist pitch length, and is not necessarily proportional to the original spectrum of field components.

The model presented here is based on a two dimensional approximation of the Biot-Savart integral. The model predicts local field changes in the coil, which strongly depend on the phases Φ_i . The two dimensional approximation neglects the convolution in equation (6.10). In a real coil, contributions of current redistributions in different parts of the coil to the field in a point (x,y,z) are smoothed along the z -axis. The full width half maximum of the smoothing is determined by two times the distance from the point (x,y,z) to the location of the current, projected onto the xy -plane. For this reason, inside the coil, the interaction between current redistribution and magnetization is localized in a region around the point (x,y,z) .

The absolute value of the filament magnetization in the coil is locally either reduced or constant, but it doesn't increase. In contrast to the self-field induced magnetization decay, the direction of the strand magnetization vector can change, and modify the spectrum of

Decay and Snapback

field harmonics. The sextupole field component can thus be locally increased or reduced, and eventually still have a structure along the twist pitch length.

In a real magnet, the contribution of the magnetization to the field decay in the center of the coil is smoothed (a second time) by the convolution integral in equation (6.10). The convolution drastically reduces the amplitude (i.e. by a factor of about 0.3) of any pattern along the z -axis, however, it leaves the average value constant. Hall detector measurements have shown that the measured pattern amplitudes don't show a significant snapback, and that the snapbacks measured in both rings of the detector have similar amplitudes. For this reason, decay and snapback are assumed to be approximately homogeneous along the axis of a real magnet.

For small field changes, the response of the magnetization is approximately linear. For this reason, local errors of the two-dimensional Biot-Savart approximation are assumed to average out in the sum over all cross sectional slices, and to deliver correct average values.

In figure 6.35 the average decay $\overline{\Delta b_{3,\Delta M,ext}}$ is plotted as a function of the current imbalance ΔI_{turn} , for magnets with different arrangements of the phases. The observed contribution to the decay is a factor 2 to 6 larger than the impact of the self-field, and

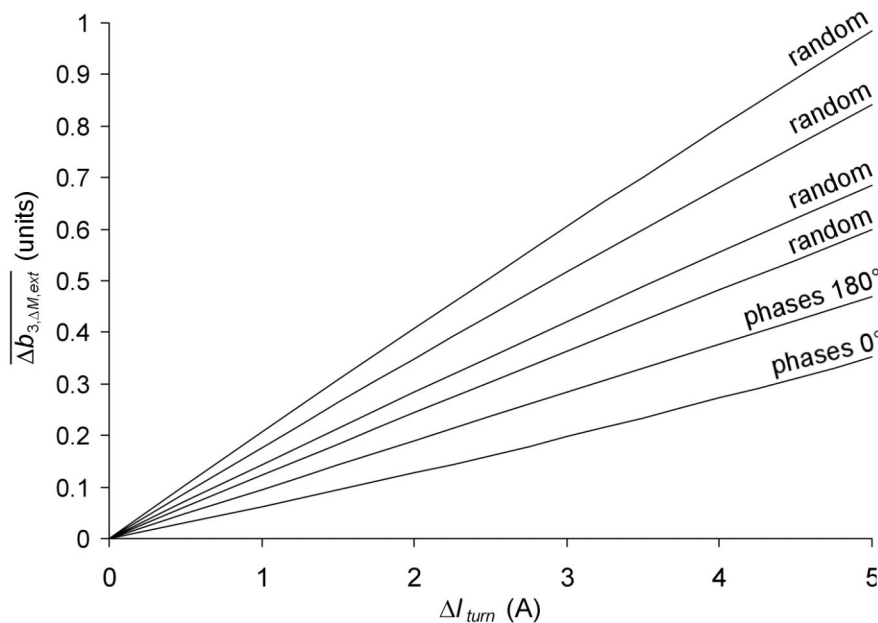


Figure 6.35 For magnets with different arrangements of the phases Φ_i , the calculated average reduction of the normal sextupole $\overline{\Delta b_{3,\Delta M,ext}}$ due to the field changes in the coil is plotted as a function of the current imbalance ΔI_{turn} .

Decay and Snapback

comparable to experimental data. The smallest decay is observed if all phases equal zero. The decay in a magnet, where the phases are shifted from turn to turn by 180° , is not very much larger. The largest decays appear in magnets with random phases.

In figure 6.36 the average magnetization decay $\overline{\Delta b_{3,\Delta M,ext}}$ is plotted as a function of the current induced pattern amplitude $\Delta b_{3,\Delta I,max}$, for several magnets with different phases.

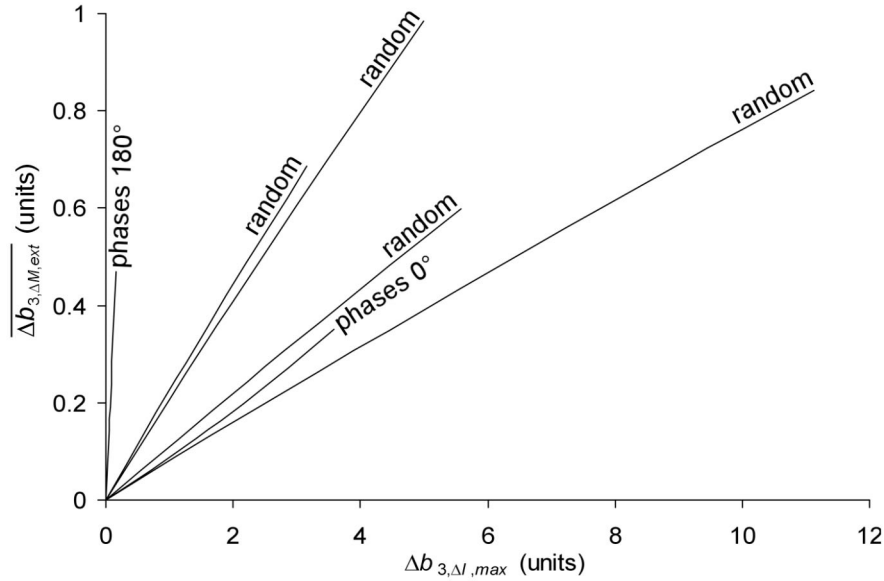


Figure 6.36 For magnets with different arrangements of the phases Φ_i , the calculated average reduction of the normal sextupole $\overline{\Delta b_{3,\Delta M,ext}}$ due to the field changes in the coil is plotted as a function of the amplitude of the current induced contribution to the periodic pattern decay $\Delta b_{3,\Delta I,max}$.

Most curves for the magnets with random phases can be found inside an angle, which is delimited by the curve for a magnet where the phases are shifted by 180° from turn to turn, and a magnet where all phases are zero. Only one curve for a magnet with random phases is found slightly outside this angle.

Calculations are also performed for different excitation currents during injection. A constant amplitude of the non-normalized average decay $\overline{\Delta B_{3,\Delta M,ext}}$ is observed.

6.3.2.2 Snapback curve

As already explained in section 4, the BICCs do not change significantly during the snapback. For this reason, the current induced contribution $b_{3,\Delta I}$ is neglected, and only the behavior of the magnetization contribution $b_{3,M}$ is simulated during the snapback. The modelling is performed for a magnet with a random arrangement of the phases Φ_i .

Decay and Snapback

The formulas (5.28)-(5.42) for the calculation of the filament magnetization during the snapback are accurate within 90% of M_p . In order to minimize the ratio between the error and the amplitude of the calculated snapback, a strongly exaggerated current imbalance ΔI_{turn} of 30 A is assumed. The snapbacks due to the self-field induced decay and due to the decay of the field in the coil are calculated separately and averaged over all cross sections. In figure 6.37 both snapbacks are plotted as functions of the dipole field increase. In addition figure 6.37 shows the sum of both effects. The data are corrected for a small offset caused by inaccuracies in the formulas (5.28)-(5.42).

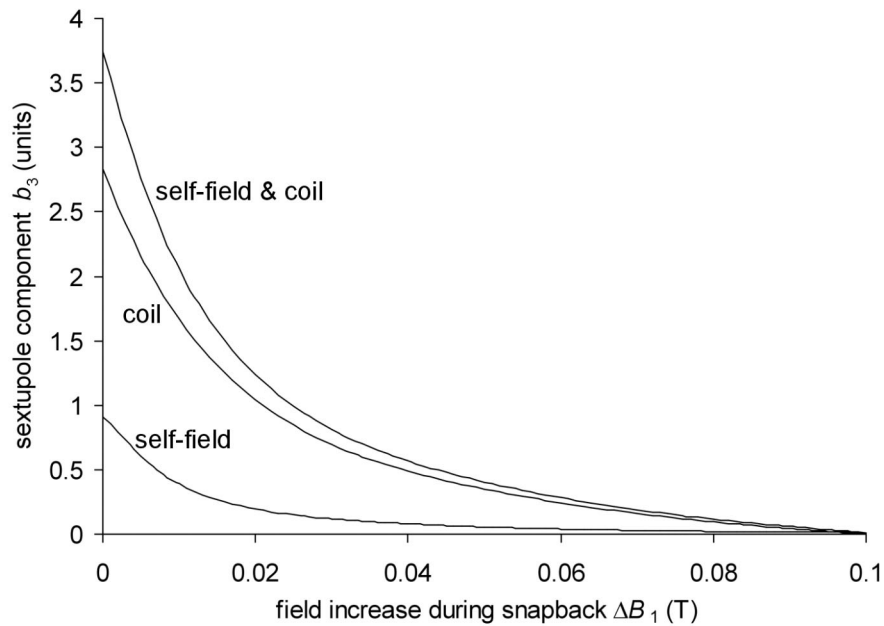


Figure 6.37 The contributions of the self-field, the field in the coil and their sum are shown during the snapback as a function of the dipole field increase. The calculations were performed for a magnet with a random arrangement of phases and for a current imbalance ΔI_{turn} of 30 A.

The sum of the snapback curves is fitted with the exponential in equation (6.7), assuming $\Delta b_{3,\Delta M,average} = 3.6$ units and $B_{sb} = 20$ mT. Both values are significantly larger, but their ratio is in the same order of magnitude as the ratios found for the data in figure 6.21, measured at a constant background field. The fit corresponds to the calculated curve in figure 6.37 within 0.15 units.

6.4 Conclusion

The principle mechanism for the interaction between current distribution and magnetization is demonstrated in a model experiment. The magnetization of the sample is measured as a function of the current in the copper wires. The results show an exponential demagnetization of the strand as a function of the applied local field. A

Decay and Snapback

snapback can be observed as soon as the external field is increased. Both, demagnetization and snapback quantitatively agree with numerical simulations. For different demagnetization currents, the snapback amplitude and the snapback penetration field are proportional. For experimental runs with equal demagnetization currents, performed at different background fields, a linear correlation between the snapback amplitude and the snapback penetration field with a non-linear saturation at background fields above 0.8 T is found.

Hall detector measurements are performed on several real-size accelerator magnets. The observation, that the amplitude of the spatially periodic field pattern in the magnets does not show a snapback, indicates that the field pattern is not significantly influenced by the magnetization. However, a correlation is found between the pattern decay and the magnetization decay during injection. The correlation clearly illustrates the interaction between current redistribution and magnetization. For measurements with different pre-cycle currents, the decay of the pattern amplitude indicates a change in sign at a flat-top current close to 2000 A, thus, suggesting current redistributions with opposite directions. Measurements with different ramp-rates after injection show the snapback to be independent of the ramp rate. For measurements at different injection currents a constant non-normalized decay amplitude $\Delta B_{3,decay}$ is found. Both results correspond very well to the linear correlation described above, since the induction of currents during ramps before and after injection is relatively small in comparison to the currents induced during the pre-cycle. The snapback amplitudes and snapback penetration fields possibly follow two different correlations. The first correlation concerns all measurements performed at the same injection current. The second correlation describes the snapback amplitude and penetration field for measurements at different injection currents. The Hall detector measurements show that flux creep, if present at all, is not more than a marginal effect.

The formulas in section 5 are implemented in a numerical model, based on a two-dimensional approximation of the Biot-Savart integral, and used to calculate the effects ‘decay’ and ‘snapback’ in a number of cross sectional slices of the coil. The model is used to analyze two different mechanisms for the interaction between current redistribution and magnetization. The first one is the reduction of the strand magnetization due to the self-field in the strands. The second mechanism describes the interaction between the current redistributions and the magnetization in different strands of the coil.

The model reveals a spatially periodic pattern, which is sinusoidal along the z -axis. Analytical considerations show that the sinusoidal shape is not changed by a convolution along the z -axis, however, the amplitude is reduced by a factor of about 0.3. The sinusoidal shape, as well as the factor 0.3 agree with experimental observations.

Decay and Snapback

The self-field induced by current redistributions decreases the absolute strand magnetization and does not change the direction of its vector. For this reason the self-field induced decay does not significantly depend on the phases Φ_i , and is approximately constant in all cross sectional slices. However, the amplitude is significantly smaller than the decay observed in real magnets. In a range between 300 and 1050 A, the non-normalized snapback amplitude does not significantly depend on the excitation current during injection.

The local field changes are not necessarily parallel to the field in the coil, and their spectrum is not necessarily proportional to the original distribution of harmonics. The average decay amplitude due to local field changes in the coil strongly depends on the phases Φ_i , and is a factor 2-6 larger than the self-field contribution. Its typical magnitude is similar to experimental observations. Also here the non-normalized snapback amplitude does not significantly depend on injection currents in a range between 300 and 1050 A. For more precise calculations a three dimensional implementation of the Biot-Savart integral is recommended.

Using the formulas in section 5, the snapback is calculated for a magnet with a random arrangement of phases Φ_i and an exaggerated current imbalance ΔI_{turn} of 30 A. Both, the self-field contribution and the contribution of the field in the coil are taken into account separately. The sum of both effects can be described by an exponential fitting function. Both, the snapback amplitude and the snapback penetration field are significantly larger than measured values, but the ratio of the two parameters is in the same order of magnitude.

Chapter 7

Conclusions

In the past flux creep was thought to be the source for field decay observed in accelerator magnets. However, the dependence of the decay on the excitation history of the magnets could not be explained, and consequently the role of flux creep was reduced, but still kept a significant contribution to the decay. Rather accurate measurements, as presented in chapter 6, clearly demonstrate that in the case of LHC magnets the flux creep contribution is not significant.

The principal source of the field decay are boundary induced coupling currents, which diffuse along the cable and redistribute among the strands. Long characteristic time constants of the current diffusion are responsible for the observed phenomenon that the magnets remember the excitation history. The redistribution of currents during the injection phase can very well explain the changing amplitude of the spatially periodic field pattern.

The comparison in chapter 4, between results of systematic measurements performed on 1 m short model dipoles and of a numerical model with a single time constant, has clearly shown that decay and snapback are due to redistributing BICCs by which the coil magnetization changes. The one-time-constant model allows for a qualitative estimation of the snapback amplitude in relation to the coil excitation history. In the future a model with a few time constants can be developed for more precise calculations of the snapback amplitude in each magnet of the collider.

The model experiment on a single strand (section 6.1) has convincingly validated the interaction between local magnetic field changes in the coil and the magnetization as the principle mechanism for decay and snapback. The measured snapbacks are fitted by exponential functions, and a clear correlation is found between the snapback amplitude and the snapback penetration field.

Conclusions

From various detailed investigations on real magnets (section 6.2) it is concluded that the spatially periodic field pattern is probably not significantly affected by the coil magnetization. The pattern decay during injection and the decay of the average magnetization are correlated. At different injection currents a constant non-normalized decay amplitude $\Delta B_{3,decay}$ and a constant non-normalized change in amplitude of the spatially periodic field pattern are found. Different ramp-rates applied after injection show a snapback which is independent of the ramp rate. The last two observations can be explained since the BICCs induced during the ramps before and after injection are relatively small in comparison to the BICCs induced during the pre-cycle. Given the accuracy of the measurements, the snapback curves can be approximated by an exponential function. The snapback amplitudes and the snapback penetration fields are correlated. The first correlation can be explained by the dependence of the BICCs on the excitation history. The BICCs at various injection currents, however, are about the same. The second correlation is eventually caused by the $J_c(B)$ dependence of the superconductor.

The behavior of a saturated cylindric superconducting filament (chapter 5) is analyzed in a changing external field. Numerical simulations are performed for field changes which are typical during decay and snapback. The calculated data are used to develop formulas that can describe the filament magnetization after field changes at different angles, with different amplitudes and after different increases of the original background field. In the future, in particular the accuracy of the fitting formulas for the snapback can be improved significantly.

The fitting formulas mentioned above are implemented into a numerical model for decay and snapback (section 6.3) based on a two dimensional approximation of the Biot-Savart integral. The numerical model represents a first step towards a tool to predict the decay, the snapback and the spatially periodic field pattern in a magnet. It helps to better understand the interaction between current distribution and magnetization. The decay is caused by two complementary mechanisms, the change of the self-field in the strands, and local field changes in the coil. The amplitude of the decay induced by the second mechanism is a factor 2-6 more important. For a more precise analysis a three-dimensional calculation of the Biot-Savart integral is recommended. Moreover, more realistic values for current redistributions in the coil, and the feedback of the magnetization on the field in the coil can be implemented.

Most 6-block magnets show higher snapback amplitudes and a stronger dependence on the flat-top current than magnets of the 5-block design. However, even among magnets with similar design parameters the variations in the measured snapback amplitudes are

Conclusions

quite large. In practice this implies that all magnets have to be measured before they are definitely installed in the LHC.

A sextupole Hall plate detector with substantially improved mechanics and electronics was developed and successfully used for various magnetic measurements on 15 m long LHC dipoles in the 'SM-18' test facility. A new calibration procedure for the first time allows quantitatively correct results. In a limited field range of around 0.5 T the device attains a resolution of 0.015 units, a reproducibility of 0.15 units, an accuracy of 0.3 units and a bandwidth of about 3.3 Hz. Based on these improvements demonstrated, a new version of the detector with six sextupole rings and two additional decapole rings is constructed and tested. The two decapole rings represent the first known realization of a decapole detector with Hall plates. This new version of the detector will allow a much more detailed analysis of correlations between decay, snapback and the spatially periodic field pattern in superconducting accelerator magnets. Apart from systematic magnetic measurements, the detector can also be used for the online-compensation of decay and snapback in the machine. In order to reach the accuracy necessary for the compensation, the calibration of the device still has to be considerably improved.

Appendix A

a) x-component											b) y-component											
	<i>e</i>	<i>f</i>	<i>g</i>	<i>h</i>	<i>k</i>	<i>l</i>	<i>m</i>	<i>n</i>	<i>o</i>		<i>e</i>	<i>f</i>	<i>g</i>	<i>h</i>	<i>k</i>	<i>l</i>	<i>m</i>	<i>n</i>	<i>o</i>			
$C_{\text{exp},x,0}$	4.4848e+0	-1.9990e+1	3.2456e-1	2.2374e+1	8.4596e-1	2.1464e+0	0	0	0		$C_{\text{exp},y,0}$	6.6683e+0	-3.4596e-1	8.5083e-1	-1.3352e+1	7.1692e-1	-1.7466e-2	2.0173e-1	-6.6550e-1			
$C_{\text{exp},x,1}$	1.2141e+0	-3.4254e+0	2.4997e-1	5.4741e+0	8.1598e-1	2.4507e+0	0	0	0		$C_{\text{exp},y,1}$	1.9211e+0	7.3112e-1	2.7576e-1	0	0	0	0	0	0		
$C_{\text{exp},x,2}$	7.0900e-1	-2.2493e+0	4.2997e-1	4.6421e+0	7.6323e-1	2.0214e+0	0	0	0		$C_{\text{exp},y,2}$	1.1257e+0	-1.3137e+0	3.8576e-1	1.7742e+0	8.9072e-1	0	0	0	0		
$d_{\text{exp},x,0}$	4.4469e-1	-8.0753e-2	1.7794e-1	-1.2715e-1	6.6738e-1	2.4721e-1	0	0	0		$d_{\text{exp},y,0}$	2.1079e-1	0	3.2728e-1	1.9383e-1	2.6445e+0	-3.9594e-1	1.2101e+0	2.6553e+0			
$d_{\text{exp},x,1}$	7.3809e-2	6.3114e-2	5.0612e-1	1.0303e-1	7.5918e-1	0.7	-5.3713e-1	5.3108e-1	2.0207e+0		$d_{\text{exp},y,1}$	-1.4690e-2	-1.1183e-1	6.3265e-1	1.4226e-1	1	0	0	0			
$d_{\text{exp},x,2}$	2.2095e-1	-3.4628e+0	2.3532e-1	4.2186e+0	8.0259e-1	2.1110e+0	1.8246e+1	2.1510e-1	2.1764e+0		$d_{\text{exp},y,2}$	4.3487e-2	3.6589e-1	9.9621e-2	-9.1935e-2	1.4088e+0	9.5591e-2	6.3556e-1	6.7492e-1			
$d_{\text{exp},x,3}$	2.3127e+1	0	0	0	0	0	0	0	0		$d_{\text{exp},y,3}$	2.3205e+1	0	0	0	0	0	0	0	0		
$d_{\text{exp},x,4}$	0	0	1.8610e-1	-3.2751e+0	1.0598e+0	2.5221e+0	4.9050e+0	8.5737e-1	2.1895e+0		$d_{\text{exp},y,4}$	1.3383e-1	-2.4678e-1	4.8099e-1	-2.3455e-1	1.1867e+0	8.2414e-1	4.7883e-1	1.4510e+0			
$d_{\text{exp},x,5}$	1.4687e+1	0	0	0	0	0	0	0	0		$d_{\text{exp},y,5}$	1.4957e+1	0	0	0	0	0	0	0	0		
$C_{\text{psh},x,0}$	-1.3153e-1	3.6109e+0	1.8969e-1	-2.9726e+0	9.3485e-1	2.7091e+0	-2.6658e+2	3.9357e-1	1.5906e+0		$C_{\text{psh},y,0}$	-1.3153e-1	3.6109e+0	1.8969e-1	-2.9726e+0	9.3485e-1	-2.6658e+2	3.9357e-1	1.5906e+0			
$C_{\text{psh},x,1}$	1.2765e+0	2.1029e+1	1.0211e-1	0	0	0	0	0	0		$C_{\text{psh},y,1}$	1.2765e+0	2.1029e+1	1.0211e-1	0	0	0	0	0	0		
$C_{\text{psh},x,2}$	1.1865e+0	-5.7230e+0	3.3601e-1	2.0681e+0	1.3337e+0	4.8036e+0	1.4509e+1	3.5380e-2	1.1978e+0		$C_{\text{psh},y,2}$	1.1865e+0	-5.7230e+0	3.3601e-1	2.0681e+0	1.3337e+0	4.8036e+0	1.4509e+1	3.5380e-2	1.1978e+0		
$C_{\text{psh},x,3}$	5.4549e+1	9.5585e+1	3.9030e-1	0	0	0	0	0	0		$C_{\text{psh},y,3}$	5.4549e+1	9.5585e+1	3.9030e-1	0	0	0	0	0	0		
$d_{\text{psh},x,0}$	5.8483e-1	-1.6737e+0	2.2823e-1	0	0	0	0	0	0		$d_{\text{psh},y,0}$	5.8483e-1	-1.6737e+0	2.2823e-1	0	0	0	0	0	0		
$d_{\text{psh},x,1}$	4.7216e-1	-9.3068e-1	1.2214e-1	0	0	0	0	0	0		$d_{\text{psh},y,1}$	4.7216e-1	-9.3068e-1	1.2214e-1	0	0	0	0	0	0		

Table A.1 The optimized fitting parameters in equation (5.41) and (5.42) are shown a) for the x-component and b) for the y-component of the magnetization vector.

References

- [1] P. W. Anderson, Theory of flux creep in hard superconductors, *Phys. Rev. Lett.* 9, 1962, p. 309.
- [2] M. Ashkin, Flux distribution and hysteresis loss in a round superconducting wire for the complete range of flux penetration, *Journal of Applied Physics*, Vol. 50, pp. 7060-7066, November 1979.
- [3] R. Bailey et al., Dynamic Effects and their Control at the LHC, *Proceedings-of-the-1997-Particle-Accelerator-Conference-Cat.-No.97CH36167.* vol.1, IEEE, Piscataway, NJ, 1998 - pp. 66-8.
- [4] C. P. Bean, Magnetization of hard superconductors, *Phys. Rev. Lett.*, vol. 8, pp. 250-253, 1962.
- [5] C. P. Bean, Magnetization of high-field superconductors, *Rev. Mod. Phys.* (1964) 31.
- [6] E. Benedico, A Fast Sextupole and Decapole Probe for Chromaticity Corrections, graduation report, Universitat Politècnica de Catalunya, Spain, April 2002.
- [7] R. A. Beth, An Integral Formula for Two Dimensional Fields, *Journal of Applied Physics*, Vol. 38, No. 12, 1967.
- [8] J. Billan, Twin Rotating Coils for Cold Magnetic Measurements of 15 m Long LHC Dipoles, *IEEE Trans. Appl. Supercond.*: 10 (2000) no.1, pp.1422-6.
- [9] L. Bottura et al., Field Quality of the Main Dipole Magnets for the LHC Accelerator, 5th European Particle Accelerator Conference-EPAC'96, Barcelona, Spain, 1996.
- [10] L. Bottura, Field Dynamics in Superconducting Magnets for Particle Accelerators, CAS - CERN Accelerator School: Measurement and Alignment of Accelerator and Detector Magnets, Anacapri, Italy, 11 - 17 Apr 1997 - CERN, Geneva, 1998.
- [11] L. Bottura et al., A Fast Sextupole Probe for Snapback Measurement in the LHC Dipoles, *IEEE Trans. Appl. Supercond.*: 10 (2000), p. 1435-8.
- [12] L. Bottura et al., Analytical Solution for the Current Distribution in Multistrand Superconducting Cables, *J. Appl. Phys.* 92 (2002), pp. 7571-7580.
- [13] L. Bottura et al., An Interactive Tool for the Analysis of Magnetic Field in Superconducting Accelerator Magnets, CERN internal report CERN-MTA-IN-2002-189.
- [14] E. H. Brandt, Superconductors of Finite Thickness in a Perpendicular Magnetic Field: Strips and Slabs, *Physical review B*, Vol 54, number 6, pp. 4246-4263, 1 August 1996 II.
- [15] M. Breschi et al., Fast measurement of field harmonics through a set of Hall probes, CERN Internal Note LHC-MTA-IN-2000-103.
- [16] M. Breschi et al., Measurements of Magnetic Field Pattern in a Short LHC Dipole Model, *IEEE Trans. Appl. Supercond.*: 11 (2001) no.1.2, pp.1605-8.

References

- [17] H. Brück et al., Time Dependence of Persistent Current Effects in the Superconducting HERA Magnets, Contribution to the 11th International Conference on Magnet Technology - MT-11, Tsukuba, Japan, Aug. 28-Sep. 1, 1989 and HERA 90-01, January 1990.
- [18] H. Brück et al., Observation of a Periodic Pattern in the Persistent-Current Fields of the Superconducting HERA Magnets, IEEE Trans. Magn.: 28 (1992) no.1.
- [19] O. Brüning, Accumulation and Ramping in the LHC, Proc. of 10th Workshop on LEP-SPS Performance, Chamonix, France, 17 - 21 Jan 2000, CERN-SL-2000-007-DI, pp.198-202.
- [20] W. Buckel, Supraleitung, 4. Auflage, VCH Verlagsgesellschaft, Weinheim, 1990.
- [21] J. Buckley et al., Dynamic Magnetic Measurements of Superconducting Magnets for the LHC, IEEE Trans. Appl. Superconduct.: 5 (1995) - pp.1024-1027.
- [22] CERN DRAWING DIRECTORY (CDD) - LHCMBA_A0001.
- [23] CERN, Experiments at CERN-Grey Book, <http://greybook.cern.ch/>
- [24] J. C. Davis, Low Temperature Testing on Niobium Diselenide, <http://ist-socrates.berkeley.edu/~davisgrp/stm/results/nbse2/>
- [25] A. Devred et al., Time Decay Measurements of the Sextupole Component of the Magnetic Field in a 4-cm Aperture, 17-m-Long SSC Dipole Magnet Prototype, SSCL-462, FERMILAB-Conf-91/148, May 1991.
- [26] L. R. Evans, LHC Status and Plans, Proceedings-of-the-1997-Particle-Accelerator-Conference-Cat.-No.97CH36167. vol.1, IEEE, Piscataway, NJ, 1998 - pp.61-5.
- [27] D. Finley et al., Time Dependent Chromaticity Changes in the Tevatron, IEEE, New York, 1987 [87CH2387-9]-pp.151-153.
- [28] R. A. Hartmann, A Contribution to the Understanding of AC Losses in Composite Superconductors, Ph.D. thesis, University of Twente, The Netherlands, 1989.
- [29] M. Haverkamp, A. Kuijper, A. den Ouden, B. ten Haken, L. Bottura, H. ten Kate, Interaction between Current Imbalance and Magnetisation in LHC Cables, Appl. Superconduct. Conf., Virginia Beach, VI, USA, 17-22 Sept. 2000. IEEE Trans. Appl. Supercond. : 11 (2001), p. 1609.
- [30] M. Haverkamp et al., Field Decay and Snapback Measurements using a Fast Hall Plate Detector, IEEE Trans. Appl. Supercond.: 12 (2002) no.1, pp.86-89.
- [31] A. Jain, Harmonic Coils, Proc. CERN Accelerator School on Measurement and Alignment of Accelerator and Detector Magnets, CERN report 98-05, pp.175-217.
- [32] K. Kassoul, Rapport de stage, Modélisation et simulation de la magnétisation d'un brin supraconducteur d'un électroaimant du LHC, Université de Paris-Sud, France, 2001.
- [33] L. Krempasky, C. Schmidt, Influence of a Longitudinal Variation of dB/dt on the Magnetic Field Distribution of Superconducting Accelerator Magnets, Appl. Phys. Lett., 66 (12), 20 March 1995.

References

- [34] L. Krempasky, C. Schmidt, Experimental Verification of ‘Supercurrents’ in Superconducting Cables exposed to AC-Fields, *Cryogenics* 39 (1999) 23-33.
- [35] L. Larsson, Sextupole Snapback Detector, Master thesis, Luleå University of Technology, May 2000.
- [36] J. V. Minervini, Two-dimensional analysis of AC loss in superconductors carrying transport current, *Adv. in Cryo. Eng. Materials*, Vol. 28, pp. 587-599, 1982.
- [37] M. Modena, Manufacture and Performance of the LHC Main Dipole Final Prototypes, 7th European Particle Accelerator Conference, Vienna, Austria, 26 - 30 Jun 2000 - E.P.S., Geneva, 2000. - pp.e-proc. 2148.
- [38] S. Le Naour et al, Magnetization Measurements on LHC Superconducting Strands, *IEEE Trans. Appl. Sup.* 9 no 2, pt. 2, pp. 1763-1766, 1999.
- [39] T. Ogitsu, Influence of Cable Eddy Currents on the Magnetic Field of Superconducting Particle Accelerator Magnets, Ph.D. thesis, Institute of Applied Physics, Tsukuba, Japan, 1994.
- [40] C. Y. Pang, Losses in type II superconducting wires due to alternating and rotating fields, Ph.D. thesis, University of Cambridge, 1980.
- [41] M. Pekeler et al., Coupled Persistent-Current Effects in the HERA Dipoles and Beam Pipe Correction Coils, DESY HERA 92-06, April, 1992.
- [42] R. Perin, Superconducting Magnets for the Large Hadron Collider, CERN-LHC-project-report-52, Geneva, 8 October, 1996.
- [43] P. Pugnât et al., Investigation of the Periodic Magnetic Field Modulation Inside Apertures of LHC Superconducting Dipole Models, 7th European Particle Accelerator Conference, Vienna, Austria, 26 - 30 Jun 2000, E.P.S., Geneva, 2000, pp.e-proc.2151.
- [44] P. C. Rem, Numerical Models for AC Superconductors, Ph.D. thesis, University of Twente, The Netherlands, 1986.
- [45] C. Riefel, Die HERA-Referenzmagnete, Diplomarbeit, Universität Hamburg, May 1992.
- [46] Courtesy of S. Russenschuck.
- [47] W. B. Sampson et al., Induced Axial Oscillations in Superconducting Dipole Windings, *IEEE Trans. Appl. Supercond.:* 5 (1995) no.2 pt.1: pp.1036-9.
- [48] P. Schmüser et al., Superconducting Accelerator Magnets, ISBN 981-02-2790-6.
- [49] M. Schneider, Decay and Snapback Studies on the LHC Dipole Model Magnets: A Scaling Law, Ph.D. thesis, TU Wien, 1998.
- [50] T. Schreiner, Current distribution inside Rutherford-type superconducting cables and impact on performance of LHC dipoles, Ph.D. thesis, Vienna University of Technology, 2002.
- [51] R. Stiening, A Possible Mechanism for Enhanced Persistent Current Sextupole Decay in SSC Dipoles, SSC Laboratory, SSCL-359, Jan. 1991.

References

- [52] D. R. Tilley and J. Tilley, *Superfluidity and Superconductivity*, Third Edition, Institute of Physics Publishing Ltd, Bristol, 1990.
- [53] D. Tommasini et al., Status of the LHC Short Dipole Model Programme, 7th European Particle Accelerator Conference, Vienna, Austria, 26-30 June 2000.
- [54] W. Venturini, The Test Facility for the Short Prototypes of the LHC Superconducting Magnets, Cryogenic Engineering Conference And International Cryogenic Materials Conference, Madison, WI, USA, 16 - 20 Jul 2001 (AIP Conf. Proc.; 613A) . - pp.106-113.
- [55] A. P. Verweij, *Electrodynamics of Superconducting Cables in Accelerator Magnets*, Ph.D. Thesis, Twente University, The Netherlands, 1995.
- [56] R. Wolf, Persistent Currents in the LHC Magnets, *IEEE Trans. Magn.*: 28 (1992) no.1 - pp.374-377.
- [57] R. Wolf, The Decay of the Field Integral in Superconducting Accelerator Magnets wound with Rutherford Cables, *Proc. of 15th Int. Mag. Tech. Conf.*, Beijing, pp. 238-241, Science Press, 1997.
- [58] M. Woudstra, *Electromagnetic Characterisation of BSCOO-2212 Multi Filament Wires*, Graduation Report, University of Twente, The Netherlands, 1995.

Summary

This thesis deals with the explanation and compensation of the effects ‘decay’ and ‘snapback’ in superconducting accelerator magnets, in particular in those used in the new Large Hadron Collider at CERN. During periods of constant magnet excitation, as for example during the injection of particles in the storage ring, the magnetic field in superconducting accelerator magnets shows a decay behavior. As soon as the particles are accelerated, the magnets are ramped, and the magnetic field ‘snaps back’ to the original hysteresis curve. Decay and snapback affect the beam in the machine and have to be compensated precisely in order to avoid losses of particles.

Historically, flux creep was thought to be the source of the field decay. However, its dependence on the excitation history of the magnets could not be explained. Today the field decay is attributed to so-called ‘Boundary Induced Coupling Currents’ (BICCs), which follow the zig-zag path along the strands, diffuse along the cable and redistribute among the strands. The BICCs can be observed as a ‘spatially periodic field pattern’ along the axis of a magnet. Long characteristic time constants of the current diffusion are responsible for the fact that the magnets remember the excitation history.

Decay and snapback are magnetization effects and call for a mechanism explaining the interaction between redistributing BICCs and the coil magnetization. The current redistributions change the self-field of the strands and induce local field changes in the coil. These field changes reduce the magnetization. As soon as the magnets are ramped after the end of injection, the coil magnetization is reestablished and ‘snaps back’. The magnetization decay and snapback can be observed in all components of the magnetic field in the center of the coil.

An advanced system with a good resolution in space and time is necessary for magnetic measurements of decay and snapback in superconducting accelerator magnets, and for their online-compensation in the machine. The development of several novel versions of a Hall detector for sextupole fields is described in chapter 3. They allow to analyze correlations between the decay, the snapback and the amplitude of the spatially periodic pattern.

In chapter 4 a comparison between systematic measurements, performed on 1 m short model dipoles and a numerical model with a single time constant, allows to understand the response of the snapback amplitude to different operation conditions and qualitatively illustrates that decay and snapback are due to an interaction between redistributing BICCs and the coil magnetization. Apart from that systematic measurements on 1 m model

Summary

dipole magnets allow to investigate the systematic appearance of decay and snapback in different components of the magnetic field, to analyze correlations between decays in different field components and to compare magnets of different geometric designs.

The behavior of the filament magnetization in the coil windings is analyzed in chapter 5. Numerical simulations are performed for field changes typically appearing during decay and snapback. The calculated data are used to develop formulas describing the filament magnetization during the decay after field changes at different angles and with different amplitudes, and during the snapback after different increases of the original background field.

In chapter 6 a demonstration experiment is presented, where decay and snapback are established on a model cable consisting of a superconducting central strand and six surrounding copper wires. The experiment validates the interaction between local field changes in the coil and the magnetization as a possible mechanism for the two effects.

In a second section of chapter 6, the Hall detector is used to perform measurements on 15 m long LHC dipoles. Correlations are analyzed between the amplitude of the spatially periodic field pattern and the parameters of decay and snapback.

The fitting formulas in chapter 5 are implemented into a numerical model for decay and snapback in a dipole coil. This is presented in a third section of chapter 6. The model takes into account two complementary mechanisms for the interaction between the current redistributions and magnetization. The first mechanism describes the reduction of the magnetization induced by the changing self-field in the strands. The second mechanism considers the impact of local field changes induced by current redistributions in other strands of the coil. Both mechanisms are complementary and add significant contributions to the decay. The model allows to analyze correlations between current redistributions in the coil, the spatially periodic field pattern and the field decay. Finally also the snapback is calculated.

The research presented in this thesis is a step towards a better understanding of ‘decay’ and ‘snapback’ in superconducting particle accelerators. The thesis provides tools for the prediction and compensation of both effects in the magnets, and for the analysis of correlations between different magnet parameters.

Samenvatting

Dit proefschrift handelt over het ontstaan en compensatie van ‘decay’ en ‘snapback’, ongewenste verschijnselen die optreden in supergeleidende versnellermagneten, in het bijzonder de magneten voor de in aanbouw zijnde Large Hadron Collider van CERN. Wanneer na opregelen de magneten een constante stroom voeren, bijvoorbeeld tijdens deeltjesinjectie in een opslagring, vertoont het opgewekte magneetveld een tijdsafhankelijk verloop naar een in het algemeen onbekende evenwichtstoestand, de zogeheten ‘decay’. Zodra vervolgens de magneten na deeltjesinjectie verder worden bekrachtigd tijdens deeltjesversnelling keert het magneetveld in zeer korte tijd terug naar de waarde die het had juist voordat de stroom tijdens de injectiefase constant werd gehouden. Deze terugkeer wordt aangeduid met ‘snapback’. Zowel decay als snapback beïnvloeden de kwaliteit van de deeltjesbundel in negatieve zin en dienen derhalve nauwkeurig gecompenseerd te kunnen worden.

Aanvankelijk werd aangenomen dat flux creep aan beide verschijnselen ten grondslag lag. Echter, hiermee kon de invloed van de bekrachtigingsgeschiedenis van de magneten op met name de amplitude van beide verschijnselen niet verklaard worden. In dit proefschrift wordt aangetoond dat beide verschijnselen veroorzaakt worden door een subtiel samenspel tussen filamentmagnetisatie en ‘Boundary Induced Coupling Currents’ (BICCs). BICCs ontstaan in de strands onder invloed van een veranderend magneetveld in de supergeleidende kabels en volgen een zigzag-patroon door de kabels waardoor zij een periodiek veldpatroon langs de magneetas genereren. De grote karakteristieke tijdconstanten waarmee BICCs diffunderen in de kabelrichting en zich herverdelen over de strands in de kabel verklaart ook de invloed van de bekrachtigingsgeschiedenis van de magneten op de amplitude van het tijdsafhankelijke gedrag van het veldpatroon als de stroom door de magneet na opregelen constant wordt gehouden (decay). Deze tijdsafhankelijke veldverandering betreft echter ook het veld in de spoelen ter plaatse van de filamenten, wat altijd de filamentmagnetisatie verlaagt hetgeen zich op zijn beurt uit in een verandering van het veldpatroon op de magneetas.

Zodra de magneetstroom na het boven beschreven decay verschijnsel wordt opgeregeld springt de filamentmagnetisatie terug naar de waarde juist voordat de decay intrad (snapback). Zowel decay als snapback kunnen worden waargenomen in alle harmonische veldcomponenten in het centrum van een versnellermagneet.

Het waarnemen en on-line compenseren van de invloed van decay en snapback op de veldcomponenten in een geïnstalleerde supergeleidende versnellermagneet vereisen een geavanceerd meetsysteem met grote temporele en spatiële resolutie. Om een nauwkeurige

Samenvatting

analyse van de correlaties tussen decay, snapback en de amplitude van het periodieke veldpatroon mogelijk te maken op basis van hun tijd- en plaatsafhankelijke invloed op de sextupool component van het magneetveld, is een sterk verbeterde Hall detector ontwikkeld waarmee de sextupoolcomponent in de boring van een versneller magneet nauwkeurig gemeten kan worden. Hiervan wordt in hoofdstuk 3 uitvoerig verslag gedaan.

Van een groot aantal 1 meter lange LHC model dipoolmagneten is systematisch het tijds- en plaatsafhankelijke gedrag van de verschillende multipoolcomponenten tijdens decay en snapback gemeten. Hiermee is voor het eerst een systematische analyse mogelijk gemaakt van het verband tussen de decay eigenschappen van verschillende multipoolcomponenten en de verschillen in deze verbanden tussen magneten met verschillende spoelgeometrie. De resultaten van deze metingen zijn vergeleken met een numerieke simulatie van de BICCs - gekarakteriseerd door slechts een enkele tijdconstante - onder verschillende bekrachtigingscondities van de magneten. Door dit model wordt met name de amplitude van de snapback kwalitatief goed beschreven hetgeen krachtig het beeld ondersteunt dat decay en snapback louter en alleen het gevolg zijn van de interactie tussen zich herverdelende BICCs en de filamentmagnetisatie in de spoelen.

Hoofdstuk 5 beschrijft een numerieke simulatie van de filamentmagnetisatie voor karakteristieke veldwaarden en veldveranderingen tijdens decay en snapback in de spoelen. Met behulp van deze simulaties zijn formules ontwikkeld voor de beschrijving van de filament magnetisatie, enerzijds tijdens de decay voor veldveranderingen van verschillende amplitude en ruimtelijke oriëntatie, anderzijds tijdens de snapback als functie van de toename van het oorspronkelijke achtergrondveld.

Hoofdstuk 6 is opgesplitst in drie samenhangende thema's. Allereerst wordt een demonstratie-experiment besproken waarin een enkele supergeleidende draad wordt onderworpen aan een axiaal periodiek roterend, transversaal magneetveld gesuperponeerd op een homogeen transversaal achtergrondveld. Resultaten van magnetisatiemetingen onder variatie van zowel het achtergrondveld als het periodieke veld valideren de interactie tussen locale veldveranderingen en de filamentmagnetisatie als mogelijk mechanisme voor het ontstaan van decay en snapback.

Vervolgens worden metingen met de eerder beschreven Hall sextupooldetector aan 15 meter lange LHC dipoolmagneten beschreven. Uit de resultaten worden de verbanden ontwikkeld tussen de amplitude van het axiaal periodieke veldpatroon in de boring van de magneten en de karakteristieken van de optredende decay en snapback.

Samenvatting

Tenslotte zijn de formules voor de filament magnetisatie uit hoofdstuk 5 ingebracht in een numeriek model voor de simulatie van decay en snapback in een dipoolmagneet. Dit model brengt twee complementaire mechanismen in rekening voor de interactie tussen stroomredistributie en filament magnetisatie. Het eerste mechanisme betreft de afname van de lokale filament magnetisatie door het verloop van het eigenveld als gevolg van een veranderende BICC in de betreffende strand. Het tweede mechanisme betreft de afname van de lokale magnetisatie door stroomherverdelingsprocessen in alle overige strands van de spoelen. Simulaties geven aan dat beide mechanismen complementair zijn en significant bijdragen aan de decay. Daarnaast verschaft dit numerieke model de mogelijkheid om onder zeer uiteenlopende operationele condities zowel het verband tussen als het verloop van stroomherverdeling in de kabels, het spatieel periodieke veld op de magneet-as, de decay en de snapback te simuleren.

Dit onderzoek heeft bijgedragen aan een beter begrip van het optreden van decay en snapback in supergeleidende versnellermagneten. De ontwikkelde numerieke modellen blijken betrouwbare middelen om hun gedrag in samenhang met de karakteristieke magneetparameters te voorspellen en compensatie van beide ongewenste verschijnselen mogelijk te maken.

Dankwoord

My education and in particular my Ph.D. thesis have been supported by many people providing valuable assistance and friendship.

I express thanks to Luca Bottura who brought me to CERN and established the contact with the University of Twente. Luca supervised my work at CERN. Herman ten Kate, Bennie ten Haken and Andries den Ouden supervised my Ph.D. project at the university and introduced me to a team with an exceptionally motivating working environment. Luca, Herman, Bennie and Andries guided my work, inspired me with brilliant ideas and made exceptional efforts to correct my text.

Four students have contributed to the success of this thesis. Linda Larsson and Eva Benedico collaborated with me at CERN on the Hall plate detector. Anton Kuijper performed measurements for the demonstration experiment at the university, and Khelil Kassoul performed magnetization calculations at CERN.

I am grateful to Michael Schneider, Stephane Sanfilippo, Walter Venturini, Pierre Pognat and Richard Mompou, who organized magnetic measurements in the 'Block-4' and 'SM-18' laboratories at CERN. At the same time, I would like to thank the operators in 'Block-4' and 'SM-18' for their skilled assistance during these experiments. Finally, many thanks also to Laurent Deniau, who provided important parts of the software for the reduction of snapback data measured in 'Block-4'.

I am also grateful to Linda Larsson, Eva Benedico, Stephane Sanfilippo, Luca Bottura, Olaf Dunkel, Marylin Gateau, Guy Deferne, Stefan Schloß, Ewald Effinger, Olivier Crettiez, Pierre Pognat, Thomas Schreiner, Andrzej Siemko, Francis Beauvais and Herve Sauze for their contributions to the Hall plate detector design and measurements performed.

Anton Kuiper, Andries den Ouden, Bennie ten Haken, Sander Wessel, Wouter Abbas and Harry Steffens contributed to the demonstration experiment in Twente, provided materials and advice. Jan Jaap Rabbers, Erik Krooshoop, Bert Metz, Olaf van der Meer, and Yuri Ilyin allowed me to use their computers for time consuming calculations.

I'd like to thank Rob Wolf, Arjan Verweij, Stephan Russenschuck, Ernst Helmut Brandt, Alexandre Akhmetov, Marco Breschi, Michael Schneider, Oliver Brüning, David Larbalestier and Alexander Squitieri for ideas and helpful discussions. Arjan Verweij and Rob Wolf provided software, LHC strand and data. Stephan Russenschuck provided

Dankwoord

software, pictures and calculations. Ernst Helmut Brandt at the Max Planck Institute in Stuttgart sent computer programs for the simulation of magnetic field penetrating into a superconducting filament. David Larbalestier and Alexander Squitieri measured the critical current density of LHC strands in great detail at the University of Wisconsin.

Pierre Schnizer assisted me with his computing knowledge, and Johannes Burger and Martin Podt helped me with the layout of the thesis.

Many thanks to Harriette Kamphuis, Harrie Plattje, Anita Borgerink, Ans Veenstra, Inke van der Werfhorst in de Wal, Rosine Leseche, Susan Maio, Huguette Gendraud and Cecile Granier.

In my private life several people contributed to the nice time I had during my Ph.D. studies. Especially my girlfriend Sofia Macedo and my family in Germany made great effort to provide continuous encouragement.